Master Thesis

Direct Numerical Simulation of supersonic flow over resolved and modeled roughness

Uttam Cadambi Padmanaban

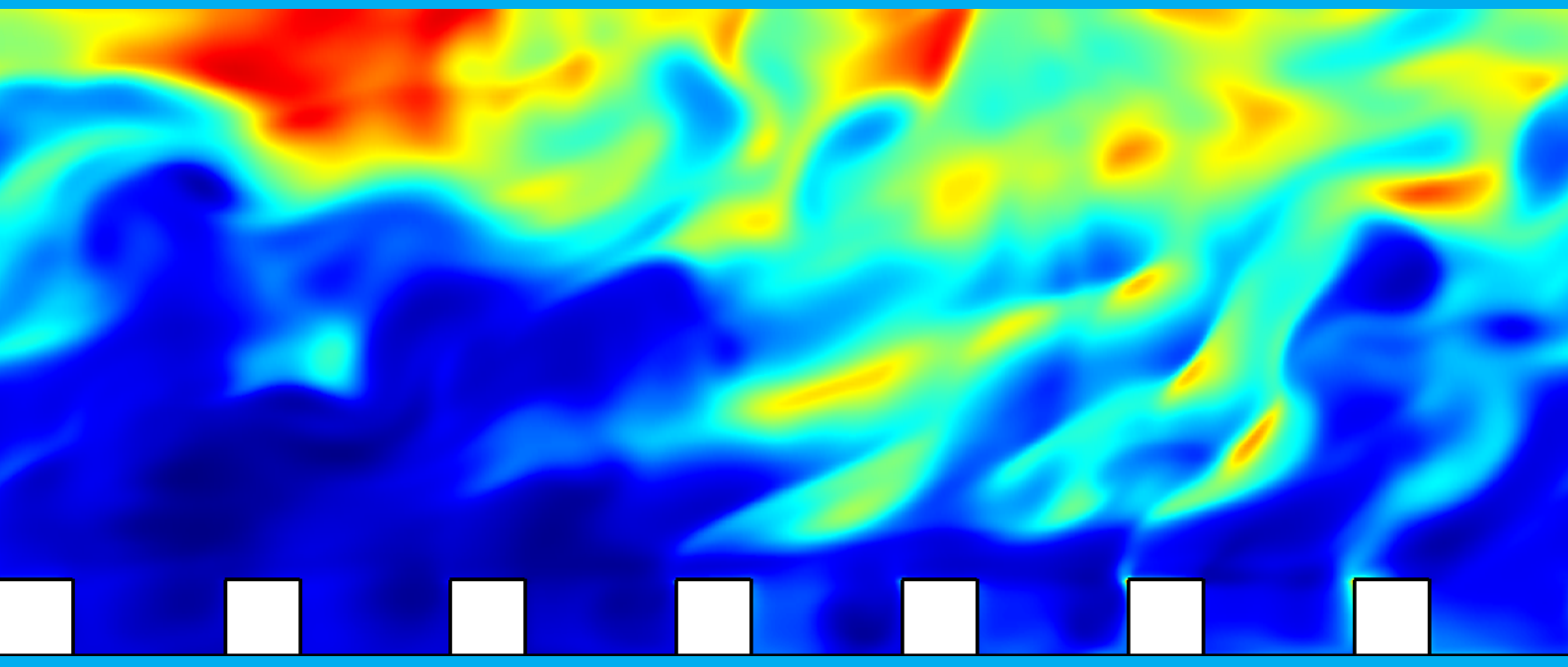

TU Delft

Master Thesis

Direct Numerical Simulation of supersonic flow over resolved and modeled roughness

by

U.Cadambi Padmanaban

to obtain the degree of Master of Science
at the Delft University of Technology,
to be defended publicly on November 15, 2021 at 09:00 AM.

Student number: 5005582

Project duration: April 1, 2021 – October 31, 2021

Thesis Committee: Dr. Davide Modesti, TU Delft, Thesis Supervisor

Dr. Stefan Hickel, TU Delft, committee member

Dr. Rene Pecnik, TU Delft, committee member

TU Delft

Acknowledgements

This master thesis is the culmination of support from numerous individuals who have guided me throughout this journey. I would like to thank my parents who have been a source of constant and immense support. The success of the master study is a testimony to their commitment in taking part not just in my successes but also in my failures. It feels surreal to be writing this section in my room where I spent nearly 15 years of my life. I owe every second of my master study to them and the sacrifices they have made to see me where I am today. I would also like to thank my sister who has moulded me into a disciplined, curious, hard-working and street-smart individual.

I would like to thank Dr. Davide Modesti for agreeing to take me as a master student. I was definitely not an easy student to work with. When I started my master thesis, I did not know how to write a single page. It was through months of tutoring and constant feedback that I have had one of the steepest learning curves in performing research, technical writing and critical thinking. His feedback and words constantly pushed me to do better and explore areas that were previously hidden to me. I would also like to thank him profusely for being exceptionally responsive through mails. I do not think I could have graduated on time had it not been for his prompt responses. He has been extremely flexible in accommodating timelines during the pandemic and I owe a great portion of my success to him. I will truly miss receiving mails from him. I hope I have been successful in making a small contribution to the world of fluids. I would like to acknowledge that the simulations performed in this study were on the hpc12 cluster of TU Delft and Snellius (earlier Cartesius) Dutch supercomputer.

I would like to thank my MSc Aerodynamics batch for being a great source of motivation for perseverance. Thank you Oscar, Xavi and Marina for teaching board games and almost motivating me to learn Spanish. Thank you so much Irene for all the support during COVID and for giving me advice when I needed it the most. I would like to also thank Muaaz who has been a model of inspiration. I hope he will forgive me for his grade getting lowered in CFD1 course. Thank you Vadim, Aniketh, Nivi, Sid, Ramu and Brian for being great classmates. I would also like to thank my seniors Kushal, Nikhilesh and Abhinand for their humility in guiding new students. Thank you Sagarika for helping with the house hunt and thank you Nivya for the occasional bike rides. I will try to be more regular. Thank you Sophie for listening and trying to be there for me when I needed you. Finally I would like to thank my lovely housemates at Geerweg 115 (Anna, Max, Naga and Aleksandra) for being cordial and allowing me to focus on my thesis during my stay.

The acknowledgement would not be complete without thanking two sets of people. Firstly, thank you Abhyuday and Parv for being my pillars during the master study. Be it late night assignment work in XIOR Phoenixstraat, or Doner at mid-night, or premier league nights at Tierney's, you guys have made life a lot easier during my stay in Delft. I cannot imagine completing my master's without the support, guidance and motivation from you guys. Thank you very much. Last, but not the least, I would like to thank a very special person. Despite some very difficult times, especially during COVID, I have always had the undivided attention, affection and care from her. She has been my critic, my compass, my lifeline and above all my best friend. Thank you very much Gauri! Hope things will get easier now that I expect to graduate.

U.Cadambi Padmanaban
Delft, November 2021

Abstract

Distributed surface roughness elements characterise Thermal Protection Systems (TPS) typical of supersonic and hypersonic flows. The presence of these distributed roughness elements cause an increase in drag and heat transfer. As opposed to incompressible flow over roughness elements, there are very few experimental and numerical studies on supersonic flow over roughness. The most fundamental computational technique wherein, all scales of turbulence is resolved is Direct Numerical Simulation (DNS). The cost of performing DNS of fully resolved roughness is even higher than canonical DNS because of the refined mesh needed to solve the roughness elements. To overcome this limitation, the current thesis aims at exploring low cost alternatives to DNS of fully resolved roughness for studying the effect of drag and heat transfer in supersonic flow over rough walls. DNS results from fully resolved full channel cube roughness for Mach 2 and Mach 4 at friction Reynolds number $Re_\tau \approx 500, 1000$ are analyzed. The results from the low cost models are compared against the fully resolved roughness simulated using full channels. Three lower-cost alternative, namely DNS of minimal channel flow of fully resolved roughness, DNS of modelled roughness and resolved RANS are considered. As for the DNS of minimal channel flow, it is found that the velocity shift ΔU^+ is predicted accurately and therefore the added drag. However, it cannot be used to predict the temperature field because of lack of outer layer similarity for the thermodynamic statistics. As for the modeled roughness, an extension of the model by Busse and Sandham originally developed for incompressible flows is considered. In this case the roughness geometry is substituted by the additional drag and heat transfer that it induces on the flow, which take the form of source terms in the momentum and energy equations. We perform 17 DNS simulations with modeled roughness and compare the results to the fully resolved simulation. We find that the parametric forcing method is able to predict the velocity shift with good accuracy, although recovering the equivalent roughness height from the model parameters can only be done *a posteriori*. The model is able to qualitatively reproduce the temperature field, but thermodynamic statistics are inaccurate when compared to DNS of the fully resolved geometry. The final computational technique is RANS. In real case applications, RANS require the use of wall functions, and in the case of rough walls knowledge of the equivalent roughness height k_s^+ is necessary. We attempt to see if RANS of fully resolved roughness can be used to estimate the velocity shift ΔU^+ and therefore k_s^+ by limiting ourself to the linear Spalart-Allmaras (SA) model. It is found to be inaccurate in computing the mean velocity profile at $k^+ \approx 40$ with improvements in accuracy observed for $k^+ \approx 80$ when compared with the results from DNS for cube roughness element. However, the accuracy is still low to be used for estimating k_s^+.

U.Cadambi Padmanaban
Delft, November 2021

Contents

List of Figures

List of Tables

List of Symbols and Abbreviations

Latin Symbols

B_q	Non-dimensional heat transfer
C_f	Skin-friction coefficient
C_p	Specific heat at constant pressure
C_v	Specific heat at constant volume
E	Total internal energy
$F(y,H)$	Forcing function
H	Roughness height parameter
L_x	Length along streamwise direction
L_y	Length along wall-normal direction
L_z	Length along spanwise direction
M	Mach number
N_x	Grid size along streamwise direction
N_y	Grid size along wall-normal direction
N_z	Grid size along spanwise direction
Pr	Prandtl number
R	Universal gas constant
Re	Reynolds number
Re_τ	Friction Reynolds number
St	Stanton number
T	Temperature
T_r	Recovery temperature
V	Volume of the fluid
b	Width
c	Speed of sound
f	Body force
h	Height
k	Roughness height
k_s	Equivalent sand grain roughness height
k_T	Thermal conductivity

l	Length
l_m	Mixing length
p	Pressure
q	Heat flux
r	Recovery factor
T_τ	Non-dimensional temperature
u	Streamwise velocity
u_τ	Viscous velocity scale
u'^2	Streamwise turbulent stress
$u'v'$	Reynolds shear stress
v'^2	Wall-normal turbulent stress
w'^2	Spanwise turbulent stress
y	Wall-normal distance
y_c	Unconfined region wall-normal height
y_r	Roughness sub-layer

Greek Symbols

δ	Boundary layer thickness
τ_w	Wall shear stress
ρ	Density
ΔU	Mean velocity shift
ν	Kinematic viscosity
λ	Wavelength
κ	von Karman constant
θ	Momentum thickness
δ_v	Viscous length scale
Φ	Bulk cooling term
σ	Viscous stress tensor
δ_{ij}	Kronecker Delta function
μ	Dynamic viscosity
γ	Ratio of specific heats
α	Roughness factor
ϵ	Virtual origin
$\eta(H)$	Auxiliary parameter

Abbreviations

DNS	Direct Numerical Simulation
GPFM	Ghost-Point-Forcing Method
HPC	High performance computing
HWA	Hot Wire Anemometry
IBM	Immersed boundary method
LDV	Laser Doppler Velocimetry
LSV	Laser Scan Microscope
MPI	Message passing interface
NASA	National Aeronautics and Space Administration
PIV	Particle Image Velocimetry
RANS	Reynolds averaged Navier–Stokes
SA	Spalart-Allmaras
SRA	Strong Reynolds Analogy
STREAmS	Supersonic turbulent accelerated Navier–Stokes solver
TPS	Thermal Protection Systems
WENO	Weighted essential non-oscillatory

Subscript

w	Property at the wall
∞	Property in free-stream
D	van Driest transformed
T	Trettel–Larsson transformed
V	Volpiani transformed
i	Streamwise direction
j	Wall-normal direction
k	Spanwise direction
b	Bulk quantity
I	Transformed incompressible co-ordinate
0	Total equivalent of the given property
e	Property at channel centerline
s	Property along a smooth wall

Superscript

$\sim$	Favre averaged quantities
$-$	Reynolds averaged quantities
$+$	Viscous scaled properties

$''$	Reynolds fluctuating quantity
$<>$	Spatial averaging
$*$	Semi-local scaling
t	Turbulent quantity
$'$	Favre fluctuating quantity

1

Introduction

The presence of surface roughness on supersonic flows has known to have detrimental effects in the form of increased skin-friction drag. This has been reported in the measurements by Gaudet and Winter (1973) where effects of different type of 'excrescences' on skin-friction drag is investigated. The detrimental effects of surface roughness is mainly seen over Thermal Protection Systems[1]. The present study focuses on ablation, a source of roughness that is very relevant to supersonic flows. This occurs over heat shields that form the TPS of space launchers, re-entry vehicles, and supersonic flight.

The advent of TPS can be traced back to World War II. There was a necessity for the development of relevant technology to safeguard systems from excessive thermal loads and design materials to act as thermal barriers to prevent failure. In the context of manned space missions, for example, there is an added responsibility of also protecting the crew from the system failure that could be fatal (Venkatapathy et al., 2009). The lack of TPS was a contributing factor towards a decelerated advancement in space launchers (Uyanna and Najafi, 2020). The TPS are classified depending on the mechanism that is used for the heat removal process and the materials that are used in doing so. The classifications is schematically depicted in Figure 1.1.

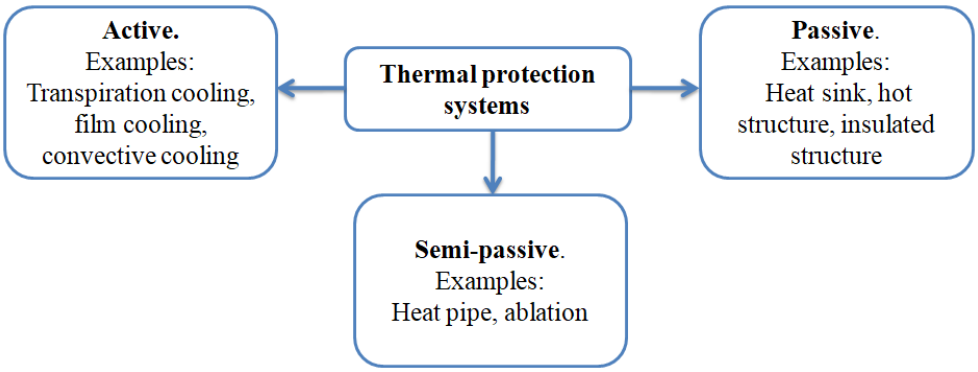

Figure 1.1: Thermal protection systems types with examples

The active and passive TPS offer a major drawback in terms of adding a weight penalty to the overall payload of space vehicles. In order to offer suitable means of protection against thermal loads and not add substantial weight to the overall system, the semi-passive TPS is preferred. It is implemented mostly through ablation. This is a method that involves heat absorption through the loss of material. It was demonstrated that there are a number of plastics reinforced with organic fibers that leave behind a carbonaceous structure upon decomposition into a gas when exposed to a high-temperature environment (Sutton, 1960). Uyanna and Najafi (2020) give a classification of these ablative materials as charring or non-charring materials based on the organic matrices that are used. In non-charring ablatives, there is no residue that is formed on the layer. Instead, the evolution of gasses from the ablatives causes a disturbance to the convective heat transfer to the material surface.

[1] hereafter referred to as TPS

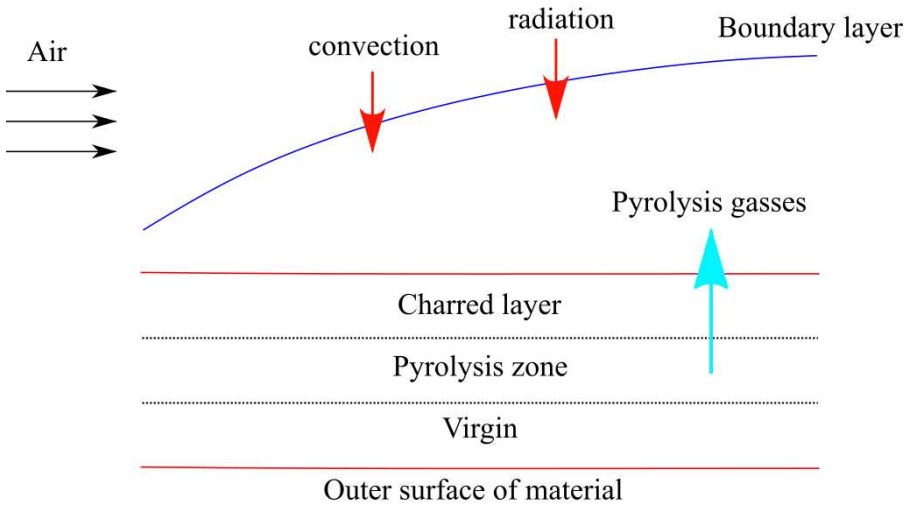

Figure 1.2: Process of ablation, figure adapted from (Uyanna and Najafi, 2020)

In the case of charring ablative materials as depicted in Figure 1.2, there is a formation of a charred layer due to heat transfer. Upon reaching a specified temperature, the material is eroded through surface shear, sublimation, or heat, leading to the formation of a porous charred layer and hot gasses. These gasses take away the heat from the incoming flow, percolate into the pyrolysis zone and provide insulation to the virgin material by increasing the internal pressure. The benefits of such ablatives are multi-fold: low density, great mechanical strength, good thermal insulation capabilities, and high heat shock resistance (Natali et al., 2018). These properties have made charring ablatives a preferred choice in today's thermal protection systems. The presence of charring ablative TPS leads to the formation of orderly distributed roughness elements. Research as early as 1968 at the Ames Research Center in NASA by Canning et al. (1968) confirmed the presence of these orderly distributed roughness elements. Canning et al. (1968) was among the first to study the roughness pattern over ablative surfaces using a body of revolution that was made from Plexiglas. The observations indicated turbulent wedges and grooves, that serves as a confirmation of preliminary studies. In addition to that, a novel discovery, which was the presence of cross-hatching on the surface due to the interlacing of longitudinal grooves, was also made. This pattern was also confirmed by Larson and Mateer (1968).

1.1. Roughness elements

Canning et al. (1968) defined the roughness elements that were formed due to the cross-hatching patterns as diamond elements. They even extended their results to include the conditions that were conducive to their formation. The results that were obtained point towards a supersonic flow that is a requirement for the formation of the flow patterns. To confirm this, experiments were conducted by Larson and Mateer (1968) on similar bodies of revolution using the same material and observed that the patterns were absent in a subsonic flow (Larson and Mateer, 1968). Since supersonic flow has been established as a basic requirement for the formation of roughness patterns, it was suggested that the origin of the formation of these patterns was pressure disturbances (Laganelli and Nestler, 1969). Another important result is that these patterns spread out around the body uniformly in the lateral and stream-wise directions which indicate a uniform distribution of the elements.

In addition to supersonic flow, Canning et al. (1968) also noticed the presence of transitional or turbulent boundary layer in regions of the roughness pattern that resembles diamond-shaped elements. Investigation of the Plexiglas flow model indicates initial laminar regions close to the tip of the body that did not develop these patterns. Further downstream, where the flow was at the end of the transitional and beginning of the turbulent region, the start of pattern formation was observed. The results also perfectly concurred with previous studies that were conducted on the visualization of flow in the region of roughness elements (Mochizuki, 1961). Although this was a necessary condition for the formation of the pattern, it was not sufficient. Larson and Mateer (1968) indicate that in addition to the presence of a turbulent boundary layer, the boundary

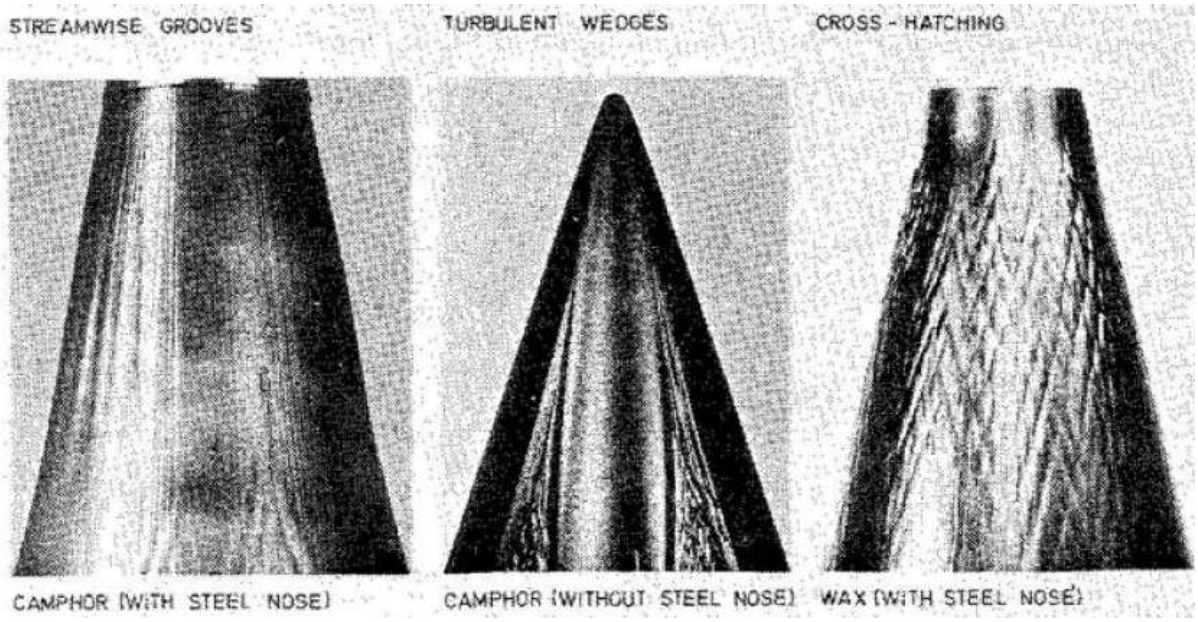

Figure 1.3: Typical roughness patterns developed on bodies of revolution of low temperature ablative materials at free stream Mach number $M_\infty = 5.3$, figure adapted from (Stock, 1975)

layer thickness δ is also an important parameter. The argument was that a thin boundary layer concerning equivalent roughness height k_s would allow proximity of the shock waves generated due to the roughness elements and the surface. This would enable better interaction and minimum viscous diffusion of the pressure disturbances that served to create the patterns (Laganelli and Nestler, 1969, Larson and Mateer, 1968).

Although there is no preference for the type of material used to observe the roughness pattern in supersonic turbulent flow conditions, it is essential that the material under investigation be ablative (Laganelli and Nestler, 1969, Larson and Mateer, 1968). There have been attempts at explaining the mechanism for the generation of these uniformly distributed roughness patterns on ablative surfaces. Canning et al. (1968) postulated longitudinal vortices that was also supported by Larson and Mateer (1968) and Laganelli and Nestler (1969). A study conducted later, revealed that there is no relation between the longitudinal vortices and the formation of the patterns (Stock, 1975). All the studies that were conducted around the generation of roughness patterns over ablative materials were experimental in nature. A very recent numerical study that was conducted in an attempt to reveal the mechanism responsible for pattern generation was also not successful (Trevino and Candler, 2015). Despite the study being on subliming ablative materials, it is safe to say that the mechanism responsible for the generation of roughness pattern is not yet fully understood or agreed upon. The current study, however, does not focus on the method of formation of roughness elements. The analysis is performed for an already existing roughness pattern on a geometry, also known as frozen roughness geometry.

Despite a noticeable dearth in available instrumentation and techniques, an experimental investigation of supersonic flow over rough walls to understand the difference in the structure of the boundary layer compared to a smooth wall was carried out by Goddard Jr (1959). The study also intended to explore any Reynolds and Mach number effects on the skin-friction drag at supersonic speed and draw comparisons with the incompressible counterpart. The paper presents some very interesting results - some of which are valid till date. 40 years following this study, the experimental work of Latin and Bowersox (2000) on supersonic flow over different roughness types provides information on mean flow and turbulence statistics of supersonic flow over rough walls. The investigation of supersonic turbulent boundary layer properties over rough surfaces gained momentum following the work of Latin and Bowersox (2000).

The studies carried out on ablative materials clearly indicate that roughness in supersonic flow is a topic that requires investigation. Unlike supersonic flows, incompressible boundary layer studies over rough walls have been more prevalent. The study of incompressible rough wall boundary layers can be traced back to the seminal work of Nikuradse et al. (1950) where skin-friction drag was experimentally ascertained by the use of water flowing through roughened pipes. Subsequent work by Hama (1954) and a detailed summary by

Clauser (1954) provide a solid knowledge base for incompressible roughness. This was later followed by many other studies by Perry et al. (1969), Krogstad et al. (1992), Jiménez (2004), Flack and Schultz (2014). All these studies collectively agree that the presence of surface roughness introduces a downward shift in the streamwise mean velocity profile $\widetilde{u}(y)$ when scaled by the friction velocity $u_\tau = \sqrt{\tau_w/\rho_w}$ where τ_w is the wall shear stress and ρ_w is the fluid density at the wall. This velocity shift is known as the Hama roughness function ΔU^+ and indicates the momentum deficit in the boundary layer. Incompressible roughness finds applications in roughness induced surfaces on hulls of ships and excrescences on turbine blades due to cavitation (Wu and Christensen, 2007). Despite the advancement in research in the area of incompressible roughness, its supersonic counterpart has progressed rather slowly. The lack of sufficient technology to carry out precise measurements may have been a contributing factor (Czarnecki, 1966).

The state of roughness is characterised by the equivalent roughness Reynolds number $k_s^+ = k_s u_\tau/\nu_w$ where k_s is the equivalent roughness height and ν_w is the fluid kinematic viscosity at the wall. While studying roughness, it became apparent that there can be a large variation in the roughness geometry and topography. To reconcile these variations and have a common 'denominator' against which the effect of roughness of different geometry can be compared, the equivalent roughness height k_s^+ is used. It is the hypothetical sand grain roughness size that is expected to produce the same drag as a rough surface of interest (Chung et al., 2021). Care should be taken to not ascribe this as a geometrical property; it is estimated *a posteriori*. The usage of k_s^+ is inspired by the work of Nikuradse et al. (1950). The classification of surfaces ensues based on k_s^+. For $k_s^+ \lessapprox 5$, the flow is considered hydraulically smooth and does not add any additional drag compared to a smooth wall. With an increase in the roughness Reynolds number ($5 \lessapprox k_s^+ \lessapprox 80$), the flow becomes transitionally rough accompanied by contributions of both pressure and viscous drag. For $k_s^+ \gtrapprox 80$, the flow enters the fully rough regime where ΔU^+ and by extension, the skin-friction coefficient no longer depends on the Reynolds number.

In addition to flow regimes, the incompressible roughness community have consensus on the Townsend's outer layer similarity hypothesis. According to this, the outer flow is not affected by the presence of the roughness elements expect for the role it plays in setting the boundary condition through u_τ. This hypothesis simplifies the analysis of rough walls. In case of supersonic flow over roughness, a lot of the aspects that have general consensus in case of incompressible roughness is still not conclusive. For instance, Goddard Jr (1959) mentions the onset of rough behaviour at $k_s^+ \gtrapprox 10$ as opposed to $k_s^+ \gtrapprox 5$. In case of supersonic flows, there exists discontinuities such as shocks and expansion waves that do not have an incompressible counterpart. These discontinuities disrupt the flow in ways that are not fully clear. As mentioned before, the study of supersonic flow over roughness has taken a backseat owing to the lack of sufficient instrumentation. After the pioneering work by Latin and Bowersox (2000), there have been limited experimental work by Ekoto et al. (2008), Peltier et al. (2016) and Kocher et al. (2018) with almost no computational work except the ones by Tyson and Sandham (2013) and Sharif and Guo (2007). The coming section attempts to gather the findings from these studies.

1.2. Experimental studies on supersonic roughness

It was mentioned earlier that the experiment of Goddard Jr (1959) was the first of its kind which was later followed by Latin and Bowersox (2000). It is interesting to see that the number of experimental studies on turbulent boundary layer over roughness in supersonic flow are very few (Ekoto et al., 2008, Kocher et al., 2018, Peltier et al., 2016). However, the results obtained are crucial and will be reviewed. Before proceeding, it should be noted that an 'incompressible' turbulent boundary layer refers to the case when $M_\infty < 0.3$ where $M_\infty = u_\infty/c_\infty$ is the ratio of the free-stream velocity u_∞ and the free-stream speed of sound c_∞ (Wenzel et al., 2018). The extensive work carried out in the Direct Numerical Simulation (DNS) of the compressible turbulent boundary layer by Wenzel et al. (2018) show that compressibility effects kick in as early as $M_\infty > 0.3$ with 2% variation in the properties compared to incompressible results and as high as 20% variation in the properties at $M_\infty = 0.85$ (Wenzel et al., 2018).

The first extensive experimental studies detailing the turbulent statistics in addition to the mean velocity profile was conducted by Latin and Bowersox (2000). The study was conducted for $M_\infty = 2.9$ and $Re_E = 2.0 \times 10^7$ where Re_E denotes the Reynolds number at the edge of the boundary layer. Three sand grain roughened and two uniformly distributed rough surfaces were investigated along with comparisons drawn to a smooth surface. The distributed two-dimensional ($2D$) roughness elements were in the form of square-shaped transverse bars and three-dimensional ($3D$) roughness elements in the form of cubes. The range of $k_s^+ = 100 - 570$ of the roughness elements that were investigated corresponds to the fully rough regime.

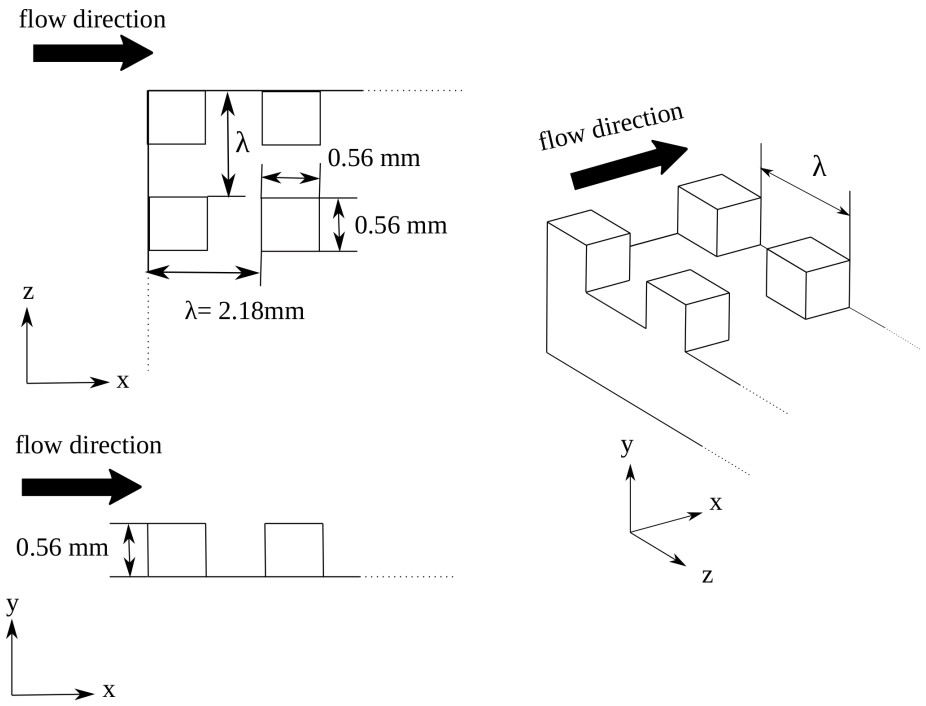

Figure 1.4: Topology of 3D roughness element depicted in top, front and isometric views along with dimensions studied by Latin and Bowersox (2000)

Since the roughness height of the sand grit papers were not known *a priori*, they were estimated using a confocal Laser Scan Microscope (LSM) with the mean calculated as $\overline{k}$. Laser Doppler velocimetry (LDV), hot wire anemometry (HWA), and schlieren photography were the techniques used to obtain measurements of the flow properties. The transverse square bars had dimensions of $0.56 \times 0.56mm$ along the streamwise and wall-normal directions with the bar spanning the entire width of the test-bed and a $\lambda = 2.18mm$. The cubic roughness elements had dimensions of $l \times b \times h = 0.56 \times 0.56 \times 0.56mm$ along streamwise, wall-normal and spanwise directions respectively with a similar $\lambda = 2.16mm$ as in the case of the 2D roughness element. The schematic of the roughness topology of the 2D roughness element along with dimensions is depicted in detail in Figure 1.5. Similar schematic for the 3D case is shown in Figure 1.4. By measuring the mean and turbulent flow properties at different streamwise locations, it was confirmed that the current investigation was of a zero pressure gradient, equilibrium boundary layer.

The van Driest transformed inner layer mean velocity profile (u_D) scaled by friction velocity (hereby referred to as the inner variables), reported by Latin and Bowersox (2000), displays a logarithmic variation in the overlap layer. In addition, there is a downward shift in the mean velocity profile of the roughness case compared to the smooth wall case. The purpose of using van Driest transformed mean velocity profile is to account for compressibility effects, such that the transformed velocity follows the incompressible law of the wall in the overlap layer given by $u_D^+ = (1/\kappa)log(y^+) + B$ where κ and B are constants. The mean velocity profiles investigated in the defect form $(u_D - u_{D_\infty})/u_\tau$ show a very good collapse for the smooth wall and roughness profiles. This lends weight to the success of the van Driest transformation applied to rough wall flows with adiabatic walls. The inner variable scaled velocity and with outer variable scaled wall normal distance shows a collapse of the mean velocity profile for all roughness types upto $y/\delta \approx 0.6$ except the 2D roughness. This hints at a possibly disparate mechanism in case of the 2D roughness. Upon closer examination, it is seen that the ratio λ/k where λ is the wavelength (indicated graphically in Figure 1.5) is ≈ 3.9. Perry et al. (1969) classify this type of roughness as 'd-type'. Therefore, it is not surprising to notice the difference in mixed scaled mean velocity profile.

The mean streamwise and wall-normal velocity fluctuations ($\widetilde{u''^2}$, $\widetilde{v''^2}$) scaled by mean streamwise velocity $\widetilde{u}$ shows a good collapse for all roughness types except for the 2D roughness. This also confirms the difference in turbulence production mechanism of the 2D roughness element. Additionally, the density scaled $(\rho/\rho_w)^{1/2}$ turbulent fluctuations behave differently. A collapse of the density scaled turbulent fluctuations of different roughness types is observed only for the streamwise turbulent fluctuations and not the wall-normal

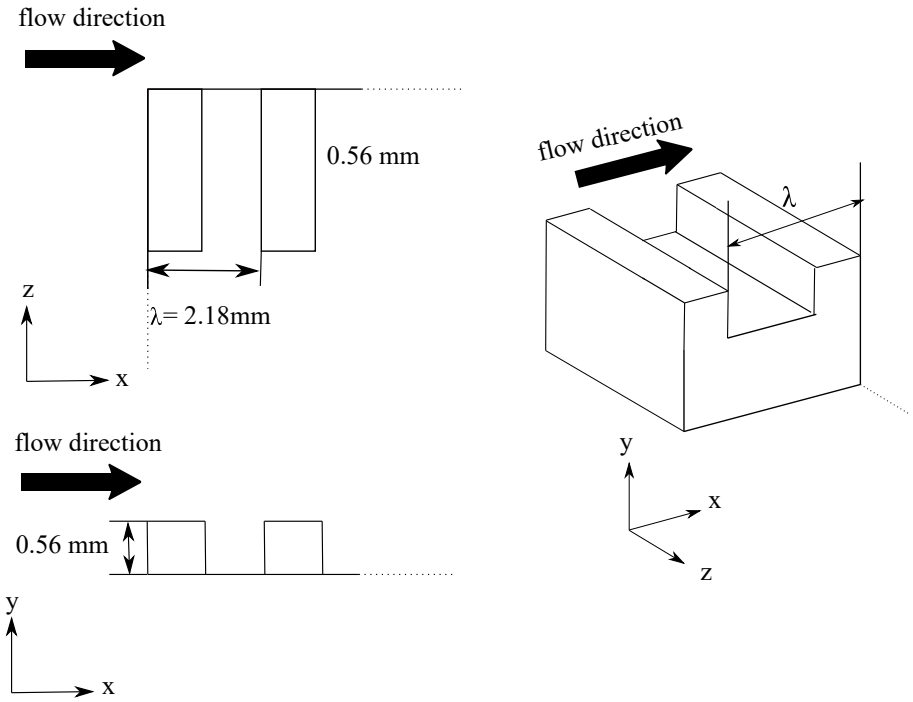

Figure 1.5: Topology of $2D$ roughness element depicted in top, front and isometric views along with dimensions studied by Latin and Bowersox (2000)

fluctuations (Latin and Bowersox, 2000). The density fluctuations, that play a crucial role in Morkovin hypothesis was also studied. According to Morkovin hypothesis, the compressible turbulent boundary layer properties will behave the same as its incompressible counterpart provided the mean density variations are taken into consideration (Morkovin, 1962). The hypothesis hinges on considering the density fluctuations to be negligible. It was observed that the difference in the peak value of density fluctuations between smooth and rough walls increases with increasing sand grain roughness height. These density fluctuations are also influenced by the nature of roughness and the topology.

The experimental studies by Ekoto et al. (2008) provides an extension of the results obtained by Latin and Bowersox (2000) by including another roughness type - the diamond roughness element. This experimental study explores the turbulence production mechanisms to explore the relation between observed physical mechanisms and roughness types. The effects of periodic roughness on the turbulent boundary layer at $M_\infty = 2.86$ and $Re_\theta = 60,000$ is characterized through experiments. Schlieren photography is performed with a knife edge aligned such that it produces gradients in density in the wall-normal direction along with particle image velocimetry (PIV), pressure-sensitive paint (PSP) and pitot pressure tubes. The viscous scaled equivalent sand grain roughness height $k_s^+ \approx 100$ indicates that the flow is in the fully rough regime. Measurements were also conducted for the smooth wall case to offer a comparison with the rough wall properties. The behavior of a canonical sand-grain type roughness, as was shown by Latin and Bowersox (2000) can be represented by a $3D$ roughness element with cubes of equal separation. This is the first type of roughness element investigated, hereby referred to as the square roughness element. A small difference is that the cavity between two adjacent roughness elements is hemispherical. The ratio $\lambda/w = 2$ indicates that this type of roughness element might be d-type. Just as in the case of incompressible flow, we expect the formation of stable vortices inside the roughness grooves (Perry et al., 1969).

The square roughness element had a length and width, corresponding to the dimensions in the streamwise and spanwise directions of $1.59mm$ each with a depth of $0.79mm$ and $\lambda = 3.18mm$. The diamond roughness element had a major axis length of $9.0mm$, spanwise width of $1.59mm$ and depth of $0.79mm$. The topology and dimensions of the elements are depicted in Figure 1.6b and Figure 1.6a. The Schlieren photography results indicate the absence of strong gradients in case of square roughness element that are present in the diamond roughness element. These waves penetrate well into the domain. This also indicates that the roughness crest in case of diamond roughness element is supersonic with the element protruding well into the supersonic region of the flow. The same cannot be said regarding square roughness element and

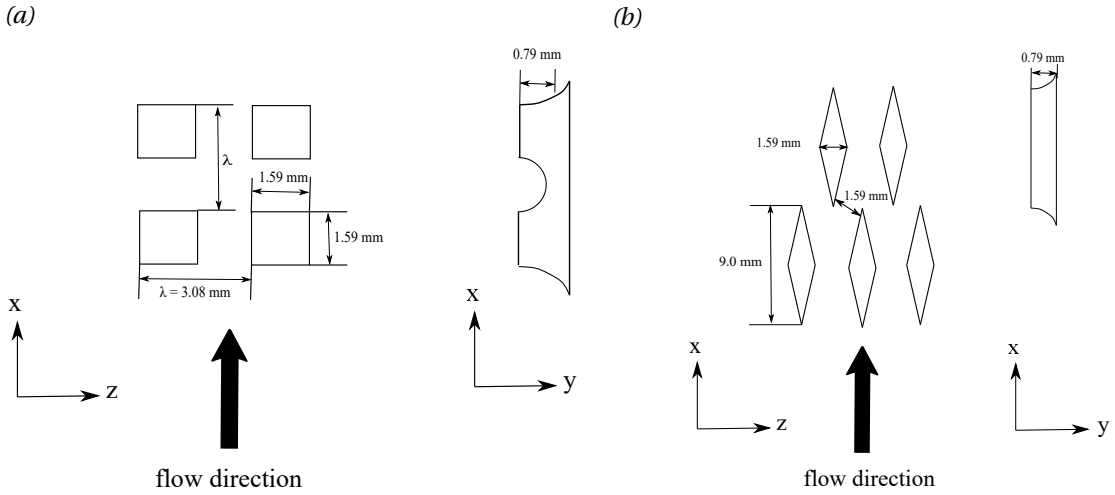

Figure 1.6: Roughness topology studied by Ekoto et al. (2008) for $Re_\theta \approx 60,000$, $M_\infty = 2.86$ and the associated dimensions for (a) Square roughness element and (b) Diamond roughness element

the smooth wall case.

The mean velocity profile of the smooth wall scaled by inner variables collapses well with the theoretical mean velocity profile calculated by using the logarithmic relation in the overlap layer and applying the van Driest compressibility transformation. There is also a downward shift in the overlap layer of the mean velocity profile for the square roughness element. Defect profiles scaled by outer variables reported by Ekoto et al. (2008) show a perfect collapse for the smooth wall compressible, incompressible and square roughness element mean velocity profiles along with the results obtained from theory. Ekoto et al. (2008) report the Reynolds shear stress profile $-\overline{\rho}\widetilde{u''v''}$ scaled by τ_w. The profile shows a good collapse for the square roughness element with the smooth wall case. The Reynolds shear stress profile of the diamond roughness element displays a reduction in Reynolds shear stress of almost 30% compared to the other two cases in the boundary layer outer region. For comparison, the compressible and incompressible smooth wall Reynolds shear stress profile of Luker et al. (2000) and Klebanoff (1955) respectively was added. The principal strain rate is defined as $d\tilde{u}/dy$ with extra strain rates as $d\tilde{v}/dx, d\tilde{v}/dy$ and $d\tilde{u}/dx$. The principal strain rates are known to have significant values for the smooth and square roughness element with extra strain rates being negligible for both. However, Figure 1.7 reported by Ekoto et al. (2008) showing the contours of $d\tilde{v}/dx$ extra strain rate for the diamond roughness pattern indicate that their presence cannot be ignored and contribute towards turbulence production mechanisms.

Peltier et al. (2016) conducted experiments that involves the influence of cross-hatched (diamond) roughness pattern with $k_s^+ = 600$ on a $M_\infty = 4.9$, $Re_\theta = 63000$ turbulent boundary layer. A quick look at the roughness Reynolds number shows that it is 6 times the value used in Ekoto et al. (2008), although the roughness heights are the same. They used PIV for the quantitative determination of properties and schlieren photography provided a qualitative description. The dimensions and topology of the roughness elements were similar to those used by Ekoto et al. (2008) (refer to Figure 1.6b for more details) in their experiments. The mean velocity profiles and turbulent stresses were estimated for the rough wall case and comparisons were drawn to the smooth wall counterpart. Flow structures in the logarithmic layer of the flow over roughness were also postulated and compared to its smooth wall counterpart. The Schlieren flow visualization of the rough wall reported by Peltier et al. (2016) shows alternating light and dark bands indicative of alternating high and low-density regions. Latin and Bowersox (2000) and Ekoto et al. (2008) report that these bands correspond to shocks and expansion waves. They penetrate well into the boundary layer implying a breakdown of the wall similarity (Peltier et al., 2016). The mean velocity profile in outer variables for the rough wall is shifted downward indicating a momentum deficit caused by the reduced velocity close to the wall. The inner variable scaling follows the logarithmic profile in the overlap region with the downward shift of $\Delta U^+ \approx 12 - 13$. These results provide further support to the results from Latin and Bowersox (2000) and Ekoto et al. (2008).Peltier et al. (2016) reported the variation of Reynolds shear stress ($-\widetilde{u''v''}$ scaled by u_∞^2) with the streamwise direction scaled by outer variables, at different wall-normal locations. The profile shows a highly oscillatory trend with large amplitudes especially for wall-normal distances close to the wall. The amplitude of the oscillations

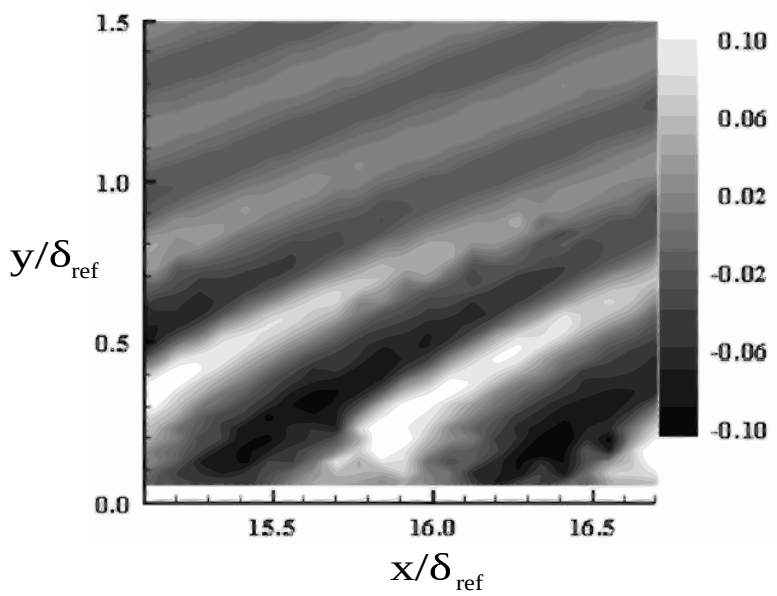

Figure 1.7: Contours of $d\tilde{v}/dx$ extra strain rate for flow over diamond roughness element at $Re_\theta \approx 60,000$ and $M_\infty = 2.86$ with $k_s^+ \approx 100$ reported by Ekoto et al. (2008) at $x/\delta_{ref} = 15.9$. Flow is from left to right and the roughness elements are at the bottom

reduces as the edge of the boundary layer is approached ($y/\delta \approx 0.7$), showing that roughness element effects penetrate well into the outer region of the boundary layer.

Perhaps the most recent experimental study of the supersonic turbulent boundary layer over roughness is presented by Kocher et al. (2018). In addition to the smooth wall and diamond roughness element case, this study also focuses on the non-uniform roughness pattern defined as the 'realistic' roughness (Wu and Christensen, 2010). Such a roughness type is found in turbine blades whose surfaces are damaged by foreign object and debris, leaving behind an irregular pattern of roughness elements with a great variety of topological scales of roughness (Wu and Christensen, 2007). Kocher et al. (2018) performed mean flow and turbulent statistics studies in a $M_\infty = 2$ turbulent boundary layer using PIV and Schlieren photography techniques. The measurements were taken at 3 locations along the streamwise direction. The diamond roughness topology was similar to that of Ekoto et al. (2008) and Peltier et al. (2016) but had a half angle of 26° and $k = 0.33mm$. Another point of difference was that the bottom edges of the diamond roughness element were inclined at 90° to the base as opposed to a hemispherical trough reported in Ekoto et al. (2008). The flow was in the fully rough regime with $k_s^+ = 270$. Figure 1.8a and Figure 1.8b shows streamwise velocity field of the diamond roughness case from Kocher et al. (2018). The thicker low velocity regions are directly behind the shock wave. The regions of expansion fans can be identified by observing the velocity vectors that are downstream of a shock and aligned parallel to the wall. These are regions where the local change in flow direction and compression caused by the presence of shock waves is reverted to the original state. Kocher et al. (2018) reported wall normal velocity streaks in the contour plot of wall normal velocity that are approximately aligned with the inclination of the shock waves. The wall normal velocity shows an upward deflection of $10m/s$ in the regions where shock waves are present. In regions of expansion waves, the flow re-aligned with the direction of the free-stream. This result is in line with the previous observations by Ekoto et al. (2008) and Peltier et al. (2016).

The mean velocity profile, as expected, shows a downward shift in the overlap region when scaled by inner variables. The outer variable scaling shows the reduction in the velocity close to the wall for the roughness case symbolic of the momentum deficit and increased drag caused by the presence of roughness. The mean velocity profile in inner variables from Kocher et al. (2018) clearly indicates a downward shift in the logarithmic region for the diamond roughness element of $\Delta U^+ = 4.5$. When comparing the $\Delta U^+ = 4.8$ obtained by Ekoto et al. (2008) for Mach 2.9 at $k_s^+ \approx 100$ and $\Delta U^+ = 12 - 13$ obtained by Peltier et al. (2016) for Mach 4.9 flow at $k_s^+ = 600$, Kocher et al. (2018) hypothesized that the roughness function could be dependent on the Mach number. The Reynolds shear stresses for the smooth and diamond roughness element cases reported by Kocher et al. (2018) converge beyond the edge of the boundary layer suggesting that the roughness effects

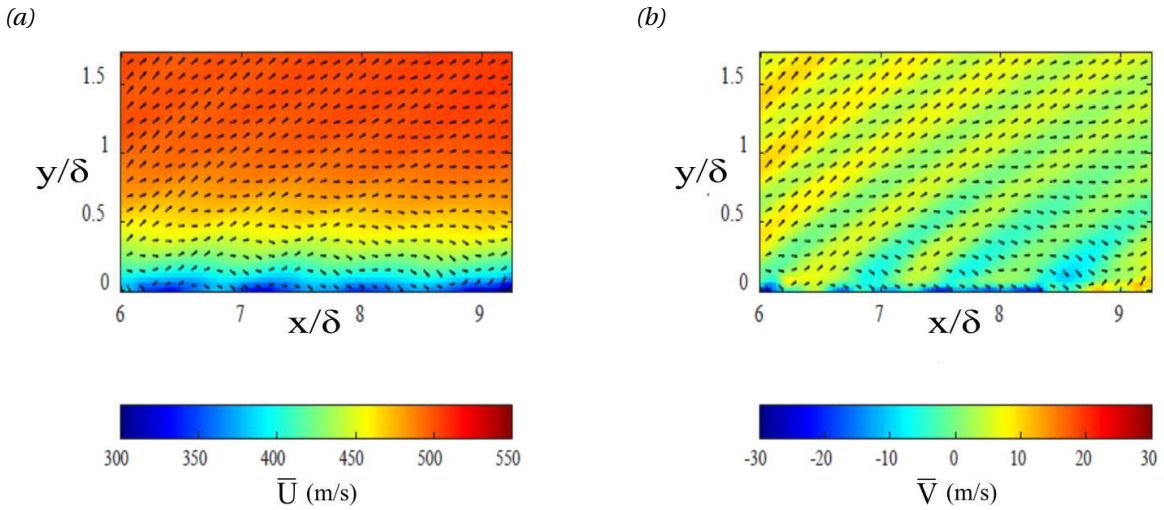

Figure 1.8: PIV velocity field results of a rough wall with diamond roughness element reported by Kocher et al. (2018) for $Re = 3.0 \times 10^7$ and $M_\infty = 2.01$ and equivalent roughness height (roughness height scaled by friction velocity u_τ), ${}_sk^+ = 270$ for (a) streamwise component and (b) wall normal component Flow is from left to right and roughness elements are at the bottom

penetrate the boundary layer. Incidentally, the magnitude of the Reynolds shear stress is the highest close to the wall and is greater for the diamond roughness element when compared to the smooth wall. The contours of Reynolds stress for the diamond roughness element display a wave-like pattern similar to the Schlieren photography results. Here, the high magnitude Reynolds stress regions correspond to shock locations and low magnitude Reynolds stress regions correspond to expansion locations. This serves as a confirmation to the local distortions caused by the presence of shocks and expansions in case of the diamond roughness element. The streamwise variation of the Reynolds shear stress was extracted at a location of $y/\delta = 0.15$. The streamwise periodic variation of the Reynolds shear stress with large amplitudes for the diamond roughness element as opposed to a relatively flat profile for the smooth wall case, further substantiates the periodic nature of the distortions caused by the roughness element.

1.3. Computational studies

Experimental studies are a good way to understand the flow physics for most problems. Within the limits of experimental uncertainties and limited spatial resolution, they provide a realistic picture of the problem. However, there are some challenges associated with performing experiments in supersonic regime. Measuring the properties close to the wall is an inherent challenge associated with wall bounded flows. Although the mean flow properties can be captured with relative ease, it was not until the study conducted by Latin and Bowersox (2000) that the first turbulent statistics for supersonic turbulent flow over roughness was reported. This is considering that the work on supersonic turbulent boundary layer over roughness started in the 1950s. The database for supersonic turbulent boundary layer has improved over the last 2 decades, but the work is not complete.

To expand the body of existing knowledge, more experiments are expected to be performed at higher Reynolds numbers, representative of actual flow conditions that not only require sophisticated data acquisition and reduction systems, but also new parameters to be investigated. For example, the measurement of wall shear stress τ_w in experiments is a notoriously difficult task (Chung et al., 2021). Additionally, as mentioned before, there is no consensus on some very basic aspects of supersonic roughness. Computational studies offer a solution in this regard. It allows flexibility in setting the parameters to be investigated and allows control of spatial resolution. There are lucrative options to change the solution strategies and analyze the changes in results that follow. Despite these options, computational studies of supersonic flow over roughness is very limited. In this review, two such studies are investigated. The first is a DNS of supersonic turbulent boundary layer over wavy surfaces. The second is a Reynolds Averaged Navier-Stokes (RANS) study attempting to validate the experimental results of Latin and Bowersox (2000) and bring out some key areas of deviation from the experimental results and a possible explanation of the same.

Tyson and Sandham (2013) performed DNS of compressible turbulent channel flow studies over wavy surfaces for $M_\infty = 0.3, 1.5$ and 3.0. The wavy surface was represented by a sine function with varying amplitudes and wavelengths. The type of surfaces investigated lie in the transitionally rough and fully rough regime. This was an attempt to characterize the effects of compressibility on the mean flow and turbulent properties. It was discovered that there is presence of shock waves in the case of $M_\infty = 3.0$. The increase in the Mach number, causes a subsequent decrease in the van Driest transformed mean velocity deficit ΔU_D^+. The presence of shock waves contributed significantly towards altering the wall normal velocity fluctuations by increasing them at the shock locations. The increase in Mach number also increases pressure drag contribution towards the overall drag experienced by the surface. The location of maximum pressure along the wall normal direction of the roughness element also moves towards the peak with an increase in the Mach number. This study brings out the feature of shock and expansion waves in a supersonic turbulent boundary layer over roughness to highlight the compressibility effects introduced by them. It identifies the changes brought about to the mean velocity profile and turbulent fluctuations.

Sharif and Guo (2007) performed a numerical investigation of a Mach 2.7, $Re = 2 \times 10^7$ supersonic turbulent boundary layer over roughness using the $k-\omega$ and stress-ω turbulence models. The results were compared with the experiments by Latin and Bowersox (2000). The roughness element types that were investigated resembled those used by Latin and Bowersox (2000). In general, the predictions of the stress-ω model of the boundary layer thickness is less accurate compared to the $k-\omega$ model possibly hinting at the inability of the ω boundary condition to capture the roughness effects close to the wall. The predictions by the turbulence models closely follow the trend observed in the experimental studies - velocity deficit for the rough wall case indicating momentum loss due to presence of roughness elements. However, both turbulence models over-predict the velocity profiles. The computational results show good agreement with the experimental results for small roughness Reynolds number (for example, the 80 grit sand paper where $k_s^+ = 104$) and progressively worsens as the roughness Reynolds number is increased for the 20 Grit plate for which $k_s^+ = 571$. The velocity defect profiles are under-predicted by the turbulence models. However, the smooth surface predictions by the turbulence models are excellent. A similar increase in the disparity of the inner variable scaled mean velocity profiles (particular focus on the log law region) is observed with an increasing roughness height. u_τ is under-predicted by almost 15%.

1.4. Reduced order models of distributed roughness

Through the years following the DNS of plane channel flow by Kim et al. (1987), it has been established that the cost of performing DNS is high. This high computational cost stems from the need to compute a large range of scales of turbulence. These range from the smallest, known as Kolmogorov scales where dissipation takes place to the energy-containing largest integral length scales. The size of the domain under study should be sufficiently large to allow the physics of the large scale to be resolved reasonably well. On the other hand, the grid resolution needs to be fine to allow the resolution of the Kolmogorov scales. The cost of performing DNS scales with Re_τ^3 (Pope, 2001). Here, $Re_\tau = u_\tau h/\nu_w$ is the friction Reynolds number with u_τ the friction velocity, h the channel half-height in case of channel flows and ν_w the kinematic viscosity at the wall. For the case of wall bounded flows with roughness elements, this cost of running DNS is further amplified due to the grid resolution requirement around the roughness elements. Additionally, the use of the equivalent sand roughness k_s^+ is not particularly sufficient when studying roughness. To begin with, it is computed *a posteriori*. Secondly, although the equivalent sand grain roughness can be interchanged with the roughness function in the fully rough asymptotic limit, which gives an idea of the shift in mean velocity profile, there is no relation between this and the effect of roughness on the turbulent fluctuations. There exists no clear correlation between k_s^+ and the geometry and topological features of roughness (Chung et al., 2021). To be able to study supersonic flow over roughness using DNS, a modelling approach has to be adopted to simplify the cost requirement. Busse and Sandham (2012) have provided a parametric forcing approach to model the effect of the roughness. An extra force term is added to the momentum equation based on the idea that the effect of roughness can be substituted by the drag that it induces. The results of Busse and Sandham (2012) show that the model roughness captures the main flow features of the roughness such as the vertical shift characterised by the Hama roughness function ΔU^+, outer layer similarity, turbulent statistics and mapping between the roughness height parameter in the modeled roughness to the equivalent roughness Reynolds number. All these features make it a promising candidate as an alternative to fully resolved roughness simulations.

In addition to the modeled roughness approach, another technique that has gained popularity in reducing computational cost is the use of minimal-span channel first described by Jiménez and Moin (1991). It

gained subsequent attention in the study of wall-bounded turbulence by Flores and Jiménez (2010), Hwang (2013) and Lozano-Durán and Jiménez (2014). It employs Townsend's outer layer similarity in arguing that the velocity shift ΔU^+ is a result of interaction of the roughness element with the flow within the roughness sub-layer, a region in the close vicinity of the roughness element. The velocity shift remains constant beyond this roughness sub-layer well into the outer layer of the flow. Since the quantity of interest from an engineering perspective is the flow retardation characterised by ΔU^+, it is sufficient to have a domain that captures the near wall cycle and is not required to resolve the largest integral length scales. If a channel flow configuration is considered with a channel half height of h, the cost of running a DNS will now scale as k_s^{+3} as opposed to Re_τ^3 (Chung et al., 2015). There is a potential reduction of $(h/k_s)^3$ compared to a conventional DNS. Studies by Chung et al. (2015) have also shown that using minimal-span channel results in a slight overestimation of the mean velocity close to the channel centerline. However, this overestimation is present in both smooth wall and a wall with resolved roughness elements thereby not affecting the velocity shift ΔU^+. Although the minimal-span channel cannot capture the mean velocity of the smooth and rough walls accurately in the outer layer, the mean velocity shift is not affected and can be accurately recovered. This technique has shown great promise in studying resolved roughness and can potentially prove to be yet another alternative to full channel resolved roughness.

1.5. Problem statement

The review on supersonic roughness presents us with a few key observations that will drive the current study. Firstly, the number of experimental investigations of supersonic roughness is limited - studies by Latin and Bowersox (2000), Ekoto et al. (2008), Peltier et al. (2016) and Kocher et al. (2018) have been among the only detailed documentations of supersonic roughness till date. They have provided some preliminary results. However, there are limitations to performing experiments in terms of the conditions, geometry of roughness and roughness topology. While it may seem that a computational study would be beneficial in these aspects, it does not come without challenges. Computationally, performing a DNS would involve elevated costs considering the resolution requirements close to the roughness element. On the other hand, there are limited attempts at studying supersonic roughness using RANS models with the only existing one in literature not showing the required level of accuracy. The modeled roughness approach by Busse and Sandham (2012) has proven to be useful in studying trends in the mean flow properties and turbulent statistics for incompressible roughness at a lower cost. However, its extension to supersonic flows and its subsequent ability to model the energy equation is still not investigated. The minimal-span channel approach has been successful in replicating the mean velocity shift ΔU^+ of the full channel simulation but at a much lower cost. This allows the computation of the drag at an accuracy level comparable with full channel simulations. The investigation of minimal-span channel for supersonic flows has not yet been carried out. With all these aspects in mind, the present work aims to assess the accuracy of cheap computational approaches for modelling supersonic flows over rough walls. In particular, three computational approaches which are cheaper than DNS of fully resolved roughness will be considered:

1. Parametric forcing of Busse and Sandham (2012)

2. Fully resolved roughness in minimal-span channel

3. Fully resolved roughness using RANS

The following research questions will be answered as part of this work

- Can approaches 1), 2) and 3) be used to accurately predict the drag variation over supersonic roughness, namely ΔU^+ and k_s^+?

- Can approaches 1), 2) and 3) be used to accurately predict the heat transport over supersonic roughness, namely Stanton number?

In this work, an attempt will be made to answer the above research questions by comparing the results of 1), 2) and 3) to the DNS of fully resolved roughness in full channel flow simulation and to experimental data available in literature.

1.6. Thesis outlook

The thesis begins with the theoretical background in Chapter 2. Here, the preliminary concepts such as Law of the wall, mathematical operations such as Reynolds averaging will be discussed along with compressibility transformations and Reynolds analogy. There is a discussion on roughness provided. Chapter 3 will focus on numerical methodologies wherein the computational techniques used in this thesis will be expounded along with the details of the solvers used. The test cases used for the study are presented with the validation of the numerical methodologies. Chapter 4 presents the results of the study along with its discussion and Chapter 5 closes with conclusions, providing answers to the research questions and recommendations for future work.

2

Theoretical framework

The chapter begins with the introduction of the governing equations of this study, namely the compressible Navier–Stokes equations. The channel flow configuration and the canonical law of the wall is introduced. It is shown that the law of the wall can be recovered in the compressible case when using compressibility transformations. Finally, the effect of roughness on the flow is described.

2.1. Governing equations

Since the study is focused on computational study of supersonic flow over roughness, the starting point of the analysis is the governing equations. They form the fundamental relations that will be solved for the flow cases investigated in this thesis. The compressible Navier–Stokes equations for a perfect heat conducting gas are:

$$\frac{\partial \rho}{\partial t} + \frac{\partial \rho u_i}{\partial x_i} = 0 \tag{2.1a}$$

$$\frac{\partial \rho u_i}{\partial t} + \frac{\partial \rho u_i u_j}{\partial x_j} = -\frac{\partial p}{\partial x_i} + \frac{\partial \sigma_{ij}}{\partial x_j} + f\delta_{i1} \tag{2.1b}$$

$$\frac{\partial \rho E}{\partial t} + \frac{\partial \rho u_j H}{\partial x_j} = -\frac{\partial q_j}{\partial x_j} + \frac{\partial \sigma_{ij} u_i}{\partial x_j} + f u_1 + \Phi \tag{2.1c}$$

where the subscript $i = 1,2,3$ represents the stream-wise, wall-normal and span-wise directions also given by x, y and z respectively, ρ, the density, p, the pressure, $E = C_v T + u_i u_i/2$ the total energy per unit mass, where C_v is the specific heat at constant volume, and $H = E + p/\rho$ the total enthalpy. The visocus stress tensor σ_{ij} and heat flux vector q_j are given by:

$$\sigma_{ij} = \mu\left(\frac{\partial u_i}{\partial x_j} + \frac{\partial u_j}{\partial x_i} - \frac{2}{3}\frac{\partial u_k}{\partial x_k}\delta_{ij}\right) \tag{2.2}$$

$$q_j = -k_T \frac{\partial T}{\partial x_j} \tag{2.3}$$

where μ is the dynamic viscosity and $k = C_p\mu/Pr$ is the thermal conductivity where $Pr = 0.72$ is the molecular Prandtl number and C_p is the specific heat at constant pressure. The dependence of viscosity on temperature is accounted through by power law with exponent 0.76. It is noted that the forcing term f ensures that there is constant mass-flow rate enforced at each time step. Similarly Φ is a bulk cooling term which is evaluated at every time step to control the bulk temperature.

2.2. Averaging

2.2.1. Reynolds averaging

Statistical averaged quantities are important while studying turbulent flows. Two types of averages are considered for Navier–Stokes equations and used in this thesis. Consider a statistically stationary variable $\phi(x, y, z, t)$

over a time interval 0 to T. The ensemble average of this quantity is given by

$$\overline{\phi}(x,y,z,t) = \frac{1}{\Delta t}\int_0^t \phi(x,y,z,\tau)d\tau \tag{2.4}$$

For a Reynolds decomposition, the variable $\phi(x,y,z,t)$ is decomposed into the sum of its ensemble average and a fluctuating component, given by

$$\phi(x,y,z,t) = \overline{\phi}(x,y,z,t) + \phi'(x,y,z,t) \tag{2.5}$$

The second type of average is the spatial average. Spatial average is used for a channel flow configuration where there is a spatial homogeneity in the streamwise and spanwise directions. It is given by

$$\langle\phi(y)\rangle = \frac{1}{L_x}\frac{1}{L_z}\int_0^{L_x}\int_0^{L_z}\overline{\phi}(x,y,z)dxdz \tag{2.6}$$

Some rules of the Reynolds averaging process are given below

$$\overline{\overline{\phi}} = \overline{\phi} \qquad \overline{\phi'} = 0 \qquad \overline{\overline{\phi}\psi'} = 0 \tag{2.7}$$

where ψ is a similar physical dynamic quantity different from ϕ. The Reynolds averaging of momentum-conservation equations yields a product of fluctuating terms, known as the Reynolds stress tensor given by $\langle u_i' u_j'\rangle$.

2.2.2. Favre averaging

The Reynolds averaging of the compressible Navier–Stokes equations has additional terms generated as a result of density fluctuations that are absent in the incompressible case. The interpretation of these terms are necessary. This challenge can be overcome by considering a density weighted average known as Favre averaging. Consider the spatial averaging and decomposition of the quantity $\phi(x,y,z,t)$ into mean and fluctuating components,

$$\phi(x,y,z,t) = \widetilde{\phi}(x,y,z,t) + \phi''(x,y,z,t) \tag{2.8}$$

where $\widetilde{\phi}(x,y,z,t)$ is the Favre averaged quantity. Care must be taken to note that $\phi^{'}$ corresponds to the fluctuating component associated with the Reynolds averaging and $\phi^{''}$ is the fluctuating component associated with the Favre averaging. There are some auxiliary relations that hold in case of Favre averaging.

$$\overline{\phi''} \neq 0 \qquad \overline{\rho\phi''} = 0 \qquad \overline{\widetilde{\rho}\phi} = \widetilde{\rho}\overline{\phi} \tag{2.9}$$

The definition of a Favre averaged quantity $\widetilde{\phi}(x,y,z,t)$ is presented. Multiplying (2.8) throughout by $\langle\rho\rangle$ and performing Reynolds averaging,

$$\begin{aligned}
\overline{\langle\rho\rangle\langle\phi\rangle} &= \overline{\langle\rho\rangle\langle\widetilde{\phi}\rangle} + \overline{\langle\rho\rangle\langle\phi''\rangle} \\
\overline{\langle\rho\rangle\langle\phi\rangle} &= \langle\overline{\rho}\rangle\langle\widetilde{\phi}\rangle \\
\langle\widetilde{\phi}\rangle &= \frac{\overline{\langle\rho\rangle\langle\phi\rangle}}{\langle\overline{\rho}\rangle}
\end{aligned} \tag{2.10}$$

The Favre decomposition is applied only to velocity, static and stagnation enthalpies. Reynolds decomposition is used for all other variables. Using this method, the Favre averaged Navier–Stokes equations can be written as

$$\frac{\partial\overline{\rho}}{\partial t} + \frac{\partial\overline{\rho}\widetilde{u_j}}{\partial x_j} = 0$$

$$\frac{\partial\overline{\rho}\widetilde{u_i}}{\partial t} + \frac{\partial(\overline{\rho}\widetilde{u_i}\widetilde{u_j})}{\partial x_j} + \frac{\partial\overline{p}}{\partial x_i} + \frac{\partial}{\partial x_j}(\overline{\rho u_i'' u_j''} - \overline{\sigma_{ij}}) = 0 \tag{2.11}$$

$$\frac{\partial\overline{\rho}\widetilde{H}}{\partial t} + \frac{\partial\overline{\rho}\widetilde{H}\widetilde{u_j}}{\partial x_j} + \frac{\partial\widetilde{u_j}\overline{p}}{\partial x_j} + \frac{\partial\overline{u_j''p}}{\partial x_j} + \frac{\partial}{\partial x_j}(\overline{q_j} + \overline{\rho H'' u_j''} - \overline{u_i\sigma_{ij}}) = 0 \tag{2.12}$$

The turbulent fluctuation term is absent in the continuity equation and the momentum equation has a single Reynolds stress term $\overline{\rho u_i'' u_j''}$ known as the Favre averaged turbulent stress. Such an averaging process also ensures that although the density fluctuations are removed from the time averaging process, they are still captured by measuring instruments. (Bradshaw, 1977).

2.3. Channel flow configuration

This study uses the channel flow configuration. The flow configuration along with its features is described below along with the simplifications. In addition, the definition of bulk quantities that is used in compressible flows is also provided.

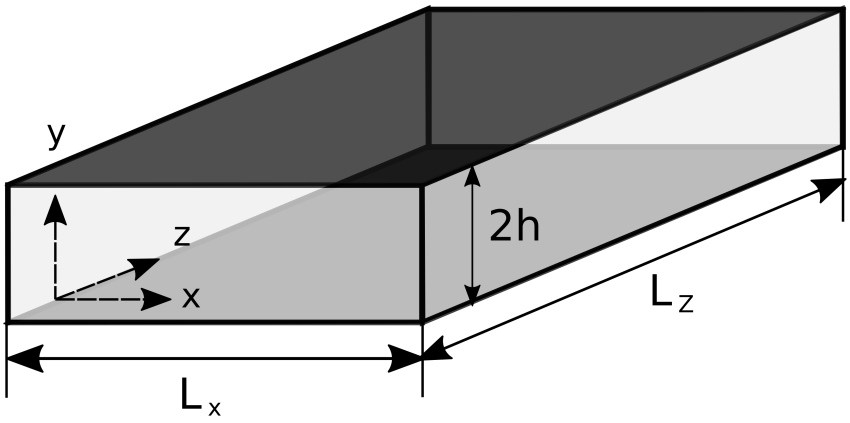

Figure 2.1: Channel flow configuration setup where $2h$ is the channel height, L_z is the width of the channel and L_x is the length of the channel

Consider Figure 2.1 for the setup of a typical channel flow configuration. It consists of two parallel walls separated by a distance $2h$ where h is the half-height of the channel. The length of the channel L_x is much larger than the channel height ($L_x/h >> 1$). The channel also has a high aspect ratio ($L_z/h >> 1$). The streamwise, wall-normal and spanwise directions are along x, y and z, respectively. The mean flow variation is along the wall-normal direction. The purpose of having a large aspect ratio is to ensure that the flow is statistically independent of the streamwise and spanwise directions. Yet another key element is the statistical symmetry of the flow properties about a plane parallel to the walls at a wall-normal distance of $y = h$. This way, the flow statistics at a wall normal distance of $y = \beta$ and $y = 2h - \beta$ are the same. The channel walls have a no-slip, isothermal boundary condition and a fixed temperature. Periodic boundary conditions are imposed in the streamwise and spanwise directions. The bulk quantities ρ_b, u_b are defined as

$$\rho_b = \frac{1}{V}\int_V \rho dV \qquad u_b = \frac{1}{\rho_b V}\int_b \rho u dV \tag{2.13}$$

where V is the fluid volume. The bulk Reynolds number Re_b, temperature T_b and bulk Mach number M_b are defined as

$$Re_b = \frac{2h\rho_b u_b}{\mu_w} \qquad T_b = \frac{1}{\rho_b u_b V}\int_V \rho u T dV \qquad M_b = \frac{u_b}{\sqrt{\gamma R T_b}} \tag{2.14}$$

where μ_w is the molecular viscosity of the fluid at the wall. It should be noted that the study also makes use of an open channel where the height of the channel is h. In this case, the channel mid-plane is a slip wall with symmetry boundary condition enforced on streamwise velocity, spanwise velocity and temperature.

The consideration of a channel flow configuration allows simplification of the averaged Navier–Stokes equations. The streamwise momentum equation shows that there is a balance between the wall-normal shear stress gradient and streamwise normal stress gradient. The mean momentum balance is given by

$$\overline{\mu}\frac{d\langle\widetilde{u}\rangle}{dy} - \langle\overline{\rho}\rangle\langle\widetilde{u''v''}\rangle = \tau_w\left(1 - \frac{y}{h}\right) \tag{2.15}$$

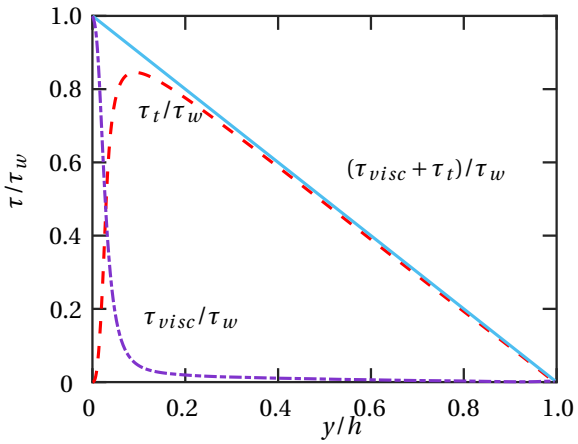

Figure 2.2: Profiles of viscous stress τ_{visc} (dot-dashed lines) and Reynolds stress τ_t (dashed lines) in a turbulent channel flow scaled by wall shear stress τ_w. The solid line indicates the sum of the viscous and Reynolds stress scaled by τ_w.

where the first and the second terms on the left hand side are viscous and Reynolds stresses respectively and τ_w is the wall shear stress. The mean momentum balance indicates that the sum of the viscous and Reynolds stress is linear. The profiles of viscous stress and Reynolds stress is shown in Figure 2.2. Further simplification of Equation 2.15 gives

$$\tau(y) = \tau_w\left(1-\frac{y}{h}\right) = \tau_{visc}+\tau_t \tag{2.16}$$

where $\tau(y)$ is the total stress given by the sum of viscous stress τ_{visc} and Reynolds stress τ_t. At $y=0$, $\tau(0)=\tau_w$. The contribution at the wall is purely viscous and is given by

$$\tau_w = \left(\overline{\mu}\frac{d\langle\tilde{u}\rangle}{dy}\right)_{y=0} \tag{2.17}$$

2.4. Law of the wall

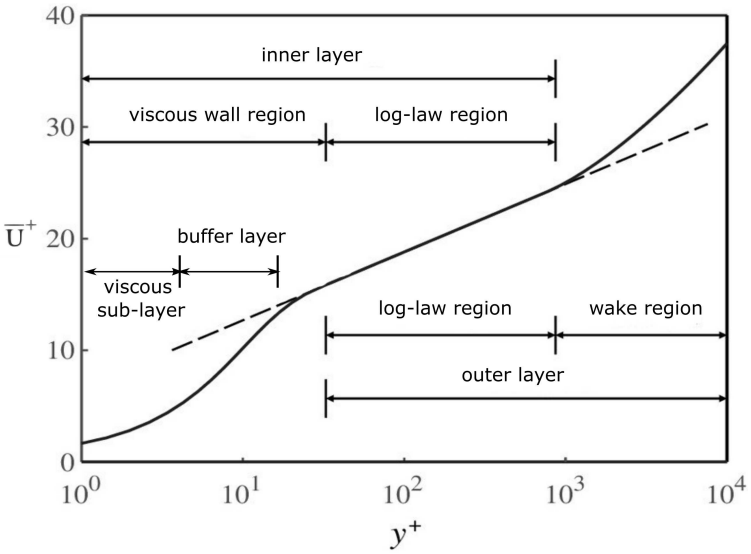

Figure 2.3: Plot indicating mean velocity profile close to the wall showing the segregation of different layers

Turbulent boundary layer flow over smooth walls has been thoroughly studied with well-documented results in books by Pope (2001), and Schlichting and Gersten (2016). Two prominent documentation of wall

turbulence was offered by Clauser (1956) and Hama (1954). The theory proposed by Richardson (1922) describes eddies of small scale responsible for dissipation by action of viscous forces. These small scale eddies are present close to the wall. The effect of viscosity enforces the no-slip boundary condition bringing the fluid velocity to zero at the wall. It is evident from (2.16) that close to the wall, kinematic viscosity ν and wall shear stress τ_w are important (Pope, 2001). This is used to define viscous length and velocity scales that are relevant in this region. The friction velocity u_τ is defined as

$$u_\tau = \sqrt{\frac{\tau_w}{\rho_w}} \tag{2.18}$$

where ρ_w is the fluid density at the wall. The friction length scale is defined as

$$\delta_\nu = \frac{\nu_w}{\sqrt{\frac{\tau_w}{\rho_w}}} = \frac{\nu_w}{u_\tau} \tag{2.19}$$

where ν_w is the kinematic fluid viscosity at the wall. The friction velocity and length scales can now be used as scaling parameters for velocity and wall-normal distance close to the wall. The wall-normal distance scaled by friction length scale is given by,

$$y^+ = \frac{y}{\delta_\nu} \tag{2.20}$$

where y^+ is the distance of the wall measured in wall units. Similarly, the mean velocity scaled by friction velocity is given by

$$\langle u \rangle^+ = \frac{\langle u \rangle}{u_\tau} \tag{2.21}$$

where $\langle u \rangle^+$ is the velocity in wall units or the non-dimensionalised velocity applicable close to the wall where viscosity dominates. Using u_τ and δ_ν, we can define the friction Reynolds number, which can also be interpreted as the ratio between the largest and smallest length scales in the fluid.

$$Re_\tau = \frac{h}{\delta_\nu} = \frac{u_\tau h}{\delta_\nu} \tag{2.22}$$

According to Prandtl hypothesis (Prandtl, 1925), $\langle u \rangle^+$ depends solely on y^+ in what is known as the law of the wall given by

$$\langle u \rangle^+ = f(y^+) \tag{2.23}$$

where f is some function. The magnitude of y^+ is important in characterising the different layers close to the wall. The different layers based on y^+ is shown in Figure 2.3. For $y^+ < 50$, there is a domination of viscous forces in a region known as the viscous-wall region. There is a direct influence of molecular viscosity on the shear stress (Pope, 2001). However, in the outer layer ($y^+ > 50$), viscosity has a negligible effect. Breaking the viscous wall region further it is observed that, $y^+ < 5$ constitutes the viscous sub-layer and $5 < y^+ < 30$ constitutes the buffer layer. The study of the viscous wall region begins by considering (2.17) and non-dimensionalising y and $\langle u \rangle$ by δ_ν and u_τ respectively

$$\frac{d\langle u \rangle^+}{dy} = 1 \tag{2.24}$$

By integrating (2.24), it is seen that $\langle u^+ \rangle = y^+$ or the mean velocity shares a linear relationship with wall-normal distance when scaled by wall-units (Kim et al., 1987). At sufficiently high Reynolds numbers, there exists an overlap layer extending from $y^+ > 50$ to $y/h < 0.1$ where there is a simultaneous validity of the relations in the inner and outer layers. The mean velocity can be completely specified by y, h,ν_w,τ_w and ρ_w. The functional relationship can be written as

$$\langle u \rangle = f_1(y, h, \nu_w, \rho_w) \tag{2.25}$$

where f_1 is some function. Using the viscous wall units, Equation 2.25 can be written as

$$\langle u \rangle = u_\tau f_1 \left(\frac{y}{h}, \frac{y}{\delta_v} \right) \tag{2.26}$$

since u_τ is a constant. In the inner layer, where viscous scales dominate

$$\langle u \rangle = u_\tau f_{inner} \left(\frac{y}{\delta_v} \right) \tag{2.27}$$

where f_{inner} describes the functional relationship in the inner layer and in the outer layer, the velocity defect form is valid

$$\langle u \rangle_c - \langle u \rangle = u_\tau f_{outer} \left(\frac{y}{h} \right) \tag{2.28}$$

where f_{outer} describes the functional relationship in the outer layer. Here, $\langle u \rangle_c$ is the mean velocity at the center of the channel. Taking derivatives of (2.27) and (2.28)

$$\frac{d\langle u \rangle}{dy} = \frac{u_\tau}{\delta_v} g_{inner} \left(\frac{y}{\delta_v} \right) \tag{2.29}$$

$$\frac{d\langle u \rangle}{dy} = -\frac{u_\tau}{h} g_{outer} \left(\frac{y}{h} \right) \tag{2.30}$$

where g_{inner} and g_{outer} are derivatives of f_{inner} and f_{outer} respectively. Since y^+ and y/h are independent of each other, the similarity of (2.29) and (2.30) is possible only if they are both equal to a constant

$$\frac{u_\tau}{\delta_v} g_{inner} \left(\frac{y}{\delta_v} \right) = \frac{1}{\kappa} = -\frac{u_\tau}{h} g_{outer} \left(\frac{y}{h} \right) \tag{2.31}$$

where κ is the von Karman constant of proportionality. By integrating, the mean velocity profile in the overlap layer is given as

$$\langle u \rangle^+ = \frac{1}{\kappa} log(y^+) + B \tag{2.32}$$

where B is a constant of proportionality. The region from $y^+ > 30$ to $y/h < 0.3$ is where the (2.32) holds and is known as the log-law layer. By performing experiments and simulations, it was found that $\kappa \approx 0.41$ and $B \approx 5.2$.

2.5. Compressible turbulent flows

2.5.1. Compressibility transformations

By virtue of the law of the wall, the universality of mean velocity profile scaled by friction velocity and friction length scale exists in the viscous and the overlap layers. In case of compressible flows, the law of the wall is valid only for the transformed velocity and wall-normal coordinate. The goal of the compressibility transformations is to transform the velocity and wall-normal coordinate to ensure this validity of the law of the wall. Supersonic flows involve large temperature gradients close to the wall, the presence of which, would lend support to the disparity between the compressible supersonic and subsonic boundary layer properties in wall-bounded turbulence. However, such a disparity is reconciled when the variation in mean flow properties that arise due to the variation in temperature in a supersonic boundary layer are suitably accounted for. This is the premise for the so-called Morkovin hypothesis that forms the basis of compressibility transformations. The hypothesis states that the dynamics of the compressible boundary layer follow the incompressible counterpart provided the fluctuating Mach number M' remains small (Morkovin, 1962, Spina et al., 1994). According to Spina et al. (1994), the fluctuating Mach number is the deviation of its instantaneous value from the mean Mach number. The fluctuating Mach number gives a measure of the compressibility effects. Yet another Mach number that is frequently used in compressible turbulent boundary layer analysis is the turbulent Mach number M_t defined as,$M_t = (\widetilde{u_i' u_i'})^{1/2}/\widetilde{c}$ where u_i' represents the velocity fluctuation in the i^{th} coordinate direction and $\widetilde{c}$ represents mean speed of sound. The limit for the applicability of the hypothesis is free stream Mach number $M_\infty \approx 4-5$ (Spina et al., 1994). All compressibility transformations that will

Transformation	**Wall distance** (f_I)	**Mean velocity** (g_I)
Van Driest (1951)	$f_D = 1$	$g_D = M$
Trettel and Larsson (2016)	$f_T = \frac{d}{dy}\left(\frac{yR^{1/2}}{M}\right)$	$g_T = M\frac{d}{dy}\left(\frac{yR^{1/2}}{M}\right)$
Volpiani et al. (2020)	$f_V = \frac{R^{1/2}}{M^{3/2}}$	$g_V = \frac{R^{1/2}}{M^{1/2}}$

Table 2.1: Compressibility transformations for mean velocity profile and wall normal distance cast into the form suggested by Modesti and Pirozzoli (2016). $M = \overline{\mu}/\overline{\mu}_w$ and $R = \overline{\rho}/\overline{\rho}_w$

be discussed can be conveniently represented using mapping functions as proposed by Modesti and Pirozzoli (2016). This allows compact representation of the transformations and also a straightforward method to implement them in numerical codes. The mapping relations are given by

$$y_I = \int_0^y f_I \, dy \tag{2.33}$$

$$u_I = \int_0^{\widetilde{u}} g_I \, d\widetilde{u} \tag{2.34}$$

where y_I and u_I are the transformed incompressible wall normal co-ordinate and mean-streamwise velocity respectively obtained from various transformations, f_I and g_I are mapping functions for wall distance and mean velocity respectively. With these transformed coordinates, it is possible to define a transformed friction Reynolds number

$$Re_{\tau I} = \frac{y_I(h)}{\delta_v} \tag{2.35}$$

For non-hypersonic flows, Morkovin (1962) postulated that the main effect of compressibility is manifested through variation in mean flow properties. The effect of compressibility on turbulent statistics is negligible if the r.m.s density fluctuations is small in comparison to the mean density. Yet another perspective is provided by Smits and Dussauge (2006) wherein a detailed analysis of the Morkovin hypothesis is reported by making use of the turbulent time and length scales. They explain the similarity in turbulence transport mechanism of low speed and high speed cases provided variable property scaling is adopted as opposed to the constant property scaling (example: u_τ). Bradshaw (1977) and Spina et al. (1994) report that in the region close to the wall, there is a zone of constant stress where the normal and shear stress distributions do not vary with Mach number. In such a zone, the effect of molecular viscosity is negligible and using (2.18) in (2.15) and neglecting the viscous stress

$$-\overline{\rho}\widetilde{u'v'} = \overline{\rho}_w u_\tau^2 \left(1 - \frac{y}{h}\right) \tag{2.36}$$

The hypothesis reduces the effects of compressibility at the wall to the variation in the mean flow properties. (2.36) shows that a modification in the scaling approach has to be adopted in the constant stress region. To achieve the similarity of the Reynolds stresses, it is imperative to consider $u_\tau(\overline{\rho}_w/\overline{\rho})^{1/2}$ instead of u_τ as a scaling parameter (Smits and Dussauge, 2006). This would lead to shear stress distributions of,

$$-\widetilde{u'v'} \approx \left(\frac{\overline{\rho}_w}{\overline{\rho}}\right) u_\tau^2$$

If an assumption is made regarding the validity of the mixing length hypothesis where the size of the eddies l_m is proportional to the perpendicular distance from the wall y, it can be shown that,

$$\tau_t = -\overline{\rho}\widetilde{u'v'} = \overline{\rho}\nu_t \frac{\partial \widetilde{u}}{\partial y} = \overline{\rho} l_m^2 \left(\frac{\partial \widetilde{u}}{\partial y}\right)^2 = \overline{\rho}_w u_\tau^2 \tag{2.37}$$

where ν_t is the eddy viscosity. The implication of the Morkovin hypothesis is that the size of the stress bearing eddies is given by $l_m = \kappa y$ which is similar to the incompressible turbulent boundary layer. Using this relation

in (2.37)

$$\overline{\rho}(\kappa y)^2\left(\frac{\partial \widetilde{u}}{\partial y}\right)^2 = \overline{\rho}_w u_\tau^2 \tag{2.38}$$

$$\frac{\partial \widetilde{u}}{\partial y} = \left(\frac{\overline{\rho}_w}{\overline{\rho}}\right)^{1/2}\frac{u_\tau}{\kappa y} \tag{2.39}$$

$$\left(\frac{\overline{\rho}}{\overline{\rho}_w}\right)^{1/2}\frac{\partial \widetilde{u}}{\partial y} = \frac{u_\tau}{\kappa y} \tag{2.40}$$

$$\frac{\partial u_D}{\partial y} = \frac{u_\tau}{\kappa y} \tag{2.41}$$

where

$$u_D = \int_0^{\widetilde{u}}\left(\frac{\overline{\rho}}{\overline{\rho}_w}\right)^{1/2} d\widetilde{u} \tag{2.42}$$

This implication leads to the logarithmic variation of mean velocity in the overlap layer. This shows resemblance to the incompressible turbulent boundary layer case given by

$$u_D^+ = \frac{1}{\kappa} log(y^+) + B \tag{2.43}$$

where u_D^+ is the inner variable scaled effective mean velocity and the transformation was proposed by Van Driest (1951). The van Driest transformation is closely coupled with the Morkovin hypothesis where it was explained that the effects of compressibility are manifested in the form of thermodynamic property variations and are independent of the Mach number upto a certain limit. There is considerable evidence supporting the hypothesis and the van Driest scaled mean velocity profiles. The review is presented in detail by Smits and Dussauge (2006). It is worth mentioning that the van Driest scaling is valid for quasi-adiabatic walls and strictly the overlap region with satisfactory results in the viscous sub-layer.

Despite the tremendous support for the Morkovin hypothesis and its ability to effectively offer scaling solutions for compressible turbulent boundary layer data, there are a few studies that question its validity, especially the one regarding the mixing length. Experiments over the years by Maise and McDonald (1968) and Bradshaw (1977) have lent weight to the dependence of the mixing length l_m on the Mach number, more so in the outer layer. This subsequently invalidates the relation provided by (2.43). Zhang et al. (2012) proposed an alternate method of scaling that introduces a Mach number invariant mixing length scaling. Notwithstanding this opposition to the limit of applicability and the subsequent validity of the hypothesis, extensive support renders this an active area of research (Wenzel et al., 2018).

There is evidence supporting the variation of the intercept B in (2.43) presented by many authors (Coleman et al., 1995, Foysi et al., 2004, Maeder, 2000). Danberg (1967) mentions in his study that the intercept in the log-law relation C, shows an increase with wall heat transfer. These are some of the observations made that question the validity of the van Driest scaling in effectively allowing a transformation of the mean velocity profile from the compressible to incompressible case so that it follows the law of the wall, in all conditions of heat transfer, Reynolds and Mach numbers. Such a transformation is imperative as it obviates the need for a modified law of the wall; the incompressible law can simply be extended to the compressible case.

The effect of heat transfer is characterized by a non-dimensional quantity,

$$B_q = \frac{q_w}{\rho_w C_p u_\tau T_w} \tag{2.44}$$

where q_w is the heat transfer at the wall and C_p is known as the specific heat capacity for a constant pressure. $B_q < 0$ signifies wall cooling. In order to show the variations in the mean velocity profile for cooled walls (heat transfer away from the wall), Trettel and Larsson (2016) performed DNS of a compressible turbulent channel flow at Mach 1.7, $Re_\tau = 663$ with a $B_q = -0.053$ that signifies weak heat transfer and another case with Mach 3.0, $Re_\tau = 650$ with a $B_q = -0.131$ that displays relatively strong heat transfer effects. When the van Driest transformed mean velocity profile in inner variables of these two results were compared with the DNS of incompressible channel flow by Moser et al. (1999), the DNS results of the mean velocity profile reported by Trettel and Larsson (2016) show a reasonably good collapse with the DNS results reported by Moser et al. (1999) for the case of weak heat transfer ($B_q = -0.053$). In contrast, the van Driest transformed mean velocity

profile of the case with strong heat transfer ($B_q = -0.131$) shows significant deviations from the reference incompressible mean velocity profile by Moser et al. (1999). The differences are attributed to the increase in the log-law layer intercept B and the viscous sub layer slope (Trettel and Larsson, 2016). This is depicted in Figure 2.4.

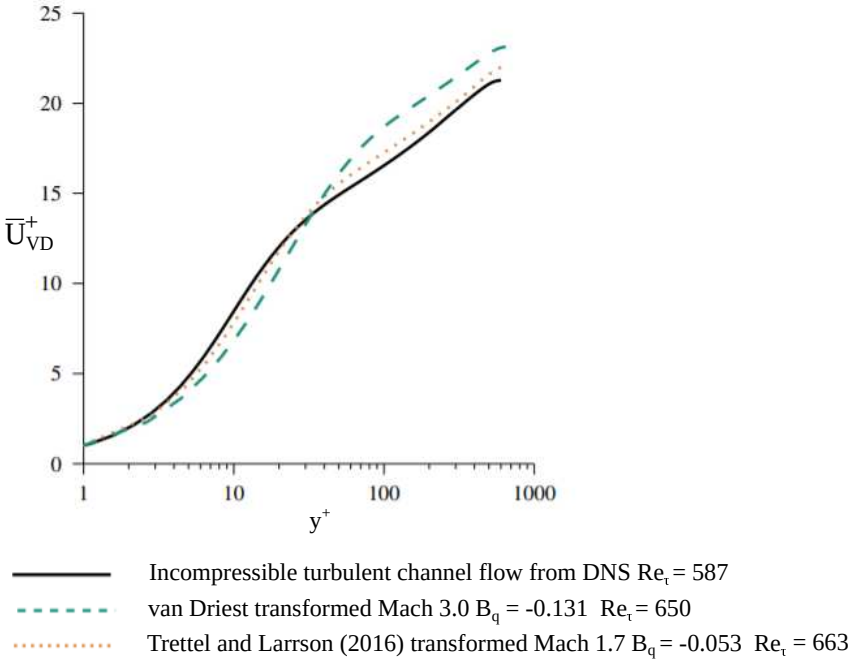

Figure 2.4: Comparison of van Driest transformed mean velocity profile of compressible flow with mild cooling at Mach 1.7, $Re_\tau = 663$ and strong cooling at Mach 3.0, $Re_\tau = 650$ reported by Trettel and Larsson (2016) with incompressible results from Moser et al. (1999) at $Re_\tau = 587$

Trettel and Larsson (2016) proposed a transformation that takes care of varying Reynolds and Mach numbers along with provisions for heat transfer. This transformation is based on two important conditions - the log-law condition and the stress balance condition. Trettel and Larsson (2016) remarked that the latter is an important component of a compressibility transformation since the momentum conservation between the raw form (compressible) and transformed form (incompressible) has to be respected. They argue that the van Driest transformation adjusts the velocity gradients of a variable density flow to a constant density one. While this may result in a matching slope of the velocity gradient, it violates the stress-balance condition Trettel and Larsson (2016). This was one of the major drawbacks of the van Driest transformation. The transformed mean velocity and wall-normal co-ordinate is presented in Table 2.1. Three experimental and one DNS study was used to validate the transformation for a supersonic flow over a boundary layer. In case of the channel flow, the results from Moser et al. (1999) was used for validation.

Huang et al. (1995) heuristically proposed to use the semi-local scaling approach wherein the flows with property variations can use the scaling given by $u^*_\tau = (\tau_w/\overline{\rho})^{1/2}$ with a length scale $\delta^*_v = \overline{\mu}/\overline{\rho}u^*_\tau$. The results also include a semi-local scaled wall normal distance given by $y^* = y/\delta^*_v$ and the associated Reynolds number Re^*_τ. The verification of this scaling approach was performed by Patel et al. (2015) where it was established well that the proposed transformations are indeed valid. In fact, Re^*_τ was also later derived by Trettel and Larsson (2016).

The topic of compressibility transformations is still being studied with improvements being made to the scaling of near wall mean velocity and wall-normal co-ordinates for a range of Reynolds and Mach numbers, and wall thermal conditions. The most recent study by Volpiani et al. (2020) enforces the universality in viscous sub-layer and the Morkovin scaled shear stress analytically, while calibrating the other parameters using a wide range of DNS data. The transformation proposes a power law relation with coefficients a and b. The transformed mean velocity and wall-normal coordinate is given by Table 2.1. Since both density and viscosity ratios depend on the temperature ratio $\overline{T}/\overline{T}_w$, a provision was made to incorporate this using the ideal gas relation. The search space for the coefficients of the power law was explored with the goal

of minimizing the L_1 norm of the difference between the transformed streamwise mean velocity and the incompressible streamwise mean velocity, particularly in the log-law region that extends from $y^+ \approx 40$ to $y^+ \approx 100$ for the present DNS data. The calibration of the coefficients was done using boundary-layer test cases ranging from Mach numbers of 2 to 6 and wall thermal conditions of adiabatic and strongly cooled. It was observed that the range that produces the lowest error for a is $1.4-1.7$ and for b is $0.4-0.6$. To produce the final transformation relation, values of $a = 1.5$ and $b = 0.5$ were chosen. It should be noted that this transformation has been tested upto a maximum $Re_\tau \approx 650$.

2.5.2. Strong Reynolds Analogy

In compressible flows, the presence of the energy equation with temperature and density being additional unknowns can prove to be challenge from a computational perspective. A way to correlate the two equations would prove largely beneficial in solving them. This is where the Reynolds analogy plays a key role. The underlying concept of a Reynolds analogy is the similarity of the momentum and energy equations when the molecular Prandtl number is unity. This is very advantageous, since consideration of such an analogy would provide a coupling between the temperature and velocity, which would necessitate solving either the momentum or energy equation. Such an analogy was first applied to steady laminar flows with zero pressure gradient and later extended to turbulent flows in what is known as the Strong Reynolds analogy (SRA). Before exploring the SRA, it is imperative to consider a few definitions first. The eddy viscosity μ_t and eddy conductivity k_t is defined as:

$$\mu_t = \frac{-\overline{\rho}\widetilde{u'v'}}{\partial\widetilde{u}/\partial y} \tag{2.45}$$

$$k_t = \frac{-C_p\overline{\rho}\widetilde{v}\widetilde{T'}}{\partial\widetilde{T}/\partial y} \tag{2.46}$$

where u', v' represent the streamwise and wall normal fluctuations and T' represents the temperature fluctuation (Smits and Dussauge, 2006). This allows for the definition of a *turbulent* Prandtl number Pr_t and mixed Prandtl number P_m given by:

$$Pr_t = \frac{\mu_t C_p}{k_t} = \frac{-\overline{\rho}\widetilde{u'v'}(\partial\widetilde{u}/\partial y)}{-\overline{\rho}\widetilde{v}\widetilde{T'}(\partial\widetilde{T}/\partial y)} \tag{2.47}$$

$$P_m = \frac{(\mu+\mu_t)C_p}{(k+k_t)} \tag{2.48}$$

By modifying (2.11) and (2.12) a little, the zero pressure gradient, steady $2D$ Favre averaged momentum and energy equation can be written,

$$\overline{\rho}\widetilde{u}\frac{\partial\widetilde{u}}{\partial x} + \overline{\rho}\widetilde{v}\frac{\partial\widetilde{u}}{\partial y} = \frac{\partial}{\partial y}\left((\mu+\mu_t)\frac{\partial\widetilde{u}}{\partial y}\right) \tag{2.49}$$

$$\overline{\rho}\widetilde{u}\frac{\partial\widetilde{H}}{\partial x} + \overline{\rho}\widetilde{v}\frac{\partial\widetilde{H}}{\partial y} = \frac{\partial}{\partial y}\left((\mu+\mu_t)\left[\frac{\partial H}{\partial y} + C_p(P_m^{-1}-1)\frac{\partial\widetilde{T}}{\partial y}\right]\right) \tag{2.50}$$

(2.49) and (2.50) are reported in Smits and Dussauge (2006) and become equivalent when $P_m = 1$, in which case if a solution exists for $\widetilde{u}$, then the solution for $\widetilde{H}$ takes the form: $\widetilde{H} = a\widetilde{u} + b$ where a and b are constants determined by the boundary conditions. Experimental study by Kistler (1959) and Morkovin (1962) show that most of the total temperature variations T_0, and by extension, H (since $H = C_p T_0$) take place close to the wall and the variation of T_0 away from the wall is negligible. The mean and the fluctuation of H can be written as,

$$\begin{aligned}
H = \widetilde{H} + H' &= \widetilde{h} + h' + \frac{1}{2}(\widetilde{u_i} + u_i')(\widetilde{u_i} + u_i') \\
\widetilde{H} &= \widetilde{h} + \frac{1}{2}(\widetilde{u_i}^2) \\
H' &= h' + \widetilde{u_i}u_i' + \frac{1}{2}(u_i'^2) \\
C_p T_0' &= C_p T' + \widetilde{u_i}u_i' + \frac{1}{2}(u_i'^2)
\end{aligned} \tag{2.51}$$

The term $(u'^2)/2$ is negligible and it was suggested by Morkovin (1962) that for an adiabatic case, $T'_0 << T'$ and (2.51) takes the form $C_p T' + \widetilde{u_i} u'_i \approx 0$. The discussion provided by Smits and Dussauge (2006) uses this relation, and puts forward the following relations

$$\frac{\sqrt{\overline{T'^2}}}{\widetilde{T}} = (\gamma - 1)\overline{M}^2 \frac{\sqrt{\overline{u'^2}}}{\widetilde{u}} \tag{2.52}$$

$$R_{u'T'} = \frac{\overline{u'T'}}{\sqrt{\overline{u'^2}}\sqrt{\overline{T'^2}}} \approx -1 \tag{2.53}$$

$$\widetilde{v'T'} = -\frac{\widetilde{u}}{C_p}\widetilde{u'v'} \tag{2.54}$$

$$\frac{\widetilde{v'T'}}{\widetilde{T}} = -(\gamma - 1)\overline{M}^2 \frac{\widetilde{u'v'}}{\widetilde{u}} \tag{2.55}$$

$$\widetilde{v'T'_0} = \widetilde{v'T'} + \frac{\widetilde{u}}{C_p}\widetilde{u'v'} = 0 \tag{2.56}$$

where $\overline{M} = \widetilde{u}/\sqrt{\gamma R \widetilde{T}}$. R is the gas constant, γ is the ratio of specific heats C_p and C_v (specific heat at constant volume). The relations in (2.52) - (2.56) are collectively the 5 SRA relations that were presented by Morkovin (1962). A detailed study of these relations are presented in Cebeci and Smith (1974), Guarini et al. (2000), Smits and Dussauge (2006).

The SRA relations are valid only for quasi-adiabatic flows and starts showing deviations when there is heat transfer at the walls (Gaviglio, 1987, Huang et al., 1995). This led to the formulation of the various other SRA relations, one of which, developed by Gaviglio (1987) is given by,

$$\frac{\sqrt{\overline{T'^2}}/\widetilde{T}}{(\gamma - 1)\overline{M}^2 \frac{\sqrt{\overline{u'^2}}}{\widetilde{u}}} \approx \frac{1}{c(1 - a(\partial \widetilde{T}_0/\partial \widetilde{T})} \tag{2.57}$$

where $c = 1$ and $a = 0$ recovers the original SRA. In the study by Guarini et al. (2000), they analyze the accuracy of the modified SRA and the constants a and c used by Huang et al. (1995) and Gaviglio (1987). Their conclusion is that $a = 1$ and $c = Pr_t$ as proposed and used by Huang et al. (1995) is the most accurate. In conclusion, care must be taken while applying the SRA or the so called modified SRA while keeping the conditions at the wall in mind. This can be crucial when considering the relationship between mean skin friction and wall heat transfer coefficient.

The relationship between velocity and temperature is an important one. With such relations, accurate predictions of velocity profiles can be used for estimating the temperature profile. A popular temperature-velocity relation, based on Reynolds analogy was put forward by(Walz, 1959). However supersonic flows at high Mach numbers with wall heat flux showed deviations from this profile as documented by Duan and Martin (2011). A modified relation was proposed by Zhang et al. (2014) to overcome these limitations and extend the applicability to non-adiabatic walls given by

$$\frac{\overline{T}}{\overline{T}_w} = 1 + \frac{T_{rg} - \overline{T}_w}{\overline{T}_w}\frac{\widetilde{u}}{\widetilde{u}_e} + \frac{T_e - T_{rg}}{\overline{T}_w}\left(\frac{\widetilde{u}}{\widetilde{u}_e}\right)^2 \tag{2.58}$$

where $T_{rg} = T_e + r_g \widetilde{u}_e^2/(2C_p)$, $r_g = 2C_p(\overline{T}_w - T_e)/\widetilde{u}_e^2 - 2Prq_w/\widetilde{u}_e\tau_w$ where q_w is the wall heat flux. Since this thesis uses a strongly cooled wall, (2.58) will be useful in computing the temperature profile using the mean velocity profile.

2.6. Effect of surface roughness

2.6.1. Incompressible flows

The pioneering work on rough wall flows is attributed to Nikuradse et al. (1950) who conducted experiments on the flow of water in pipes roughened by sand. Perhaps the most crucial result was the identification of three regimes in the flow where the resistance to the flow of water is dependent on the average roughness height k. For values of k that are comparatively smaller than δ, it is reported that the rough wall behaves similarly to its smooth wall counterpart in terms of offering resistance to the flow. When the magnitude of k

is comparable to δ, it is observed that there is an increase in the resistance to the water flow with an increase in Reynolds number (Nikuradse et al., 1950). Finally, when the magnitude of k is large enough in comparison to δ, there is no change observed in the resistance to the flow of water with an increase in Reynolds number. The schematic description of roughness is shown in (2.5). The roughness heigh k is a geometric parameter and λ, the pitch of the roughness element defined as the distance between two successive leading edges of the crests of the roughness elements.

Clauser (1956) used $k^+ = ku_\tau/\nu_w$, known as the roughness Reynolds number, that is calculated based on the height k of the roughness element to arrive at similar results. A sufficiently small value of k^+ would imply that the roughness element would lie well inside the viscous sub-layer, offering no changes in the resistance to the flow. Such a surface is known as hydraulically smooth. As the magnitude of k^+ increases, there is a regime that involves a change from smooth to rough behavior which is defined as transitionally rough. The term, 'fully rough', is assigned to the case with a sufficiently high value of k^+ and indicates the complete disappearance of the laminar sub-layer accompanied by the absence of inner layer dependence on viscosity (Clauser, 1956). Schlichting and Gersten (2016) introduce equivalent sand grain roughness height k_s and the equivalent roughness Reynolds number $k_s^+ = u_\tau k_s/\nu_w$ in terms of it. Chung et al. (2021) provides a definition for k_s as the hypothetical sand grain roughness height that is expected to produce the same drag as the rough surface of interest. This poses a problem that k_s cannot be determined *a priori*. Additionally, there is no direct relation between k_s and the geometrical roughness parameter such as k. This definition allows the assignment of limits to characterize a hydraulically smooth ($k_s^+ \lesssim 5$), transitionally rough ($5 \lesssim k_s^+ \lesssim 80$) and fully rough regime ($k_s^+ \gtrsim 80$) (Nikuradse et al., 1950, Wu and Christensen, 2007).

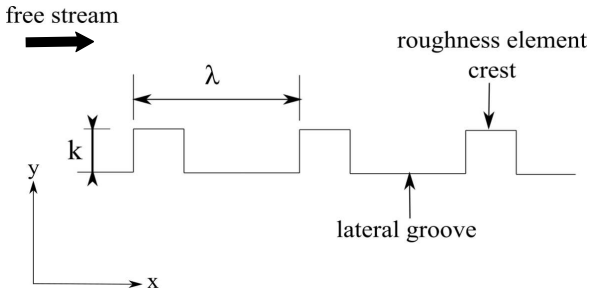

Figure 2.5: Schematic of a typical $2D$ rough surface

In fully rough flows, the surface shear due to viscosity in the case of smooth flows is replaced by the form drag on the roughness elements (Raupach et al., 1991). A similar explanation was provided by Furuya et al. (1976) who conducted experimental studies of a turbulent boundary layer on flat plate roughened by transverse wires. Another interpretation offered by Flack and Schultz (2014) to explain the different regimes is in terms of the perturbations caused due to the existence of roughness. In the case of a hydraulically smooth surface, the perturbations caused due to the roughness elements are damped by the strong presence of the viscous layer. However, as these perturbations grow in strength with increasing k_s^+, it is observed that the viscosity is no longer able to damp the perturbations caused by the roughness elements until it reaches a point where the dominant mechanism is simply the form drag on the elements. This argument is also supported and expounded mathematically by Jiménez (2004).

When discussing roughness, a concept that comes to mind is the Townsend outer layer similarity hypothesis (Townsend, 1980). There have been studies that provide tremendous support for the hypothesis by Jiménez (2004), Flack et al. (2005), Kunkel et al. (2007) and Chung et al. (2014). The underlying assumption is that the behaviour of the smooth wall and rough wall is similar away from the wall. The function of roughness is to set the boundary conditions through the friction velocity. This is based on the dimensional argument as presented in (2.28) where u_τ and h are important in the outer layer. The effect of roughness is confined to a region very close to the wall ($y < y_r$) where y_r is the height of the roughness sub-layer. Assuming that the $y_r \approx 3k$, the condition for outer layer similarity to hold is $k/h \lessapprox 1/40$ (Jiménez, 2004). However, this cannot be guaranteed but the review by Flack and Schultz (2014) specify that outer layer similarity holds in the case of sufficiently large scale separation. Leonardi et al. (2007) propose that checks at higher h/k and fixed k^+ is required to gauge the validity of the hypothesis.

The effect of roughness is to produce a downward shift in the logarithmic layer of the viscous scaled mean velocity profile. This shift in velocity is known as the Hama roughness function $\Delta U^+ = \Delta U/u_\tau$. In the hy-

draulically smooth regime, the logarithmic law of the wall relation holds

$$\langle u_s \rangle^+ = \frac{1}{\kappa} log(y^+) + B \tag{2.59}$$

where $\langle u_s \rangle^+$ and y^+ respectively are the smooth wall mean-velocity and wall normal coordinate. As the value of k^+ increases and enters the transitionally rough regime, the same logarithmic law of the wall relation holds in y/k

$$\langle u_r \rangle^+ = \frac{1}{\kappa} log\left(\frac{y}{k}\right) + B_R(k^+) \tag{2.60}$$

with the exception of the intercept $B_R(k^+)$ which is no longer a constant but depends on the roughness Reynolds number and the roughness topography (Chung et al., 2021). The term $\langle u_r \rangle^+$ is the mean velocity of the rough wall. This effect of roughness depicted through the shift in the smooth-wall mean velocity profile is shown in Figure 2.6. The shift is quantified as ΔU^+. For $k^+ >> 1$, $B_R(k^+)$ no longer depends on the roughness Reynolds number but only depends on the roughness topography and approaches a finite value B_R (Chung et al., 2021). The velocity shift or Hama roughnes function ΔU^+ is defined as the difference between (2.59) and (2.60)

$$\Delta U^+(k^+) = \langle u_s \rangle^+ - \langle u_r \rangle^+ = \frac{1}{\kappa} log(k^+) + B - B_R(k^+) \tag{2.61}$$

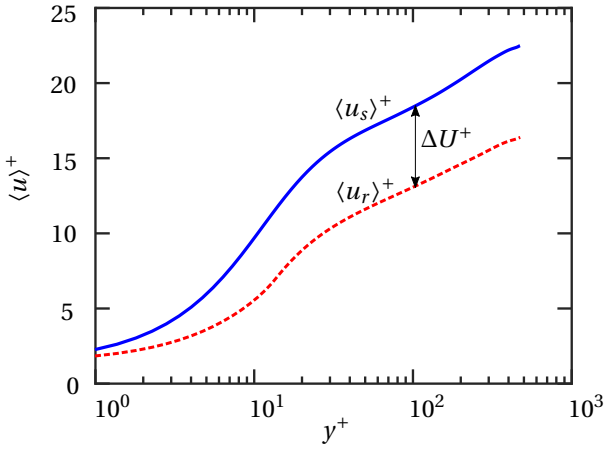

Figure 2.6: Mean velocity profile of a smooth wall and rough wall scaled by friction velocity u_τ and friction length scale δ_v. Solid line represents the smooth wall mean velocity profile and dashed line represents the rough wall mean velocity profile. The Hama roughness function is given by ΔU^+.

For $\Delta U^+ > 0$, there is a momentum deficit caused due to the downward shift in the mean velocity profile in wall units. The flow incurs an additional drag penalty. The description of Hama roughness function so far has been in terms of k^+. However, k_s^+ is a better parameter since it accounts for the drag producing features of the surface despite not having an explicit relationship with geometrical parameters. Additionally, k_s serves as a common parameter that allows the comparison of different roughness types. It is also capable of collapsing the roughness functions of different roughness types on a single theoretical profile in the fully rough limit. (2.61) can be written in terms of k_s^+ by multiplying k^+ with a factor k_s/k. This is particularly an important result and one that will be used in the thesis.

$$\Delta U^+(k_s^+) = \frac{1}{\kappa} log(k_s^+) + B - B_S(k_s^+) \tag{2.62}$$

In the fully rough regime, $B_S(k_s^+)$ attains a finite value ($B_S \approx 8.5$) (Schlichting and Gersten, 2016). Without the fully rough condition, B_S and B_R remain as functions of k_s^+ and k^+ respectively. The Hama roughness function in the fully rough regime is given by

$$\Delta U^+ = \frac{1}{\kappa} log(k_s^+) + B - B_S \tag{2.63}$$

The variation of ΔU^+ with k^+ and k_s^+ is depicted in Figure 2.7a and Figure 2.7b respectively. Assume there exists two different roughness types identified by the letters P (depicted by triangles) and Q (depicted by circles). When ΔU^+ is calculated and plotted against k^+, there is a gradual increase in the ΔU^+ with k^+. In this region, $B_R(k^+)$ or the intercept in (2.60) is not constant. For large values of k^+, the Hama roughness function asymptotes to a constant intercept B_R which no longer depends on k^+. An important observation is that the intercept B_R is different for different roughness types. Additionally, the profiles do not collapse onto the theoretical relation of Hama roughness function given by (2.61) as seen in Figure 2.7a. To ensure that the two roughness types collapse onto a single profile, it is essential to multiply k^+ with k_s/k which is different for the two roughness types ($k_s/k = 5$ for P and $k_s/k = 0.25$ for Q). It is seen in Figure 2.7b that the profiles of the two different roughness types collapse onto the relation given by (2.61) along with the roughness data of Nikuradse et al. (1950). The usage of k_s^+ seems to allow a seamless collapse of the profiles since now the intercept B_S is constant for all roughness types in the fully rough limit.

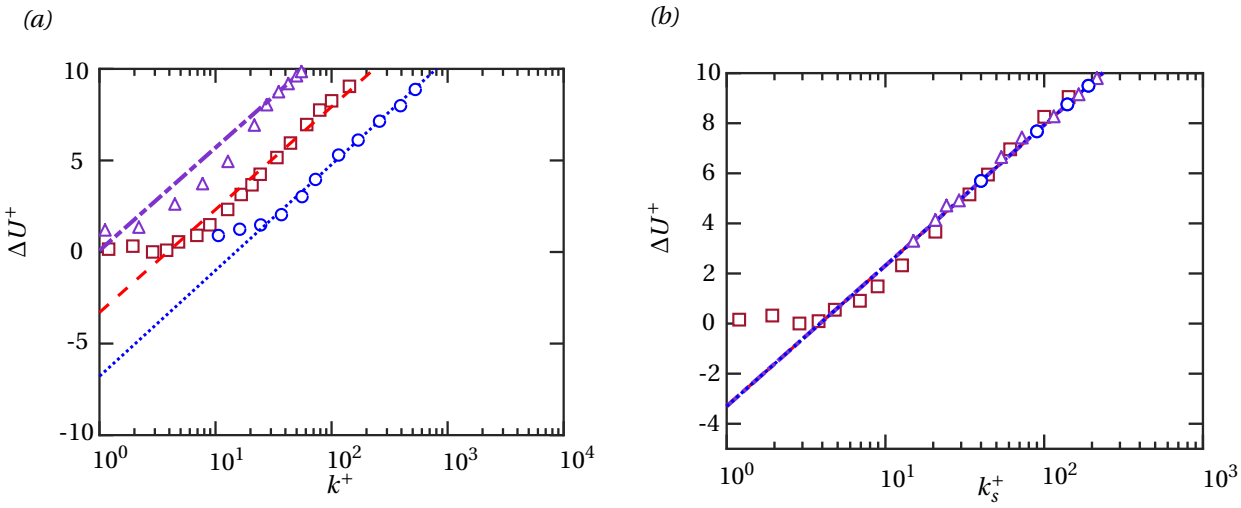

Figure 2.7: Variation of ΔU^+ with (a) k^+ and (b) k_s^+ for two roughness geometries P (triangles) and Q (circles). Dashed line is the theoretical ΔU^+ relation in the fully rough regime and the Nikuradse et al. (1950) roughness (squares) co-inciding with the theoretical profile in the fully rough limit.

A concept to consider while studying the outer layer similarity in rough wall turbulent boundary layers is the virtual origin. Defined as wall offset by Chung et al. (2021). The outer layer of the flow does not always perceive the origin to be at $y = 0$. This causes issues in analysis of ΔU^+ for cases with strong roughness effects. The rough wall mean velocity profile is not exactly shifted parallel to the smooth wall mean velocity profile in the log-law region. This results in a non-horizontal ΔU^+ profile when plotted against y^+. To resolve this issue, the origin of the rough wall is set at $y = \epsilon$ as depicted in Figure 2.8. The value of ϵ can be set anywhere from the roughness trough to the roughness crest based on the distribution of the roughness elements. Since the current thesis does not deal with very sparse or very densely packed roughness elements, the virtual origin is set at a height that will provide a near horizontal ΔU^+ profile when plotted against y^+.

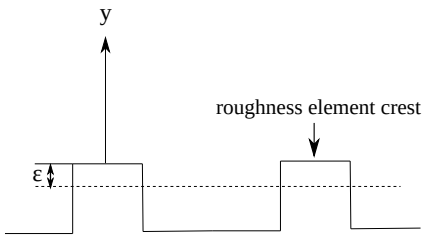

Figure 2.8: Schematic depiction of virtual origin for rough surfaces

2.6.2. Compressible flows

The discussion on surface roughness is incomplete without the study of drag and heat transfer. It is important to see the variation in drag introduced by the presence of roughness on a surface in comparison with a smooth surface. To characterise this, the drag variation of a rough surface in comparison to a smooth surface is given by

$$D_v = 1 - \frac{C_f}{C_{fs}} = 1 - \frac{1}{\left(1 - \frac{\Delta U^+}{U^+_{cs}}\right)^2 \frac{R_c}{R_{cs}}} \tag{2.64}$$

where $R_c = \langle \rho_c \rangle / \langle \rho_w \rangle$, the skin-friction coefficient $C_f = 2\tau_w/(\rho_c U_c^2)$, $U_c = \langle \widetilde{u} \rangle (h)$ is the channel centerline velocity and subscript s indicates smooth surface. The Hama roughness function ΔU^+ can be given as

$$\Delta U^+ = U^+_{cs} - U^+_c \approx \langle \widetilde{u}_s \rangle^+ (y) - \langle \widetilde{u}_r \rangle^+ (y), \qquad 100 < y^+ < 0.30 Re_\tau \tag{2.65}$$

where the second identity holds in the case of outer layer similarity. Hence it is important to correctly predict the Hama roughness function ΔU^+ to ensure accurate quantification of the skin-friction coefficient.

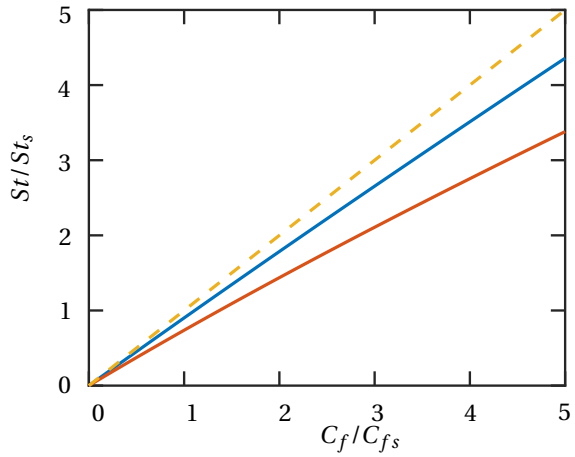

Figure 2.9: Staton number and skin-friction coefficient augmentation using (2.69). The solid lines indicate $\alpha_1 = 0.4, 1.3$ and the dashed lines indicate the case when $St/St_s = Cf/Cf_s$.

One of the important aspects of supersonic flows is the heat transfer. It is important to characterize the heat transfer at the surface due to viscous heating. In supersonic flows, the high speed of the fluid in the freestream is brought to zero at the wall over a very thin region. In the region close to the wall, this results in heating of the fluid due to viscosity offered by the fluid and the presence of the no-slip boundary condition at the wall. The viscosity ensures dissipation of kinetic energy which is manifested as increase in temperature of the fluid. A non-dimensional parameter known as the Stanton number is used to characterize the rate of heat transfer at the wall. The Stanton number is the ratio of the heat transfer coefficient to the thermal capacity of the fluid. It is given by

$$St = \frac{q_w}{\rho u C_p (T_w - T_r)} \tag{2.66}$$

where T_r is the recovery temperature given by

$$T_r = T_c \left[1 + \frac{\gamma - 1}{2} r M_c^2\right] \tag{2.67}$$

where r is the recovery factor and M_c and T_c are the Mach number and temperature at the channel centerline respectively. The recovery factor can be thought of as the amount of kinetic energy recovered from the flow. The stagnation temperature T_0 of a fluid is defined as the temperature that it attains when it is isentropically brought to rest on an insulated wall from the free-stream region of the flow. On the other hand, the recovery temperature is the temperature the fluid attains when it is brought to rest on an insulated wall from the

viscous region. Due to this, the process of bringing the fluid to rest is not fully isentropic and not all of the kinetic energy is dissipated. The recovery factor is given as

$$r = \frac{T_r - T}{T_0 - T} \tag{2.68}$$

where T is the static temperature.

When studying drag and heat transfer over roughness elements, it is important to characterise the effect of one relative to the other. This is done by using an augmentation formula for heat transfer given by Hill et al. (1980) as

$$\frac{St}{St_s} \approx \frac{Cf}{Cf_s}\left[1 + \alpha_1 \sqrt{\frac{\overline{T}_w}{\overline{T}_e}\frac{Cf}{2}}\, k^{0.45} Pr^{0.8}\right] \tag{2.69}$$

where α_1 is a constant that can be varied from 0.4 to 1.3. This was also documented by Bowersox (2007) while documenting the results of supersonic flow over rough surfaces. The plot of (2.69) is shown in Figure 2.9. It is clear from Figure 2.9 that for the case of non-adiabatic walls, the increase in heat transfer due to roughness element compared to smooth wall case is less pronounced compared to increase in skin friction coefficient (Bowersox, 2007). This is because of the additional pressure drag provided by the roughness, which does not have an equivalent for the heat transfer.

3

Numerical Methodologies

The thesis uses four different numerical methods to study compressible flow over roughness. They are 1) DNS of resolved roughness using immersed boundary method (IBM) 2) Resolved roughness in minimal-span channel 3) DNS of modeled roughness using parametric forcing approach by Busse and Sandham (2012) and 4) RANS of fully resolved roughness using body fitted grid. This chapter introduces the three methodologies along with the solvers that will be used. Additionally, the results from validation simulations for the three methods will also be presented.

3.1. Full channel DNS with Immersed Boundary Method

The most fundamental computational technique in terms of providing a complete, comprehensive picture of the entire range of scales that constitute turbulence is Direct numerical simulation (DNS). It was first used by Orszag and Patterson Jr (1972) for simulating homogeneous isotropic turbulence and then used by Kim et al. (1987) for simulating turbulent channel flow at friction Reynolds number $Re_\tau = 180$. The plane channel flow simulation was later followed by advances incorporating pressure gradients, heat transfer, transpiration, and roughness. Despite possessing the capability of providing flow statistics over a large range of length and time scales, DNS is computationally demanding because the cost of performing DNS scales with the Reynolds number (Re^3).

In case of compressible flows, the study by Coleman et al. (1995) serves as a standard where DNS was carried out for a supersonic turbulent flow in a plane channel with isothermal walls. When it comes to compressible flows, in addition to the already existing cost constraint posed by DNS, the additional complexities will be expounded. Compressible flows have discontinuities such as shocks that require certain modifications to the solver. One of the most baffling issues that researchers face while studying flows with turbulence and shocks is the contradictory nature of solution methodologies that are required to study these two features. The presence of shocks, that are very thin regions with width of the order of a few mean free paths has to be represented accurately on a grid. This is done by adding artificial dissipation that 'smears' the shock across a few grid points. This may resolve the issue of shock representation on a finite grid. But, it is detrimental to the small scales of turbulence as artificial dissipation adds to the physical dissipation.

A solver capable of handling these discontinuities in compressible flows is required if a highly accurate dataset of compressible flow over roughness is to be generated. The DNS solver used in this thesis is a high-fidelity, compressible solver STREAmS (Supersonic TuRbulEnt Accelerated navier-stokes Solver) for the DNS of canonical wall-bounded turbulent flows namely supersonic plane channel, zero-pressure-gradient developing over a flat plate and shock wave/turbulent boundary layer interaction (Bernardini et al., 2021). It is capable of producing highly accurate results for a wide range of Mach numbers, from low subsonic to hypersonic flows. The solver is highly-parallelised through message passing interface (MPI) parallelisation and can be used on modern high performance computing (HPC) platforms. The convective terms are discretised using a hybrid energy-conservative shock capturing scheme in locally conservative form making use of the approximation of arbitrary order put forward by Pirozzoli (2010). The shock capturing abilities depend on the usage of Lax-Friedrichs flux vector splitting and weighted non-oscillatory (WENO) reconstruction. To switch between energy preserving and shock capturing regions, the solver makes use of the modified version of the Ducros shock sensor (Ducros et al., 1999). The time advancement is through a three-stage, third-order

Runge-Kutta scheme.

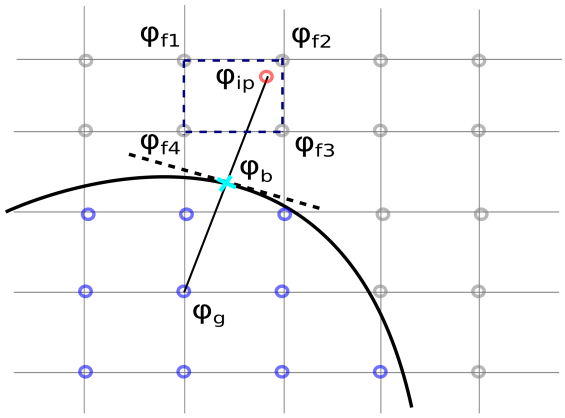

Figure 3.1: Visual description of the Ghost-Point-Forcing Method (GPFM) by De Vanna et al. (2020). Grey points correspond to the fluid region and blue points correspond to the ghost region. The two are separated by a solid line (boundary). ϕ_g, ϕ_f and ϕ_{ip} represent the fluid properties in the ghost, fluid regions and at the image point respectively. Dashed lines represent the tangent to the point (marked with a cross) where ϕ_b, the boundary condition is defined.

Two types of methods can be used to generate computational grids required to perform DNS of resolved roughness. The first one is the Body Fitted Grid Method and the second, is the Immersed Boundary Method (IBM). The former employs a body fitted grid to the surface of the roughness element. The latter allows for the roughness element or any geometry to cut across the cells of the computational grid. There are various kinds of IBM that have been studied over the last two decades. In this thesis, the Ghost-Point-Forcing Method (GPFM) is used as described in De Vanna et al. (2020). In GPFM, the computational domain is divided into three regions: the fluid region, the solid region and the ghost region. Let the flow property at the solid, fluid and ghost region be represented as ϕ_s, ϕ_f, ϕ_g respectively. The ghost region consists of layers that are present within the solid region. For every ghost point, a corresponding point in the fluid region is identified as the image point where the flow property is ϕ_{ip} as shown in Figure 3.1. Each image point has an associated unique ghost point. The surface of the solid is equidistant from the the ghost point and its associated image point. It is also perpendicular to the line connecting it with the ghost and image points respectively. Once the image point is identified, the flow properties such as velocity, density and temperature are interpolated using the neighbouring grid points (ϕ_{f1},ϕ_{f2},ϕ_{f3} and ϕ_{f4} in Figure 3.1) where these flow properties are stored. The boundary condition ϕ_b is then used to reflect the flow properties onto the ghost point.

$$\phi_g = 2\phi_b - \phi_{ip} \tag{3.1}$$

There are three layers of ghost nodes defined. The properties calculated on these ghost nodes serve as the boundary condition on the object surface. The geometry of the solid body is presented in OFF format. The computational geometry library CGAL (The CGAL Project 2021) is used to perform ray-tracing algorithm used to flag the grid points as solid points and fluid points. The ray-tracing algorithm works by shooting a ray in a random direction from every cell. If this ray crosses a surface an odd number of times, the cell is located within the solid object. However, if the ray crosses a surface an even number of times, the cell is located outside the solid boundary. The solution at the image point is interpolated from its neighbouring points using an inverse interpolation.

The DNS of fully resolved roughness using a full channel is carried out on cube roughness elements. This is defined as a $3D$ roughness since three separate dimensions are required to fully describe the geometry of the roughness element. The DNS dataset of the cubes was already available and is only analyzed in this thesis. The setup of the $3D$ roughness is explained first. The roughness elements are cubes placed on the channel walls. $3D$ resolved roughness is computationally the most expensive because of the complete resolution of the region close to the roughness elements. Additionally, three independent values are required to fully describe the roughness element. The dimensions of the domain is given by $6h \times 2h \times 3h$ with constant mesh spacing in the streamwise and spanwise directions. The distribution of mesh points in the wall-normal direction is based on an error function which clusters the points close to the roughness crest. Periodic boundary

conditions are enforced on the streamwise and spanwise boundaries and no-slip isothermal boundary conditions on the channel walls. The computations are initiated with a parabolic velocity profile with superposed random perturbations and uniform values of density and temperature. The bulk cooling term Φ ensures that constant bulk temperature is controlled at every time step. It is evaluated at every time step to such that only 35% of the bulk flow kinetic energy is used to increase the wall temperature namely $T_w = T_b(1 + 0.35\Pi M_b^2)$ where $\Pi = 0.178$. For the case of $M_b = 2$, this gives

$$T_w = T_b\left(1 + 0.35 \times 0.178 \times 2^2\right) \tag{3.2}$$

$$\frac{T_b}{T_w} = \frac{1}{1.2492} \approx 0.8 \tag{3.3}$$

Similarly for the case of $M_b = 4$, the bulk temperature is set to $T_b/T_w = 0.5$.

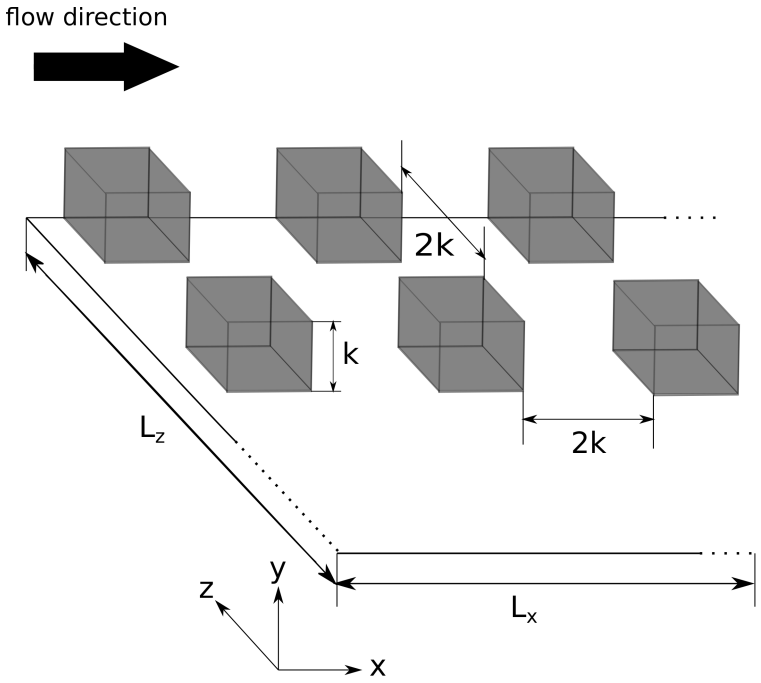

Figure 3.2: Schematic of the channel wall with cube roughness element. L_x is the streamwise domain length, L_z is the spanwise domain length and k is the geometrical roughness height

The DNS dataset is developed using the strategy of fixing the roughness height k/h and varying the friction Reynolds number. The roughness Reynolds numbers is given by $k^+ = k/\delta_\nu$. The friction Reynolds number is set at $Re_\tau \approx 500$ and $Re_\tau \approx 1000$ which corresponds to two roughness Reynolds numbers, $k^+ \approx 40$ and $k^+ \approx 80$ respectively. The spacing between two roughness elements is $2k$. A schematic of the channel wall with the roughness elements is shown in Figure 3.2. The choice of the roughness Reynolds numbers is to ensure that there is one case in the transitional regime and another one in the fully rough regime. Two separate supersonic cases are considered at $M_b = 2$ and $M_b = 4$. Smooth wall supersonic channel flow simulations are carried out at matching bulk Mach number and friction Reynolds numbers. This will allow comparison and also aid in the calculation of Hama roughness function ΔU^+.

3.2. Minimal-span channel DNS using Immersed Boundary Method

According to the physical setup of the channel flow configuration, the large value of the length of the channel along with a high aspect ratio means that the size of the domain under study increases. A larger domain requires greater computational resources if all the turbulent length scales are required to be sufficiently resolved. This problem of a large domain can be partially overcome with the use of a minimal-span channel. Jiménez and Moin (1991) studied the minimal flow units of wall turbulence by using a reduced streamwise and spanwise domain. They concluded that the near-wall turbulent cycle can be captured with a spanwise domain length of $100\nu/u_\tau$. Future studies by Jiménez and Pinelli (1999), Flores and Jiménez (2010)

and Hwang (2013) also support the results of minimal-flow units. The work of Flores and Jiménez (2010) demonstrated that the minimal-span channel can be used to capture the logarithmic layer of turbulent flows.

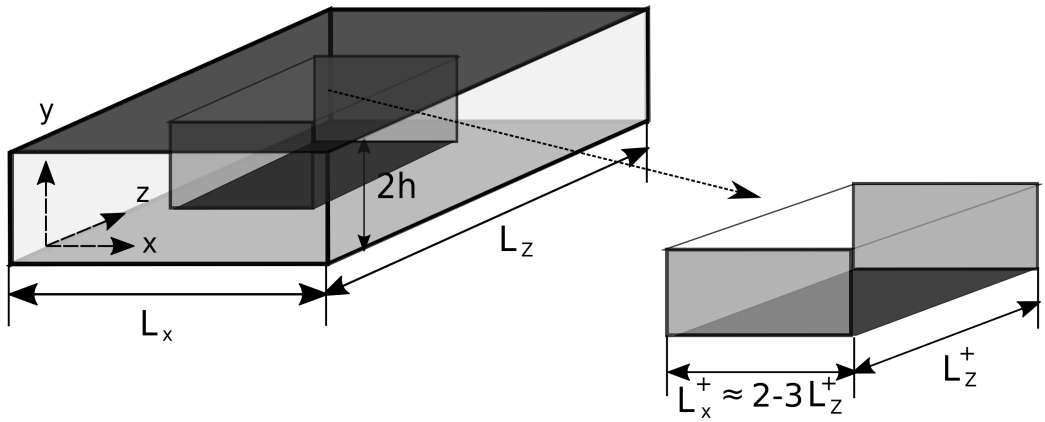

Figure 3.3: Geometric description of minimal-span channel as derived from full channel. L_x^+ and L_z^+ represent the viscous scaled domain lengths along streamwise and spanwise directions respectively. The size of the domain in the streamwise direction $L_x^+ \approx 2-3L_z^+$ is per the recommendation of Chung et al. (2015)

A more systematic study on minimal channel is offered by Chung et al. (2015). They investigated the effect of two different spanwise domain lengths with varying streamwise domain lengths on the mean flow and turbulent statistics. The condition for choosing a spanwise domain length proposed by Jiménez and Moin (1991) is further extended. It was observed that there is a close match between the mean velocity profile of full and minimal-span channels up to a wall normal height $y_c^+ \approx 0.4L_z^+$ provided this lies in the logarithmic layer (Chung et al., 2015). This region was termed as the 'unconfined' region meaning that the turbulence is faithfully captured without being constained due to the minimal span. The criteria for choosing the spanwise dimension was put forward as $L_z \gtrapprox max(100\nu/u_\tau, k/0.4, \lambda_{r,z})$ where $\lambda_{r,z}$ is a characteristic spanwise length scale. It is also recommended that the streamwsie domain length would benefit from being 1000 viscous units. As such, it was proposed to ensure $L_x^+ \gtrapprox max(1000\nu/u_\tau, 3L_y+, \lambda_{r,x})$ where $\lambda_{r,x}$ is some characteristic streamwise length scale. The simulations performed by Chung et al. (2015) however, indicated that it is acceptable to have $L_x^+ \approx 2-3L_z^+$. A very important result is the applicability of minimal-span channel for the resolved roughness cases. Chung et al. (2015) used sinusoidal roughness element of $h/k = 18$ and performed simulations for full channel and minimal-span channel incompressible flow over smooth and rough walls at $Re_\tau \approx 180$. The mean velocity profile adapted from Chung et al. (2015) for this particular case is presented in Figure 3.5. The full channel results are shown in solid and dashed lines without square symbols and the minimal-span channel results are shown with solid and dashed lines with square symbols. The inset shows the velocity shift in both cases. The simulation was performed in a domain with $L_z^+ \approx 141$ so the extent of unconfined region would then be $y_c^+ = 0.4L_z^+ = 0.4 \times 141 \approx 54$. The vertical dashed line in Figure 3.5 clearly shows that the roughness element is well inside $y_c^+ \approx 54$ ensuring the validity of the results obtained using minimal-span channel. Although the minimal-span channel is unable to capture the mean velocity profile of smooth and rough walls in the outer layer, the mean velocity shift is not altered. This confirms the soundness of the choice of minimal-span channel in this thesis to study resolved roughness. The physical description of the minimal-span channel that will be used in this thesis is shown in Figure 3.3. A portion of the full channel is taken out to graphically explain the concept of minimal-span channel.

The DNS of transverse bar roughness elements in a minimal-span channel is considered. The DNS of this roughness type has been performed in this thesis. The dimensions along the streamwise and wall-normal directions are the same as that of $3D$ roughness element ($k/h = 0.08$). The only difference is that the roughness element extends throughout the entire spanwise direction. This way, two independent values are sufficient to fully describe the roughness element earning it the name of $2D$ roughness element. The schematic of a channel wall with bar roughness elements is shown in Figure 3.4. In addition to being an open channel, the computational domain is also a minimal-span channel. The dimensions of the box is $1.68h \times 1h \times 0.75h$. The choice of the spanwise domain size is motivated by the results from MacDonald et al. (2017). For a roughness height of $k = 0.08$, the influence of roughness extends up to $y = 3k = 0.24$ from the roughness crest or $y = 0.32$

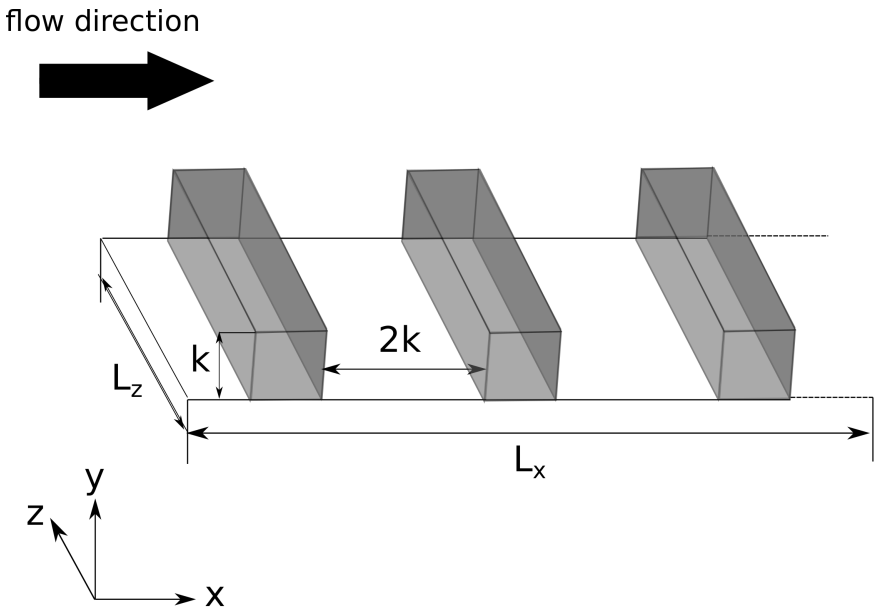

Figure 3.4: Schematic of the channel wall with bar roughness element. L_x is the streamwise domain length, L_z is the spanwise domain length and k is the geometrical roughness height

from the wall. The spanwise domain length should be chosen in such a way that the roughness element and its region of influence is immersed in the unconfined area, given by $y_c = 0.4L_z$. For $y = 0.32$, this would be $L_z = 0.32/0.4 = 0.8$. Considering this as an upper limit, a spanwise domain length of $L_z/h = 0.75$ has been chosen with the streamwise domain length being $L_x/h = 1.68$. The simulations are performed at $Re_\tau \approx 500$ and $Re_\tau \approx 1000$ giving two roughness Reynolds number $k^+ \approx 40,80$ at $M_b = 2$. The channel height is $h = 1$ with a slip wall at the channel mid-plane enforcing symmetry boundary conditions on u_1, u_3 and forcing $u_2 = 0$. The details of the test cases are tabulated in Table 3.1.

3.3. DNS with parametric forcing

Due to the high cost of performing DNS in general and more so for compressible flows, an alternative approach should be adopted. In case of roughness, the cost of performing DNS is further exacerbated by the resolution requirements close to the roughness element. A more fundamental issue in studying roughness is the inability to ascribe the equivalent sand grain roughness k_s to the measured topological features (Chung et al., 2021). The estimation of k_s is done *a posteriori* and is not known before hand. A simpler and low-cost model is required to overcome these challenges. It is also necessary to correlate the topological features of roughness to a parameter and increase the confidence in the model to represent roughness effects.

The central theme of the thesis is the model developed by Busse and Sandham (2012). The goal of the model is to explore the effect of roughness using a distributed drag force. This is done by introducing an additional force term in the momentum equation that consists of three parameters - a roughness height parameter, a roughness factor and a shape function. Collectively, they are known as the roughness force term. The roughness force term will be represented as Γ_i and is given by:

$$\Gamma_i = \alpha_i F_i(y, H_i) \rho u_i |u_i| \tag{3.4}$$

where α_i is the roughness factor, $F_i(y, H_i)$ is the roughness shape function and H_i is the roughness height parameter. The subscript $i = 1,2,3$ denotes the co-ordinate directions of streamwise along x, wall-normal along y and spanwise along z respectively. The nature of the term $u_i|u_i|$ has a damping effect (Busse and Sandham, 2012). Since the thesis involves study of channel flow, only the streamwise forcing term is relevant.

$$\Gamma_1 = \alpha F_1(y, H_1) \rho u_1 |u_1| \tag{3.5}$$

A short description of each of the parameters in the roughness force term will be provided to understand their functionality.

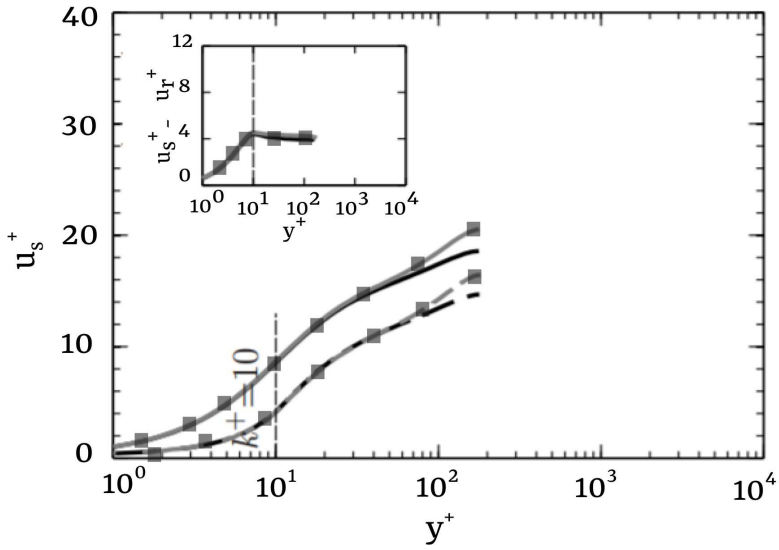

Figure 3.5: Incompressible mean velocity profile of smooth wall full channel (solid line) and full channel wall with sinusoidal roughness (dashed lines) compared against smooth wall minimal-span channel (solid line with square symbols) and sinusoidal roughness minimal-span channel (dashed line with square symbols) at $Re_\tau \approx 180$, $h/k = 18$ in a domain with spanwise dimension scaled by δ_ν of $L_z^+ \approx 141$ adapted from Chung et al. (2015). The vertical dashed lines indicate the wall normal location of the roughness element crest. The figure inset shows the mean velocity shift $\Delta U^+ = u_s^+ - u_r^+$ as a difference of smooth and rough wall mean velocity profile of full and minimal-span channels.

The roughness factor α_i has dimensions of line density $[L^{-1}]$ and represents the density of roughness elements. Dense roughness would have a higher value of the roughness factor whereas sparse roughness would have a lower value. Busse and Sandham (2012) performed DNS to quantify the effect of varying α on the mean velocity profile. By fixing the roughness shape function and roughness height parameter, different combinations of α_1, α_2 and α_3 were studied setting the parameters to either 1 or 0. It was observed that the wall-normal roughness factor α_2 contributed the least towards the shift in mean-velocity profile. For this reason, α_2 was set to 0. In addition, $\alpha_1 = \alpha_3 = \alpha$ was also ensured. An important observation was that for $\alpha = 1$, the variation of Hama roughness function ΔU^+ was negligible with roughness function except for the lower and upper extremes of roughness factors.

The roughness height parameter H_i can be thought of as an indication of the effect of the physical roughness height. It is known that an increase in the physical roughness height increases the magnitude of the Hama roughness function. Busse and Sandham (2012) report that although there exists no explicit relationship between the roughness height parameter and the physical roughness height, the roughness height parameter increases with increase in physical roughness height. The roughness shape function $F_i(y, H_i)$ gives the expression that identifies the region of influence of the roughness in a domain. The input is the roughness height parameter and the wall normal distance. Depending on the wall-normal distance, the roughness shape function exerts the influence of roughness on the flow. To simplify the analysis, Busse and Sandham (2012) introduce an auxillary parameter $\eta(H)$ which is defined by:

$$H = \frac{\int_0^{\eta(h)} F(y,H)\, y\, dy}{\int_0^{\eta(h)} F(y,H)\, dy} \tag{3.6}$$

in case of a channel flow where h denotes the channel half-height. It was observed that the Hama roughness function ΔU^+ increases for increasing roughness height parameter and roughness factor. Different combinations of roughness height parameter and roughness factor produce almost the same result in velocity defect profile in the outer layer which also collapses with the smooth wall profile. The exception is for extremely rough cases; this observation is in line with the expectation of the rough wall velocity defect profile to show universal behaviour in accordance with the outer layer similarity for mean velocity profile.

Busse and Sandham (2012) use six different shape functions, but they found little differences between them, and they suggested the use of a step function.

$$F(y,H) = \begin{cases} 1 & y \le \eta(H) \\ 0 & y > \eta(H) \end{cases} \tag{3.7}$$

By using (3.7) and integrating (3.6), $\eta(H) = 2H$.

The parametric forcing approach that was introduced and studied by Busse and Sandham (2012) is for incompressible flows. The same model requires an extension to compressible flows to conduct study of supersonic flow over roughness. This will require the modification of the energy equation in addition to the momentum equation. The force term in the momentum equation is given by

$$\Gamma_m = \alpha F_1(y,H_1)\rho u_1|u_1| \tag{3.8}$$

Notice the inclusion of ρ in (3.8) due to the compressible nature of the flow. In case of the energy equation, two terms are added. The first one is representative of the work done by the roughness force term which is simply a product of the velocity and the force term. The second, is a term that accounts for the additional heat transfer caused by the roughness and can be called the roughness heat transfer term.

$$\Sigma_h = \rho u_1^2|u_i|F_1(y,H_1)\alpha + \rho u_1 C_p(T_w - T_r)F_1(y,H)\alpha \tag{3.9}$$

The second term in (3.9) is motivated by the idea that the heat transfer is proportional to $q_w \propto \rho u C_p(T_w - T_r)$ just the same way the additional force term is proportional to $D \propto \rho u^2/2$. This adds the effect of roughness to the heat transfer which is incorporated in the energy equation. It is worth mentioning that T_r in (3.9) is calculated using the local Mach number and not the Mach number at the channel centerline.

The simulations for modeled roughness are performed in an open channel box of dimensions $3.12h \times 1h \times 1.5h$. As opposed to the resolved roughness case, the strategy adopted in the modeled roughness case is to increase the roughness height parameter for a fixed friction Reynolds number of Re_τ. Specifically, the auxiliary parameter $\eta(H)$ is increased from $\eta(H) = 0.01$ to $\eta(H) = 0.08$. This is done since the implementation of the modeled roughness force term in the solver is such that, the auxiliary parameter can be provided as an input. Therefore, increasing the auxiliary parameter is much easier than progressively increasing the friction Reynolds number. The box profile is chosen since it closely resembles the available resolved roughness data of transverse rectangular bars and cubes. The legend for the cases of modeled roughness is explained. The first two letters denote the magnitude of the auxiliary parameter $\eta(H)$ with $K1, K2$ and so on upto $K8$ denoting $\eta(H) = 0.01, 0.02$ to $\eta(H) = 0.08$ respectively. The last two letters indicate the Mach number with $M_b = 2$ represented as $M2$ and $M_b = 4$ represented as $M4$.

3.4. Reynolds Averaged Navier–Stokes

The goal of the thesis is to explore the possibility of reducing the cost of running rough wall simulations of supersonic flows. A computational method that is very popular in industry and can be performed easily at a low cost is the Reynolds Averaged Navier–Stokes (RANS) simulations. By performing Reynolds averaging on the Navier–Stokes equations, the RANS equations are obtained. As described in subsection 2.2.1, the averaging procedure introduces the Reynolds stress which is the root cause of the closure problem. RANS models are broadly based on two different approaches; the first one stems from an analogy between the Reynolds stress and the viscous stress in what will be called the eddy viscosity models. These are also known as first-order closures. The second one, known as the Reynolds stress models are second-order closures and postulate a transport equation for the Reynolds stress. These models are out of the scope of the study and will not be elaborated. Eddy viscosity models are based on the eddy-viscosity hypothesis according to which, it is possible to relate the Reynolds stress to the mean strain rate tensor. For incompressible flow, this can be given as,

$$a_{ij} = -2\nu_T S_{ij} \qquad S_{ij} = \frac{1}{2}\left(\frac{\partial \overline{u}_i}{\partial \overline{x}_j} + \frac{\partial \overline{u}_j}{\partial \overline{x}_i}\right) \tag{3.10}$$

where, the anisotropic Reynolds stress tensor $a_{ij} = -\overline{u_i' u_j'} - 2/3\delta_{ij}K$, where K is the turbulent kinetic energy and $-\overline{u_i' u_j'}$ is the Reynolds stress tensor and ν_T, the eddy viscosity.

The model proposed and expounded by Spalart and Allmaras (1992) (SA model) is used in this thesis. It is also calibrated on mixing layers, wakes and flat plate boundary layers and is based on a transport equation

for ν_T (Spalart and Allmaras, 1992). The model has shown tremendous success and is widely accepted and used to date. In its most general form, the SA model is a balance between the material derivative of eddy viscosity and production and diffusion terms. The material derivative of a quantity β is given by

$$\frac{D\beta}{Dt} = \frac{\partial \beta}{\partial t} + \vec{u}.\nabla\beta \tag{3.11}$$

In case of near wall region, an additional destruction term is added to account for the blockage effect of the wall. The transport equation for ν_T is given by

$$\frac{D\widetilde{\nu}}{Dt} = c_{b1}(1-f_{t2})\widetilde{S}\widetilde{\nu} - \left[c_{w1}f_w - \frac{c_{b1}}{\kappa^2}f_{t2}\right]\left(\frac{\widetilde{\nu}}{d}\right)^2 + \frac{1}{\sigma}\left[\frac{\partial}{\partial x_j}\left((\nu+\widetilde{\nu})\frac{\partial \widetilde{\nu}}{\partial x_j}\right) + c_{b2}\frac{\partial \widetilde{\nu}}{\partial x_i}\frac{\partial \widetilde{\nu}}{\partial x_i}\right] \tag{3.12}$$

where the turbulent eddy viscosity is computed using

$$\nu_T = \widetilde{\nu} f_{v1} \qquad f_{v1} = \frac{\chi^3}{\chi^3 + c_{v1}^3} \qquad \chi = \frac{\widetilde{\nu}}{\nu} \tag{3.13}$$

Additional definitions are given by

$$\widetilde{S} = \Omega + \frac{\widetilde{\nu}}{\kappa^2 d^2} f_{v2} \qquad \Omega = \sqrt{W_{ij}W_{ij}} \tag{3.14}$$

where Ω is the magnitude of vorticity and d is the distance from the field point to the nearest wall and

$$f_{v2} = 1 - \frac{\chi}{1+\chi f_{v1}} \tag{3.15}$$

$$f_w = g\left[\frac{1+c_{w3}^6}{g^6 + c_{w3}^6}\right] \tag{3.16}$$

$$g = r + c_{w2}(r^6 - r) \tag{3.17}$$

$$r = min\left[\frac{\widetilde{\nu}}{\widetilde{S}\kappa^2 d^2}\right] \tag{3.18}$$

$$f_{t2} = c_{t3} exp(-c_{t4}\chi^2) \tag{3.19}$$

$$W_{ij} = \frac{1}{2}\left(\frac{\partial u_i}{\partial x_j} - \frac{\partial u_j}{\partial x_i}\right) \tag{3.20}$$

The values of the constants are provided in Spalart and Allmaras (1992). The wall and free-stream boundary conditions are given by

$$\widetilde{\nu}_{wall} = 0 \qquad \widetilde{\nu}_{far-field} = 3\nu_\infty - 5\nu_\infty \tag{3.21}$$

where ν_∞ is the free-stream kinematic viscosity. The SA model was originally developed for incompressible flows. The modified equations to account for compressibility is given by

$$\frac{D\rho\widetilde{\nu}}{Dt} = c_{b1}(1-f_{t2})\rho\widetilde{S}\widetilde{\nu} - \left[c_{w1}f_w - \frac{c_{b1}}{\kappa^2}f_{t2}\right]\rho\left(\frac{\widetilde{\nu}}{d}\right)^2 + \frac{1}{\sigma}\left[\frac{\partial}{\partial x_j}\left(\rho(\nu+\widetilde{\nu})\frac{\partial \widetilde{\nu}}{\partial x_j}\right) + c_{b2}\rho\frac{\partial \widetilde{\nu}}{\partial x_i}\frac{\partial \widetilde{\nu}}{\partial x_i}\right] \tag{3.22}$$

Resolved Roughness																	
Case	M_b	Re_τ	$Re_{\tau T}$	$Re_{\tau V}$	Re_b	k^+	T_b/T_w	L_x/h	L_y/h	L_z/h	N_x	N_y	N_z	Δx^+	Δy^+	Δz^+	$St \times 10^{-3}$	$C_f \times 10^{-3}$
Smooth	2	488	697	681	11039	0	0.8	6	2	3	512	384	384	5.71	0.96 – 4.63	3.96	2.49	3.81
Smooth	2	1003	1431	1403	25077	0	0.8	6	2	3	1024	688	768	5.87	0.97 – 5.88	4.07	2.04	3.14
Rough	2	498	740	665	6831	39.85	0.8	6	2	3	3088	384	1536	0.97	0.98 – 4.73	1.01	5.16	10.04
Rough	2	1034	1551	1377	13922	82.62	0.8	6	2	3	3088	688	1536	2.08	1.00 – 6.06	2.09	4.44	10.28
Smooth	4	493	1662	1580	20094	0	0.5	6	2	3	512	384	384	5.81	0.97 – 4.71	4.02	6.98	2.81
Smooth	4	995	2972	2874	39650	0	0.5	6	2	3	1024	688	768	5.83	0.96 – 5.83	4.04	5.71	2.42
Rough	4	516	1711	1349	12591	41.48	0.5	6	2	3	3088	384	1536	1.00	1.07 – 4.92	1.05	12.88	5.93
Rough	4	1069	3660	2668	24435	85.76	0.5	6	2	3	3088	688	1536	2.08	1.04 – 6.28	2.17	13.44	6.31
Minimal-span channel																		
Case	M_b	Re_τ	$Re_{\tau T}$	$Re_{\tau V}$	Re_b	k^+	T_b/T_w	L_x	L_y	L_z	N_x	N_y	N_z	Δx^+	Δy^+	Δz^+	$St \times 10^{-3}$	$C_f \times 10^{-3}$
Smooth	2	511	749	714	12044	0	0.8	1.68	1	0.75	96	192	64	8.94	0.40 – 3.58	5.99	2.29	3.52
Smooth	2	1068	1484	1505	27729	0	0.8	1.68	1	0.75	96	192	128	9.34	0.85 – 9.34	6.25	1.73	2.91
Rough	2	466	708	721	8660	37.26	0.8	1.68	1	0.75	840	192	64	0.93	0.37 – 3.26	5.45	4.60	7.21
Rough	2	1111	1694	1512	17526	88.86	0.8	1.68	1	0.75	840	192	128	2.22	0.89 – 7.78	6.50	3.84	7.84

Table 3.1: DNS dataset of supersonic channel flow over resolved roughness with cubic roughness elements and minimal-span channel flow with transverse bar roughness elements. $Re_\tau = u_\tau h/\nu_w$ is the friction Reynolds number with u_τ, h and ν_w respectively the friction velocity, channel half height and kinematic viscosity at the wall, $Re_{\tau T}$ and $Re_{\tau V}$ are the transformed friction Reynolds numbers according to Trettel–Larsson (Trettel and Larsson, 2016) and Volpiani (Volpiani et al., 2020) transformations respectively, $Re_b = 2h\rho_b u_b/\mu_w$ the bulk Reynolds number with ρ_b, u_b the bulk density and bulk velocity respectively and μ_w, the dynamic viscosity at the wall. k^+ is the roughness Reynolds number. T_b/Tw is the ratio of bulk temperature to temperature at the wall, $L_x/h \times L_y/h \times L_z/h$ is the length along the streamwise, wall-normal and spanwise directions respectively scaled by the channel half-height h with N_x, N_y, N_z indicating the number of mesh points along the same directions. Δx^+, Δy^+, Δz^+ is the viscous scaled mesh spacings in the same direction. St and C_f represent the Stanton number and skin-friction co-efficient respectively.

Modeled Roughness

$Case$	M_b	Re_τ	$Re_{\tau T}$	$Re_{\tau V}$	Re_b	$\eta(H)$	H^+	T_b/T_w	L_x/h	L_y/h	L_z/h	N_x	N_y	N_z	Δx^+	Δy^+	Δz^+	$Stx10^{-3}$	$C_f x10^{-3}$
Smooth	2	474	681	663	10806	–	–	0.8	3.12	1	1.5	192	192	128	7.70	0.38 – 3.32	5.55	2.49	3.77
K1M2	2	474	674	662	10560	0.01	2.37	0.8	3.12	1	1.5	192	192	128	7.70	0.37 – 3.32	5.55	2.61	3.94
K2M2	2	473	684	656	9583	0.02	4.73	0.8	3.12	1	1.5	192	192	128	7.69	0.37 – 0.33	5.54	2.84	4.75
K3M2	2	476	690	657	8616	0.03	7.13	0.8	3.12	1	1.5	192	192	128	7.73	0.38 – 3.33	5.57	3.17	5.91
K4M2	2	482	706	658	7425	0.04	9.63	0.8	3.12	1	1.5	192	192	128	7.83	0.38 – 3.37	5.64	3.73	8.09
K5M2	2	484	713	655	6720	0.05	12.10	0.8	3.12	1	1.5	192	192	128	7.86	0.38 – 3.39	5.64	4.04	9.90
K6M2	2	475	706	637	6023	0.06	14.25	0.8	3.12	1	1.5	192	192	128	7.72	0.38 – 3.33	5.56	4.56	11.78
K7M2	2	478	722	635	5793	0.07	16.71	0.8	3.12	1	1.5	192	192	128	7.76	0.38 – 3.34	5.59	4.89	12.79
K8M2	2	478	722	629	5335	0.08	19.13	0.8	3.12	1	1.5	192	192	128	7.77	0.38 – 3.35	5.60	5.38	15.01
Smooth	4	478	1443	1374	17348	–	–	0.5	3.12	1	1.5	192	192	128	7.77	0.38 – 3.35	5.60	1.31	1.43
K1M4	4	483	1406	1379	17174	0.01	2.41	0.5	3.12	1	1.5	192	192	128	7.84	0.38 – 3.38	5.65	1.26	1.48
K2M4	4	486	1523	1371	16134	0.02	4.85	0.5	3.12	1	1.5	192	192	128	7.89	0.39 – 3.40	5.69	1.34	1.69
K3M4	4	485	1515	1340	14588	0.03	7.28	0.5	3.12	1	1.5	192	192	128	7.88	0.38 – 3.40	5.68	1.49	2.04
K4M4	4	492	1479	1314	12892	0.04	9.83	0.5	3.12	1	1.5	192	192	128	7.98	0.39 – 3.44	5.76	1.65	2.64
K5M4	4	493	1677	1286	12053	0.05	12.32	0.5	3.12	1	1.5	192	192	128	8.01	0.39 – 3.45	5.77	1.84	2.99
K6M4	4	501	1704	1270	11387	0.06	15.03	0.5	3.12	1	1.5	192	192	128	8.14	0.40 – 3.14	5.87	2.01	3.42
K7M4	4	500	1647	1225	10725	0.07	17.50	0.5	3.12	1	1.5	192	192	128	8.12	0.40 – 3.50	5.86	2.28	3.80

RANS

$Case$	M_b	Re_τ	$Re_{\tau T}$	$Re_{\tau V}$	Re_b	k^+	T_b/T_w	L_x	L_y	L_z	N_x	N_y	N_z
Smooth	2	505	652	659	22500	-	0.8	0.075	2	0.075	4	128	4
Smooth	2	1047	1351	1370	50000	-	0.8	0.075	2	0.075	4	128	4
Rough	2	493	649	631	18400	39.44	0.8	0.24	2	0.24	30	180	30
Rough	2	1038	1355	1326	34000	83.04	0.8	0.24	2	0.24	30	180	30

Table 3.2: DNS dataset of supersonic channel flow over modeled roughness using parametric forcing approach of Busse and Sandham (2012) and RANS dataset for smooth and rough wall fully resolved channel flow configuration. $Re_\tau = u_\tau h/\nu_w$ is the friction Reynolds number with u_τ, h and ν_w respectively the friction velocity, channel half height and kinematic viscosity at the wall, $Re_{\tau T}$ and $Re_{\tau V}$ are the transformed friction Reynolds numbers according to Trettel–Larsson (Trettel and Larsson, 2016) and Volpiani (Volpiani et al., 2020) transformations respectively, $Re_b = 2h\rho_b u_b/\mu_w$ the bulk Reynolds number with ρ_b, u_b the bulk density and bulk velocity respectively and μ_w, the dynamic viscosity at the wall. $\eta(H)$ is the auxiliary parameter and $H^+ = (H/h)Re_\tau$ is viscous scaled the roughness height parameter as described in Busse and Sandham (2012). T_b/Tw is the ratio of bulk temperature to temperature at the wall, $L_x/h \times L_y/h \times L_z/h$ is the length along the streamwise, wall-normal and spanwise directions respectively scaled by the channel half-height h with N_x, N_y, N_z indicating the number of mesh points along the same directions. Δx^+, Δy^+, Δz^+ is the viscous scaled mesh spacings in the same direction. St and C_f represent the Stanton number and skin-friction co-efficient respectively.

The RANS simulations in this thesis is performed for a channel flow configuration using a low-dissipative solver for turbulent compressible flows on unstructured meshes as proposed by Modesti and Pirozzoli (2017) which uses almost the same numerics as in STREAmS but it is implemented inside the popular open source library OpenFOAM. Conservation properties is ensured on unstructured meshes through localised augmentation of the numerical flux with AUSM pressure diffusive flux (Modesti and Pirozzoli, 2017). Enhanced shock-capturing capabilities are incorporated through the localised AUSM diffusive flux. The algorithm is described in detail in Modesti and Pirozzoli (2017). An implementation of the algorithm in OpenFOAM is used for the simulations in this thesis. OpenFOAM (Weller et al., 1998) is an open source library released under General Public License (GPL) which is popular among the industry fraternity.

The smooth wall simulations is performed using $N_y = 128$ at $Re_\tau \approx 500, 1000$ and $M_b = 2$ with clustering of points close to the walls along the wall-normal direction. This is done to ensure $y^+ \approx 1$. No-slip, isothermal boundary condition applied to the channel walls. The simulation is initialised with a parabolic velocity profile. The simulations are carried out until steady state was reached. In case of $3D$ cube roughness, only one roughness element is simulated and the computational box dimensions are $0.24h \times 2h \times 0.24h$ with a grid size of $30 \times 180 \times 30$. Constant mesh spacing is ensured along streamwise and spanwise directions with clustering of points close to the channel walls along the wall normal coordinate. The cube roughness has dimensions of $k/h = 0.08$ with a spacing of $2k$ units between two roughness elements. This was done to allow comparison with the available DNS data on the same roughness geometry. The simulations are performed at $Re_\tau \approx 500, 1000$ giving two different roughness Reynolds numbers of $k^+ \approx 40, 80$.

3.5. Validation

Before performing analysis on roughness, it is important to show the confidence in results obtained by the solver. This can be done by comparing the results against those available in literature. Additionally, it is important to establish the accuracy of the compressibility transformations in collapsing the compressible mean velocity profile onto the incompressible log-law relation with the same constants of proportionality. The validation procedure will be proceed as follows

1. Validation of STREAmS solver for full channel, smooth wall, compressible flow against data available from Moser et al. (1999).

2. Validation of accuracy of minimal-span channel mean velocity profile up to y_c^+ for the case at $M_b = 0.3$ and comparison with data from MacDonald et al. (2017). Validation of supersonic minimal-span channel mean velocity profile.

3. Validation of modeled roughness case implemented in STREAmS with a standard test case from Busse and Sandham (2012) offered for both open and full channels.

4. Validation of compressible mean velocity profile for full channel computed using RANS SA model against data from DNS for smooth wall simulations.

3.5.1. STREAmS validation of smooth wall

The Volpiani-transformed (Volpiani et al., 2020) mean velocity profiles for a smooth wall, compressible full channel flow at $Re_\tau \approx 500$ and $Re_\tau \approx 1000$ at $M_b = 2$ are shown in Figure 3.6a to Figure 3.6b. Further details can be gathered from Table 3.3. For purpose of comparison, the smooth wall, incompressible channel flow data from Moser et al. (1999) is also presented. The transformation by Volpiani (Volpiani et al., 2020)is the most accurate transformation in accounting for compressibility effects. There is a very good collapse of the transformed mean velocity with the nearly incompressible profile for both $Re_\tau \approx 500$ and $Re_\tau \approx 1000$ cases.

The mean momentum balance for the full channel smooth wall case of $Re_\tau = 500$ in outer and wall units is presented in Figure 3.7a and Figure 3.7c respectively. The same is presented for $Re_\tau = 1000$ in Figure 3.7b and Figure 3.7d. The profiles in outer units show the expected trend as discussed in section 2.3. Close to the wall, the viscous contribution dominates and the Reynolds stress is zero. The wall shear stress in this case is completely due to the viscous contribution. As the center of the channel is approached, the contribution of the viscous stress drops further such that the sum of the viscous and Reynolds stress tends to a linear profile as shown by the solid (purple) line. In outer units, it is observed that the crossover point of the viscous and Reynolds stresses is closer to the wall in case of $Re_\tau = 1000$ in Figure 3.7b compared to the $Re_\tau = 500$ case in Figure 3.7a. However, when the same mean momentum balance is depicted in wall units as in Figure 3.7c and

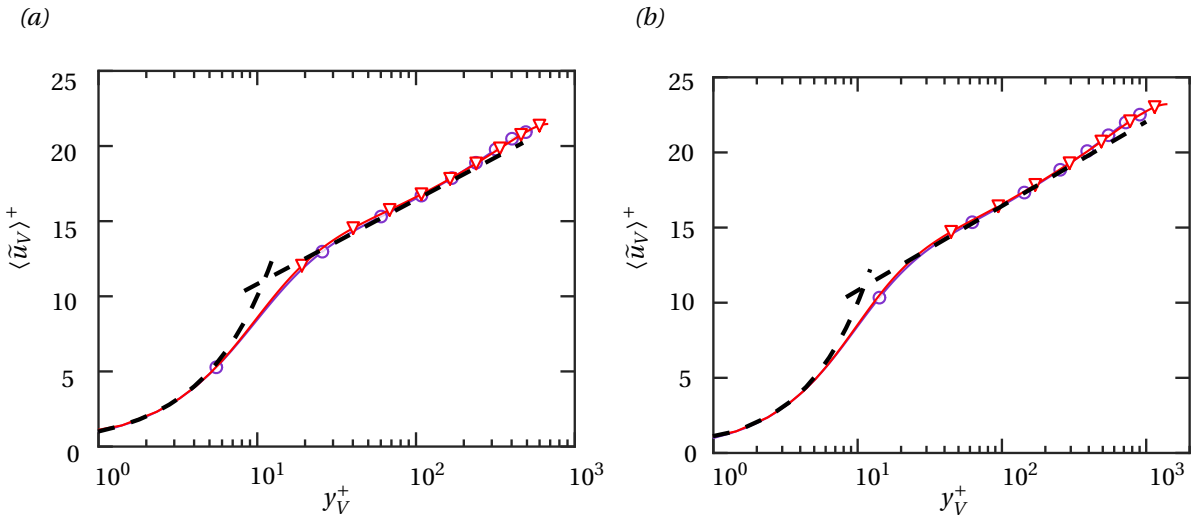

Figure 3.6: Mean velocity profile of full channel smooth wall compressible flow transformed by Volpiani transformation Volpiani et al. (2020) (downward pointing triangles) at (a) $Re_\tau \approx 500$ and (b) $Re_\tau \approx 1000$, $M_b = 2$. Incompressible smooth wall channel flow data by Moser et al. (1999) (circles) included for comparison. Dashed lines represent incompressible law of the wall given by $\langle u^+ \rangle = y^+$ and $\langle u^+ \rangle = (1/\kappa) log(y^+) + B$.

Figure 3.7d, it is clearly seen that the crossover point is at $y^+ \approx 12$. This lies in the buffer layer and indicates the location where the contribution from viscous and Reynolds stresses is equal. This is also the region where turbulence production is maximum. The mean momentum balance is an indicator of simulation convergence for a channel flow configuration. The results from Figure 3.7a and Figure 3.7b suggest that the simulations have converged when the output statistics were collected. The criteria for convergence of the simulation in this thesis will be linearity of the total stress. The simulations are performed until the sum of the viscous and Reynolds stress is linear.

STREAmS validation test case											
Sl No	Wall	Domain	Re_τ	M_b	H^+	L_x/h	L_y/h	L_z/h	N_x	N_y	N_z
1	Smooth	Full Channel	488	2	-	6	2	3	512	384	384
2	Smooth	Full Channel	1003	2	-	6	2	3	1024	688	768

Table 3.3: Validation data set for DNS of compressible smooth wall, full channel configurations using STREAmS. Re_τ is the friction Reynolds number, M_b is the bulk Mach number, H^+ is the scaled roughness height parameter from Busse and Sandham (2012), $L_x/h \times L_y/h \times L_z/h$ and $N_x \times N_y \times N_z$ is the grid size and number of points along streamwise, wall normal and spanwise directions respectively.

3.5.2. Minimal-span channel validation

The minimal-span channel is considered next. A standard test case is chosen from MacDonald et al. (2017). The dimensions of the box $L_x/h \times L_y/h \times L_z/h$ are $0.5\pi \times 2 \times 0.6$ and in wall units, $L_x^+ = 930$ and $L_z^+ = 354$. The simulation is performed at $Re_\tau \approx 590$ with a grid size $N_x \times N_y \times N_z$ of $96 \times 256 \times 72$. The test case is incompressible and the details of it are tabulated in Table 3.4. The mean velocity profile from the simulation performed using STREAmS and compared against the results from MacDonald et al. (2017) is presented in Figure 3.8. The Volpiani-transformed (Volpiani et al., 2020) mean velocity profile of an open minimal-span channel, smooth wall, compressible flow is also presented for the purpose of comparison. A very good agreement is observed between the results of MacDonald et al. (2017) and that obtained from STREAmS. Additionally, a very good agreement is also seen between full channel Volpiani-transformed Volpiani et al. (2020) mean velocity and the minimal-span channel mean velocity up to a wall-normal height of $y^+ \approx 145$. This height is termed as critical height by MacDonald et al. (2017) and is $y_c^+ \approx 0.4 L_z^+$. The results from Figure 3.8 confirm the presence of y_c^+ which directly confirms the possibility of using minimal-span channel for analysis of rough wall

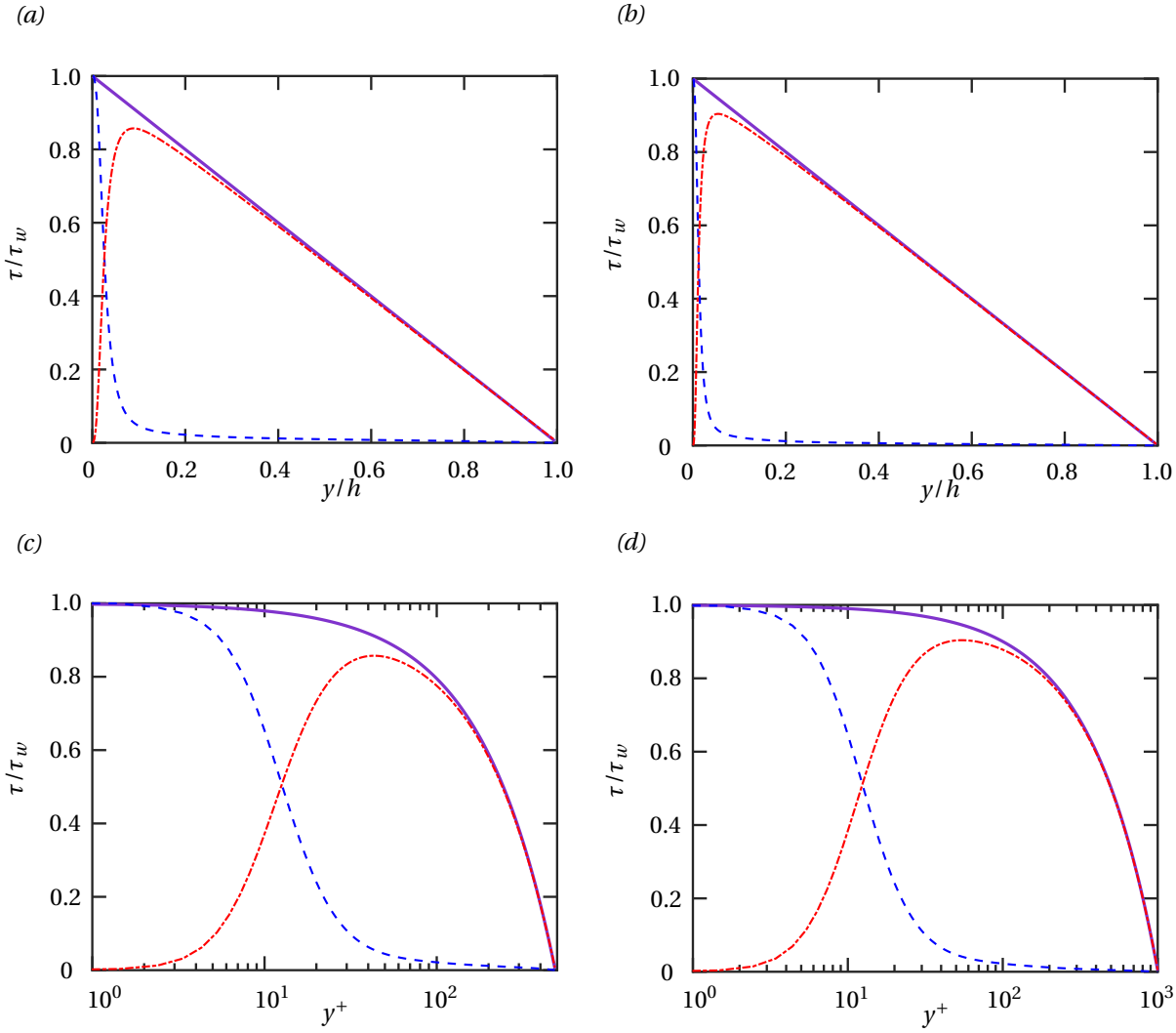

Figure 3.7: Mean momentum balance of smooth wall full channel case for (a) $Re_\tau = 500$ and (b) $Re_\tau = 1000$ in outer units and (c) $Re_\tau = 500$ and (d) $Re_\tau = 1000$ in wall units. The solid line represents the sum of the viscous and Reynolds stresses scaled by wall shear stress τ_w. The dashed line is the viscous stress where $\tau = \tau_{visc}$ and the dot-dashed line is $\tau = \tau_t$.

Minimal-spam channel validation test cases											
Sl No	Wall	Domain	Re_τ	M_b	H^+	L_x/h	L_y/h	L_z/h	N_x	N_y	N_z
1	Smooth	Minimal-span channel	590	0.3	-	0.5π	2	0.6	96	256	72
2	Smooth	Full Channel	488	2	-	6	2	3	512	384	384
3	Smooth	Open Channel	474	2	-	3.12	1	1.5	192	192	128
4	Smooth	Minimal-span Channel	462	2	-	1.56	1	0.75	96	192	64

Table 3.4: Validation data set for DNS of compressible and incompressible smooth wall, minimal-span channel configurations using STREAmS. Re_τ is the friction Reynolds number, M_b is the bulk Mach number, H^+ is the scaled roughness height parameter from Busse and Sandham (2012), $L_x/h \times L_y/h \times L_z/h$ and $N_x \times N_y \times N_z$ is the grid size and number of points along streamwise, wall normal and spanwise directions respectively.

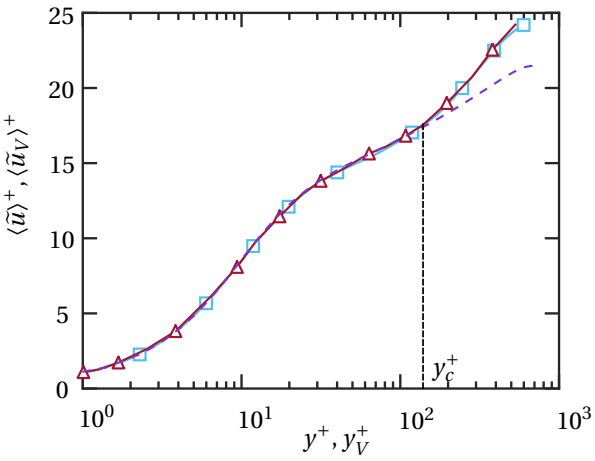

Figure 3.8: Mean velocity profile of incompressible smooth wall minimal-span channel flow performed at $Re_\tau \approx 590$ using STREAmS (squares) and extracted from MacDonald et al. (2017) (upward pointing triangles). The Volpiani transformed mean velocity profile (dashed lines) from a full channel compressible simulation at $Re_\tau \approx 500$ and $M_b = 2$ is presented. y_c^+ is the critical height or the wall-normal height upto which the results from full channel and minimal-span channel agree with each other.

channel flow MacDonald et al. (2017).

The accuracy of mean velocity up to y_c^+ is now demonstrated for a case of and open minimal-span channel compressible smooth wall DNS case. The test cases are presented as 3 and 4 in Table 3.4. Compressible open channel simulation are performed at $Re_\tau \approx 475$ and $M_b = 2$ with box size $L_x/h \times L_y/h \times L_z/h$ of $3.12 \times 1 \times 1.5$ and grid size $N_x \times N_y \times N_z$ of $192 \times 192 \times 128$. This is compared against a minimal-span channel with $L_x/h \times L_y/h \times L_z/h = 1.56 \times 1 \times 0.75$ and grid size $N_x \times N_y \times N_z$ of $96 \times 192 \times 64$. The domain has been halved along the streamwise and spanwise directions which is expected to increase the speed of execution by four times. The mean velocity profile transformed using van Driest (Van Driest, 1951), Trettel–Larsson (Trettel and Larsson, 2016) and Volpiani (Volpiani et al., 2020) transformations along with the mean density and temperature scaled by their corresponding values at the wall and the turbulent normal and shear stresses are presented in Figure 3.9a to Figure 3.9g. A few things are evident from these figures. Firstly, there is a an agreement with the full channel and minimal-span channel mean velocity profile up to y_c^+. Secondly, there is a good agreement between the mean temperature and mean density profiles of minimal-span and full channel cases in Figure 3.9e and Figure 3.9f respectively. Finally, the density scaled turbulent stresses are compared in Figure 3.9g. The wall-normal and spanwise turbulent normal stresses and the turbulent shear stress show very good agreement between the minimal-span and full channel cases. The streamwise normal turbulent stress is slightly under-predicted for the minimal-span channel case as the center of the channel is approached. This demonstrates that the usage of open minimal-span channel will still give accurate results when compared against an open channel configuration up to y_c^+. This is sufficient to accurately compute mean velocity shift ΔU^+.

3.5.3. DNS of modeled roughness

The validation of the implementation of the roughness term in STREAmS is offered. A standard case is picked from Table 3.5. The roughness shape function chosen is the box profile. The simulation is performed at $Re_\tau \approx 180$ and $M_b = 0.3$. The roughness height parameter scaled by friction length scale is $H^+ = 10$ and roughness factor $\alpha = 1$. Since the solver uses $\eta(H)$

$$\eta(H) = 2H \implies \frac{2H^+}{Re_\tau} = 0.11 \tag{3.23}$$

A value of $\eta(H) = 0.11$ is implemented in the solver. The size of the box is $7h \times 3.5h \times 2h$ with a grid size of $128 \times 128 \times 128$. A comparison of mean velocity profile and turbulent stresses is offered in Figure 3.10a to Figure 3.10e. It is observed that there is a very good agreement between the results of Busse and Sandham (2012) and that obtained from the implementation of the model in STREAmS. A small underprediction in the mean velocity is observed towards the center of the channel in Figure 3.10a. It should be noted that the

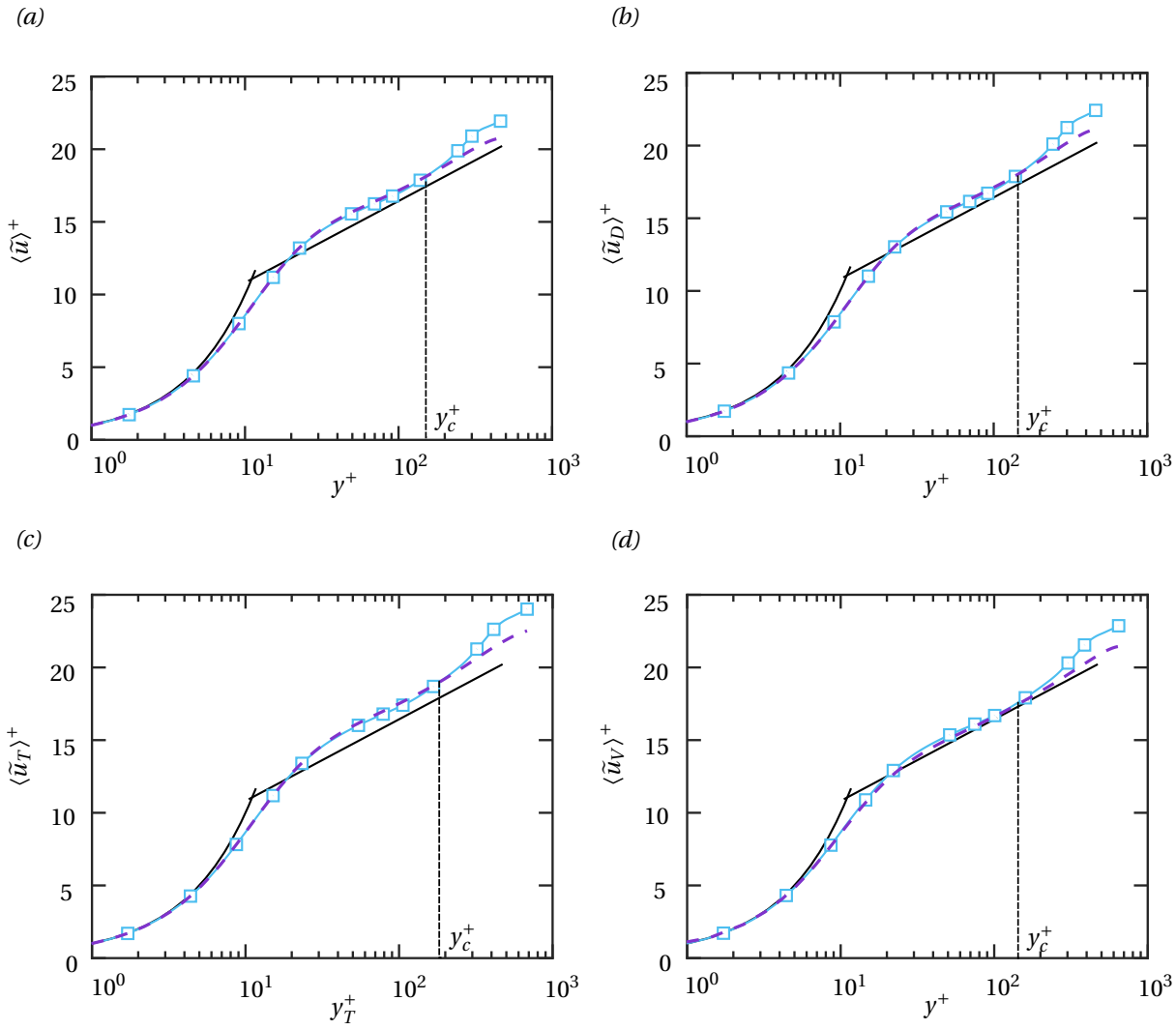
(a)
(b)
(c)
(d)
$\langle \tilde{u} \rangle^+$
$\langle \tilde{u}_D \rangle^+$
$\langle \tilde{u}_T \rangle^+$
$\langle \tilde{u}_V \rangle^+$
y^+
y_T^+
y_c^+
y_ℓ^+
0
5
10
15
20
25
10^0
10^1
10^2
10^3

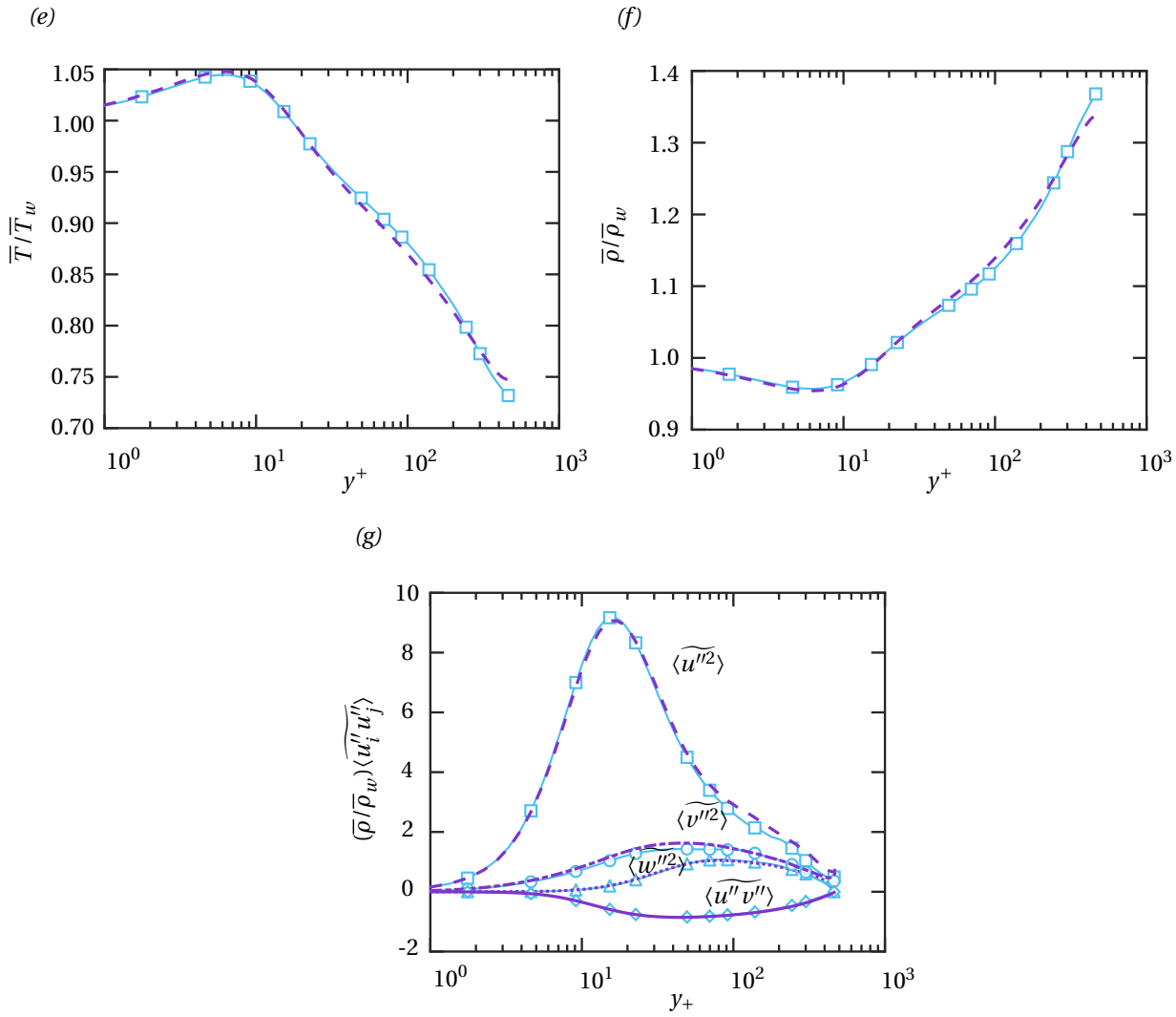

Figure 3.9: Comparison of compressible open channel flow at $Re_\tau \approx 475$, $M_b = 2$ and $T_b/T_w = 0.8$ with an open minimal-span channel: Mean velocity (a) untransformed, transformed by (b) van Driest (Van Driest, 1951) (c) Trettel–Larsson (Trettel and Larsson, 2016) (d) Volpiani (Volpiani et al., 2020) transformations (e) mean temperature (f) mean density and (g) turbulent stresses. The vertical dashed lines in (a)-(d) indicate the extent of unconfined region denoted by y_c^+ up to which open and minimal-span channel mean velocity profiles collapse on each other. For (a)-(f), The solid line with squares indicate the results from minimal-span channel and the dashed line, from the full-span channel. For (a)-(d), solid black lines are the incompressible law of the wall relation $\langle u^+\rangle = y^+$ and $\langle u^+\rangle = (1/\kappa) log(y^+) + B$. For (g), turbulent normal stress along streamwise (squares), wall-normal (circles), spanwise (triangles) and shear stress (diamonds) represent minimal-span channel with dashed, dot-dahsed, dotted and solid lines representing the same quantities for the full channel counterpart.

validation case using STREAmS was performed at $Re_\tau = 183$. This gives an $H^+ \approx 10.06$ which is slightly larger than $H^+ = 10$ used by Busse and Sandham (2012). Since H^+ from the solver is slightly higher compared to that of Busse and Sandham (2012) (10.065 > 10), it is expected that the downward shift in mean velocity profile is large. At such low Reynolds numbers, the flow properties are very sensitive to small changes in the roughness height parameter. The small deviation in the mean velocity profile and the subsequent turbulent stresses could be explained on this basis. Another possibility is the order of accuracy - STREAmS is a 6^{th} accurate solver whereas the solver used by Busse and Sandham (2012) is 2^{nd} order accurate.

Modeled roughness validation test cases											
Sl No	Wall	Domain channel	Re_τ	M_b	H^+	L_x/h	L_y/h	L_z/h	N_x	N_y	N_z
1	Modeled roughness	Full Channel	183	0.3	10.065	7	2	3.5	128	128	128
2	Modeled roughness	Open Channel	183	0.3	9.955	7	1	3.5	128	64	128

Table 3.5: Validation data set for modeled roughness test case from Busse and Sandham (2012) in the full channel and open channel configurations. Re_τ is the friction Reynolds number, M_b is the bulk Mach number, H^+ is the scaled roughness height parameter from Busse and Sandham (2012), $L_x/h \times L_y/h \times L_z/h$ and $N_x \times N_y \times N_z$ is the grid size and number of points along streamwise, wall normal and spanwise directions respectively.

A potential way of reducing cost of running simulations is by considering an open channel whose wall normal height is half of a full channel. The simulations are performed for modeled roughness using an open channel at the same conditions as that of the full channel. The details of the simulation are given by case 2 in Table 3.5. The results of mean velocity and turbulent statistics are superposed on the full channel results in Figure 3.10a to Figure 3.10e. There is a good agreement between the mean velocity, streamwise normal and turbulent shear stresses. The wall normal turbulent stress in Figure 3.10c for the open channel configuration goes to zero as the channel mid-plane is approached. This is because of the impermeability boundary condition set at the channel mid-plane for open channel flow configuration. This boundary condition ensures that both velocity and the velocity fluctuation are identically zero at the channel mid-plane.

There is a good agreement between the open channel, full channel data obtained using STREAmS and data from Busse and Sandham (2012) for the wall normal turbulent normal stress upto $y/h \approx 0.7$ or $y^+ \approx 126$ as shown in Figure 3.10c. The scaled roughness height $H^+ = 10$ lies well within this region $H^+ << 126$. This confirms that usage of an open channel is not detrimental to the near wall dynamics of modeled roughness and will be used in this thesis to study modeled roughness.

3.5.4. Validation of RANS results of smooth wall

RANS validation test cases										
Sl No	Re_τ	Re_b	M_b	Turbulence Model	L_x/h	L_y/h	L_z/h	N_x	N_y	N_z
1	500	50000	2	SA	0.075	2	0.075	4	128	4
2	1047	22500	2	SA	0.075	2	0.075	4	128	4

Table 3.6: Simulation dataset of the validation test cases for compressible, full channel, smooth wall RANS. Re_τ is the friction Reynolds number, M_b is the bulk Mach number, Re_b is the bulk Reynolds number, Turbulence Model used is SA (Spalart-Allmaras). Dimensions of the box are given by $L_x/h \times L_y/h \times L_z/h$ with grid size $N_x \times N_y \times N_z$.

The untransformed mean velocity profile along with mean temperature and mean density profiles computed using RANS with the SA turbulence model at $Re_\tau \approx 500$ and $Re_\tau \approx 1000$ and $M_b = 2$ is presented in Figure 3.11a to Figure 3.11f. The results from DNS of compressible full channel smooth wall computed using STREAmS is also superposed for the purpose of comparison. It is observed that the mean velocity is overpredicted in the viscous wall region for untransformed profiles. In case of the overlap region, the mean velocity is under predicted. The mean temperature (Figure 3.11c and Figure 3.11d) and mean density (Figure 3.11e and Figure 3.11f) profiles computed from RANS show a good agreement with DNS data.

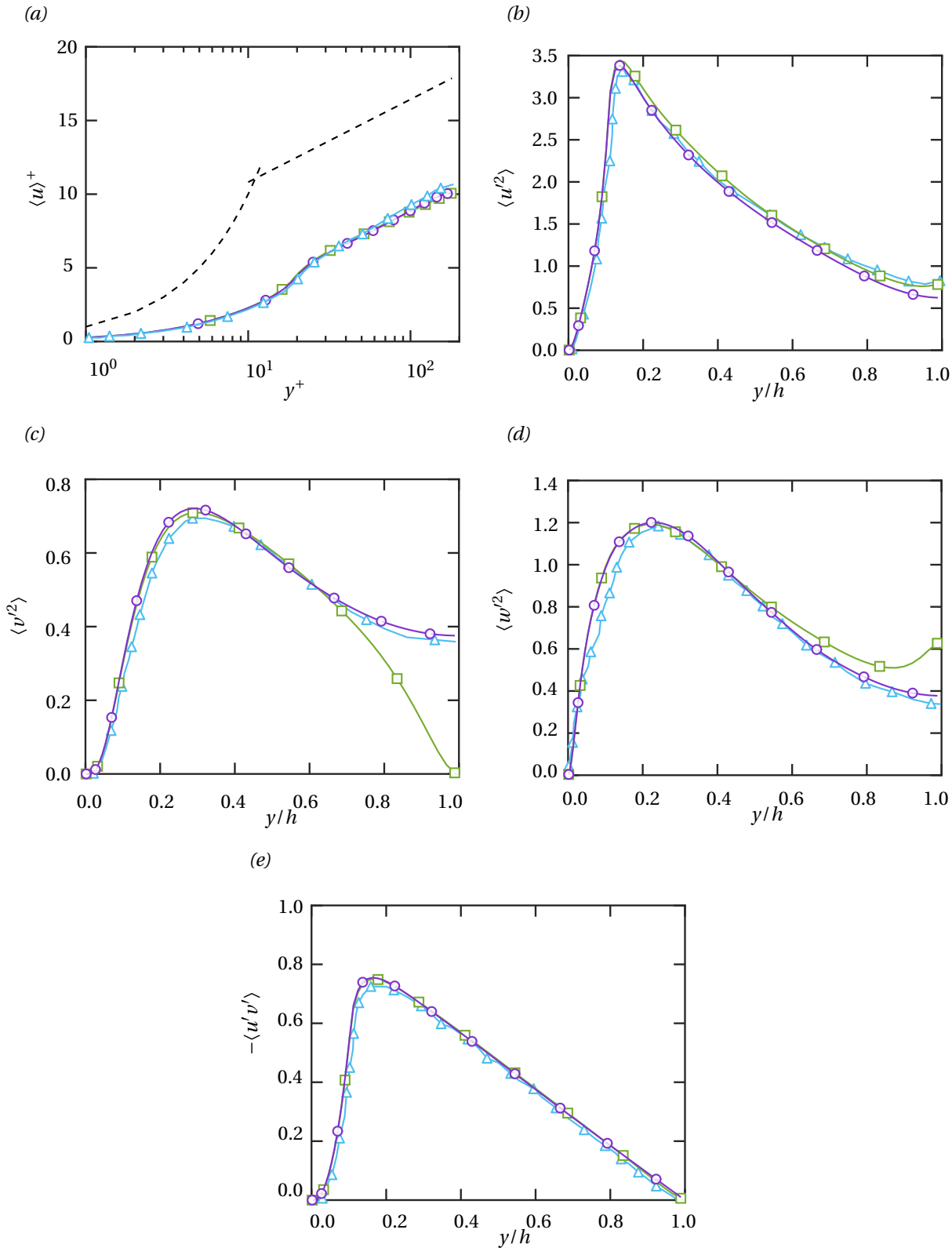

Figure 3.10: Mean flow statistics of incompressible, rough wall, full channel flow (circles) and open channel flow (squares) at $Re_\tau \approx 180$ and $H^+ = 10$ using parametric forcing approach by Busse and Sandham (2012) implemented in STREAmS: (a) mean velocity (dashed lines representing incompressile law of the wall relations for smooth wall) (b) streamwise (c) spanwise (d) wall normal turbulent normal and (e) shear stresses. Data from Busse and Sandham (2012) (triangles) included for comparison.

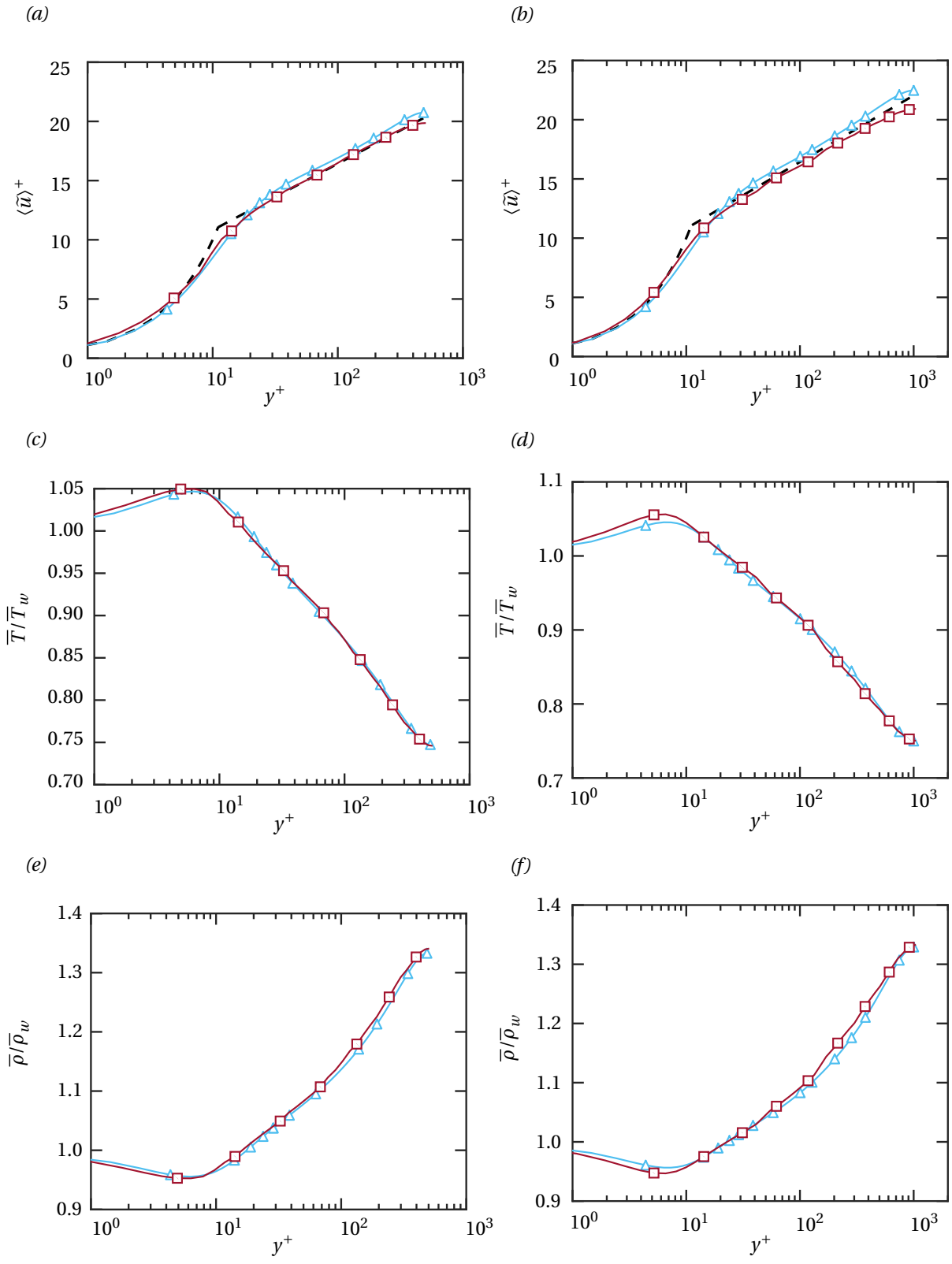

Figure 3.11: Mean flow statistics computed using RANS (squares) of full channel smooth wall compressible flow at $M_b = 2$, $Re_\tau \approx 500$ (left column of images) and $Re_\tau \approx 1000$ (right column of images): (a,b) untransformed, (c,d) mean temperature (e,f) mean density profiles. Compressible full channel smooth wall DNS results (upward pointing triangles) computed using STREAmS at the same conditions is also presented for comparison. Dashed lines represent incompressible law of the wall given by $\langle u^+ \rangle = y^+$ and $\langle u^+ \rangle = (1/\kappa) log(y^+) + B$.

4

Results and discussion

This chapter is aimed at presenting and discussing the extensive set of results obtained through the numerical simulations performed. It begins with the discussion of smooth wall and $3D$ resolved roughness using full channel and $2D$ resolved roughness using minimal-span channel. The modeled roughness results is then presented with the results of resolved and minimal-span channel superposed on it. This is done to offer a direct comparison and explore the possibility of using a modeled roughness approach to substitute the computationally intensive resolved roughness simulations. The chapter concludes with the results of RANS SA model being explained.

4.1. DNS using IBM

4.1.1. Full channel

The results of DNS using IBM for full channel $3D$ resolved roughness with $k/h = 0.08$ is presented here. The mean velocity profile and its accompanied compressibility transformations for smooth and rough wall at $Re_\tau \approx 500$ (circles) and $Re_\tau \approx 1000$ (diamonds), $M_b = 2$ (solid lines) and $M_b = 4$ (dashed lines) are shown in Figure 4.1a to Figure 4.1h. There is a vertical downward shift in the mean velocity profile in case rough wall Mach 2 at $Re_\tau \approx 500$ and $Re_\tau \approx 1000$ compared to their smooth wall counterparts. This is the Hama roughness function ΔU^+ and represents the momentum deficit caused due to the presence of roughness elements. The shift is greater in the rough wall case of $Re_\tau \approx 1000$ compared to the case $Re_\tau \approx 500$ since the roughness Reynolds number $k^+ \approx 80$ is higher than $k^+ \approx 40$. The Volpiani-transformed (Volpiani et al., 2020) mean velocity profile shown in Figure 4.1g and Figure 4.1h for case the smooth wall cases display a very good agreement with the nearly incompressible law of the wall profiles. On the other hand, the van Driest-transformed (Van Driest, 1951) (Figure 4.1c and Figure 4.1d) and in particular the Trettel–Larsson transformed (Trettel and Larsson, 2016) (Figure 4.1e and Figure 4.1f) mean velocity profiles for the smooth wall cases at $Re_\tau \approx 500, 1000$ do not show a very good agreement and are less accurate.

The results at $M_b = 4$ are reviewed. Figure 4.1g shows that the Volpiani transformation (Volpiani et al., 2020) is again successful in transforming the mean velocity of the smooth wall case at $Re_\tau \approx 500$ in Figure 4.1g and $Re_\tau \approx 100$ in Figure 4.1h with a good agreement with the nearly incompressible flow case. This highlights the accuracy of the Volpiani transformation (Volpiani et al., 2020) at high Mach number. The Trettel–Larsson-transformed (Trettel and Larsson, 2016) mean velocity profile for the smooth wall case for $M_b = 4$ at $Re_\tau \approx 500$ in Figure 4.1e and at $Re_\tau \approx 1000$ in Figure 4.1f shows a greater deviation from the nearly incompressible mean velocity profile compared to the Mach 2 smooth wall case at the same Reynolds number. Upon examining the rough wall mean velocity profiles, a vertical downward shift is observed as was in the case of Mach 2. However, the velocity shift observed in all cases (untransformed and using compressibility transformations) for $M_b = 2$ is not equal to that observed for $M_b = 4$ despite sharing the same k^+. This shows visible compressibility effects since none of the compressible transformations are capable of accounting for this discrepancy. This questions the use of roughness Reynolds number in characterising the flow regime in case of compressible flows.

The untransformed mean velocity defect profiles scaled by u_τ is depicted for $Re_\tau \approx 500$ in Figure 4.2a and for $Re_\tau \approx 1000$ in Figure 4.2b. There is a very good agreement between the smooth wall and rough wall mean velocity defect profiles for $M_b = 2$ from $y/h \approx 0.1$. This is observed at $Re_\tau \approx 500$ and $Re_\tau \approx 1000$. However,

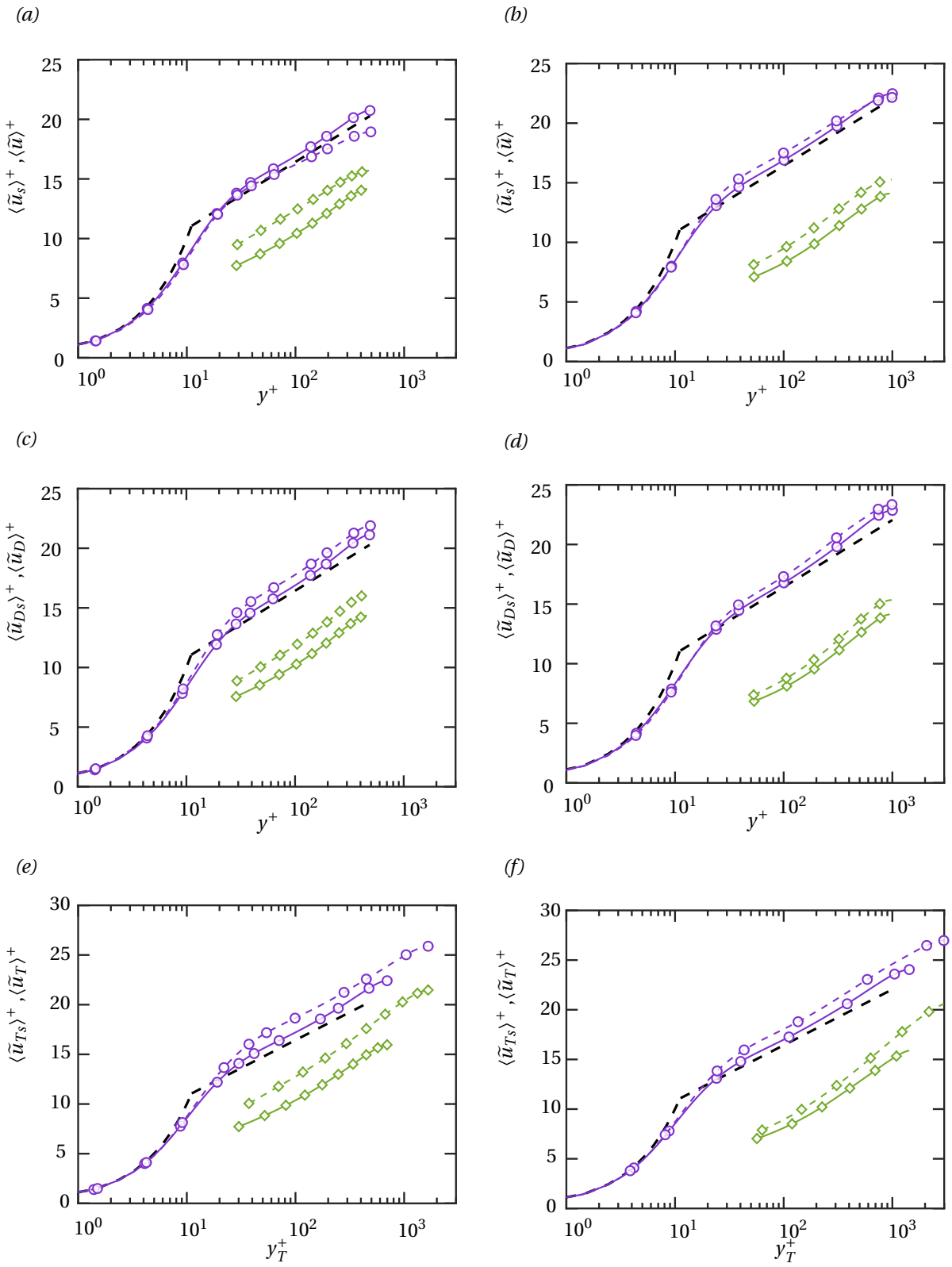
(a)
(b)
(c)
(d)
(e)
(f)
$\langle \widetilde{u}_s \rangle^+, \langle \widetilde{u} \rangle^+$
$\langle \widetilde{u}_{Ds} \rangle^+, \langle \widetilde{u}_D \rangle^+$
$\langle \widetilde{u}_{Ts} \rangle^+, \langle \widetilde{u}_T \rangle^+$
y^+
y_T^+

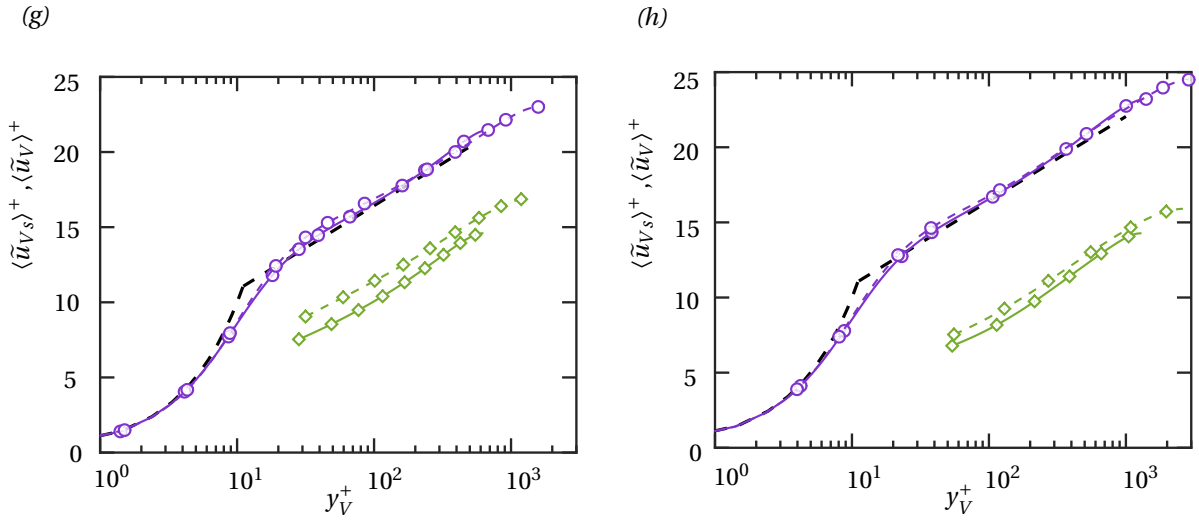

Figure 4.1: Mean velocity (a,b) untransformed (c,d) van Driest-transformed (Van Driest, 1951) (e,f) Trettel-Larsson transformed (Trettel and Larsson, 2016) (g,h) Volpiani-transformed (Volpiani et al., 2020) for smooth wall (circles) compared against $3D$ cube roughness (diamonds) at $Re_\tau \approx 500$ (left column of images) and $Re_\tau \approx 1000$ (right column of images). The roughness height $k/h = 0.08$ corresponds to $k^+ \approx 40$ at $Re_\tau \approx 500$ and $k^+ \approx 80$ at $Re_\tau \approx 1000$. Solid lines with symbols indicate $M_b = 2$ and dashed lines with symbols indicate $M_b = 4$. Dashed lines without symbols indicate incompressible law of the wall relations given by $\langle u \rangle^+ = y^+$ and $\langle u \rangle^+ = (1/\kappa) log(y^+) + B$. The rough wall profiles have been shifted by $\epsilon = 0.95k$.

the mean velocity defect profiles at $M_b = 4$ (dashed lines) using the untransformed mean velocity does not collapse on the profiles at $M_b = 2$. This displays compressibility effects and the need to account for them using compressibility transformations. To overcome this, the van Driest transformation (Van Driest, 1951) is used and the associated mean velocity defect profiles are displayed in Figure 4.2c and Figure 4.2d. Modesti and Pirozzoli (2016) proposed a parabolic relation for the van Driest-transformed (Van Driest, 1951) mean velocity defect profile given by

$$-(\langle \widetilde{u}_D \rangle^+ - \langle \widetilde{u}_{Dc} \rangle^+) = \frac{1}{2c_\mu^*} \left(1 - \frac{y}{h}\right)^2 \tag{4.1}$$

The mean velocity defect profile, untransformed and van Driest-transformed (Van Driest, 1951) with (4.1) is shown in Figure 4.2a to Figure 4.2d. It can be seen immediately that there is a good collapse observed for the van Driest-transformed (Van Driest, 1951) mean velocity defect profile and (4.1) compared to the untransformed mean velocity defect profile. Additionally, the mean velocity defect profiles at $M_b = 4$ also show a very good collapse with the results from $M_b = 2$. This collapse of mean velocity defect profiles at $M_b = 2$ and $M_b = 4$ lends weight to the outer layer similarity hypothesis.

Before presenting the results on ΔU^+, it is important to justify the significance of using the virtual origin while estimating it. Throughout the thesis, the virtual origin concept will be used for resolved roughness while presenting the mean velocity profile. The mean velocity profile incorporated with the virtual origin is called as shifted profile. The mean velocity profile of the resolved roughness presented without incorporating the virtual origin is called unshifted profile. Figure 4.3 shows the Hama roughness function ΔU^+ calculated for shifted and unshifted mean velocity profiles at $Re_\tau \approx 500$ and $Re_\tau \approx 1000$. For the unshifted profile, there is a large uncertainty in ΔU^+ over the range $100 < y^+ < 0.3Re_\tau$ which leads to ambiguity in the accurate value of ΔU^+. On the other hand, the shifted profile reduces this ambiguity in calculating ΔU^+ since the profile of ΔU^+ with respect to y^+ is horizontal. This represents a perfectly vertical downward shift in mean velocity profile of a rough wall case. The virtual origin is calculated as follows

$$\epsilon = 0.95k \tag{4.2}$$

The factor of 0.95 in (4.2) indicates that the virtual origin is close to the roughness crest. This factor is chosen to ensure that the Hama roughness function ΔU^+ is horizontal with respect to y^+. This way, ΔU^+ can be

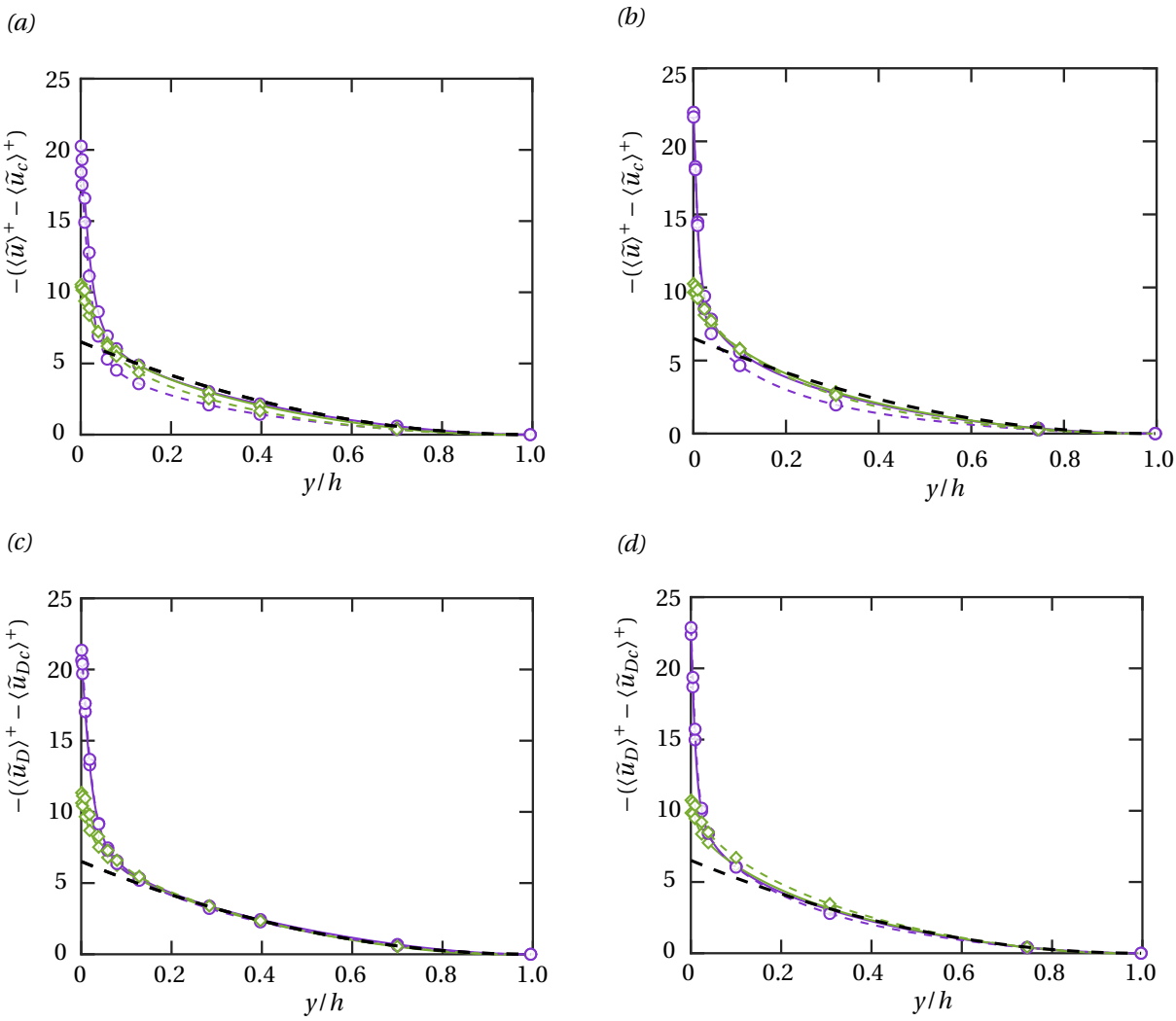

Figure 4.2: Mean velocity defect (a,b) untransformed and (c,d) van Driest (Van Driest, 1951) transformed profiles at $Re_\tau \approx 500$ (left column of images) and $Re_\tau \approx 1000$ (right colum of images) of smooth wall (circles) and shifted profile of $3D$ cube roughness (diamonds) at $M_b = 2$ (solid lines with symbols) and $M_b = 4$ (dashed lines with symbols). The dashed lines without symbols is the relation given by (4.1).

collected at any wall-normal height in the region $100 < y^+ < 0.15Re_\tau$ with reduced uncertainty. In this thesis, the value of ΔU^+ will be collected at $y_I^+ = 250$.

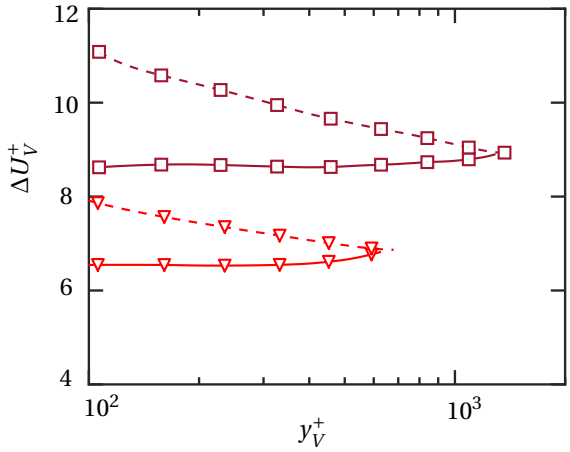

Figure 4.3: Hama roughness function ΔU^+ calculated using (a) shifted (solid lines) (b) unshifted (dashed lines) Volpiani-transformed (Volpiani et al., 2020) mean velocity profile at $Re_\tau \approx 500$ (lower pointing triangles) and $Re_\tau \approx 1000$ (squares), $M_b = 2$ for $3D$ cube roughness element

The definition of equivalent incompressible roughness height k_I is unambiguous in case of incompressible regime ($k_I = k$). However, there are multiple options to consider when defining k_I for the compressible regime. Two such options are considered in this thesis. The first one stems directly from compressibility transformations for wall normal coordinate

$$k_I = y_I(k) \tag{4.3}$$

(4.3) has the benefit of being consistent with the transformed velocity shift ΔU_I^+. However, it is hard to estimate this from experimental data. The second option considered in this thesis is

$$k_* = k\frac{\nu_w}{\nu(k)} \tag{4.4}$$

There is a variation in density from the trough to the crest of the roughness element. Such density variations are suitably accounted for by using (4.3) and (4.4) as the length scales.

The velocity shift of $3D$ cube roughness elements (solid diamonds) as a function of equivalent roughness Reynolds number k_{sI}^+ for all compressibility transformations used in this thesis is shown in Figure 4.4a to Figure 4.4d. A factor of $k_{sI}^+/k_I^+ = 1.9$ is used for all transformations. The rough wall data from Goddard Jr (1959), Reda et al. (1974),Berg (1979), Latin and Bowersox (2000) and Ekoto et al. (2008) are included in Figure 4.4b for the purpose of comparison. It is observed that the ΔU^+ for the untransformed mean velocity profile does not collapse on the asymptotic fully rough profile or the incompressible sand grain roughness data of Nikuradse et al. (1950). The accuracy of the ΔU^+ improves for van Driest and Trettel and Larsson compressibility transformations. The data reported in Figure 4.4b from other supersonic rough wall studies have been performed at adiabatic wall conditions. The results presented in this thesis are for strongly cooled walls. Therefore, there is a strong variation in thermodynamic properties in the vicinity of the roughness element crests. These variation in properties are not suitably accounted for by using k_s^+. In case of $M_b = 4$, there is an even greater deviation in velocity shift for the untransformed mean velocity profile (Figure 4.4a). The accuracy is seen to improve and is the best for ΔU_V^++ in Figure 4.4d.

While using k_I ensured that the Volpiani-transformed (Volpiani et al., 2020) mean velocity shift ΔU_V^+ collapses well with the incompressible data by Nikuradse et al. (1950), the same cannot be said regarding other compressibility transformations. The use of (4.4) allows for a better agreement with incompressible data for all compressibility transformations. The velocity shift as a function $k_{s*}^+ = 1.9k_*^+$ for untransformed and compressibility transformations is shown in Figure 4.5a to Figure 4.5d. It is easy to see that ΔU_I^+ shows good correlation with the incompressible data particularly in the case of Volpiani transformed ΔU_V^+ when k_{s*}^+ is used as shown in Figure 4.5d. The transformed roughness Reynolds number from (4.4) is able to account for compressibility effects both in the transitionally rough and fully rough regimes. The transitionally rough

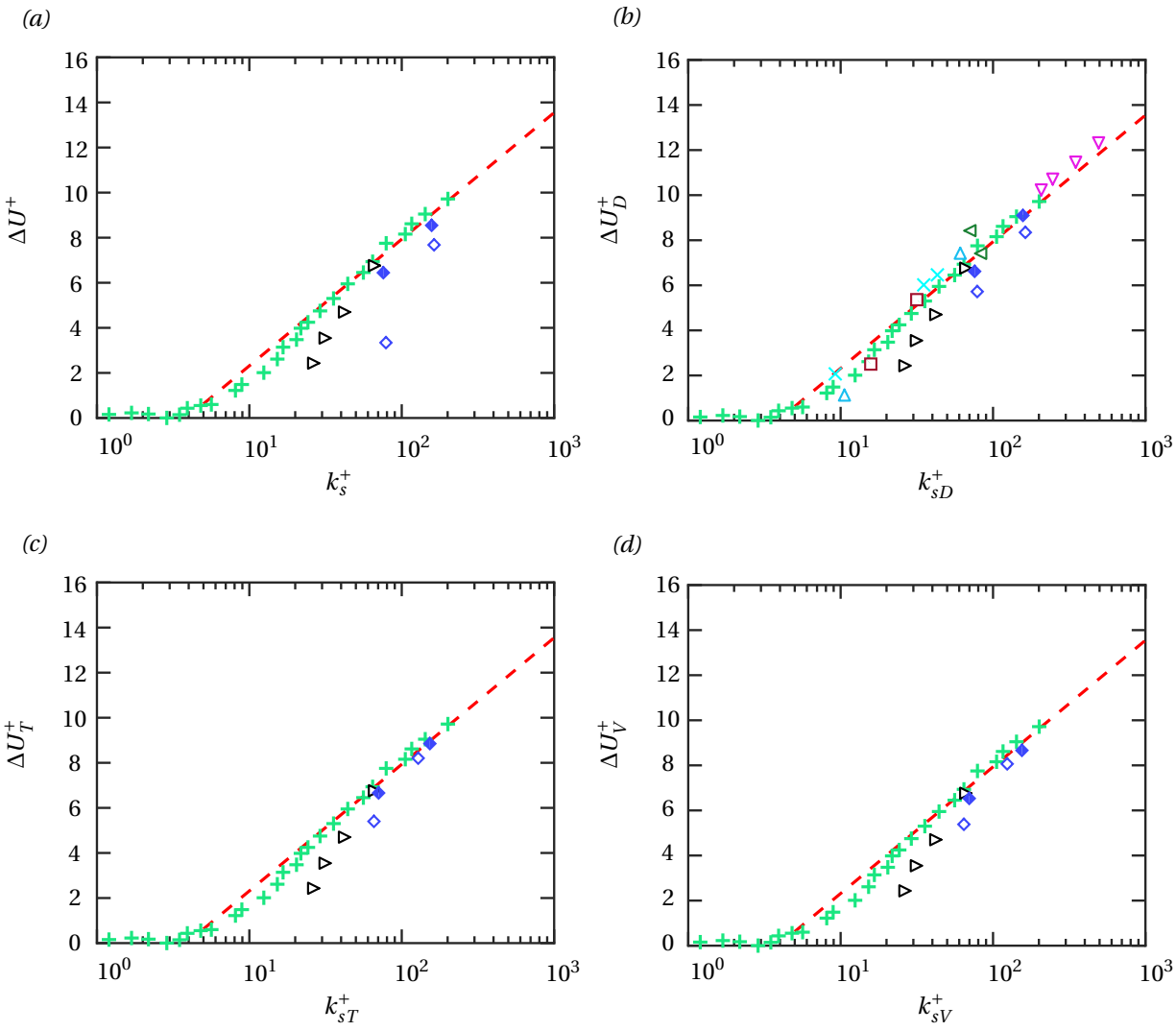

Figure 4.4: Mean streamwise velocity shift ΔU^+ (a) untransformed (b) van Driest-transformed (Van Driest, 1951) (c) Trettel–Larsson-transformed Trettel and Larsson (2016) (d) Volpiani-transformed (Volpiani et al., 2020) at $M_b = 2$ (solid diamonds) and $M_b = 4$ (hollow diamonds) for $3D$ cube roughness with roughness Reynolds numbers $k^+ \approx 40,80$ and sand grain roughness Reynolds number $k_s^+ = 1.9k^+$ and $k_{sI}^+ = 1.9k_I^+$. Dashed line is the theoretical asymptotic relation between equivalent sand grain roughness and Hama roughness function given by $\Delta U^+ = (1/\kappa)log(k_s^+) + B - B_S$. The incompressible roughness data from Nikuradse et al. (1950) (+ symbols) is also shown. In (b) experimental data of supersonic boundary layer are reported: Goddard Jr (1959) (squares), Berg (1979) (crosses), Reda et al. (1974) (upward pointing triangles, Latin and Bowersox (2000) (downward pointing triangles), Ekoto et al. (2008) (left pointing triangles). Incompressible transitionally rough data for the same geometry is also included from Abderrahaman-Elena et al. (2019) (right pointing triangles)

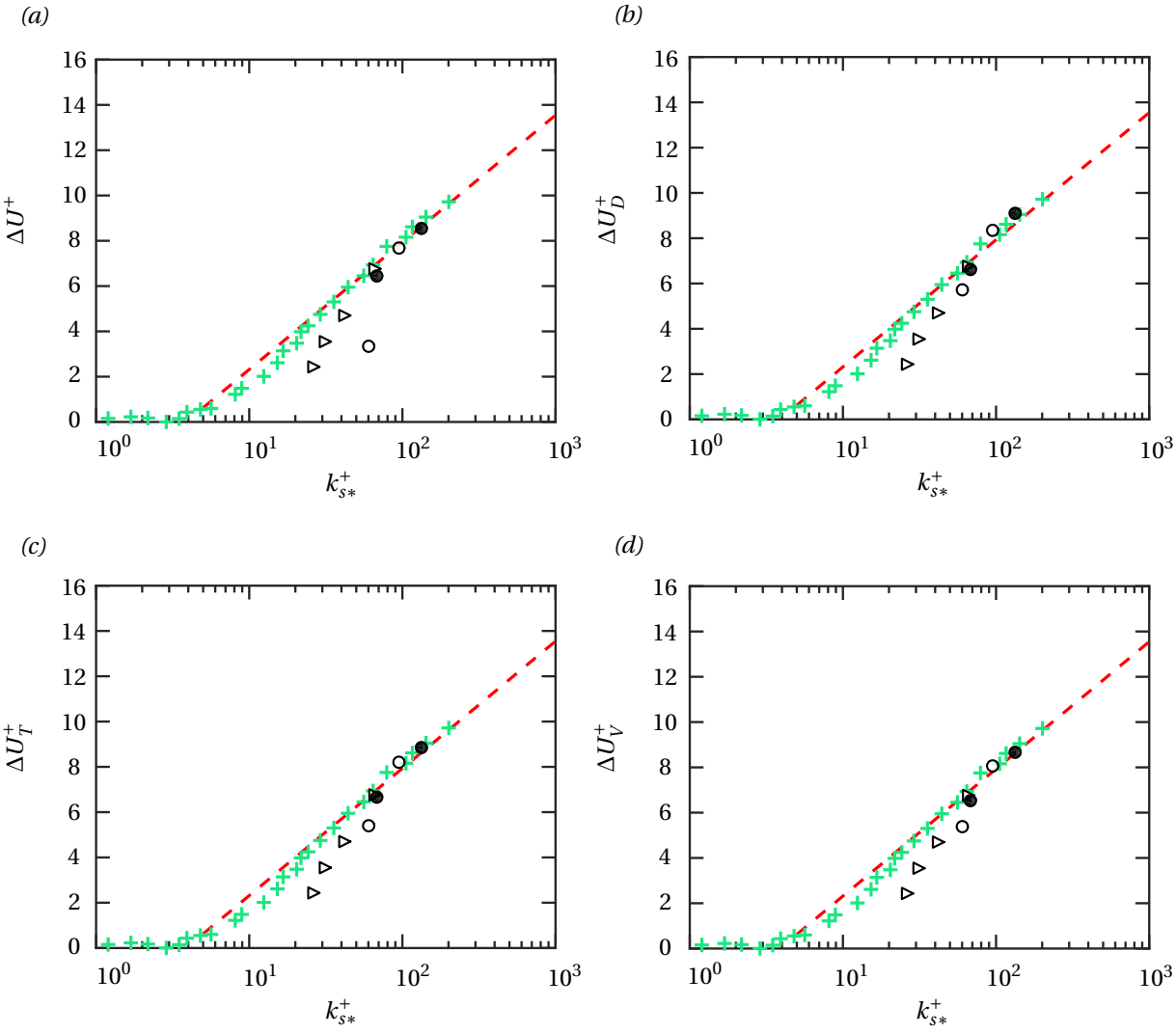

Figure 4.5: Mean streamwise velocity shift ΔU^+ (a) untransformed (b) van Driest-transformed (Van Driest, 1951) (c) Trettel–Larsson-transformed (Trettel and Larsson, 2016) (d) Volpiani-transformed (Volpiani et al., 2020) at $M_b = 2$ (solid circles) and $M_b = 4$ (hollow circles) for $3D$ cube roughness with roughness Reynolds numbers $k^+ \approx 40, 80$ and sand grain roughness Reynolds number $k_{s*}^+ = 1.9k_*^+$. Dashed line is the theoretical asymptotic relation between equivalent sand grain roughness and Hama roughness function given by $\Delta U^+ = (1/\kappa)log(k_s^+) + B - B_S$. The incompressible roughness data from Nikuradse et al. (1950) (plus symbols) is also shown. Incompressible transitionally rough data for the same geometry is also included from Abderrahaman-Elena et al. (2019) (right pointing triangles)

mean velocity shift ΔU_V^+ at $M_b = 4$ presented in Figure 4.5d is seen to be in close agreement with the incompressible data from Abderrahaman-Elena et al. (2019) for the same roughness geometry. The idea behind using length scales k_* and k_I is to account for the density variations between the roughness trough and crest. These length scales allow a better comparison with incompressible data.

The turbulent stresses are discussed next. The density scaled turbulent normal stress profiles are presented in Figure 4.6a to Figure 4.6f and the density scaled turbulent shear stress profiles in Figure 4.6g to Figure 4.6h. Both smooth wall and $3D$ cube roughness results at Mach number $M_b = 2, 4$ are presented in the same plot for $Re_\tau \approx 500$ and $Re_\tau \approx 1000$ respectively. It is observed that the streamwise turbulent stress peak shifts towards the channel centerline in case of Mach 2 rough wall compared to smooth wall for $Re_\tau \approx 500$ as seen in Figure 4.6a. The same is observed for the smooth and rough walls at $Re_\tau \approx 1000$ in Figure 4.6b. In addition, the peak value of the stress is reduced considerably (almost halved) in both cases. There is a gradual increase in the turbulent stress towards the crest of the roughness element followed by a sudden jump right above it. The presence of roughness elements cause a disruption in the near wall cycle of turbulence and is responsible for the reduction in peak of streamwise turbulent stress peak. The roughness elements cause a break up of the coherent structures in the buffer layer (namely the streamwise vortices) that is responsible for turbulence production mechanisms. This decrease in peak of streamwise turbulent stress is observed in the case of incompressible flows as reported in Krogstad et al. (2005), Lee et al. (2011) and Krogstadt and Antonia (1999). Included in both plots is the profile from Moser et al. (1999). A good collapse is observed for the smooth wall case at $M_b = 2$ with the profile from Moser et al. (1999) indicating that the density scaling is successful at accounting for compressibility effects at this Mach number. However, in case of Mach 4 (dashed lines), there is an increase in the stress peak for the smooth wall cases at both $Re_\tau \approx 500, 100$ compared to their smooth wall counterparts at Mach 2 in the buffer layer observed in Figure 4.6a and Figure 4.6b. The difference between the peak value of streamwise turbulent stress at Mach 2 and Mach 4 is greater at $Re_\tau \approx 500$ compared to $Re_\tau \approx 1000$. An important result noticed in all the cases is the presence of outer layer similarity. The profiles of smooth and rough walls at $M_b = 2$ and $M_b = 4$ collapse on each other beyond $y_r^+ \approx 140$ for $Re_\tau \approx 500$ and $y_r^+ \approx 250$ for $Re_\tau \approx 1000$ case respectively. This results in $y_r \approx 3k$. Jiménez (2004) and Raupach et al. (1991) suggest two to five times the roughness height above the roughness crest as the extent of the roughness sub-layer. However, as documented in the recent review by Chung et al. (2021), it is not clear if this is the equivalent roughness height k_s or roughness height k. The results obtained here point towards the usage of k in determining the extent of the roughness sub-layer. This is the wall normal height up to which the direct effect of roughness is felt by the mean flow. The effect of roughness cannot be neglected in this region.

The wall normal turbulent stresses are considered next. The density scaled wall-normal turbulent stress profile for the smooth wall at both $M_b = 2$ and $M_b = 4$ collapse well on the nearly incompressible profile from Moser et al. (1999). This is seen at for both $Re_\tau \approx 500$ and $Re_\tau \approx 1000$ in Figure 4.6c and Figure 4.6d respectively. The growth in the stress profile is more gradual for the rough wall when compared to the smooth wall. There is no significant change in the peak stress when the rough wall profile is considered. Yet another observation is the similarity of the rough wall profiles at $M_b = 2$ and $M_b = 4$. This is seen to extend upto the roughness crest. Beyond the roughness crest, the rough wall profile of $M_b = 2$ shows a very good outer layer similarity with the smooth wall profile at both $Re_\tau \approx 500$ and $Re_\tau \approx 1000$. However, a small deviation is observed in the rough wall profiles at $M_b = 4$. All wall normal turbulent stresses approach zero at the wall due to the presence of the impermeable wall boundary condition. The spanwsie turbulent stresses on the other hand, show a very good outer layer similarity for both Mach 2 and Mach 4 cases at $Re_\tau \approx 500$ and $Re_\tau \approx 1000$. Additionally, the smooth wall profiles at Mach 4 and Mach 2 collapse on each other and show good agreement with the profile from Moser et al. (1999) particularly in the outer layer. A similar collapse is observed between the rough wall profiles at these two Mach numbers beyond the roughness sublayer. The compressibility effect is not very pronounced for spanwise turbulent stresses as compared to their streamwise counterpart. The peak stress of rough wall profile is reduced to a greater extent at $Re_\tau \approx 1000$ in comparison to the reduction in peak at $Re_\tau \approx 500$ for both Mach numbers. Finally, the turbulent shear stress is considered. A near perfect collapse of the turbulent shear stress profile for smooth wall cases at Mach 2 and Mach 4 with the data from Moser et al. (1999) indicates that density scaling for turbulent stresses is most successful in case of shear stresses. In addition, the outer layer similarity also holds very well in both these cases. The peak value of turbulent shear stress is lower in case of Mach 2 rough wall compared to smooth. The peak is also shifted slightly towards the channel centerline. The increase in the turbulent shear stress is gradual up to the roughness crest. This is followed by a steep increase and a subsequent decrease beyond the peak value. The rough wall Reynolds stress profiles at $M_b = 2$ and $M_b = 4$ nearly collapse on each other indicating that the

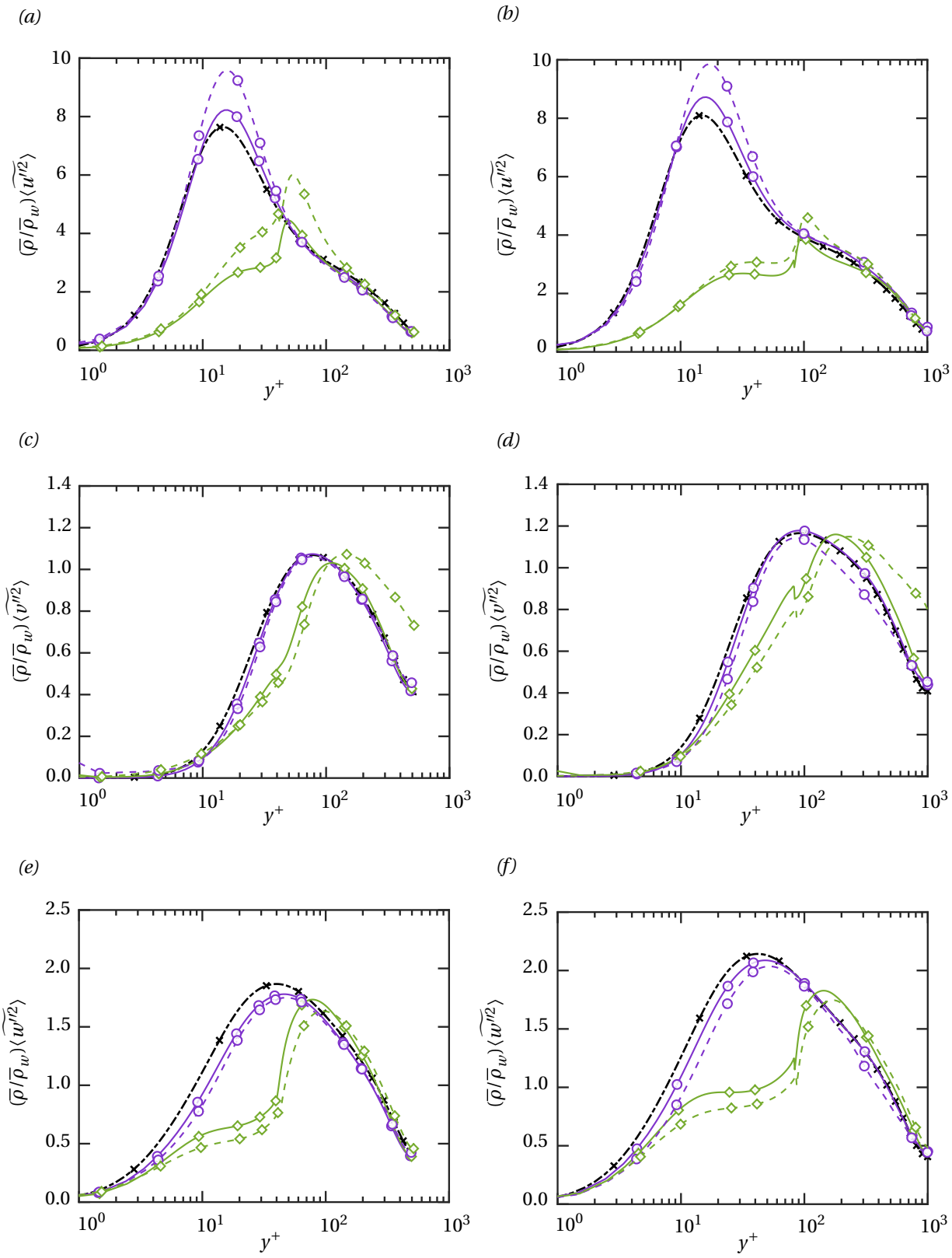
(a)
(b)
(c)
(d)
(e)
(f)
$(\overline{\rho}/\overline{\rho}_w)\langle u''^2\rangle$
$(\overline{\rho}/\overline{\rho}_w)\langle v''^2\rangle$
$(\overline{\rho}/\overline{\rho}_w)\langle w''^2\rangle$
y^+
10^0
10^1
10^2
10^3

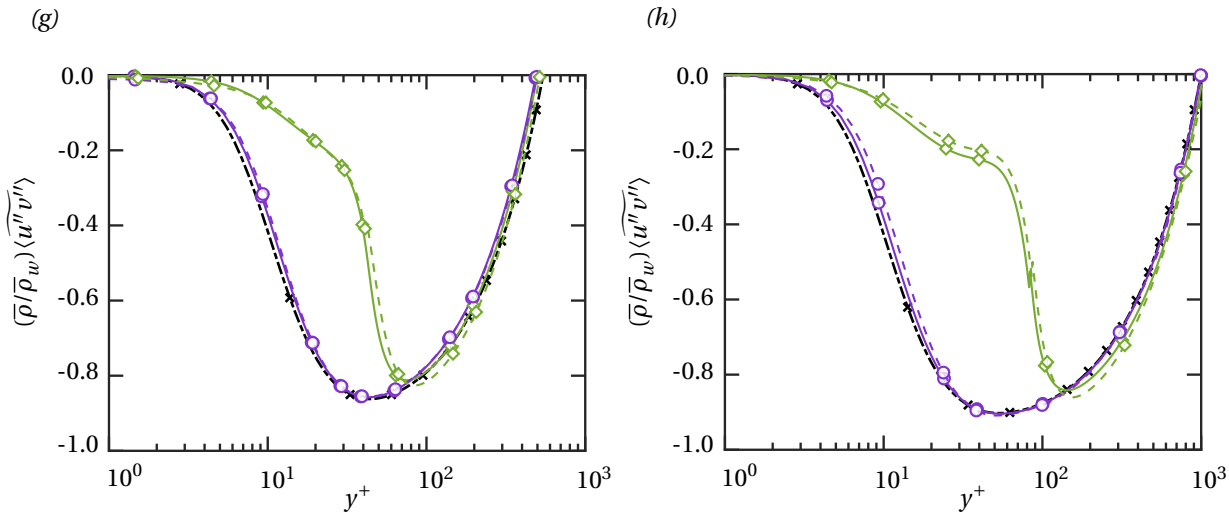

Figure 4.6: Density scaled turbulent (a,b) streamwise (c,d) wall-normal (e,f) spanwise and (g,h) shear stress profile of smooth wall (circles) and $3D$ resolved cube roughness (diamonds) at $Re_\tau \approx 500$, $k^+ \approx 40$ (left column of images) and $Re_\tau \approx 1000$, $k^+ \approx 80$ (right column of images). Turbulent stress profiles at $M_b = 2$ are represented by solid lines and at $M_b = 4$ are represented by dashed lines with the same symbols. Incompressible data from Moser et al. (1999) (dot-dashed lines with × symbols) also included.

Mach number effect does not permeate into Reynolds shear stress in case of wall with roughness.

The mean temperature of the flow is a very important quantity in compressible flows as it is used for estimating the heat transfer coeffecient. Since $T_b/T_w = 0.8$, there is a strong cooling at the wall. This is particularly important for dissipation of the energy generated as a result of viscous heating in compressible wall bounded flows. The mean temperature scaled by wall temperature T_w for Mach 2 smooth and rough wall at $Re_\tau \approx 500$ is shown in Figure 4.7a and at $Re_\tau \approx 1000$ in Figure 4.7b. Included in Figure 4.7a are the smooth and rough wall Mach 4 cases. It is observed that there is a steep gradient of mean temperature beyond the roughness crest for both the rough wall cases at $Re_\tau \approx 500, 1000$ compared to their smooth wall counterparts in Figure 4.7a and Figure 4.7b. The mean temperature gradient is much steeper for Mach 4 cases (both smooth and rough wall) compared to Mach 2. Similarly the mean density scaled by density at the wall $\overline{\rho}_w$ for the two sets of cases is displayed in Figure 4.7c and Figure 4.7d. The mean density variation across the channel wall normal direction is small for cases Mach 2 smooth and rough wall at $Re_\tau \approx 500$ in comparison to Mach 4 at the same Reynolds numbers. The mean density peak is at the channel centerline and happens to coincide with the point of minimum mean temperature. The mean density variation for $M_b = 4$ cases are a lot steeper in comparison to the flow cases at $M_b = 2$.

The temperature fluctuations profiles comparing smooth and rough wall Mach 2 cases at $Re_\tau \approx 500$ and $Re_\tau \approx 1000$ are shown in Figure 4.8a and Figure 4.8b respectively. The temperature fluctuations are scaled by $T_\tau^2 = q_w/\rho_w C p u_\tau$ where q_w is the wall heat flux. The peak of the temperature fluctuations for Mach 2 case smooth and rough walls at $Re_\tau \approx 500$ is comparable as seen in Figure 4.8a. The fluctuations are very small and do not show an appreciable growth in the viscous sub-layer in the smooth wall case. However, the fluctuations have a more steep increase up to the roughness crest in the rough wall case. There is a small dip at the crest of the roughness elements followed by a further increase. The temperature fluctuations for $Re_\tau \approx 1000$ in Figure 4.8b show a significant increase in the peak value of rough wall compared to smooth wall. The smooth wall case follows a similar trend of negligible variation in the viscous sub-layer. The Mach 4 smooth and rough wall temperature fluctuations are also presented in Figure 4.14a for $Re_\tau \approx 500$. It is observed that the peak value for the smooth wall case at Mach 4 is greater than Mach 2 at this Reynolds numbers. Additionally, it is also greater than the rough wall temperature fluctuation peak at Mach 4. In case of $Re_\tau \approx 1000$ in Figure 4.8b, a similar trend in Mach 4 is observed where the peak fluctuation of smooth wall exceeds that of the rough wall case.

The mean density fluctuations for smooth and rough wall Mach 2 and Mach 4 cases at $Re_\tau \approx 500$ are depicted in Figure 4.8c. They are scaled by the mean density at the wall $\overline{\rho}_w$. A quick examination of the mean

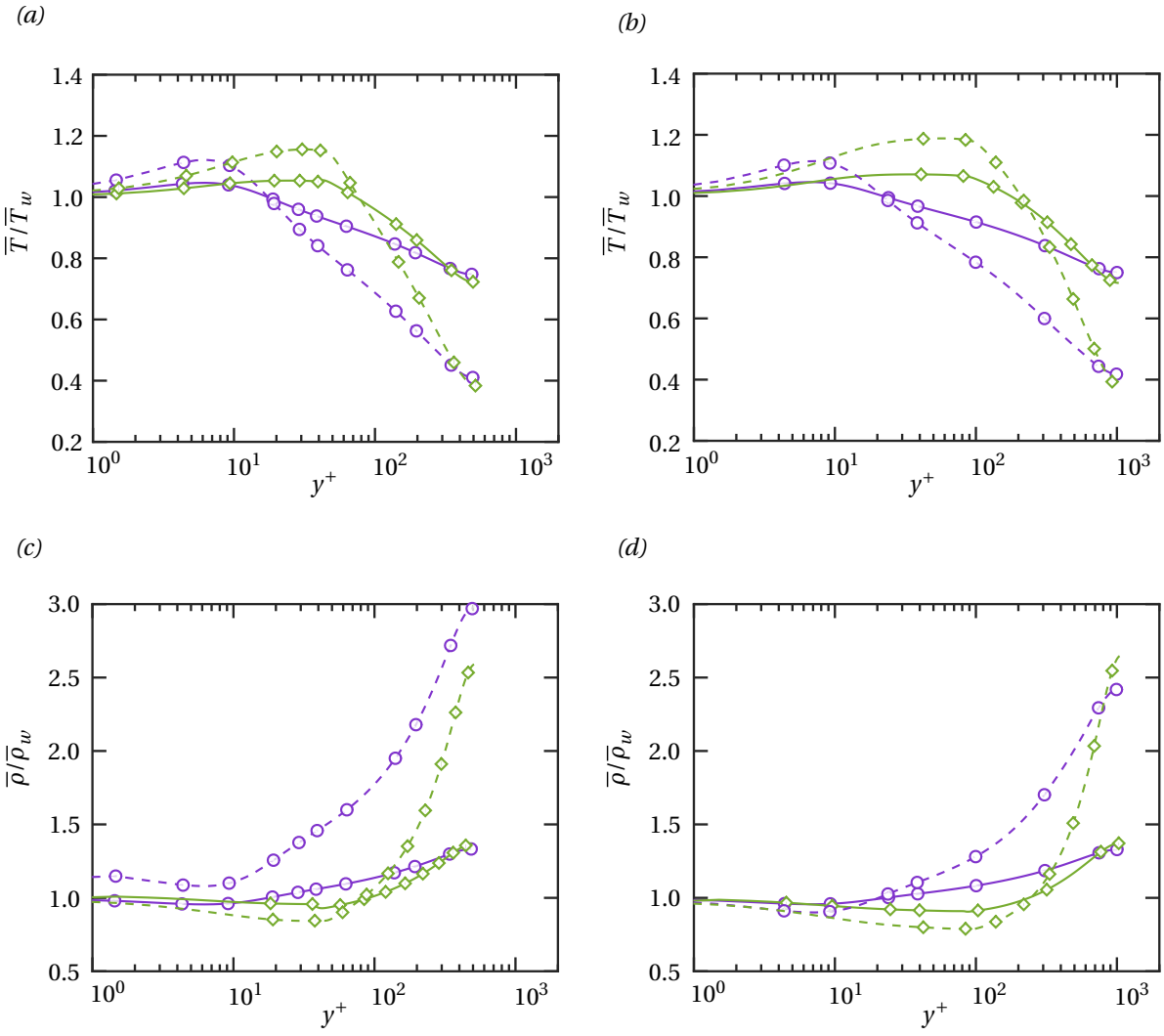

Figure 4.7: (a,b) Mean temperature profile scaled by wall temperature $\overline{T}_w$ (c,d) and mean density scaled by density at the wall $\overline{\rho}_w$ for smooth wall (solid lines, circles) and rough wall (solid lines, diamonds) with roughness height $k/h = 0.08$ for $3D$ cube roughness at $Re_\tau \approx 500$ (left column of images), $Re_\tau \approx 1000$ (right column of images). $M_b = 2$ data represented as solid lines with symbols and $M_b = 4$ data represented as dashed lines with symbols.

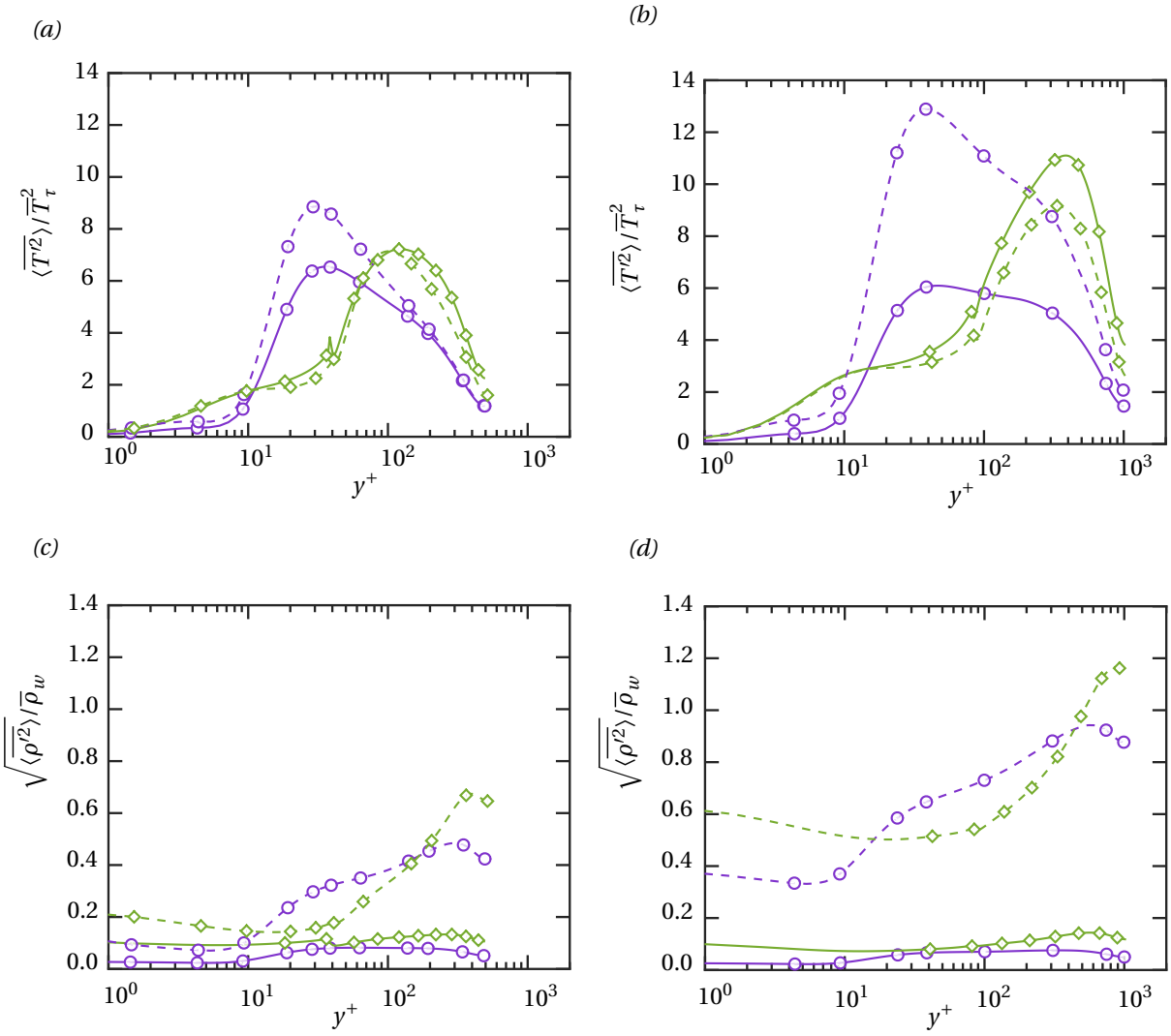

Figure 4.8: (a,b) Mean temperature fluctuations scaled by T_τ^2 where $T_\tau = q_w/\rho_w C p u_\tau$ where q_w is the wall heat flux (c,d) and mean density fluctuations scaled by density at the wall $\overline{\rho}_w$ for smooth wall (solid lines, circles) and rough wall (solid lines, diamonds) with roughness height $k/h = 0.08$ for $3D$ cube roughness at $Re_\tau \approx 500$ (left column of images) and $Re_\tau \approx 1000$ (right column of images). $M_b = 2$ data represented as solid lines with symbols and $M_b = 4$ data represented as dashed lines with symbols

density fluctuations plots show that their magnitude is very small (of the order of 10^{-1}) for Mach 2 smooth and rough wall cases at $Re_\tau \approx 500$. This is particularly important as it forms the basis for the Morkovin hypothesis. Hence, the usage of mean density scaling to account for the property variations in supersonic flows at Mach 2 is suitably justified. However, as the Mach number is increased, it is observed that the density fluctuations obtain values that cannot be easily neglected. Particularly, in case of Mach 4, for the smooth and rough walls at $Re_\tau \approx 500$, it is observed that the magnitude of the peak is almost $6-7$ times larger than the Mach 2 case. In such circumstances, the Morkovin hypothesis is challenged as it is particularly valid till $M_b \approx 5$. Since the van Driest (Van Driest, 1951) transformation is based on the Morkovin hypothesis, the breakdown of the Morkovin hypothesis is manifested as deviations in mean velocity from the incompressible law of the wall relations observed in Figure 4.18d. There is a steep increase in the density fluctuations of the Mach 4 rough wall case at $Re_\tau \approx 500$ beyond the roughness crest (Figure 4.8c). The results at $Re_\tau \approx 1000$ for Mach 2 (solid lines) and Mach 4 (dashed lines) are shown in Figure 4.8d. The results are included for smooth and rough walls. As seen in the case of $Re_\tau \approx 500$, the Mach 2 mean density fluctuations are negligibly small. However, the growth in these fluctuations at Mach 4 for both smooth and rough walls is high. The peak mean density fluctuation for Mach 4 case of $Re_\tau \approx 1000$ is almost twice as high as compared to the case at $Re_\tau \approx 500$. All these point towards the breakdown of Morkovin hypothesis.

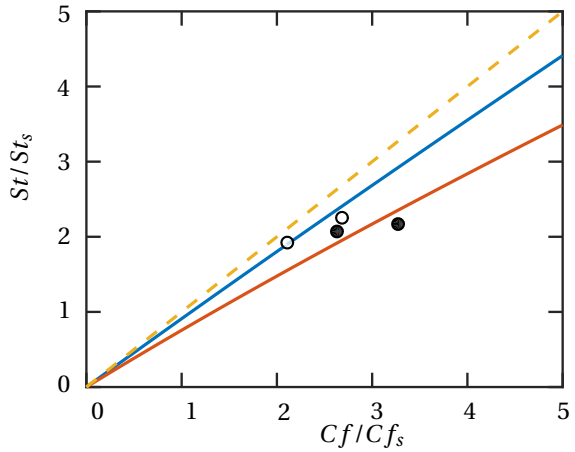

Figure 4.9: Staton number and skin-friction coefficient augmentation using (2.69). The solid lines indicate $\alpha = 0.4, 1.3$ and the dashed lines indicate the case when $St/St_s = Cf/Cf_s$. The results at $M_b = 2$ are shown as solid circles and the results at $M_b = 4$ are shown as hollow circles.

The Stanton number and skin-friction coefficient augmentation is presented in Figure 4.9. The solid lines indicate the empirical relation given in (2.69). The figure shows that in case of Mach 2 ,the increase in skin-friction coefficient of the rough wall is greater compared to the increase in heat transfer. The roughness Reynolds number does not seem to affect the increase in wall heat transfer of a rough wall compared to a smooth wall as much as it affects the increase in drag. In case of Mach 4, a similar trend is observed where the increase in drag is greater compared to increase in heat transfer. The drag is also lower compared to the Mach 2 cases. The empirical relation (2.69) is able to represent the heat transfer increase as a function of drag for Mach 2 with $\alpha = 0.4$ and for Mach 4 with $\alpha = 1.3$. This is the range put forward by Hill et al. (1980) for compressible flow over roughness.

4.1.2. Minimal-span channel

The mean velocity profile untransformed and its associated compressibility transformations for minimal-span channel smooth and rough wall with $2D$ transverse bar elements at $Re_\tau \approx 500$ is presented in Figure 4.10a, Figure 4.10c, Figure 4.10e and Figure 4.10g respectively. A general observation that is noticed is the increase in the mean velocity as the center of the channel is approached. This is a result of the reduced domain along streamwise and spanwise directions. This does not permit the capturing of the large scale structures thereby increasing the mean velocity in the outer layer. This increase is also observed for the rough wall case. Due to this, the velocity shift is not significantly affected. The reduction in the domain does not affect the near wall cycle of turbulence. The untransformed smooth wall mean velocity profile in Figure 4.10a does not show a good collapse with the theoretical incompressible law of the wall relation in the log-law re-

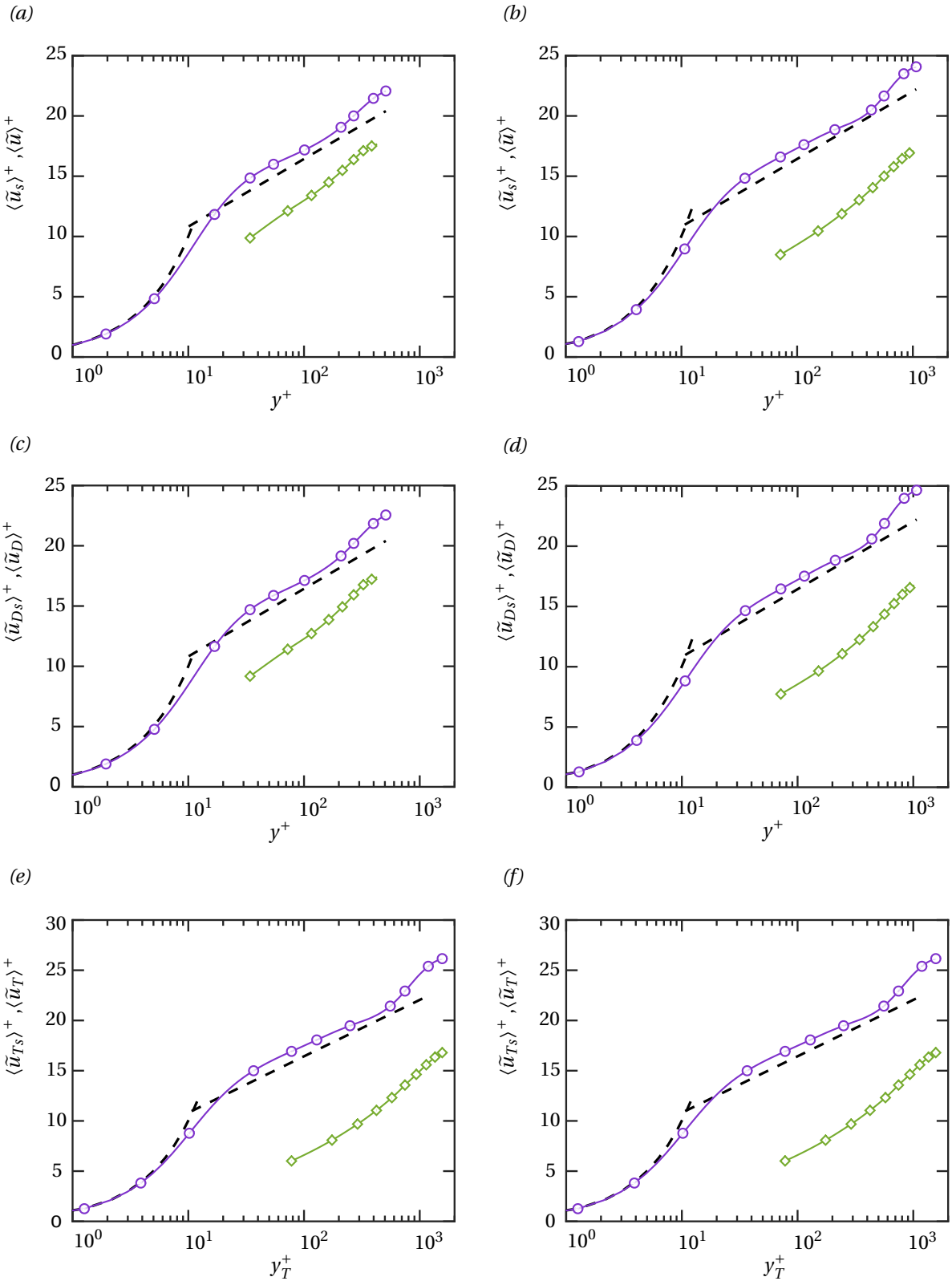
(a)
(b)
(c)
(d)
(e)
(f)
$\langle \widetilde{u}_S \rangle^+, \langle \widetilde{u} \rangle^+$
$\langle \widetilde{u}_{DS} \rangle^+, \langle \widetilde{u}_D \rangle^+$
$\langle \widetilde{u}_{TS} \rangle^+, \langle \widetilde{u}_T \rangle^+$
y^+
y_T^+
0
5
10
15
20
25
30
10^0
10^1
10^2
10^3

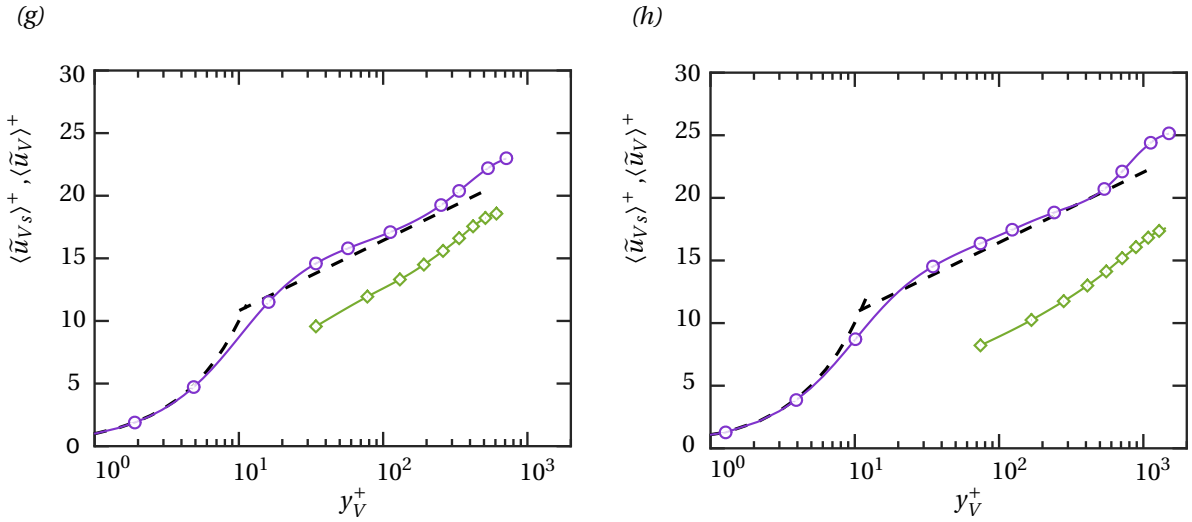

Figure 4.10: Minimal-span channel mean velocity (a,b) untransformed (c,d) van Driest-transformed (Van Driest, 1951) (e,f) Trettel-Larsson transformed (Trettel and Larsson, 2016) (g,h) Volpiani-transformed (Volpiani et al., 2020) for smooth wall (circles) compared against $2D$ transverse bar roughness (diamonds) at $M_b = 2$, $Re_\tau \approx 500$ (left column of images) and $Re_\tau \approx 1000$ (right column of images). The roughness height $k/h = 0.08$ corresponds to $k^+ \approx 40$ at $Re_\tau \approx 500$ and $k^+ \approx 80$ at $Re_\tau \approx 1000$. Dashed black lines indicate incompressible law of the wall relations given by $\langle u \rangle^+ = y^+$ and $\langle u \rangle^+ = (1/\kappa) log(y^+) + B$. The rough wall profiles have been shifted by $\epsilon = 0.95k$.

gion. The collapse improves almost negligibly for the case of van Driest-transformed (Van Driest, 1951) mean velocity profile. The Trettel–Larsson-transformed (Trettel and Larsson, 2016) mean velocity profile shows a greater deviation compared to the previous two cases just as it did for $3D$ cube roughness mean velocity profiles. The Volpiani-transformed (Volpiani et al., 2020) mean velocity profile is yet again the most accurate compressibility transformation. The trends for $Re_\tau \approx 1000$ case, minimal-span channel smooth and $2D$ bar roughened walls are similar to the case of $Re_\tau \approx 500$. The mean velocity shift is greater owing to a larger k^+. The increase in the mean velocity towards the centre of the channel is more prominent in case of $Re_\tau \approx 1000$. An observation that is crucial is the Trettel–Larsson-transformed (Trettel and Larsson, 2016) mean velocity profile for rough wall in Figure 4.10f. The shift in transformed mean velocity profile of the rough wall in comparison to the smooth wall is greater in comparison to the untransformed profile and other compressibility transformations. The Volpiani-transformation (Volpiani et al., 2020) has once again proven to be the most accurate in collapsing the smooth wall compressible minimal-span channel mean velocity profile onto the nearly incompressible profile.

The untransformed (ΔU^+) and compressibility transformed mean velocity shift (ΔU_I^+) as a function of k_{s*}^+ is presented in Figure 4.11a to Figure 4.11d. The equivalent roughness height using the roughness length scale k_{s*} is calculated as $k_{s*}^+ = 1.1 k_*^+$. This length scale has been used owing to the prior success in case of $3D$ cube roughness. The factor k_{s*}/k_* is lower compared to the $3D$ cube roughness element. Included in Figure 4.11d is the ΔU^+ data from DNS of fully resolved $3D$ cube roughness. The added drag in case of bar roughness is a lot lower in comparison to the cube roughness element. A good agreement is observed in Figure 4.11d for $k^+ \approx 80$ case with the theoretical asymptotic fully rough profile (dashed lines) and the incompressible sand grain roughness results from Nikuradse et al. (1950). The $k^+ \approx 40$ case does not collapse on the fully rough profile indicating that it is in the transitionally rough regime. This is in stark contrast to the $3D$ roughness case where both $k^+ \approx 40$ and $k^+ \approx 80$ cases collapsed on the theoretical fully rough profile. This indicates that the drag producing capabilities of bar roughness element is much lower in comparison to the cube roughness element going by the equivalent sand grain roughness definition. $k_s/k \approx 1.9$ for cube roughness is higher in comparison to $k_s/k \approx 1.1$ in case of bar roughness element. Yet another peculiar result observed is in Figure 4.11c. The Trettel–Larsson-transformed (Trettel and Larsson, 2016) mean velocity shift is much higher in comparison to the others. This could be due to the disparate mechanism of turbulence observed in minimal-span channels of supersonic flows compared to the concepts used to build the transformation itself.

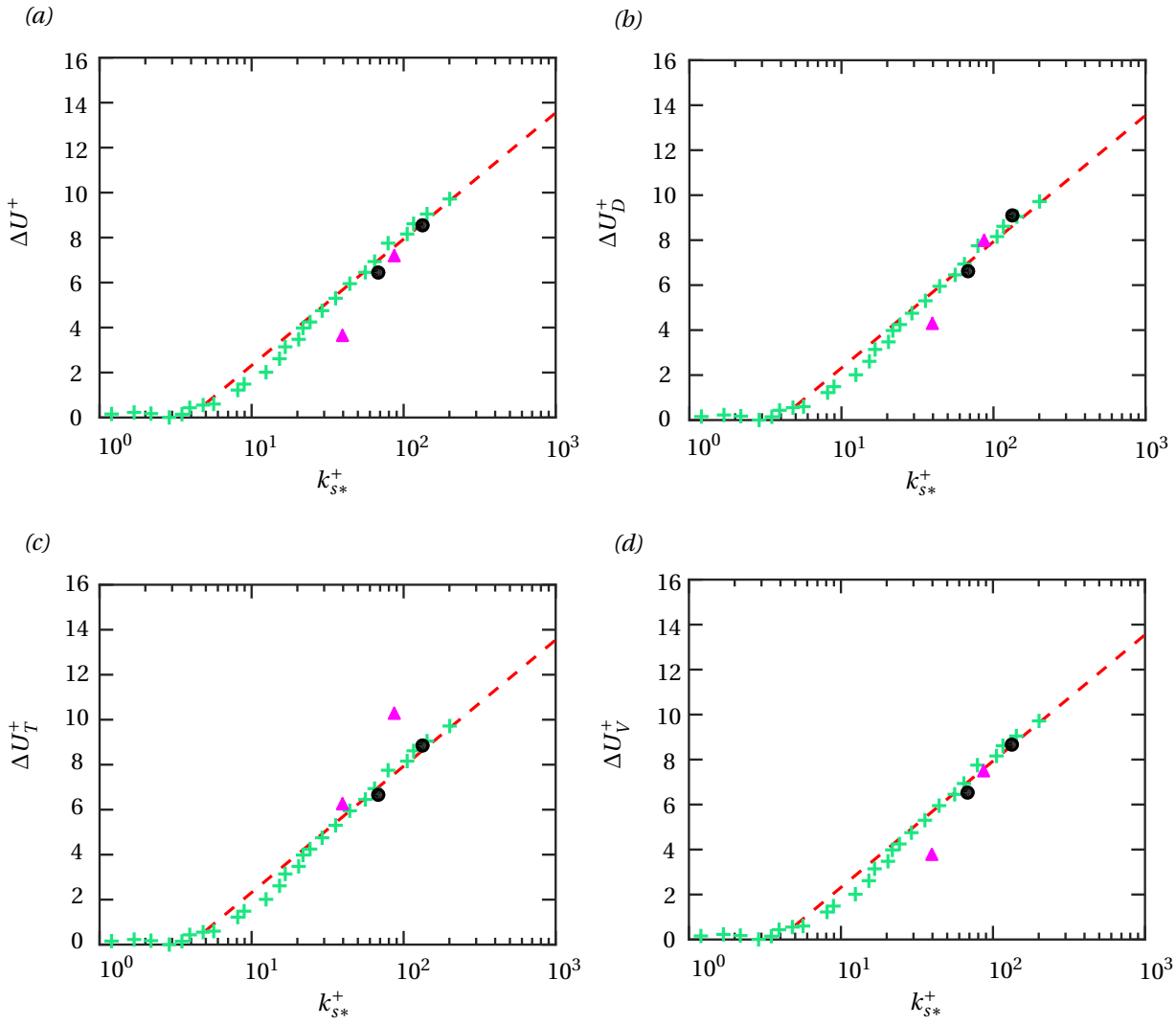

Figure 4.11: Mean streamwise velocity shift ΔU^+ (a) untransformed (b) van Driest-transformed (Van Driest, 1951) (c) Trettel–Larsson-transformed (Trettel and Larsson, 2016) (d) Volpiani-transformed (Volpiani et al., 2020) at $M_b = 2$ (solid triangles) for $2D$ bar roughness in minimal-span channel with roughness Reynolds numbers $k^+ \approx 40, 80$ and sand grain roughness Reynolds number $k_{s*}^+ = 1.1k_*^+$. DNS data of fully resolved, full channel rough wall ΔU^+ of $3D$ cube roughness (solid circles) at $k^+ \approx 40$ and $k^+ \approx 80$ is also included. Dashed line is the theoretical asymptotic relation between equivalent sand grain roughness and Hama roughness function given by $\Delta U^+ = (1/\kappa)log(k_s^+) + B - B_S$. The incompressible roughness data from Nikuradse et al. (1950) (plus symbols) is also shown.

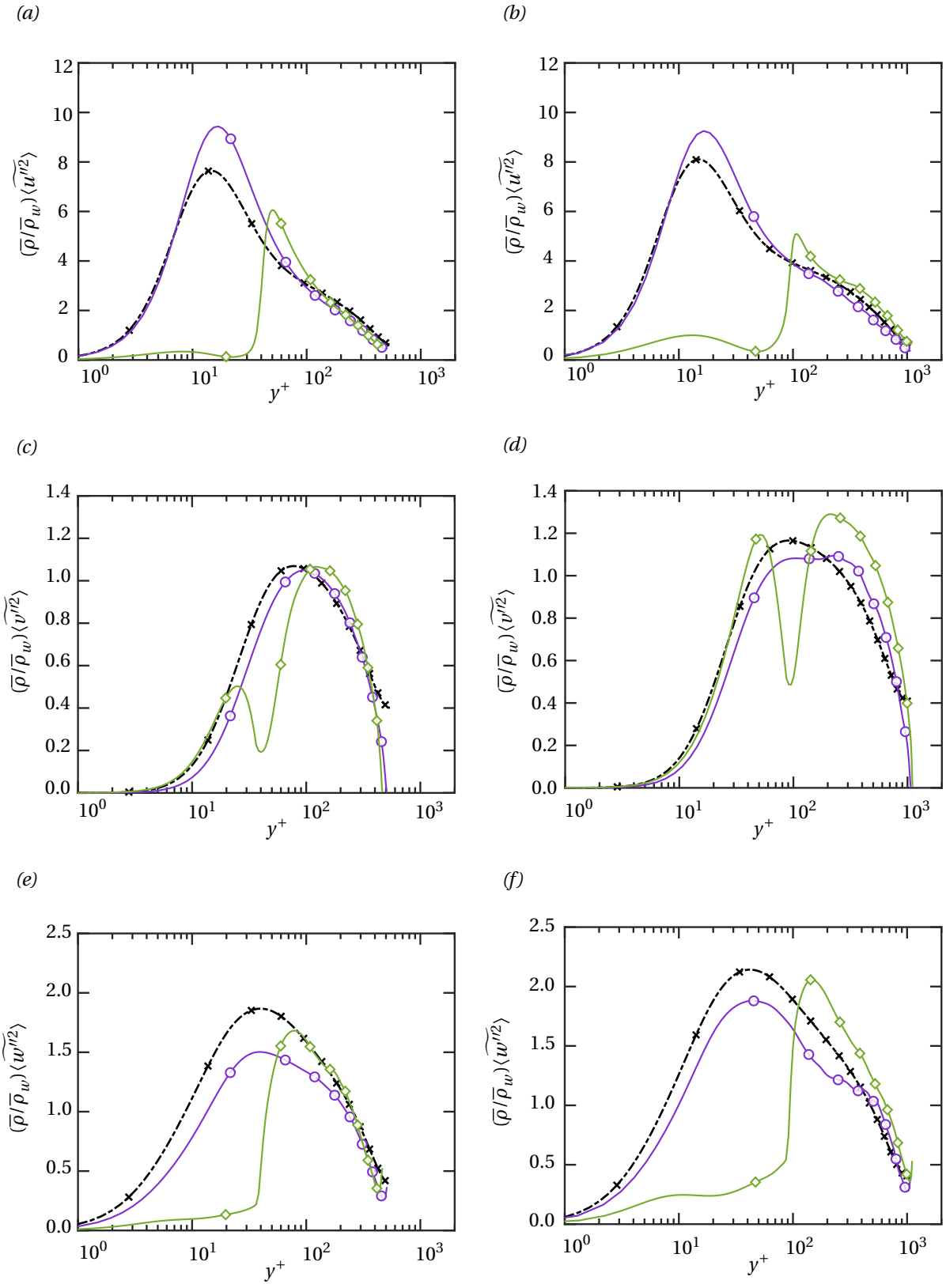
(a)
(b)
(c)
(d)
(e)
(f)
$(\overline{\rho}/\overline{\rho}_w)\widetilde{\langle u''^2\rangle}$
$(\overline{\rho}/\overline{\rho}_w)\widetilde{\langle v''^2\rangle}$
$(\overline{\rho}/\overline{\rho}_w)\widetilde{\langle w''^2\rangle}$
y^+
10^0
10^1
10^2
10^3

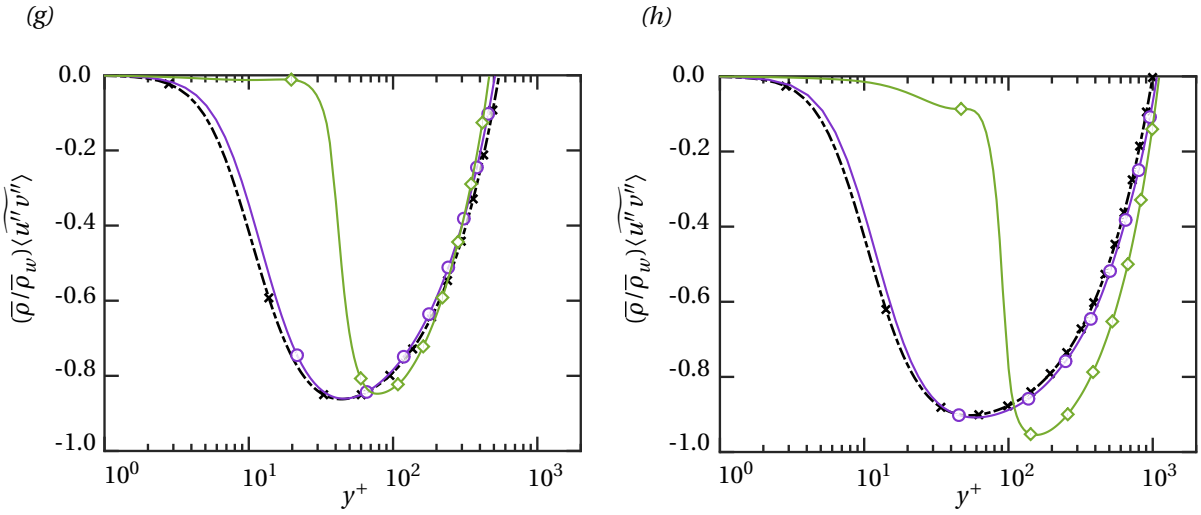

Figure 4.12: Density scaled turbulent (a,b) streamwise (c,d) wall-normal (e,f) spanwise and (g,h) shear stress profile of smooth wall (circles) and $2D$ resolved bar roughness (diamonds) in minimal-span channel at $Re_\tau \approx 500$, $k^+ \approx 40$ (left column of images) and $Re_\tau \approx 1000$, $k^+ \approx 80$ (right column of images). Incompressible data from Moser et al. (1999) (dot-dashed lines with × symbols) also included.

The streamwise turbulent stress profiles scaled by density for $Re_\tau \approx 500$ is presented in Figure 4.12a. The data from Moser et al. (1999) is also included to facilitate comparison. The smooth wall minimal-span channel result (circles) is superposed with rough wall (diamonds) minimal-span channel data. The first observation is that the streamwise density-scaled turbulent stress profile for smooth wall minimal-span channel flow shows an excellent agreement with the data from Moser et al. (1999) up to $y^+ \approx 10$. Beyond this, there is some over-prediction of the turbulent stress that extends till $y^+ \approx 100$. However, it has to be noted that this over-prediction was already observed to exist in the case of $3D$ cube roughness also in Figure 4.6a and Figure 4.6b. The agreement of compressible minimal-span channel data with full channel has already been shown to exist in Figure 3.9g. An added reason could be the size of the domain which is slightly less than $1000\nu/u_\tau$ for the minimal-span channel test case at $Re_\tau \approx 500$. This local increase in streamwise turbulent stress has also been reported in the case of incompressible minimal-span channel simulations of streamwise domain lenth less than $1000\nu/u_\tau$ (Chin et al., 2010, Toh and Itano, 2005). The turbulent stress profile in the outer layer shows reasonable agreement with the data from Moser et al. (1999). The key take back from this is the outer layer similarity observed for the rough wall data. The rough wall streamwise turbulent stress profile is damped almost completely up to $y^+ \approx 20$. There is a steep increase till the roughness crest at $y^+ \approx 40$ and a good agreement with the smooth wall data beyond $y^+ \approx 100$. In case of $Re_\tau \approx 1000$ presented in Figure 4.12b, the smooth wall profile is in closer agreement with the data of Moser et al. (1999). The rough wall profile trend is similar to that of $Re_\tau \approx 500$. The extent of outer layer similarity observed is sufficient to consider the results from minimal-span channel as accurate.

The density scaled wall-normal turbulent stress profiles for smooth and rough wall minimal-span channel at $Re_\tau \approx 500$ are depicted in Figure 4.12c. The smooth wall profile shows a much better agreement with the data from Moser et al. (1999). In case of rough wall, there is a local peak in the stress observed at $y^+ \approx 25$ followed by damping upto the roughness crest. Good outer layer similarity of the profile for rough wall is observed with the smooth wall profile. It should be noted that the wall-normal turbulent stress profile goes to zero at the channel centerline due to the open channel configuration and the nature of boundary condition applied to wall-normal velocity at the channel mid-plane. The smooth wall profile at $Re_\tau \approx 1000$ shows slight deviations from the profile by Moser et al. (1999) in the outer layer as seen in Figure 4.12d. In case of the rough wall profile, the magnitude of the first peak in stress is almost the same as the second one beyond the roughness crest. This indicates a strong sense of recirculation in the wall-normal direction. The outer layer similarity is weakly upheld. Just as in the case of $Re_\tau \approx 500$, the wall normal turbulent stress is damped at the roughness crest and increases beyond it.

In case of smooth wall, the density scaled spanwise turbulent stress profile at $Re_\tau \approx 500$ in Figure 4.12e, the

magnitude is underpredicted for most of the channel when compared with the data from Moser et al. (1999). The spanwise stress profile for rough wall shows an agreement with smooth wall profile in the outer layer. The trends for minimal-span channel smooth and rough wall streamwise turbulent profiles at $Re_\tau \approx 1000$ (Figure 4.12f) are similar to the case at $Re_\tau \approx 500$. The collapse of smooth and rough wall profiles takes place closer to the channel centerline. Finally, the density scaled Reynolds shear stress profiles of minimal-span channel smooth wall show excellent agreement with the nearly incompressible profile of Moser et al. (1999) at both $Re_\tau \approx 500$ (Figure 4.12g) and $Re_\tau \approx 1000$ (Figure 4.12h). The collapse of rough wall profile in the outer layer is better at $Re_\tau \approx 500$ compared to $Re_\tau \approx 1000$.

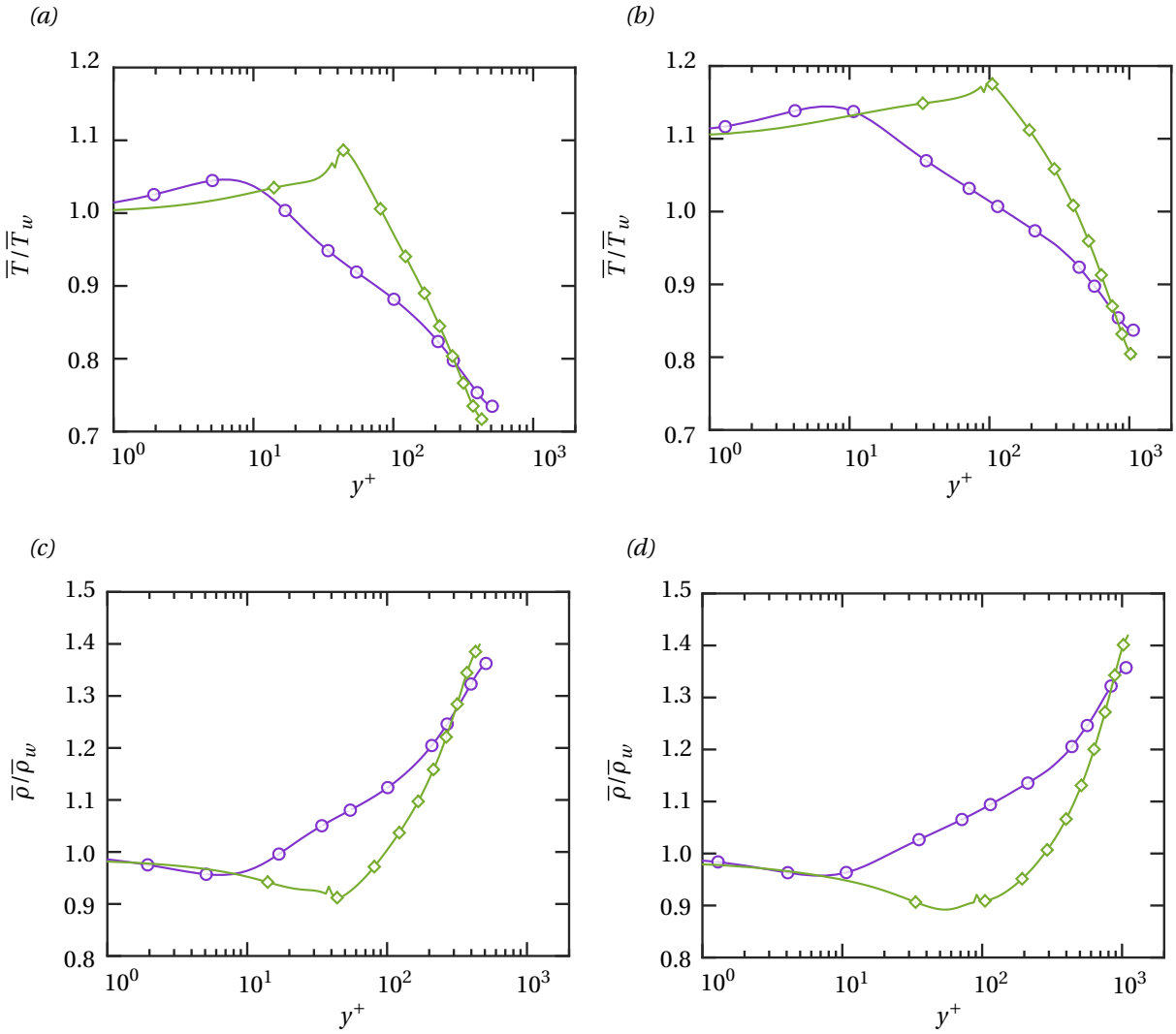

Figure 4.13: Minimal-span channel (a,b) mean temperature profile scaled by wall temperature $\overline{T}_w$ and (c,d) mean density scaled by density at the wall $\overline{\rho}_w$ for smooth wall (solid lines, circles) and rough wall (solid lines, diamonds) with roughness height $k/h = 0.08$ for $2D$ bar roughness at $M_b = 2$. Left column of images represent flow case at $Re_\tau \approx 500$ and right column of images represent flow case at $Re_\tau \approx 1000$.

The mean temperature profile scaled by T_w of smooth and rough wall minimal-span channel cases at $Re_\tau \approx 500$ is presented in Figure 4.13a and at $Re_\tau \approx 1000$ in Figure 4.13b. It is observed that the peak in mean temperature of the rough wall case is shifted to just above the roughness crest. The trends in the mean temperature profile is similar for $Re_\tau \approx 500$ and $Re_\tau \approx 1000$ cases for smooth and rough walls in minimal-span channel. It is also similar to the $3D$ cube roughness of full channel. In case of mean density profile scaled by density at the wall in Figure 4.13c and Figure 4.13d, the point of minimum density is shifted to just above the roughness crest. This is followed by an increase in the mean density as the channel centerline is approached.

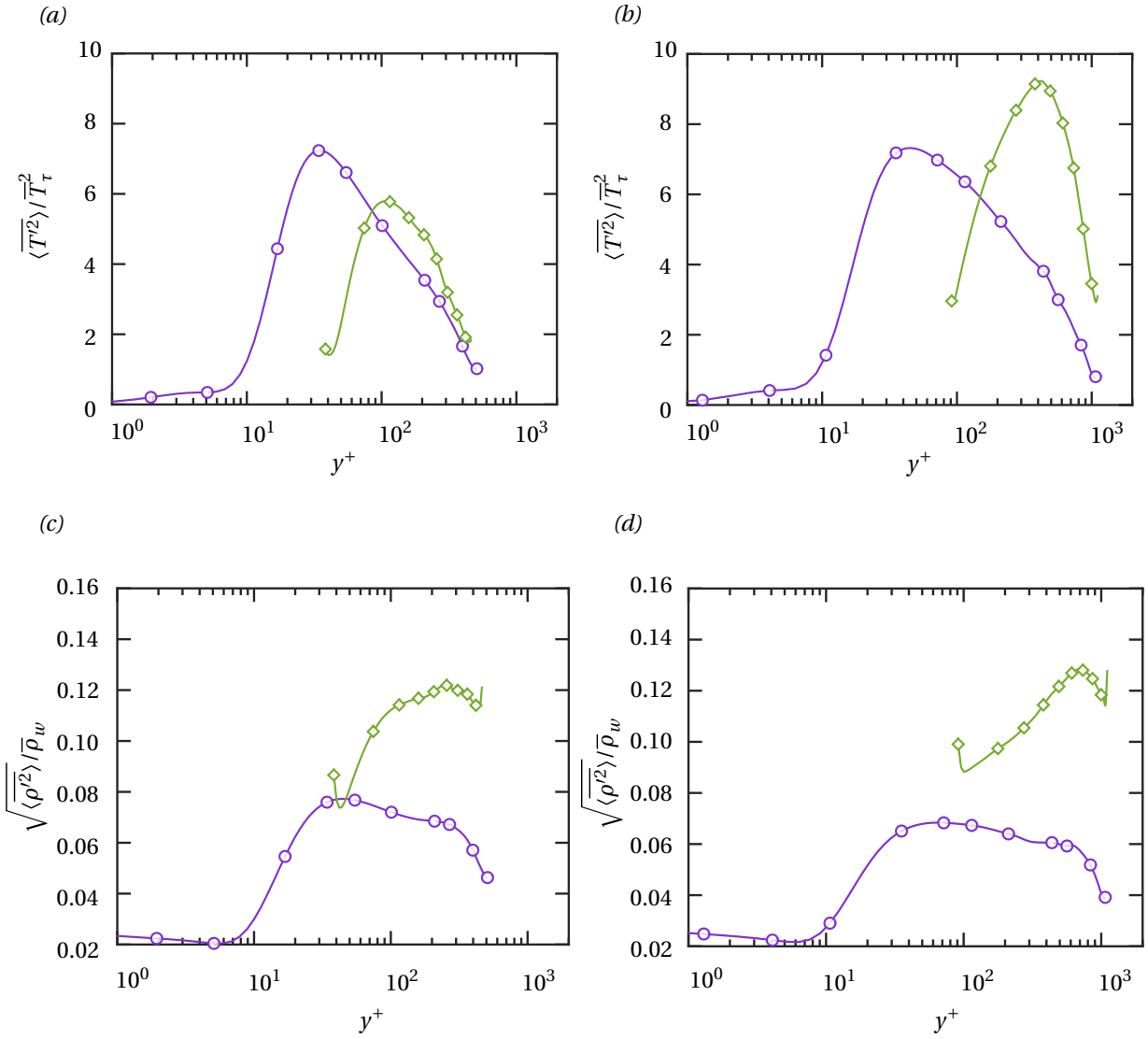

Figure 4.14: Minimal-span channel (a,b) mean temperature fluctuations profile scaled by T_τ^2 and (c,d) mean density fluctuations scaled by density at the wall $\overline{\rho}_w$ for smooth wall (solid lines, circles) and rough wall (solid lines, diamonds) with roughness height $k/h = 0.08$ for $2D$ bar roughness at $M_b = 2$. Left column of images represent flow case at $Re_\tau \approx 500$ and right column of images represent flow case at $Re_\tau \approx 1000$.

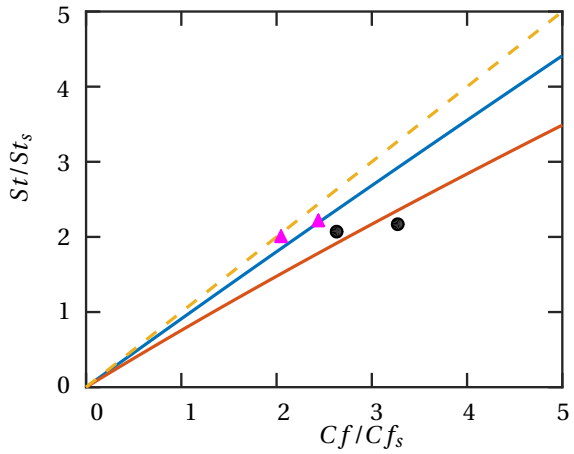

Figure 4.15: Staton number and skin-friction coefficient augmentation using (2.69). The solid lines indicate $\alpha = 0.4, 1.3$ and the dashed lines indicate the case when $St/St_s = Cf/Cf_s$. The results are indicated as solid triangles.

The temperature fluctuations for Mach 2 smooth and rough wall minimal-span channel at $Re_\tau \approx 500$ scaled by T_τ is presented in Figure 4.14a. The magnitude of the peak of temperature fluctuations as well as its profile for the Mach 2 smooth wall case using minimal-span channel (Figure 4.14a) is comparable to that of full-channel smooth wall at Mach 2 (Figure 4.8a). However, the peak of temperature fluctuations for the bar roughness at $Re_\tau \approx 500$ is slightly lower compared to its smooth wall counterpart. This is in contrast to the Mach 2 cube roughness case at $Re_\tau \approx 500$ where it was comparable to its smooth wall counterpart. In case of $Re_\tau \approx 1000$, the peak of the mean temperature fluctuations is greater for the rough wall when compared to the smooth wall. The profiles for smooth and rough wall mean temperature fluctuations at $Re_\tau \approx 500$ and $Re_\tau \approx 1000$ for bar roughness in minimal-span channel resemble that of the cube roughness in full channel. The density fluctuations scaled by $\overline{\rho}_w$ is reported in Figure 4.14c. The plateau of density fluctuations in the log-law region is observed in case of Mach 2 smooth wall at $Re_\tau \approx 500$ (Figure 4.14c). However, the peak of density fluctuations is almost 1.5 times in the case of bar roughness counterpart. The trends are similar for $Re_\tau \approx 1000$ smooth and rough wall cases as shown in Figure 4.14d. The relation between heat transfer and skin-friction coefficient for $2D$ bar roughness is presented in Figure 4.15. A first observation is that the increase in heat transfer of $2D$ bar roughness at $k^+ \approx 40$ compared to its smooth wall counterpart is comparable to the increase in drag of the rough wall compared to its smooth wall counterpart. Additionally, the heat transfer and drag increase is represented by the lower bound in the empirical relation (2.69) proposed by Hill et al. (1980).

In addition to averaged profiles of velocity, density and temperature, mean flow fields give a good picture of the dynamics of the flow. The contour plots of mean streamwise velocity $\widetilde{u}^+$ along the $x-y$ plane for a smooth wall and a wall with $2D$ bar roughness is shown in Figure 4.16a and Figure 4.16b respectively. Included in the plot is the streamlines. In case of the rough wall, a few interesting things are observed. Firstly, the gaps in between the roughness elements have a moderately strong recirculation indicated by the negative value of the mean streamwise velocity and the streamlines in Figure 4.16b. It appears that the direction of rotation of these vortices is clockwise. These recirculation zones or vortices are stronger close to the upstream face of the roughness elements. The mean temperature contours on the $x-y$ plane are shown in Figure 4.16g for smooth wall and in Figure 4.16d for $2D$ roughness. The smooth wall case displays a higher temperature close to the wall. This is due to aerodynamic heating where dissipation of kinetic energy of the flow takes place close to the wall. The mean temperature decreases towards the channel centerline. However, in case of $2D$ roughness, the region of high mean temperature extends beyond a thin region close to the wall due to the roughness elements. The presence of the roughness elements increases the aerodynamic heating as is observed in Figure 4.16d.

The $x-z$ mean flow field is considered next. The profile is extracted at a wall normal height of $y^+ \approx 12$ which lies in the buffer layer. This is also the wall normal height at which turbulence production is maximum indicated by equal contribution of viscous and Reynolds shear stresses. A quick look at Figure 4.16e indicates

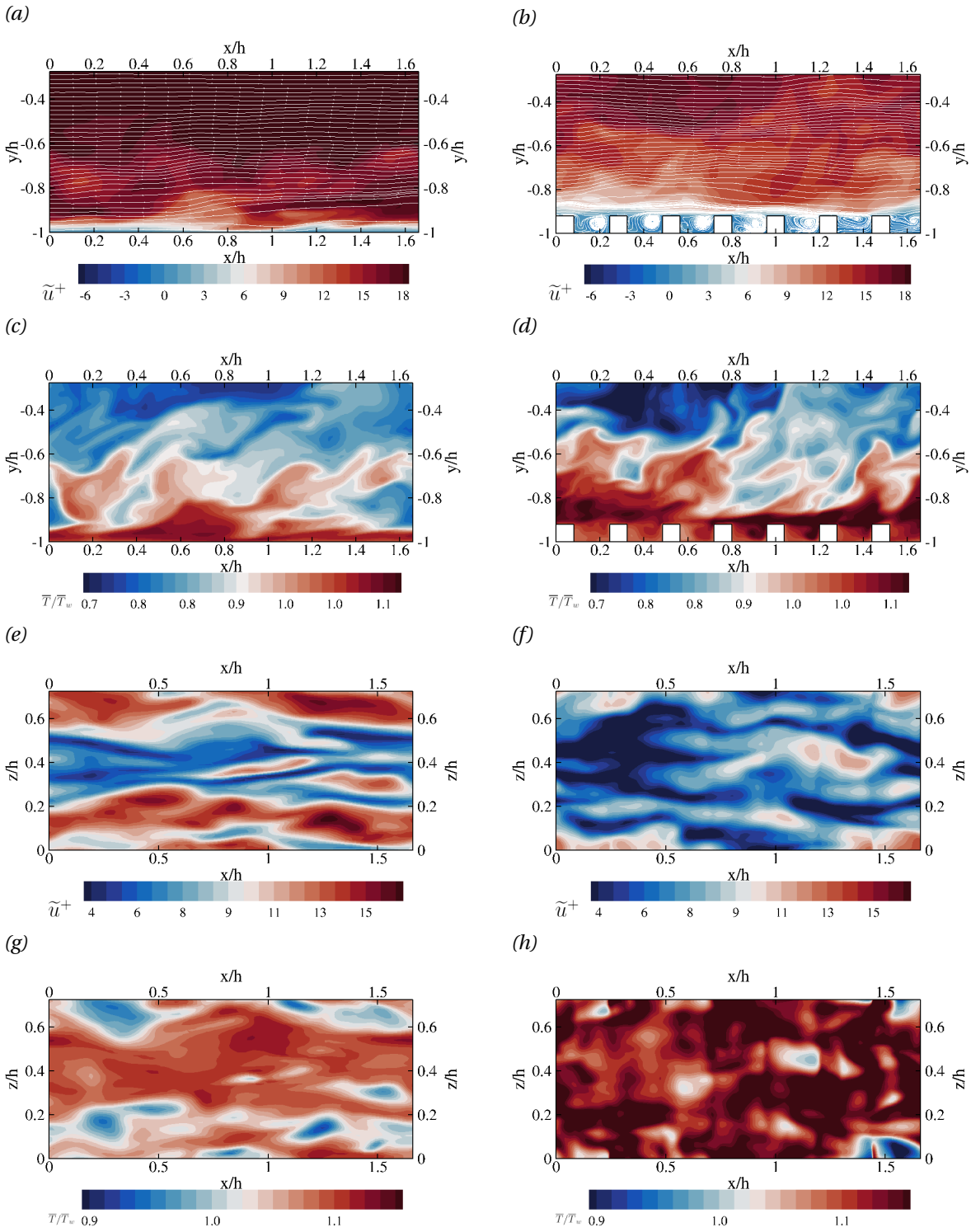

Figure 4.16: Mean flow fields of $\widetilde{u}^+$ along (a,b) $x-y$ plane at spanwise distance $z/h = 0.375$ and (c,d) $x-z$ plane at a given wall normal distance of $y^+ \approx 12$ of minimal-span channel (a,c) smooth wall and (b,d) $2D$ bar roughness at $k^+ \approx 40$, $Re_\tau \approx 500$, $M_b = 2$. Mean flow fields of $\overline{T}/T_w$ along (e,f) $x-y$ plane at spanwise distance $z/h = 0.375$ and (g,h) $x-z$ plane at a given wall normal distance of $y^+ \approx 12$ of minimal-span channel (e,g) smooth wall and (f,h) $2D$ bar roughness at $k^+ \approx 40$, $Re_\tau \approx 500$, $M_b = 2$.

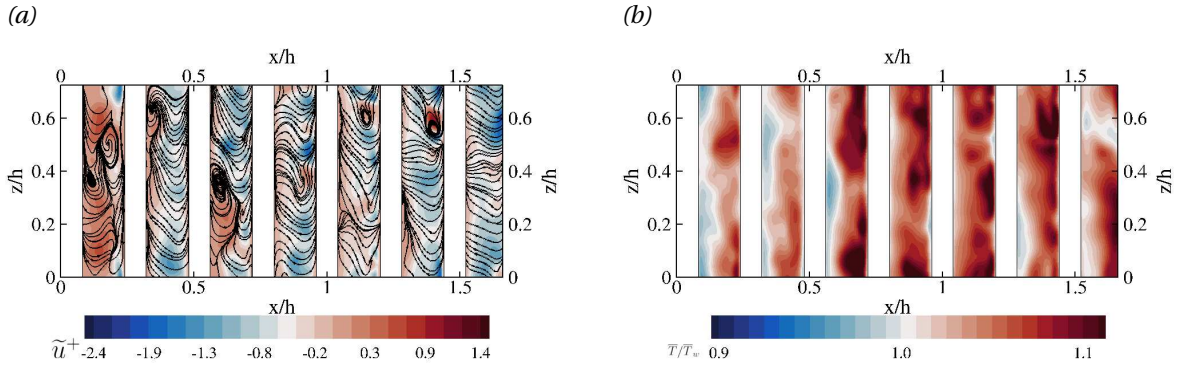

Figure 4.17: Mean flow fields of (a) $\widetilde{u}^+$ and (b) $\overline{T}/\overline{T}_w$ along $x-z$ plane at wall normal height $y^+ \approx 20$ of minimal-span channel $2D$ bar roughness at $k^+ \approx 40$, $Re_\tau \approx 500$, $M_b = 2$.

the presence of elongated structures of high and low speeds. In general, the flow is expected to organize itself into recognizable patterns. These include presence of low speed streaks of length $L_x^+ \approx 1000$ and spaced $L_z^+ \approx 100$ apart (Pope, 2001). In Figure 4.16e, there is a presence of these high and low speed streaks. However, they are not organized as expected. This is an expected consequence of the minimal span channel. The channel streamwise length is $L_x^+ \approx 840$ which is smaller than the minimum length of the low speed streaks. The reduced domain is unable to fully capture these. The mean flow field of streamwise velocity for $2D$ bar roughness as shown in Figure 4.16f. It is easy to observe that the elongated high speed streaks that were present in case of the smooth wall have been broken down. The structures are no longer in the form of streaks. The roughness elements break down the high and low speed streaks in the buffer layer. This disrupts the near wall turbulence production cycle and contributes towards the disparity in properties. The mean temperature contour plot of the $x-z$ plane at the same wall normal height, for the smooth wall is displayed in Figure 4.16g. The plane is mostly dominated by high temperature regions with pockets of low temperature regions mostly observed close to the spanwise boundaries. In case of the $2D$ roughness, Figure 4.16h also shows a domination of high temperature regions in the plane. However, it is easy to observe the increased mean temperature of the high temperature region and much smaller pockets of low temperature regions. This directly supports the profile on the $x-y$ plane.

To get a much better understanding of the flow field, the $x-z$ mean flow field in case of $2D$ roughness at $y^+ \approx 20$ is presented for $\widetilde{u}^+$ and $\overline{T}/\overline{T}_w$ in Figure 4.17a and Figure 4.17a respectively. The $2D$ velocity streamlines are included in Figure 4.17a. The flow fields suggests that the region between the first and second $2D$ bars from the left, the flow reversal is weak (it is directed along the positive streawise direction). However, the flow reversal begins immediately after the second roughness element and continues throughout. Recirculating vortices are observed in the gaps in all except the last one. The direction of the streamlines suggest that there is good mixing of the flow between the roughness elements. All the gaps are the same in a statistical sense. The temperature field in Figure 4.17b suggests that the gaps hold fluid at a high temperature.

4.2. Modeled roughness

The results of modeled roughness using the parametric forcing approach by Busse and Sandham (2012) is presented in this section. The auxiliary parameter $\eta(H)$ is varied from $\eta(H) = 0.01 - 0.08$ and the simulations are performed at $Re_\tau \approx 500$. Both $M_b = 2$ and $M_b = 4$ are considered to study the effects of varying Mach number on the effectiveness of the model. The mean velocity profile untransformed, van Driest-transformed (Van Driest, 1951), Trettel–Larsson-transformed (Trettel and Larsson, 2016) and Volpiani-transformed (Volpiani et al., 2020) at $M_b = 2$ is presented in Figure 4.18a, Figure 4.18c, Figure 4.18e and Figure 4.18g respectively. Similarly, the results at $M_b = 4$ are presented in Figure 4.18b, Figure 4.18d, Figure 4.18f and Figure 4.18h. The concept of virtual origin is not used in case of modeled roughness. This is because the effect of roughness is distributed in case of the parametric forcing approach as opposed to localised in case of the resolved roughness. The variations in properties is not as abrupt as in the case of resolved roughness. For this reason, the logarithmic region of the mean velocity profile for all the roughness cases is shifted downward perfectly parallel to the logarithmic region of the smooth wall mean velocity profile.

It is observed that with an increase in $\eta(H)$, the downward velocity shift increases starting from $\eta(H) =$

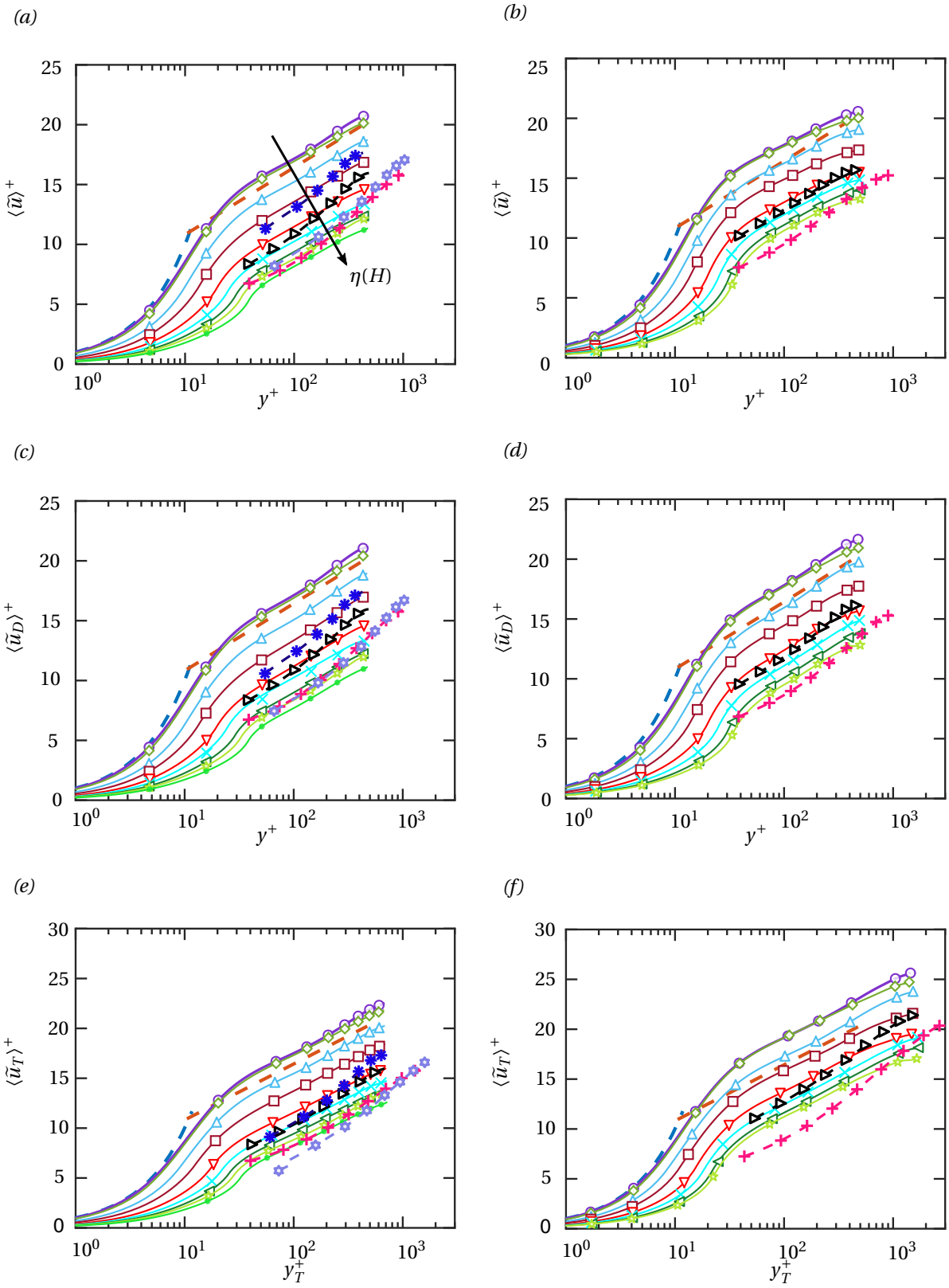
(a)
(b)
(c)
(d)
(e)
(f)
$\langle\widetilde{u}\rangle^+$
$\langle\widetilde{u}_D\rangle^+$
$\langle\widetilde{u}_T\rangle^+$
y^+
y_T^+
$\eta(H)$

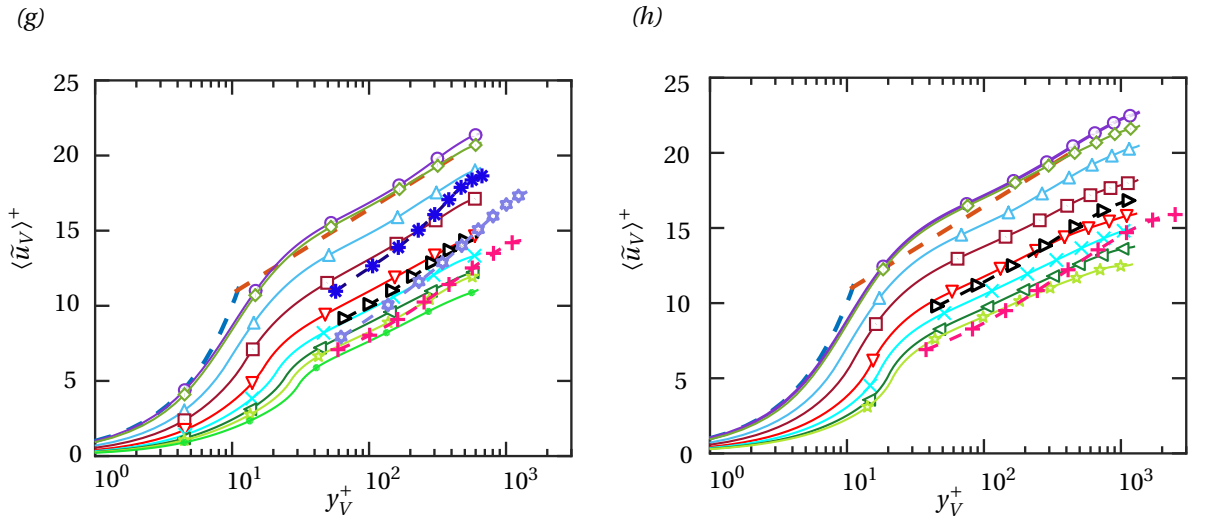

Figure 4.18: Mean velocity profile (a,b) untransformed (c,d) van Driest-transformed (Van Driest, 1951) (e,f) Trettel–Larsson-transformed (Trettel and Larsson, 2016) (g,h) Volpiani-transformed (Volpiani et al., 2020) at $Re_\tau \approx 500$ and $M_b = 2$ (left column of images), $M_b = 4$ (right column of images) for modeled roughness using the approach by Busse and Sandham (2012). The roughness height parameter is varied through an auxiliary parameter $\eta(H)$ as $\eta(H) = 0.01$ (diamonds), $\eta(H) = 0.02$ (upper-pointing triangles), $\eta(H) = 0.03$ (squares), $\eta(H) = 0.04$ (downward pointing triangles), $\eta(H) = 0.05$ ($\times$ symbols), $\eta(H) = 0.06$ (left-pointing triangles), $\eta(H) = 0.07$ (star symbols), $\eta(H) = 0.08$ (filled circles).Included is the data from $3D$ cube roughness at $Re_\tau \approx 500$ (right pointing triangles) and $Re_\tau \approx 1000$ (+ symbols) and and minimal-span channel $2D$ bar roughness ($*$ symbols) at $k/h = 0.08$. The dashed lines indicate the incompressible law of the wall relations: $\langle \widetilde{u}^+ \rangle = y^+$ and $\langle \widetilde{u}^+ \rangle = (1/\kappa) log(y^+) + B$.

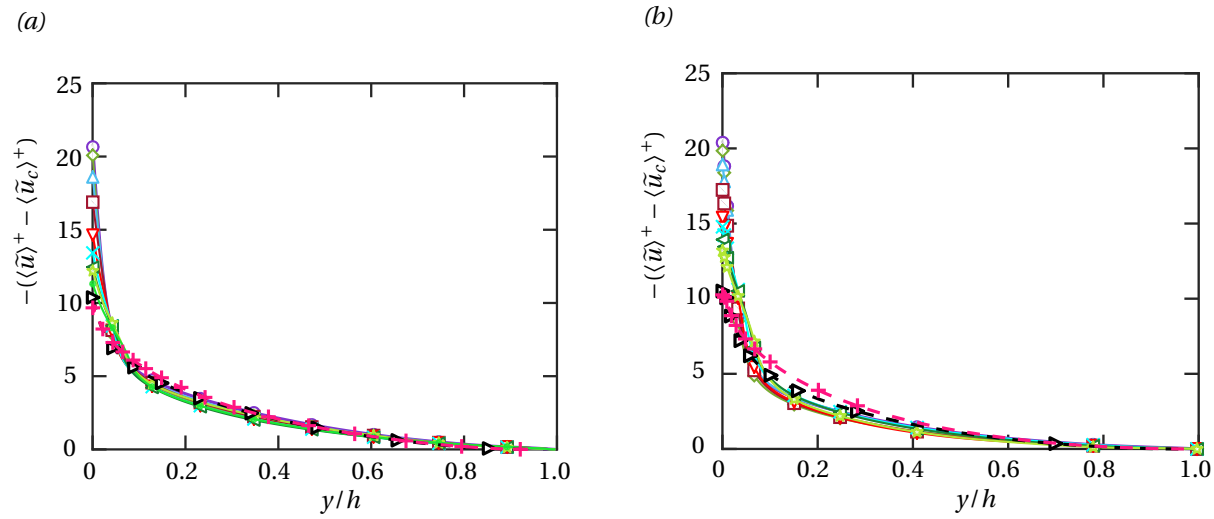

Figure 4.19: Untransformed Mean velocity defect profiles at $Re_\tau \approx 500$, (a) $M_b = 2$ and (b) $M_b = 4$ of smooth wall and modeled roughness. Defect profiles of $3D$ resolved roughness at $k^+ \approx 40$ (right pointing triangles) and $k^+ \approx 80$ (+ symbols) also included. The legend for modeled roughness is the same as in Figure 4.18a to Figure 4.18h

0.01 to $\eta(H) = 0.08$. This reinforces the explanation provided for the definition of the roughness height parameter H as analogous to the roughness height k. Included in these plots are the results from $3D$ cube roughness using full channel at $k^+ \approx 40$ (right pointing triangles), $k^+ \approx 80$ (+ symbols) at $M_b = 2$ and $M_b = 4$. In addition, the results from $2D$ bar roughness ($*$ symbols) using minimal-span channel at $k^+ \approx 40$ performed at $M_b = 2$ is included. The smooth wall results (circles) show a good agreement with the nearly incompressible law of the wall relations (dashed lines) for the Volpiani-transformed (Volpiani et al., 2020) mean velocity profile in Figure 4.18g at $M_b = 2$ and in Figure 4.18h at $M_b = 4$. Since the smooth wall mean velocity profile transformed using the Volpiani transformation (Volpiani et al., 2020) is the most accurate in comparison to the law of the wall relations, the velocity shift ΔU^+ will be determined using this profile. It is very encouraging to notice that the Volpiani-transformed (Volpiani et al., 2020) mean velocity profile for the Mach 2 cube roughness case at $Re_\tau \approx 500$ can be represented by the modeled roughness case K4M2 with $\eta(H) = 0.04$ (Figure 4.18g). Similarly, the mean velocity profile of cube roughness at $Re_\tau \approx 1000$ can also be represented with the case K6M2. The minimal-span channel mean velocity profile of bar roughness at $Re_\tau \approx 500$ and $Re_\tau \approx 1000$ is also seen to show agreement with the profiles of case K3M2 and K3M5 respectively. These results display the accuracy in using a modeled approach to represent the effects of roughness in supersonic flows. In case of $M_b = 4$, it is observed that the mean velocity profile of cube roughness at $Re_\tau \approx 500$ shows agreement with the modeled roughness mean velocity profile of K4M4 and the mean velocity profile of cube roughness at $Re_\tau \approx 1000$ shows agreement with K6M4. (Figure 4.18h).

The mean velocity defect profile scaled by u_τ for the modeled roughness cases is presented in Figure 4.19a at $M_b = 2$ and Figure 4.19b at $M_b = 4$. Superposed on these profiles, is the result from Mach 2 cube roughness flow cases at $Re_\tau \approx 500$ and $Re_\tau \approx 1000$ in Figure 4.19a and Mach 4 case at $Re_\tau \approx 500$ and $Re_\tau \approx 1000$ in Figure 4.19b. It is observed that the mean velocity defect profiles of modeled roughness cases K1M2 through K8M2 collapse on each other and on the smooth wall profile. The mean velocity defect profiles of Mach 2 and Mach 4 cube roughness at $Re_\tau \approx 500, 1000$ are also in agreement with the profiles of the modeled roughness flow cases. The modeled roughness is capable of displaying outer layer similarity when the roughness height parameter H is increased. This lends support towards the capability of the model to study resolved roughness mean velocity profiles. However, in Figure 4.19b, it is observed that the collapse of mean velocity defect profile of cube roughness at $Re_\tau \approx 500$ is not perfect on the profiles of the modeled roughness flow cases. The $Re_\tau \approx 1000$ cube roughness profile at Mach 4 also shows slight deviation from the rest of the profile computed using modeled roughness.

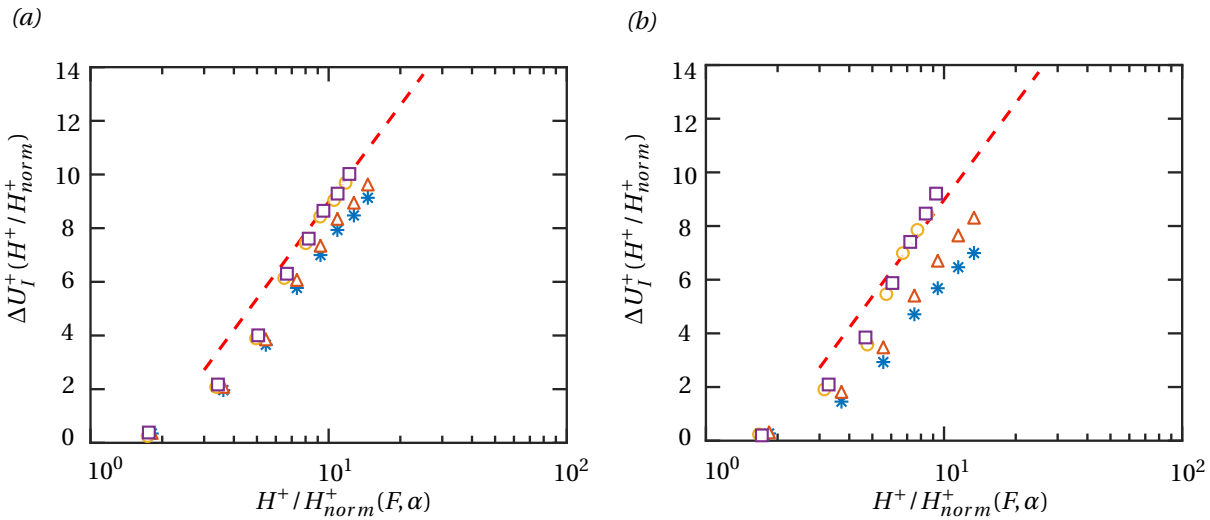

Figure 4.20: Roughness function ΔU_I^+ for untransformed ($*$ symbols), van Driest-transformed (Van Driest, 1951) (upper pointing triangles), Trettel–Larsson transformed (Trettel and Larsson, 2016) (circles) and Volpiani-transformed (Volpiani et al., 2020) as a function of H^+/H^+_{norm} at (a) $M_b = 2$ and (b) $M_b = 4$ where $H^+_{norm} = 1.31$. Dotted lines indicate $\Delta U_I^+(H^+/H^+_{norm}) = 5.2log(H^+/H^+_{norm}) - 3$ (Busse and Sandham, 2012)

The process of representing the velocity shift as a function of equivalent sand grain roughness height in case of modeled roughness is not so straightforward. The first step is to estimate H^+_{norm} which will be used

to scale the roughness height factor H^+. This is done by choosing a factor which ensures that ΔU_V^+ from the modeled roughness cases can be fit on curve given by the equation

$$\Delta U_I^+(H^+/H_{norm}^+) = 5.2log(H^+/H_{norm}^+) - 3 \tag{4.5}$$

Busse and Sandham (2012) performed DNS simulations by varying α, $F(\alpha, H)$ and H in (3.4) for the modeled roughness and estimated the velocity shifts in all cases. They showed that when scaled by H_{norm}^+, all the data fit on the curve given by (4.5). The factor turns out to be $H_{norm}^+ = 1.31$ and will be used throughout the reminder of the thesis. It should be noted that H_{norm}^+ is calculated by considering the Volpiani-transformed (Volpiani et al., 2020) mean velocity shift ΔU_V^+ owing to its accuracy in transforming the compressible mean velocity to match the incompressible law of the wall relations.

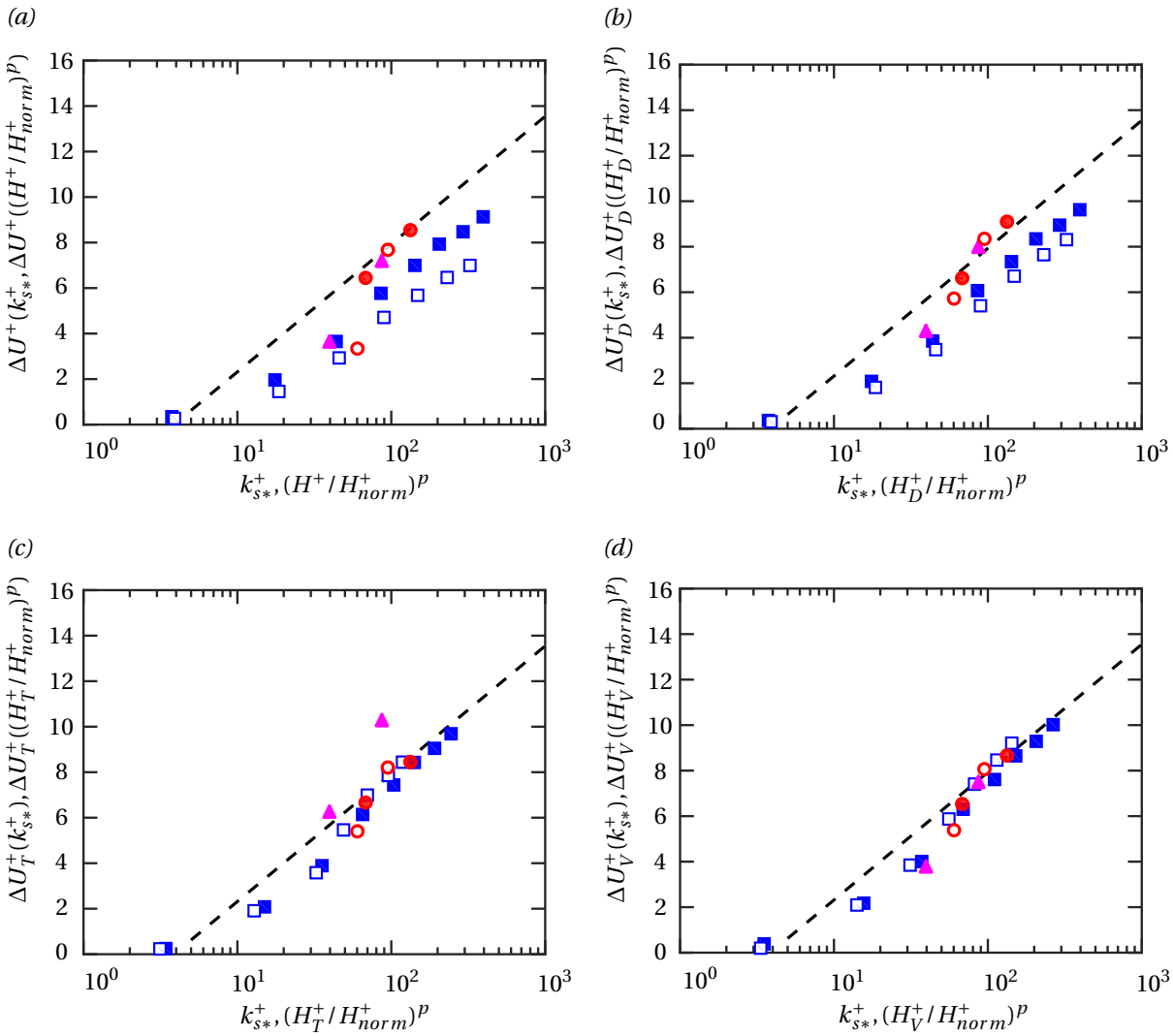

Figure 4.21: Mean velocity shift as a function of k_{s*}^+ for $3D$ cube roughness (circles) and as a function of $(H_I^+/H_{norm}^+)^p$ where $p = 2.23$ for modeled roughness using parametric forcing approach by Busse and Sandham (2012) (squares). The profiles (a) untransformed (b) van Driest-transformed (Van Driest, 1951) (c) Trettel–Larsson-transformed (Trettel and Larsson, 2016) and (d) Volpiani-transformed (Volpiani et al., 2020). The solid symbols represent the flow case at $M_b = 2$ and the hollow symbols represent the flow case at $M_b = 4$ in case of modeled roughness. The dashed line is the theoretical asymptotic fully rough relation $\Delta U^+ = (1/\kappa)log(k_s^+) + B - B_S$

The velocity shift as a function of scaled roughness height parameter H^+ using modeled roughness is presented for the case of $Re_\tau \approx 500$, $M_b = 2$ in Figure 4.20a and $M_b = 4$ in Figure 4.20b. By using an $H_{norm}^+ = 1.31$,

it is clearly observed that there is a good match between ΔU_V^+ and the theoretical profile. The mean velocity shift untransformed, van Direst-transformed (Van Driest, 1951), Trettel–Larsson-transformed (Trettel and Larsson, 2016) in Figure 4.20a are not very accurate. In case of modeled roughness at $M_b = 4$, the deviation from the theoretical profile of the untransformed and van Driest-transformed (Van Driest, 1951) mean velocity shifts (Figure 4.20b) are a lot more when compared to their respective deviations from the theoretical profile of modeled roughness at $M_b = 2$. This highlights the effect of compressibility, accentuated with the increase in Mach number and the importance of the Volpiani-transformation (Volpiani et al., 2020) in accounting for these compressibility effects. It also displays the receding power of van Driest-transformation (Van Driest, 1951) in accounting for compressibility effects with increasing Mach numbers.

There exists a relation between the scaled roughness height parameter and equivalent sand grain roughness which will be discussed. The fully rough asymptotic relation in terms of scaled roughness height parameter is given by (Busse and Sandham, 2012)

$$\Delta U_I^+(H_I^+/H_{norm}^+) = \frac{1}{\kappa} log((H_I^+/H_{norm}^+)^p) + B - B_S \tag{4.6}$$

where p is an exponent that is used to relate the scaled roughness height parameter with the equivalent sand grain roughness height. By using the Volpiani-transformed (Volpiani et al., 2020) mean velocity shift as a function of scaled roughness height parameter, it is estimated that $p \approx 2.23$. Therefore, the relation

$$k_{sV}^+ = (H_V^+/H_{norm}^+)^{2.23} \tag{4.7}$$

holds. The exponent $p \approx 2.23$ is very close to that obtained by Busse and Sandham (2012) ($p \approx 2.08$). The result of using this exponent to represent the relation between the scaled roughness height parameter and velocity shift for untransformed and compressibility transformed mean velocity profiles is presented in Figure 4.21a to Figure 4.21d. The result of mean velocity shift as a function of k_{s*}^+ for $3D$ resolved cube roughness in full channel and $2D$ bar roughness in minimal-span channel is also included for the purpose of comparison. It should be noted that k_{s*}^+ is used instead of k_{sV}^+ simply because of its higher accuracy. On the contrary, it is not used for the case of modeled roughness. The modeled roughness technique represents the effect of roughness uniformly through the domain. There is no localised roughness effect as is observed in the case of resolved roughness where property variations from roughness trough to crest need to be accounted for.

Case	M_b	$(H_V^+/H_{norm}^+)^p$	ΔU_V^+	Geometry	Domain	M_b	k_{s*}^+	ΔU_V^+
K4M2	2	69.10	6.30	Cube	Full-span	2	68.03	6.53
K6M2	2	151.71	8.64	Cube	Full-span	2	133.08	8.66
K3M2	2	37.19	4.00	Bar	Minimal-span	2	39.62	3.78
K5M2	2	110.45	7.61	Bar	Minimal-span	2	86.80	7.49
K4M4	4	55.77	5.87	Cube	Full-Span	4	60.21	5.38
K4M6	4	114.42	8.46	Cube	Full-Span	4	93.29	8.06

Table 4.1: Comparison between real roughness velocity shift as a function of k_{s*}^+ and modeled roughness velocity shift as a function of $(H_V^+/H_{norm}^+)^p$ where $H_{norm}^+ = 1.31$ and $p \approx 2.23$. The flow cases are fully described in Table 3.1

The untransformed mean velocity shift as shown in Figure 4.21a does not perform very well for both $M_b = 2$ and $M_b = 4$ cases for modeled roughness. There are large deviations from the asymptotic fully rough profile. This is due to the compressibility effects that necessitate compressibility transformations. The most celebrated van Driest transformation (Van Driest, 1951) is applied and the mean velocity shift is recorded in Figure 4.21b. While there is an improvement in the accuracy of the results obtained, it is not sufficient to be used for further study. Figure 4.21c represents the Trettel–Larsson-transformed (Trettel and Larsson, 2016) mean velocity shift. There is a marked improvement compared to the previous compressibility transformation. A comparison between the mean velocity shift of resolved roughness and modeled roughness using Volpiani-transformation ΔU_V^+ is offered in Table 4.1. The roughness scaled k_* is used for resolved roughness and k_s is used for modeled roughness. There is a good match obtained between the velocity shifts and roughness length scales of resolved and modeled roughness. The small discrepancies between k_{s*}^+ and $(H_V^+/H_{norm}^+)^p$ is due to the fixed number of $\eta(H)$ that was tested at specific values during the simulations of modeled roughness. A better choice of $\eta(H)$ can provide a closer match between the roughness length

scales. It is not possible to pick the exact value of $\eta(H)$ to match k_* *a priori*. In essence, the equivalent roughness height cannot be recovered *a priori* from the model parameters. This is an accepted shortcoming of the model. However, the benefit of the model is seen only when used in conjunction with fully resolved DNS. With a tuned model and one single DNS case of a given geometry, it is possible to estimate k_s. This reduces the cost of performing fully resolved DNS by a little less than half since results for *at least* two roughness Reynolds numbers are required to estimate k_s.

The streamwise density scaled turbulent normal stress profile for $M_b = 2$ and $M_b = 4$ is presented in Figure 4.22a and Figure 4.22b respectively. With an increase in $\eta(H)$, there is a decrease in the peak value of the stress. Additionally, the peak is shifted towards the centerline. This was also observed for the case of $3D$ cube roughness and $2D$ bar roughness profiles that are superposed on the results of the modeled roughness in Figure 4.22a. All the stress profiles collapse beyond the roughness sublayer indicating outer layer similarity. Since the effect of the roughness is modeled uniformly, the roughness sublayer profile from the modeled roughness cases are not supposed to match the profile from resolved roughness cases that show sharp variations between the base and the crest of the roughness elements. The $3D$ cube roughness in full channel profile at $k^+ \approx 80$ (+ symbols) and minimal-span channel $2D$ bar roughness at $k^+ \approx 80$ profiles (star symbols) differ from the modeled roughness profiles since they are at $Re_\tau \approx 1000$. A similar trend is noticed in case of $M_b = 4$ profiles in Figure 4.22b. The peak stress of the modeled roughness case at the same $\eta(H)$ is higher in case of $M_b = 4$ compared to $M_b = 2$. Nonetheless, outer layer similarity is achieved.

The wall-normal turbulent stress profile is presented in Figure 4.22c for $M_b = 2$ and Figure 4.22d for $M_b = 4$. The first observation is that the wall normal stress goes to zero as the wall is approached. This is due to the boundary condition that is impermeable to the flow at the wall. Hence, the wall normal velocity and its associated fluctuations are zero. Additionally, for the modeled roughness case, the same behaviour is observed as the channel centerline is approached. This is because of the open channel that is used for modeled roughness cases. The wall impermeable boundary condition is also set on the channel mid plane that brings the wall normal velocity and its associated fluctuations to zero. Good outer layer similarity is observed with the peak stress value progressively decreasing and shifting slightly towards the channel centerline with an increasing $\eta(H)$. However, this decrease in peak stress value is not as severe as was in the case of streamwise turbulent stress. In Figure 4.22d, the wall normal turbulent stress profile for the Mach 4 cube roughness at $Re_\tau \approx 500$ does not collapse on the other profiles in the outer layer. This is because the modeled roughness cases are performed on open channels as opposed to the cube roughness simulations that are done on full channels.

The spanwise turbulent stress profiles show a similar trend and are depicted in Figure 4.22e and Figure 4.22f. The modeled roughness profiles collapse on each other in the outer layer for both Mach 2 and Mach 4 cases confirming outer layer similarity. When compared with Mach 2 cube roughness (right triangles) at $Re_\tau \approx 500$, the match with the modeled roughness profiles begin to appear only beyond $y^+ \approx 200$ as opposed to $y^+ \approx 100 - 150$ for streamwise and wall-normal turbulent stresses. In case of Mach 4, the collapse of the cube roughness profile with profiles from modeled roughness is not observed (Figure 4.22f). The inner layer profiles for the modeled roughness flow cases progress a lot differently as compared to the fully resolved roughness flow cases. There is no change in magnitude of the stress peaks for $M_b = 4$ flow cases compared to $M_b = 2$ flow cases. The Reynolds shear stress profiles for the modeled roughness flow cases show perfect collapse for all values of $\eta(H)$ beyond the roughness sublayer. In addition, the resolved roughness flow cases for $3D$ and $2D$ roughness, at $M_b = 2$ and $M_b = 4$ show perfect agreement with the modeled roughness profiles in the outer layer. This reinforces the strength of density scaling for accounting for compressible effects in case of Reynolds shear stress and the success of the outer layer similarity.

The mean temperature profiles are presented next. The mean temperature profile for modeled roughness superposed with the profiles of resolved roughness is presented in Figure 4.23a and Figure 4.23b. With an increase in $\eta(H)$, the temperature gradient beyond $2H^+$ becomes steeper. The mean temperature peak is shifted to just beyond the roughness height parameter. The resolved roughness profiles for Mach 2 cube roughness and minimal-span channel bar roughness at $Re\tau \approx 500$ follow the K7M2 profile in Figure 4.23a. The Mach 2 cube roughness and minimal-span channel bar roughness profiles at $k^+ \approx 80$ are different from the modeled roughness cases since it is at $Re_\tau \approx 1000$. However, it is observed that they collapse on each other. In case of Mach 4, the cube roughness case at $Re_\tau \approx 500$ follows the case K6M4 beyond the roughness crest $k^+ \approx 40$. The general trend seems to be captured when the roughness height parameter is increased. The mean temperature peak shifts to a wall normal height that coincides with the roughness height parameter in the modeled roughness case just as it shifts to the roughness crest in case of resolved roughness. The $M_b = 4$ profiles are a lot steeper, with a higher peak values compared to the $M_b = 2$ flow case at the same

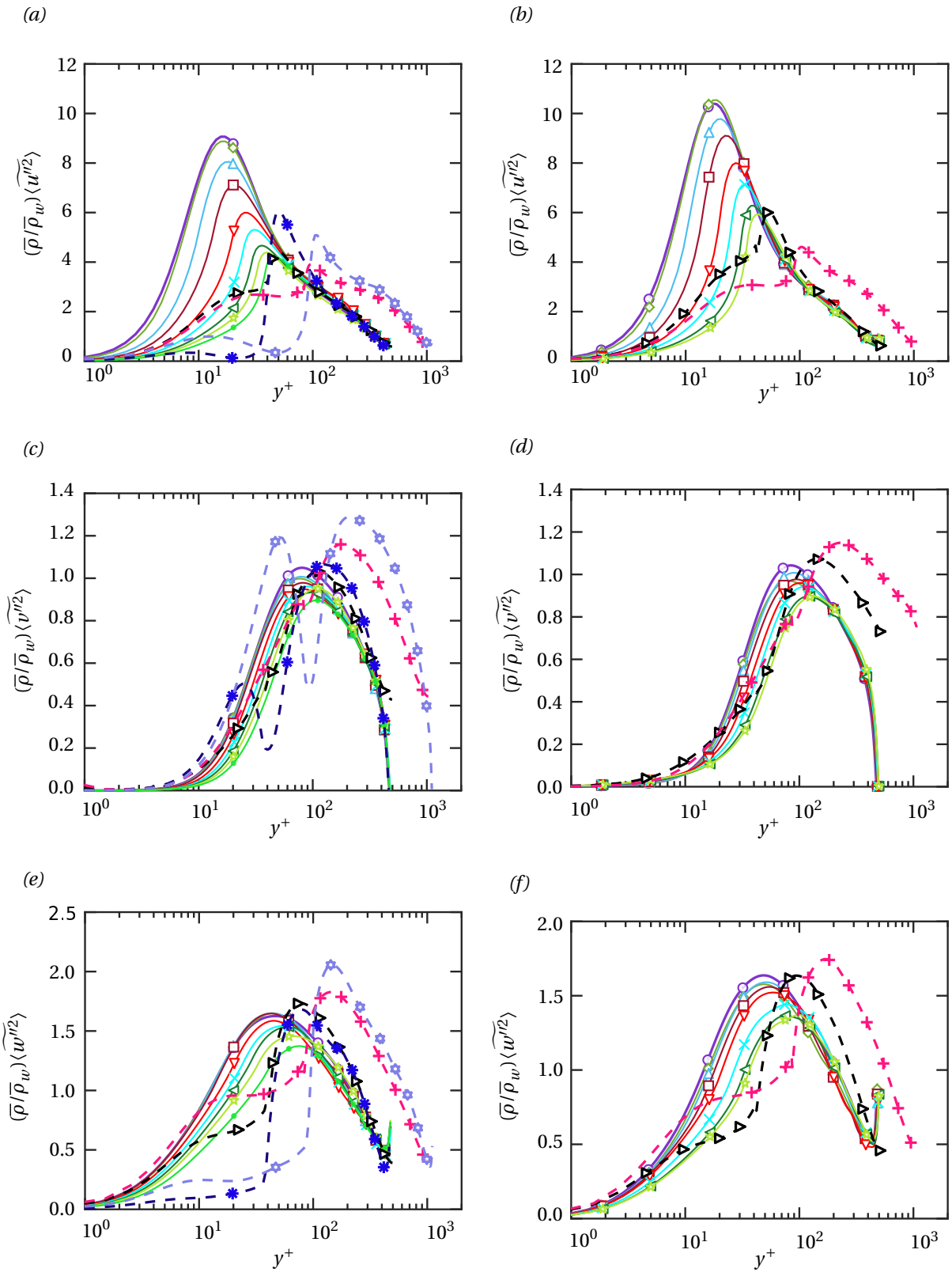
(a)
(b)
(c)
(d)
(e)
(f)
$(\overline{\rho}/\overline{\rho}_w)\widetilde{\langle u''^2\rangle}$
$(\overline{\rho}/\overline{\rho}_w)\widetilde{\langle v''^2\rangle}$
$(\overline{\rho}/\overline{\rho}_w)\widetilde{\langle w''^2\rangle}$
y^+
10^0
10^1
10^2
10^3

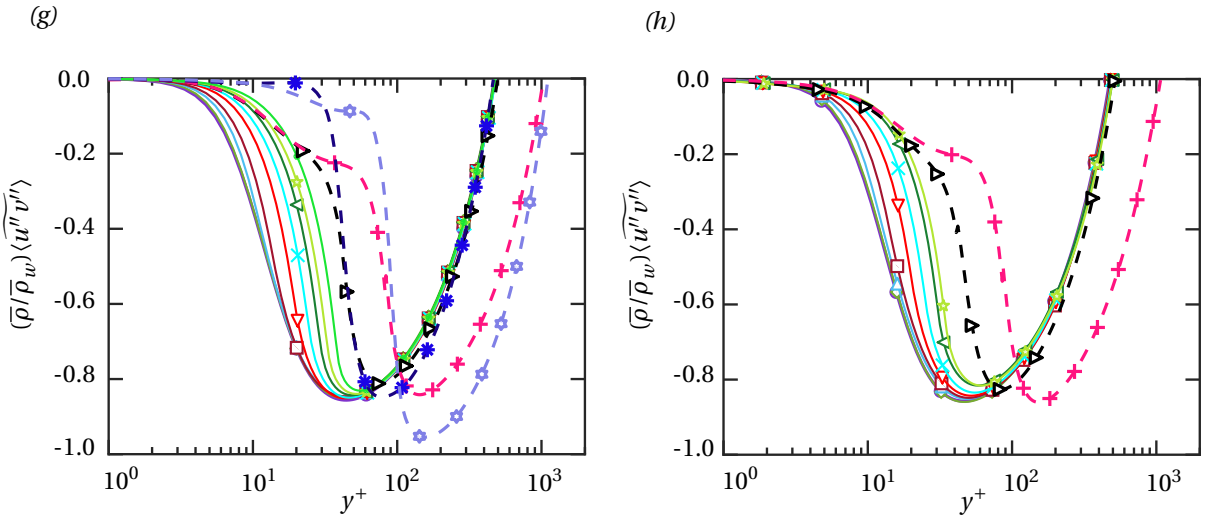

Figure 4.22: Density scaled turbulent (a,b) streamwise (c,d) wall-normal (e,f) spanwise stresses and (g,h) shear stress profile of modeled roughness at $M_b = 2$ (left column of images) and $M_b = 4$ (right column of images). The simulations are run at $Re_\tau \approx 500$. Included is the DNS data of $3D$ resolved roughness at $k^+ \approx 40$ (right pointing triangles, $k^+ \approx 80$ (+ symbols) and and minimal-span channel $2D$ bar resolved roughness using minimal-span channel at $k^+ \approx 40$ ($*$ symbols). The legend for modeled roughness is the same as in Figure 4.18a to Figure 4.18h

$\eta(H)$. The mean density profiles in Figure 4.24c and Figure 4.24d show an inverted trend compared to the mean temperature profiles. The minimum density keeps reducing with an increase in the roughness height parameter for modeled roughness. Due to strong compressibility effects, the mean density variation is more in case of $M_b = 4$ compared to $M_b = 2$. This results in a steeper mean density gradient and much greater variation across the channel.

The temperature fluctuations scaled by T_τ^2 are presented in Figure 4.24a for $M_b = 2$ case and in Figure 4.24b for $M_b = 4$ case. With an increase in $\eta(H)$, the temperature fluctuation peak increases and is shifted just above $2H^+$. On the other hand, the density fluctuations profile presents some interesting results. The profile at $M_b = 2$ is shown in Figure 4.24c for $M_b = 2$. It is observed that the mean density fluctuations are almost negligible. This is important since it forms the basis of the Morkovin hypothesis. A quick look at $M_b = 4$ case in Figure 4.24d suggests something different. The magnitude of density fluctuations no longer become negligible and increases with increasing roughness height parameter. It is almost 1.0 for a roughness height parameter of $2H = 0.07$. This indicates that the limit of applicability of the Morkovin hypothesis is reached. One consequence of this is the poor performance of the van Driest transformation (Van Driest, 1951) since it is based on the Morkovin hypothesis. Indeed, Figure 4.18d shows that the van driest-trasformed (Van Driest, 1951) smooth wall mean velocity profile in the log-law region shows a large mismatch with the incompressible law of the wall relation.

The Stanton number skin-friction coefficient augmentation for modeled roughness (squares) is presented in Figure 4.25. The results from $M_b = 2$ (solid symbols) and $M_b = 4$ (hollow symbols) are included along with the results from resolved roughness of $3D$ cubes (circles) at $M_b = 2$ and $M_b = 4$ and $2D$ bar roughness (triangles) at $M_b = 2$. The empirical relation from (2.69) is shown with $\alpha = 0.4, 1.3$. The modeled roughness results for $\eta(H) = 0.01, 0.02, 0.03$ at $M_b = 2$ and $M_b = 4$ are within the range given by the empirical relation (2.69). On the other hand, the range is unable to include roughness results at higher k^+. The relative increase in skin friction compared to heat transfer is greater in case of $M_b = 2$ and $M_b = 4$. The model is able to predict the drag increase accurately but the prediction of heat transfer increase is not as accurate.

The contours of $\langle\widetilde{u}\rangle^+$ on an $x-y$ plane for modeled roughness case at Mach 2 is presented in Figure 4.26b to Figure 4.26i. The smooth wall contour plot is shown in Figure 4.26a for the purpose of comparison. It is observed that there is a retardation of the flow as the value of $\eta(H)$ is increased from $\eta(H) = 0.01$ to $\eta(H) = 0.08$. The effect of roughness is seen to increase with $\eta(H)$. It is also noted that this effect that is modeled, is uniformly distributed close to the wall. A better idea of the roughness effect can be gathered from Figure 4.27b

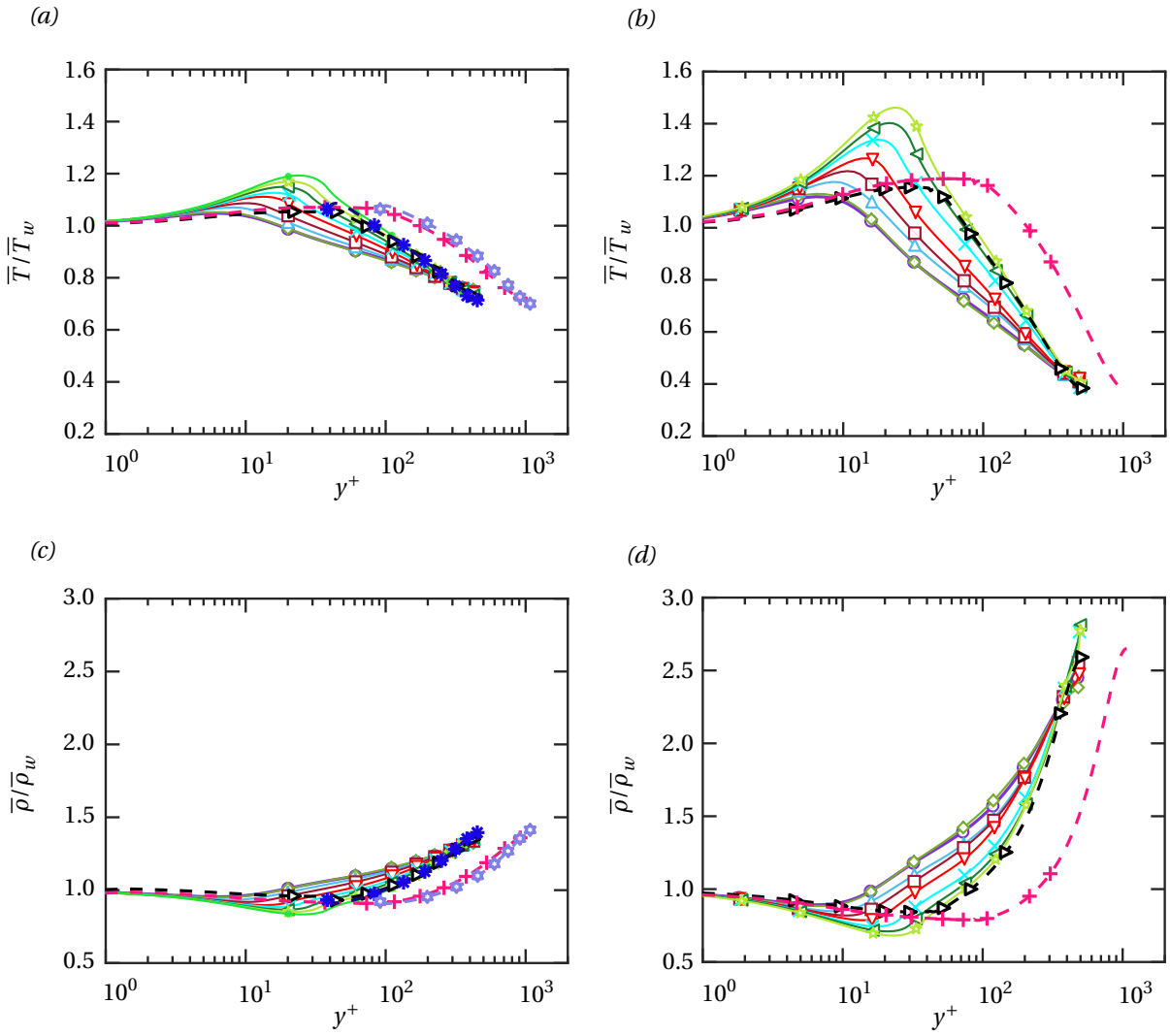

Figure 4.23: (a,b) Mean temperature profile scaled by wall temperature T_w (c,d) and mean density scaled by density at the wall $\overline{\rho}_w$ for modeled roughness at (a,c) $M_b = 2$ smooth wall and (b,d) $M_b = 4$. Included is the data from $3D$ cube roughness at $Re_\tau \approx 500$ (right pointing triangles) and $Re_\tau \approx 1000$ (+ symbols) and and minimal-span channel $2D$ bar roughness ($*$ symbols) at $k/h = 0.08$. The legend for modeled roughness is the same as in Figure 4.18a to Figure 4.18h

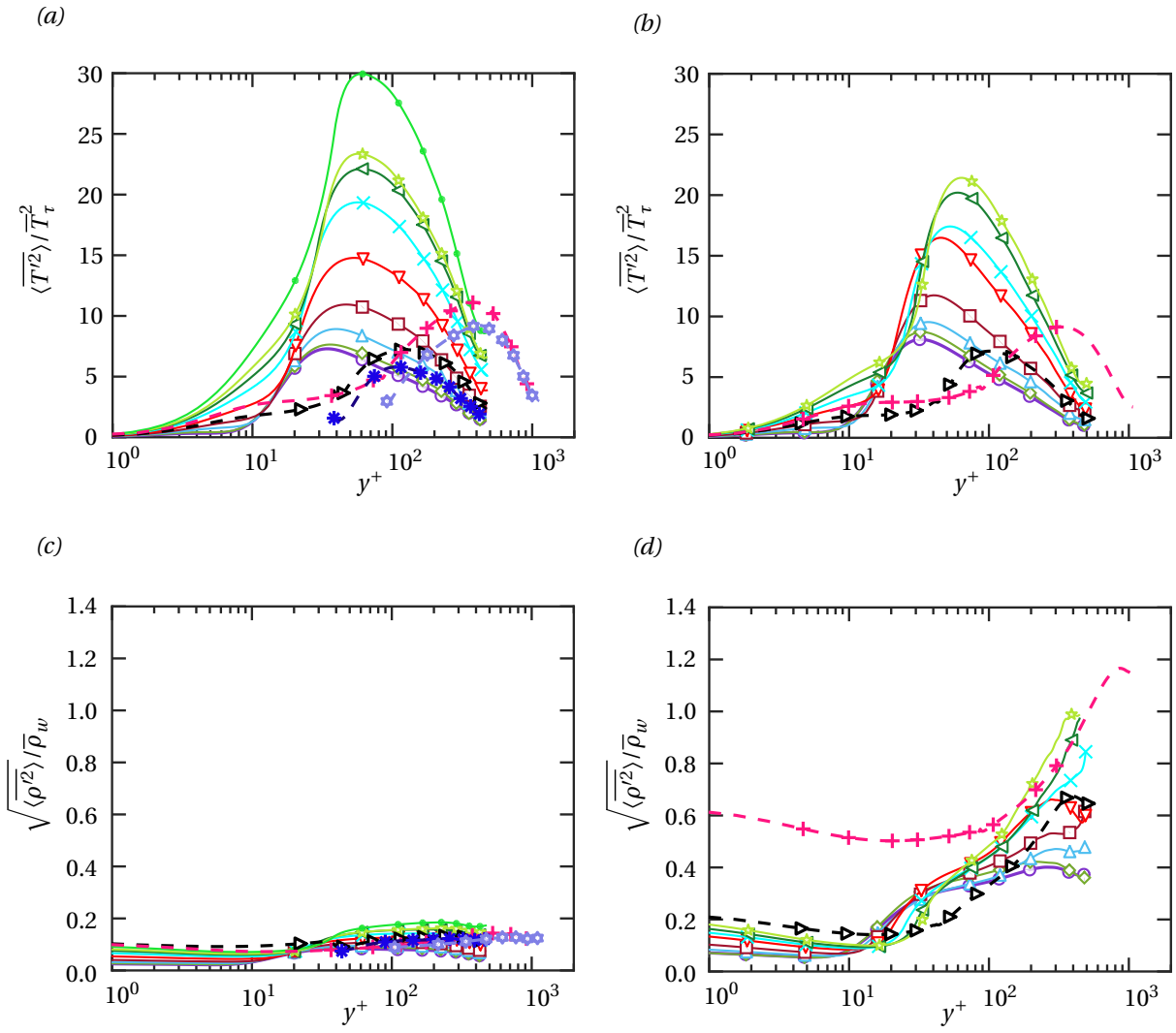

Figure 4.24: (a,b) Mean temperature fluctuations profile scaled by T_τ^2 (c,d) and mean density fluctuations scaled by density at the wall $\overline{\rho}_w$ for modeled roughness at (a,c) $M_b = 2$ and (b,d) $M_b = 4$. Included is the data from $3D$ cube roughness at $Re_\tau \approx 500$ (right pointing triangles) and $Re_\tau \approx 1000$ (+ symbols) and minimal-span channel $2D$ bar roughness ($*$ symbols) at $k/h = 0.08$. The legend for modeled roughness is the same as in Figure 4.18a to Figure 4.18h The legend for modeled roughness is the same as in Figure 4.18a to Figure 4.18h

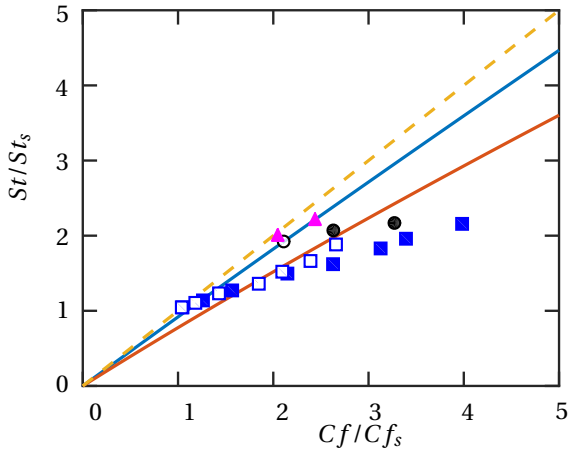

Figure 4.25: Staton number and skin-friction coefficient augmentation using (2.69) for modeled roughness (squares). $M_b = 2$ data presented as solid symbols and $M_b = 4$ data presented as hollow symbols. $3D$ cube resolved roughness (circles) and $2D$ bar roughness (triangles) also included. The dashed lines indicate the case when $St/St_s = Cf/Cf_s$ and the solid lines indicate $\alpha = 0.4, 1.3$ in (2.69).

to Figure 4.27i where the $x-z$ plane mean velocity contours are displayed. The wall normal distance where the profiles are extracted is located at a height of 12 viscous wall units above the imaginary roughness crest denoted by $\eta(H)$. This is done to capture the flow physics in the buffer layer. For example: at $\eta(H) = 0.04$, the value of $2H^+ \approx 19$. The profile in this case is extracted at $y^+ \approx 19 + 12 \approx 31$. The smooth wall data presented in Figure 4.27a shows the presence of the well known coherent structures (high speed and low speed streaks). As the value of $\eta(H)$ is increased, it is quickly observed that the high speed streaks are broken down and eventually disappear as $\eta(H)$ approaches 0.08. This disruption in near wall cycle is an effect of the modeled roughness term that is successful in producing the required effect of a roughness element.

The contours of mean temperature on the $x-y$ plane at Mach 2 is presented for modeled roughness cases $\eta(H) = 0.01 - 0.08$ in Figure 4.28b to Figure 4.28i. The reference sooth wall case is presented in Figure 4.28a. It is observed that the region close to the wall has a higher mean temperature due to viscous heating. The temperature progressively decreases towards the channel centerline. In case of modeled roughness cases, the thickness of the high temperature region close to the wall increases accompanied with an increase in the temperature within this region. The effect of the roughness work and heat transfer terms are observed as $\eta(H)$ is increased. The contour plots on the $x-z$ plane portray a similar trend. There are pockets of low temperature dispersed in a high temperature field. With an increase in $\eta(H)$, the magnitude of high temperature field increases without noticeable changes to the low temperature pockets. This is observed in Figure 4.29b to Figure 4.29i.

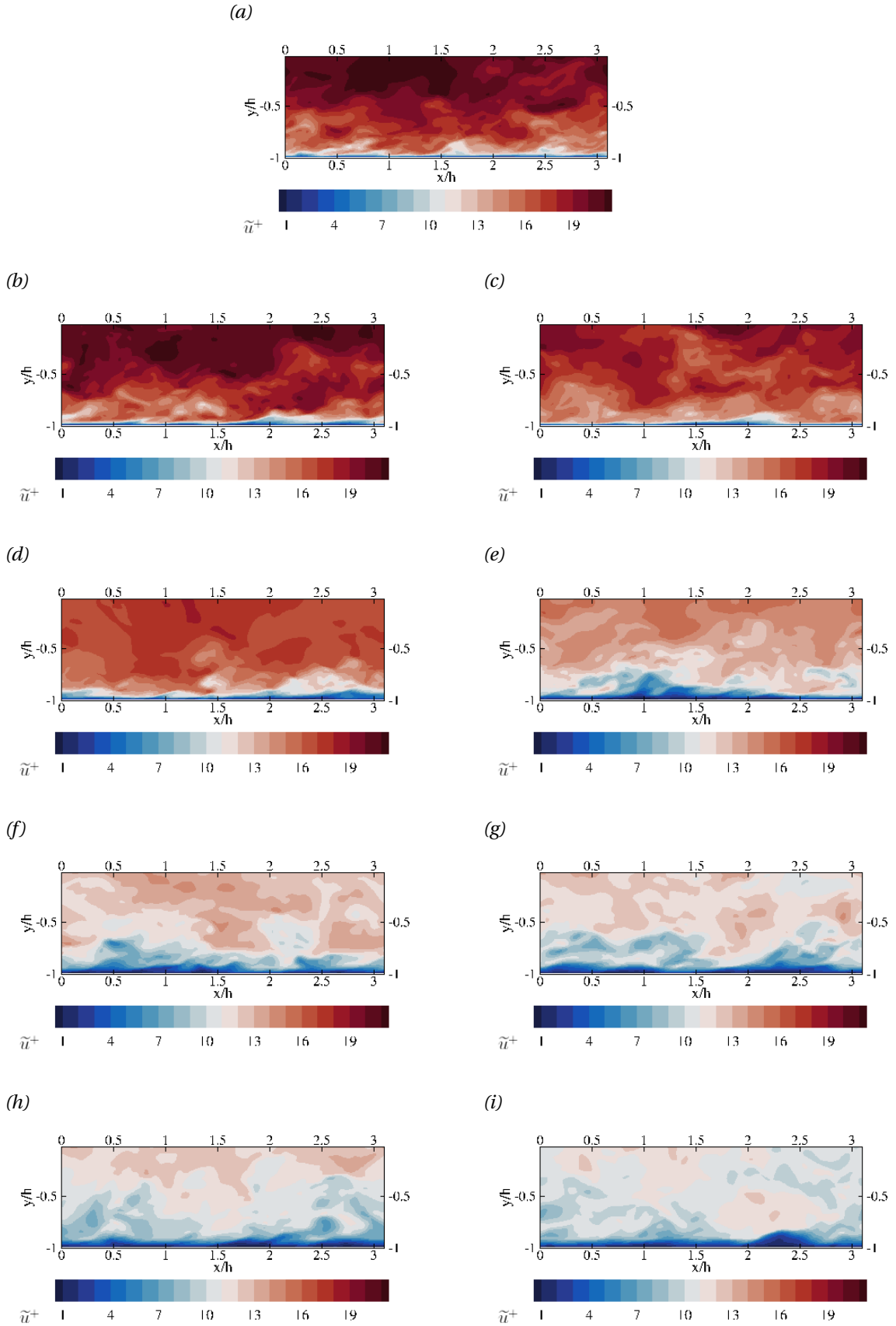

Figure 4.26: Contour plots of $\widetilde{u}^+$ along $x-y$ plane of supersonic flow over modeled roughness in an open channel at $Re_\tau \approx 500$ and $M_b = 2$ (a) smooth wall (b) $\eta(H) = 0.01$ (c) $\eta(H) = 0.02$ (d) $\eta(H) = 0.03$ (e) $\eta(H) = 0.04$ (f) $\eta(H) = 0.05$ (g) $\eta(H) = 0.06$ (h) $\eta(H) = 0.07$ (i) $\eta(H) = 0.08$

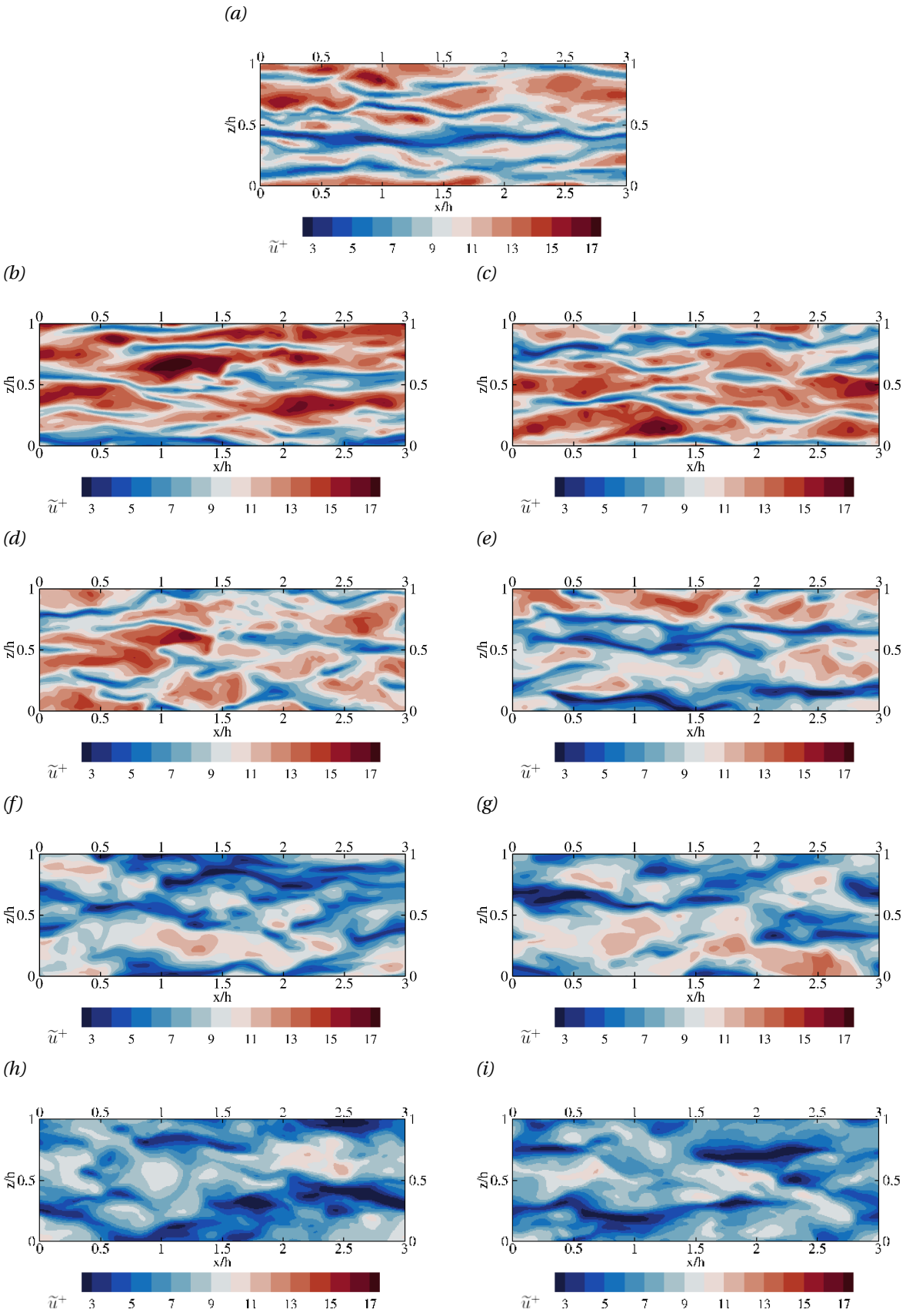

Figure 4.27: Contour plots of $\widetilde{u}^+$ along $x-z$ plane at a wall normal distance $y^+ \approx 12$ (above $2H^+$ in case of roughness cases) of supersonic flow over modeled roughness in an open channel at $Re_\tau \approx 500$ and $M_b = 2$ (a) smooth wall (b) $\eta(H) = 0.01$ (c) $\eta(H) = 0.02$ (d) $\eta(H) = 0.03$ (e) $\eta(H) = 0.04$ (f) $\eta(H) = 0.05$ (g) $\eta(H) = 0.06$ (h) $\eta(H) = 0.07$ (i) $\eta(H) = 0.08$

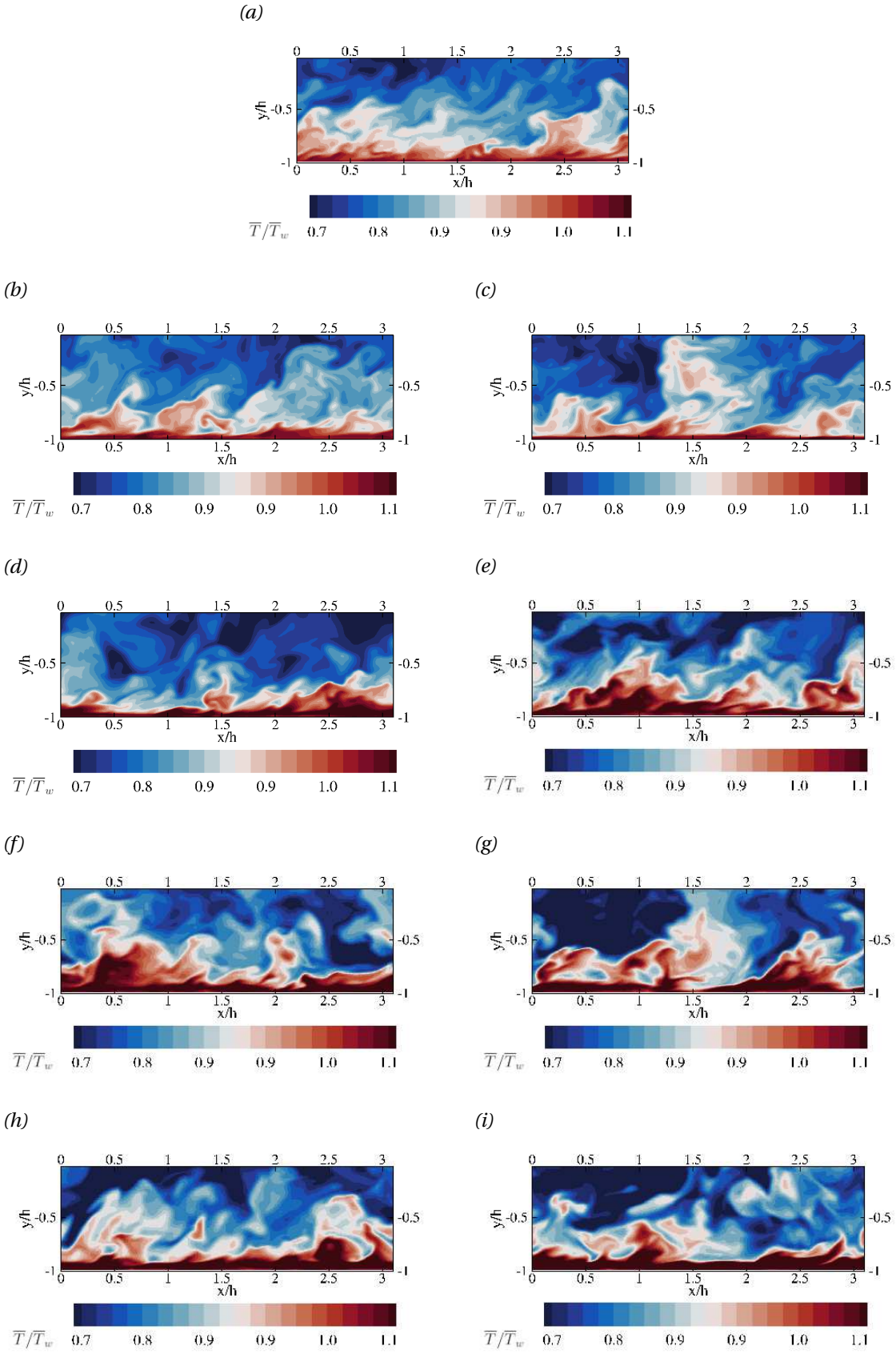

Figure 4.28: Contour plots of $\overline{T}/\overline{T}_w$ along $x-y$ plane at a spanwise distance $z/h = 0.75$ of supersonic flow over modeled roughness in an open channel at $Re_\tau \approx 500$ and $M_b = 2$ (a) smooth wall (b) $\eta(H) = 0.01$ (c) $\eta(H) = 0.02$ (d) $\eta(H) = 0.03$ (e) $\eta(H) = 0.04$ (f) $\eta(H) = 0.05$ (g) $\eta(H) = 0.06$ (h) $\eta(H) = 0.07$ (i) $\eta(H) = 0.08$

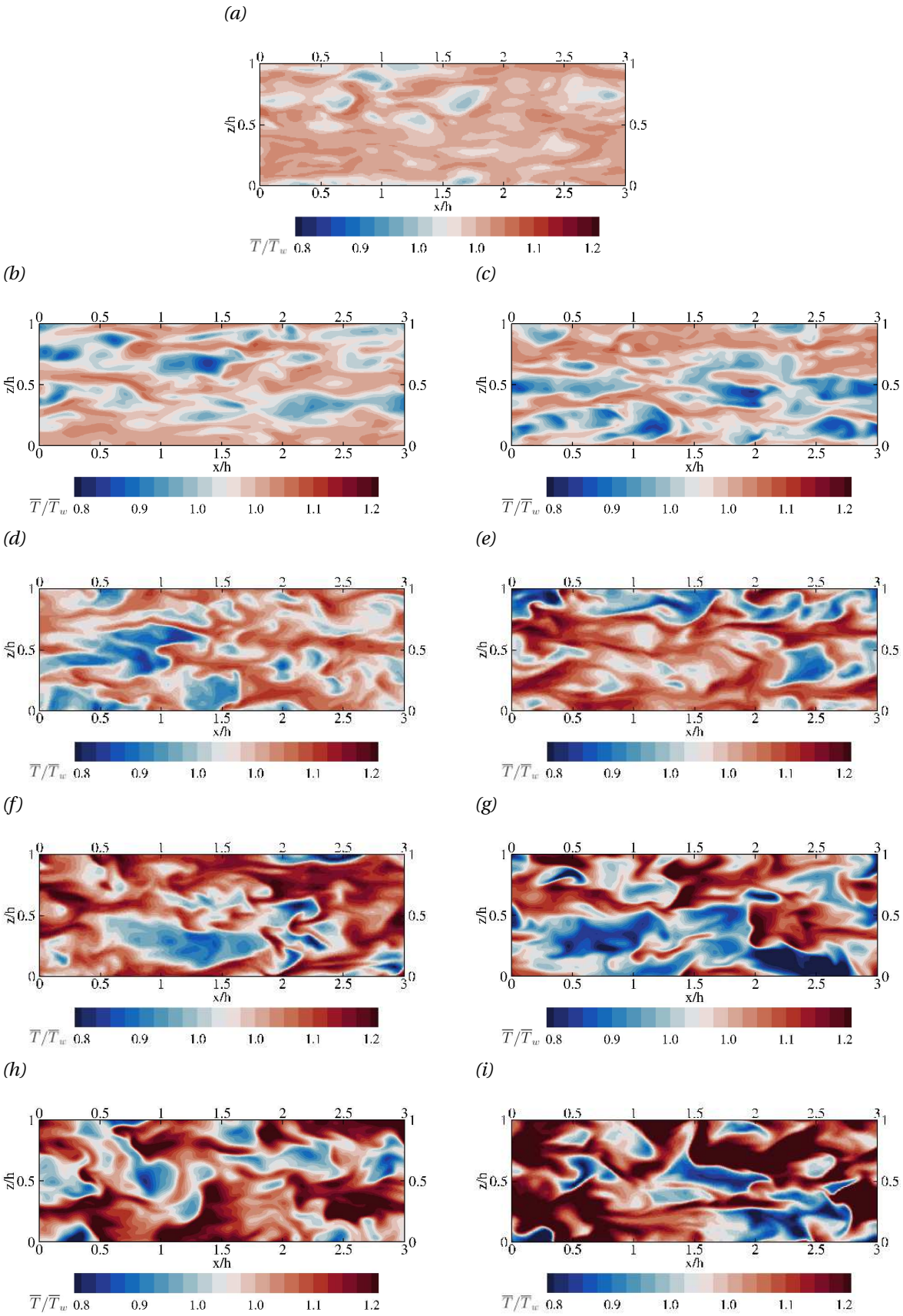

Figure 4.29: Contour plots of $\overline{T}/\overline{T}_w$ along $x-z$ plane at a wall normal distance $y^+ \approx 12$ (above $2H^+$ in case of roughness cases) of supersonic flow over modeled roughness in an open channel at $Re_\tau \approx 500$ and $M_b = 2$ (a) smooth wall (b) $\eta(H) = 0.01$ (c) $\eta(H) = 0.02$ (d) $\eta(H) = 0.03$ (e) $\eta(H) = 0.04$ (f) $\eta(H) = 0.05$ (g) $\eta(H) = 0.06$ (h) $\eta(H) = 0.07$ (i) $\eta(H) = 0.08$

4.3. RANS

The results from RANS with SA model is discussed in this section. The untransformed mean velocity profile at $M_b = 2$ for smooth wall (solid lines with squares) and $3D$ cube roughness using RANS (dashed lines with squares) is presented in Figure 4.30a for $Re_\tau \approx 500$ and in Figure 4.30b for $Re_\tau \approx 1000$. Included in the plot is the result from DNS test case of smooth wall (solid line with triangles) channel flow of full channel at Mach 2, $Re_\tau \approx 500$ and fully resolved cube roughness at $Re_\tau \approx 500$ (dashed line with triangles). It is easy to notice that rough wall mean velocity profile computed using RANS for $Re_\tau \approx 500$ shows a large deviation from the DNS profile for untransformed case (Figure 4.30a) . Since the untransformed mean velocity profile at $Re_\tau \approx 500$ for the rough wall case (which corresponds to $k^+ \approx 40$) is not accurate, the compressibility transformations will also not yield accurate results. This is observed in the van Driest (Van Driest, 1951) and Trettel–Larsson Trettel and Larsson (2016) compressibility transformations (Figure 4.30c and Figure 4.30e) for the flow case at $Re_\tau \approx 500$. On the other hand, the untransformed mean velocity profile computed using RANS for $k^+ \approx 80$ shows a closer agreement to the DNS result (Figure 4.30b) compared to the case at $k^+ \approx 40$. Though the accuracy of untransformed mean velocity profile computed using RANS has improved for $Re_\tau \approx 1000$, it is still not sufficient to warrant the usage of compressibility transformations. However, this indicates that the mean velocity profile computed using RANS (in particular the SA model) is more accurate at a higher roughness Reynolds number k^+ (particularly, when it is well into the fully rough regime).

The mean velocity shift computed using RANS for $k^+ \approx 40, 80$ is presented in Figure 4.31a to Figure 4.31d. Just as in the case of DNS, a $k^+_{sV} = 1.9k^+_V$ is applied to the RANS results to match the velocity shift with the theoretical asymptotic fully rough profile. Figure 4.31a shows the untransformed velocity shift as a function of k^+_s. The results obtained from RANS (hollow diamonds) show a large deviation from the DNS results (solid diamonds). However, the deviation is reduced at a higher k^+ (a relative error of $\approx 72\%$ for $k^+ \approx 40$ as opposed to $\approx 43\%$ for $k^+ \approx 80$). Despite an improvement in ΔU^+ with higher k^+, the relative errors are too high.

The mean temperature profile is presented in Figure 4.32a for the flow case at $Re_\tau \approx 500$ and in Figure 4.32b for the flow case at $Re_\tau \approx 500$. Both smooth wall (solid lines) and $3D$ cube roughness (dashed lines) results computed using RANS (squares) and DNS (triangles) are included. It is observed that there is a good agreement between the mean temperature profile of smooth wall computed using RANS and the one computed using DNS for both $Re_\tau \approx 500, 1000$. However, there are deviations above the roughness crest that is observed in case of $3D$ roughness mean temperature profiles. The mean temperature is underpredicted both in the case of $Re_\tau \approx 500, 100$ when using RANS. The mean density profile of smooth wall computed using RANS shows a good agreement with the mean density profile computed using DNS. However, a slight overprediction of mean density in Figure 4.32c and Figure 4.32d is observed in the RANS profiles when compared to the DNS profile.

The Stanton number and skin-friction augmentation is presented in Figure 4.33. The results from DNS of fully resolved cube roughness is included as solid circles and the results from RANS SA model is included as hollow circles. It is observed that the RANS SA model is capable of replicating the general trend of increase in heat transfer and drag in case of cube roughness. With an increase in k^+, a greater increase in drag compared to increase in heat transfer is observed. However, there are large discrepancies in the actual magnitude of heat transfer and drag increase. This points to the inability of RANS SA model to replicate the effects of increase in drag and heat transfer for a cube roughness element.

The mean flow fields of mean velocity and temperature for RANS and DNS $3D$ cube roughness is presented to get a better idea of the flow field. A single roughness element is isolated and presented to allow a more closer study at the near wall properties. The mean velocity computed using DNS for $3D$ cube roughness at $M_b = 2$ and $Re_\tau \approx 500$ is presented in Figure 4.34a along with the RANS contour plot in Figure 4.34b. The $u - v$ velocity streamlines are also included. The primary observation is the effective retardation of the flow along the streamwise direction is more in case of DNS when compared to RANS. This was also evident in the mean velocity profile in wall units presented in Figure 4.30a. The momentum deficit caused by the roughness element is not computed accurately using RANS. Secondly, the flow field features are very different. The DNS flow field presents a recirculation zone with its core located upstream of the roughness element. The core is also roughly at the center of the roughness element in the wall normal direction. However, it is easy to notice in Figure 4.34b that the albeit the existence of a recirculation zone, its core is located more towards the crest of the roughness element. Similar flow fields are observed at $Re_\tau \approx 1000$ in Figure 4.34c and Figure 4.34d. An additional feature in case of Figure 4.34c is the presence of a very small vortex at the base of the roughness element on the downstream side. Safe to say, this is not captured by RANS. The flow fields along the $x - z$ plane are also analyzed. Figure 4.34f has $u - w$ streamlines included and is the flow field at $Re\tau \approx 500$ ($k^+ \approx 40$) computed using DNS. There are two counter rotating vortices downstream of the roughness element, typical

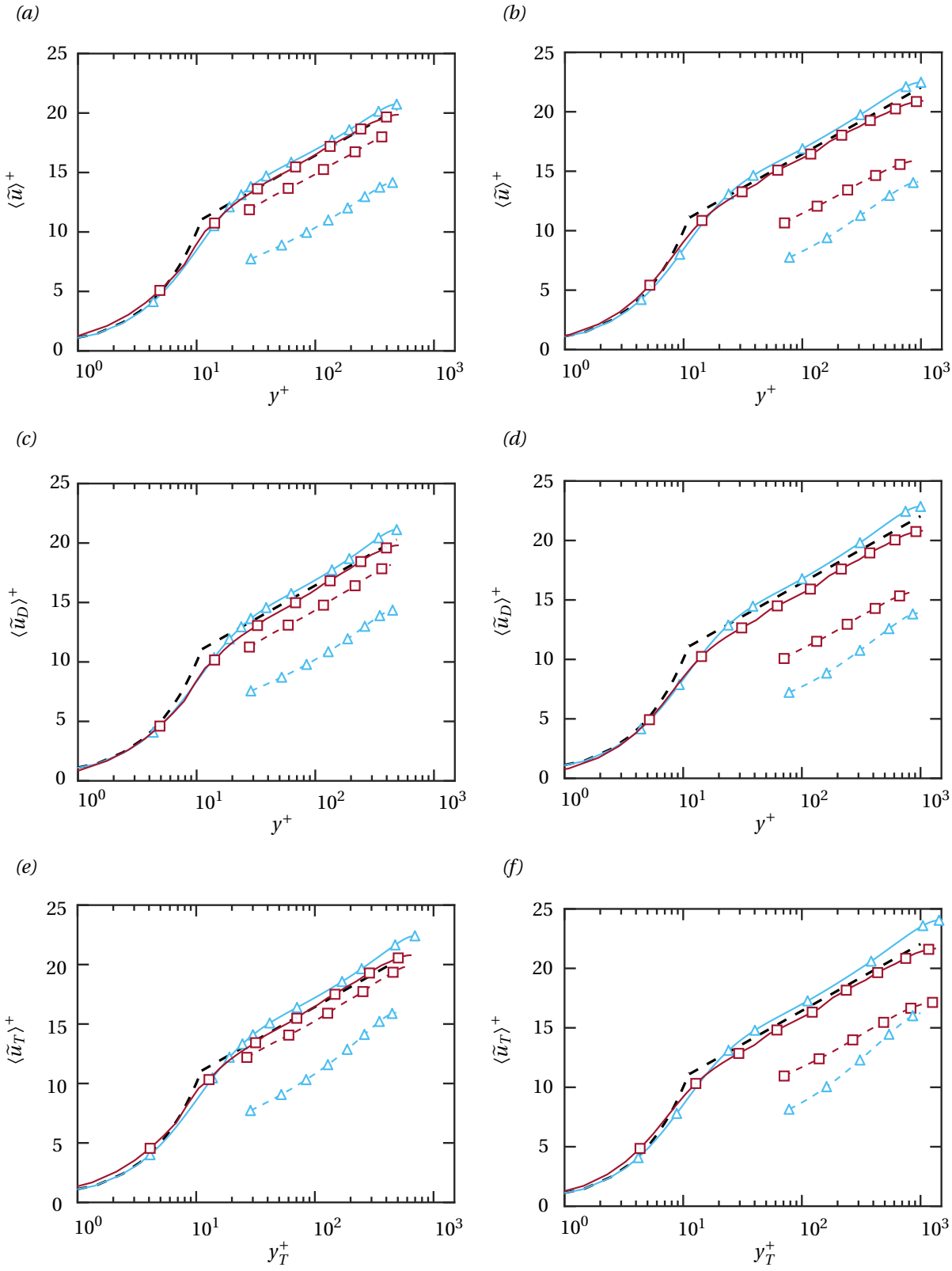
(a)
(b)
(c)
(d)
(e)
(f)
$\langle \widetilde{u} \rangle^+$
$\langle \widetilde{u}_D \rangle^+$
$\langle \widetilde{u}_T \rangle^+$
y^+
y_T^+
0
5
10
15
20
25
10^0
10^1
10^2
10^3

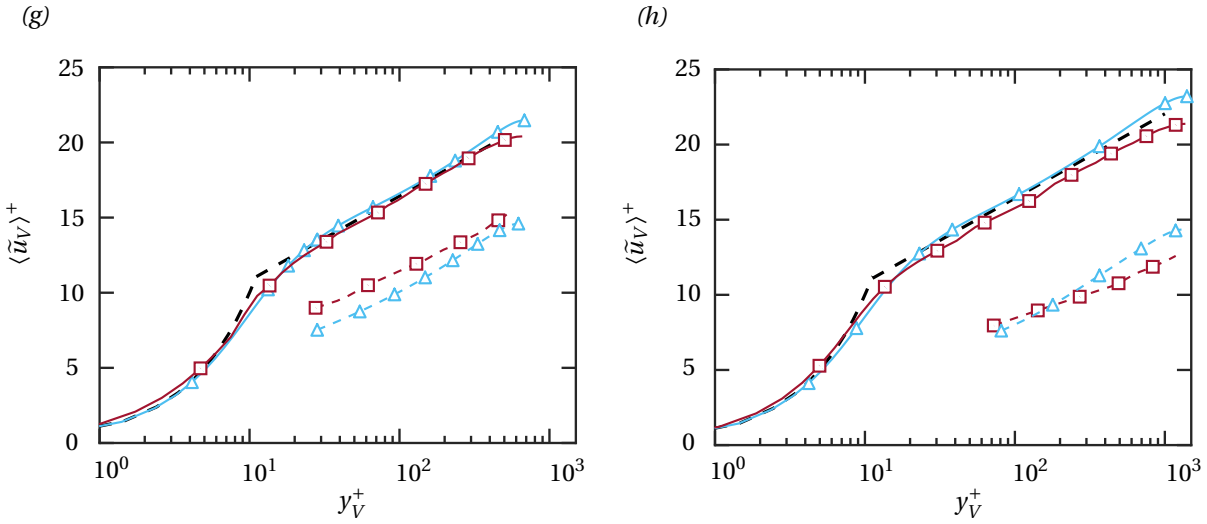

Figure 4.30: Mean velocity profile (a) untransformed (c) van Driest-transformed (Van Driest, 1951) (e) Trettel–Larsson-transformed Trettel and Larsson (2016) (g) Volpiani-transformed (Volpiani et al., 2020) computed using RANS (squares) and compared against DNS (triangles) at $Re_\tau \approx 500$, $M_b = 2$. Solid lines indicate smooth wall data and dashed lines indicate surface roughness with $k/h = 0.08$. The mean velocity profile and its associated compressibility transformations at $Re_\tau \approx 1000$ are given in the second column of figures in (b,d,f,h).

of flow around a cube. This contributes to the drag in addition to the already existing skin-friction drag. The flow field features are very different in case of Figure 4.34f that is computed using RANS. The two counter rotating vortices are absent. The flow retardation is less in the vicinity of the cube when compared to the DNS case as observed by the velocity contours. The results at $Re_\tau \approx 1000$ ($k^+ \approx 80$) do not show much variation.

The mean temperature contours are discussed next. Figure 4.35a shows the temperature contour plot along the $x-y$ plane at $Re_\tau \approx 500$. There is a region of high temperature that is located upstream of the roughness element with a region of maximum mean temperature located just beyond the edge of it. As you progress away from the roughness element, the mean temperature decreases. The increase in temperature close to the roughness element is due to the aerodynamic heating. It is more pronounced on the upstream side of the roughness element compared to the downstream side. A quick look at Figure 4.35b suggests that the mean temperature variation is a lot more rapid in case of RANS when compared to DNS. The results are similar for $Re_\tau \approx 1000$. Analyzing the $x-z$ plane mean temperature contour plots captured at a wall normal height of $y^+ \approx 20$ gives a lot of insight. The DNS result in Figure 4.35a is considered first. It is observed that there is a region of high temperature on upstream of the cube. Interestingly, the downstream of the cube has a lower temperature. This mean temperature difference between the upstream and downstream sides is small. This region of low temperature coincides with the region of counter rotating vortices. The contours from RANS in Figure 4.35f is markedly different. The region upstream of the cube has a higher temperature compared to the region downstream just as in the case of DNS. However, the overall mean temperature in the region surrounding the cube is not as high compared to the DNS case. The results at $Re_\tau \approx 1000$ ($k^+ \approx 80$) case are reviewed. The contour from Figure 4.35h suggest that the upstream mean temperature is close to the DNS case in Figure 4.35g. However, the downstream mean temperature contours are totally different. In the wake of the roughness element, the central portion has a higher temperature in RANS when compared to DNS.

The eddy viscosity ν_t profile of DNS and RANS SA model scaled by ν_w for smooth and cube roughness is presented in Figure 4.36a for $Re_\tau \approx 500$ and in Figure 4.36b for $Re_\tau \approx 1000$. There are discrepancies observed in the profiles of DNS (solid lines) and RANS (dashed lines). There is a good agreement between the profiles of DNS and RANS SA model in the viscous sub-layer for the smooth wall. The eddy viscosity tends to zero in this region as is expected due to the presence of viscous damping in the region close to the wall. However, general trend observed outside this layer is the over-prediction of eddy viscosity by RANS SA model in comparison to DNS for both $Re_\tau \approx 500$ and $Re_\tau \approx 1000$. In addition, there is a kink in the eddy viscosity profile of rough wall observed between $y/h = 0$ and $y/h = 0.1$ which is not modeled by the SA turbulence model. This local peak in eddy viscosity is below the roughness crest ($y/h = 0.08$). The eddy viscosity further increases beyond the

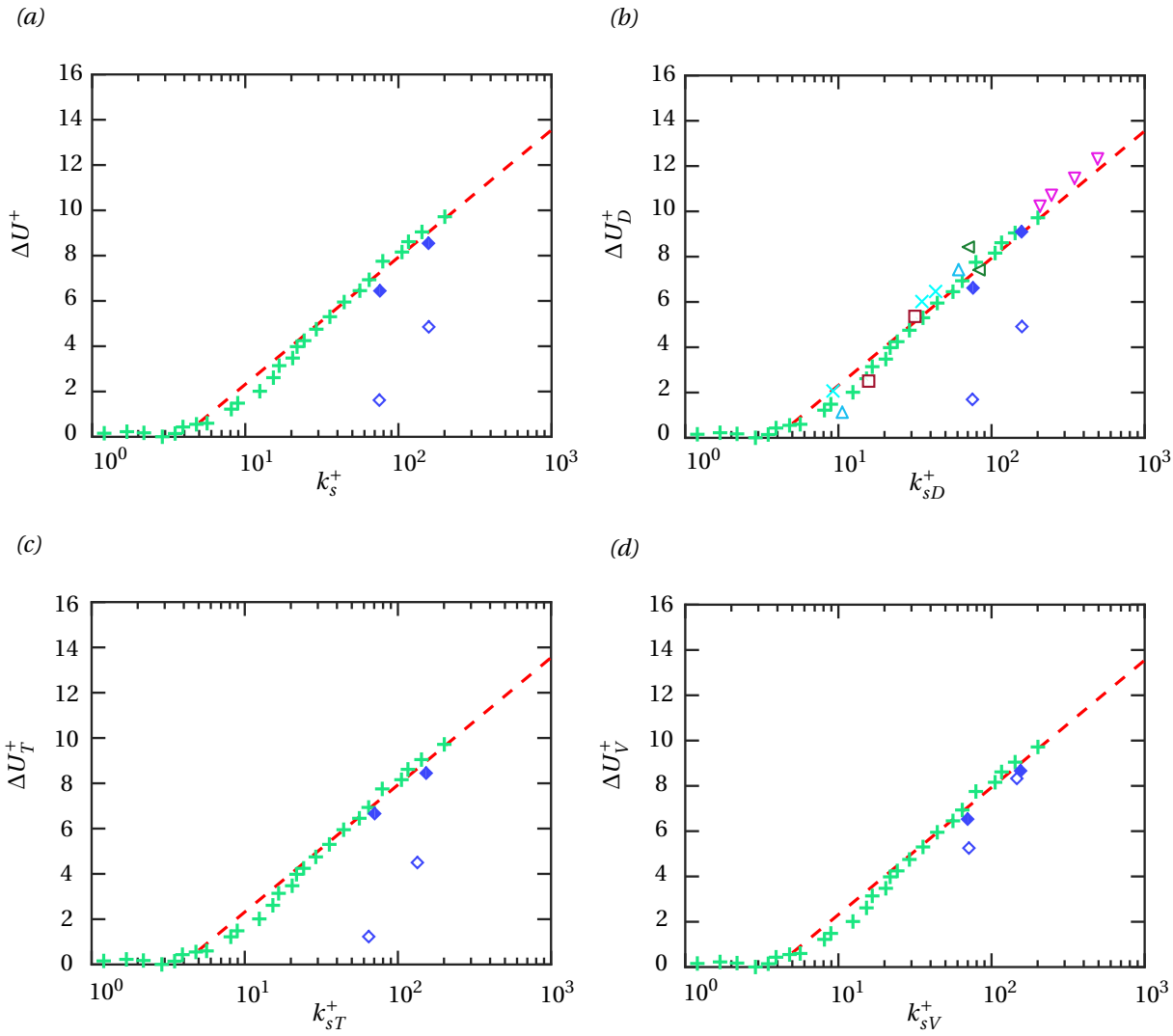

Figure 4.31: Mean streamwise velocity shift ΔU^+ of different compressibility transformations: (a) untransformed (b) van Driest (c) Trettel and Larsson (d) Volpiani at $M_b = 2$ computed using RANS (hollow diamonds) and DNS (solid diamonds) $3D$ cube roughness with roughness Reynolds numbers $k^+ \approx 40,80$ and sand grain roughness Reynolds number $k_s^+ = 1.9k^+$ and $k_{sI}^+ = 1.9k_I^+$. Dashed line is the theoretical asymptotic relation between equivalent sand grain roughness and Hama roughness function given by $\Delta U^+ = (1/\kappa)log(k_s^+) + B - B_S$. The incompressible roughness data from Nikuradse et al. (1950) (+ symbols) is also shown. In (b) experimental data of supersonic boundary layer are reported: Goddard Jr (1959) (squares), Berg (1979) (crosses), Reda et al. (1974) (upward pointing triangles, Latin and Bowersox (2000) (downward pointing triangles), Ekoto et al. (2008) (left pointing triangles)

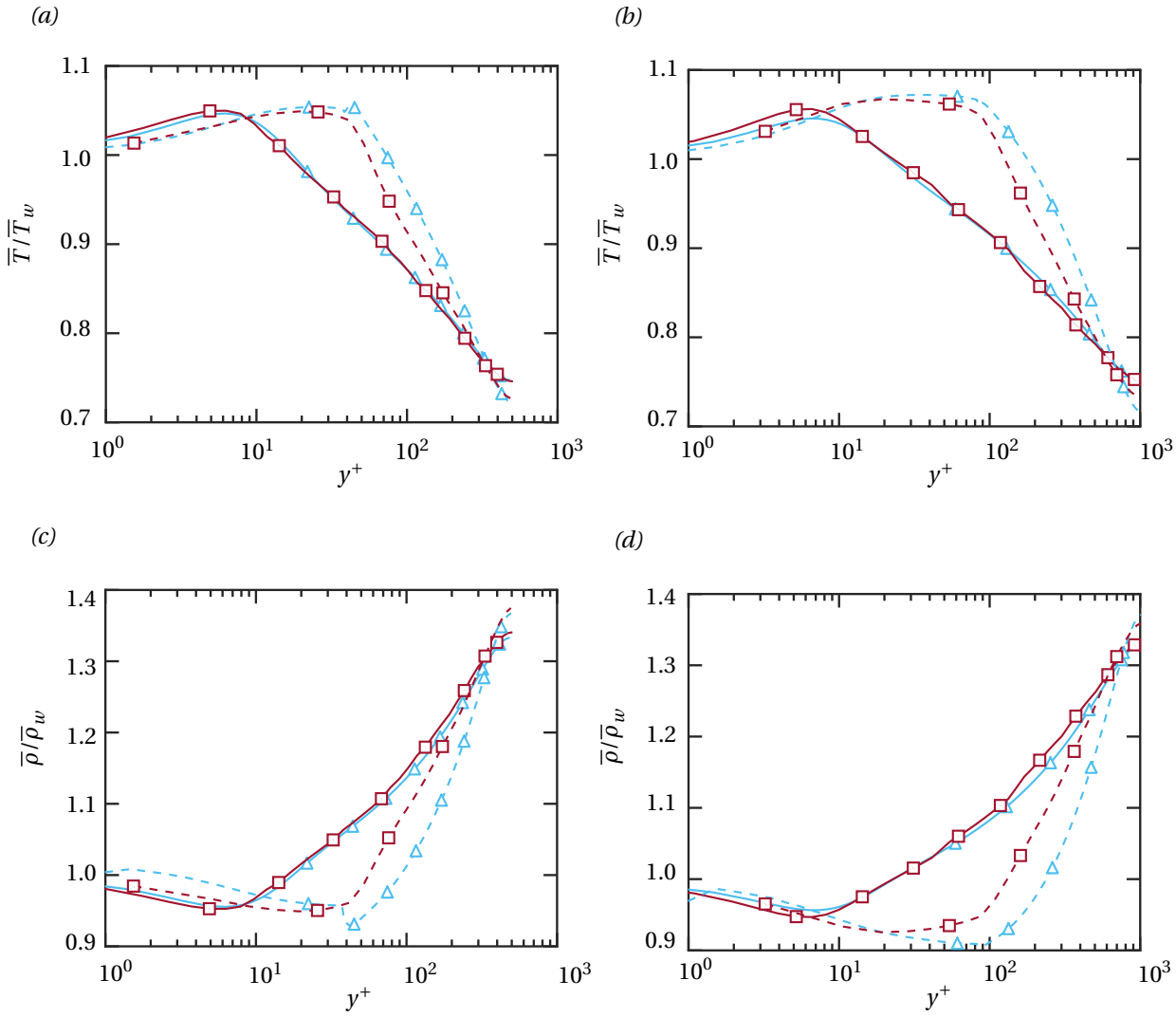

Figure 4.32: (a,b) Mean temperature profile scaled by wall temperature $\overline{T}_w$ (c,d) and mean density scaled by density at the wall $\overline{\rho}_w$ for smooth wall (solid lines) and rough wall (dashed) with roughness height $k/h = 0.08$ computed using RANS (squares) and DNS (triangles) for $3D$ cube roughness at (a,c) $Re_\tau \approx 500$ (b,d) $Re_\tau \approx 1000$ and $M_b = 2$.

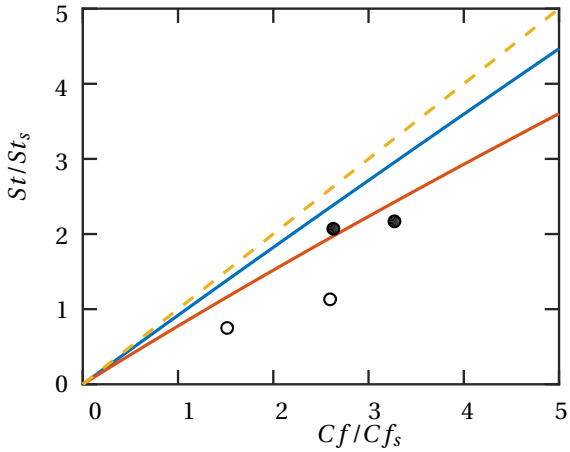

Figure 4.33: Staton number and skin-friction coefficient augmentation using (2.69) for fully resolved cube roughness compared against RANS SA model for $k^+ \approx 40,80$ at $M_b = 2$. Solid circles indicate DNS data and hollow circles indicate data computed using RANS SA model. The dashed lines indicate the case when $St/St_s = Cf/Cf_s$ and the solid lines indicate $\alpha = 0.4, 1.3$ in (2.69).

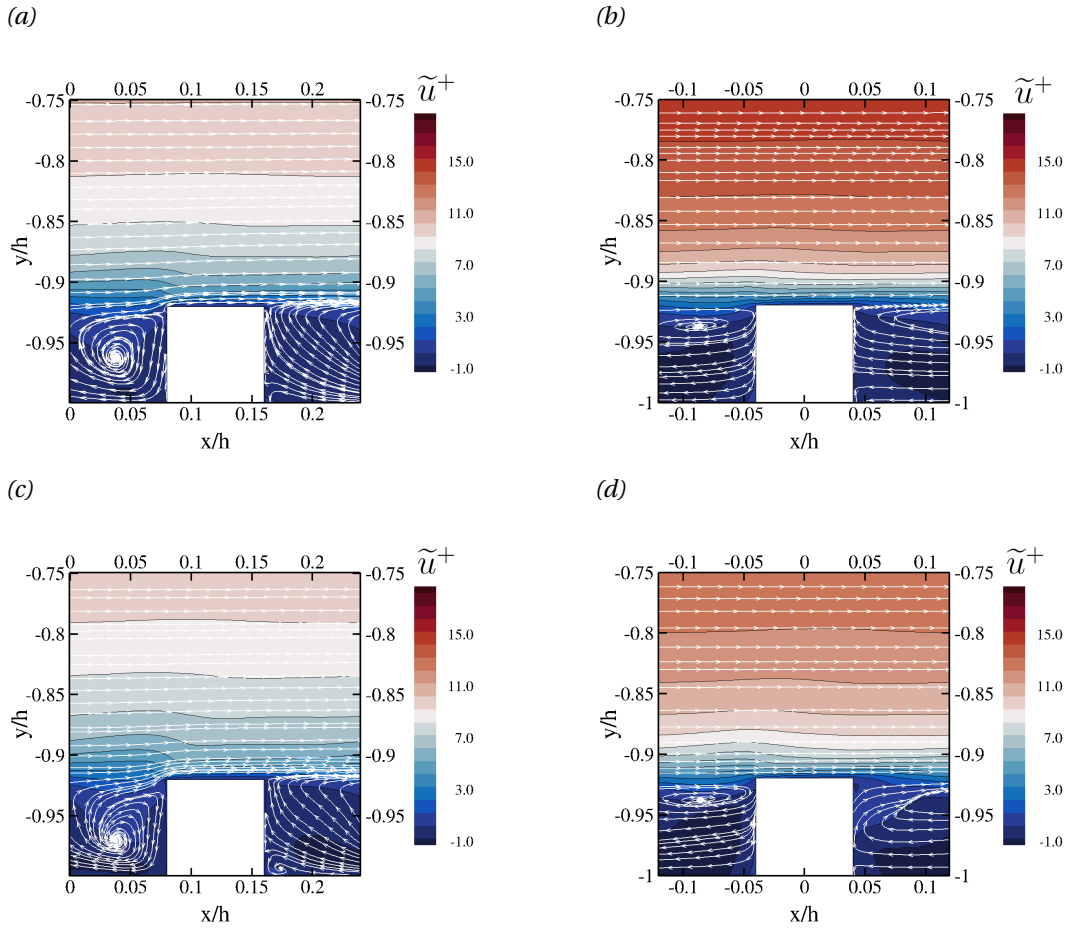

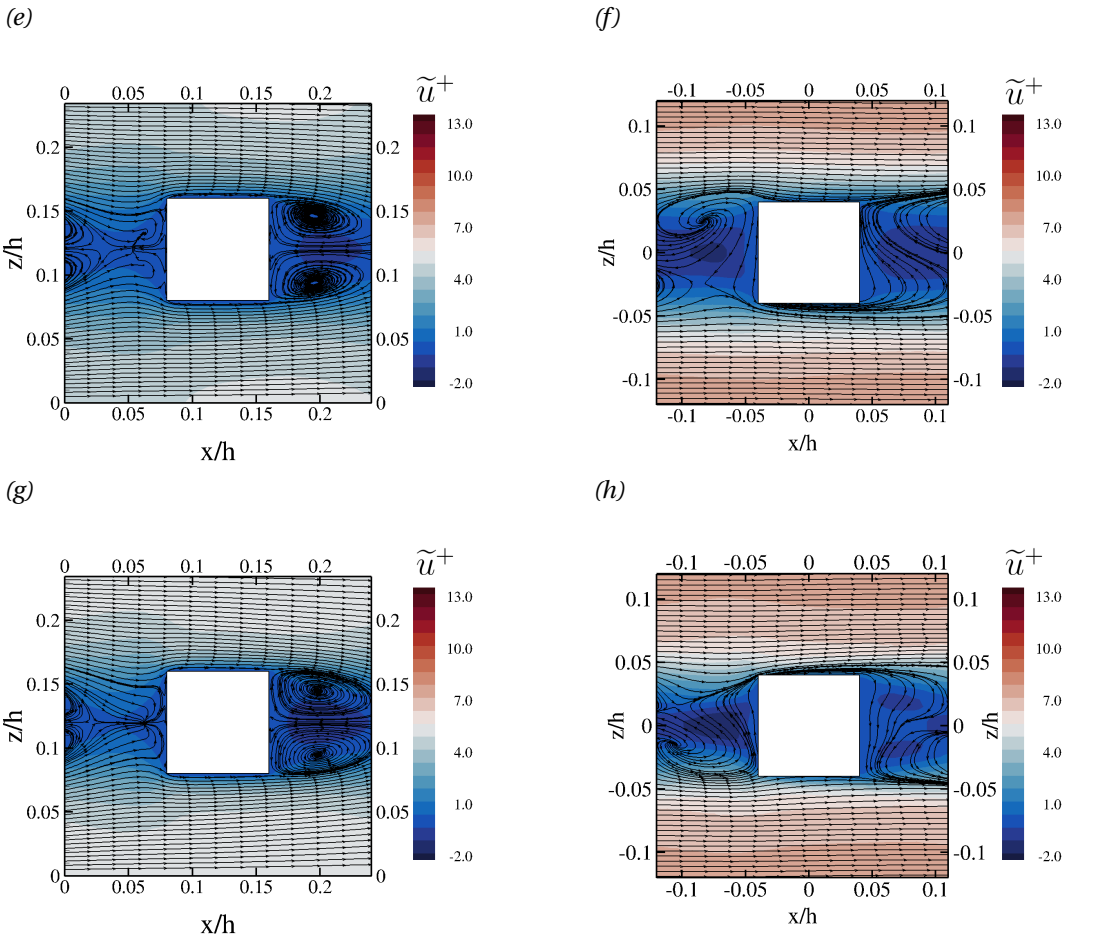

Figure 4.34: Mean flow fields of $\widetilde{u}^+$ of $3D$ cube roughness element at (a-d) $x-y$ plane extracted along the spanwise direction through the center of the channel and (e-h) $x-z$ plane extracted at a wall normal height of $y^+ \approx 20$. Left column of images are results from DNS and right column of images are results from RANS. (a,b,e,f) $Re_\tau \approx 500$ and (c,d,g,h) $Re_\tau \approx 1000$ at $M_b = 2$.

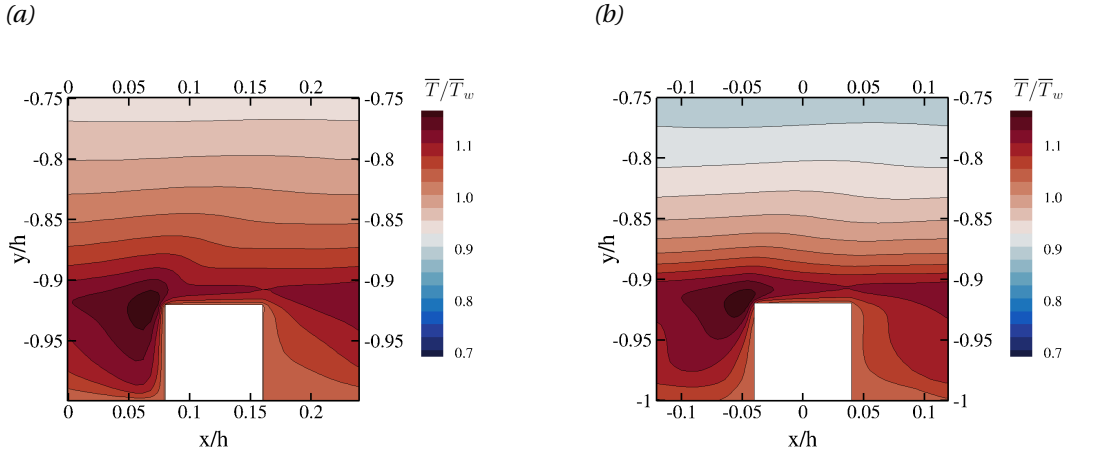

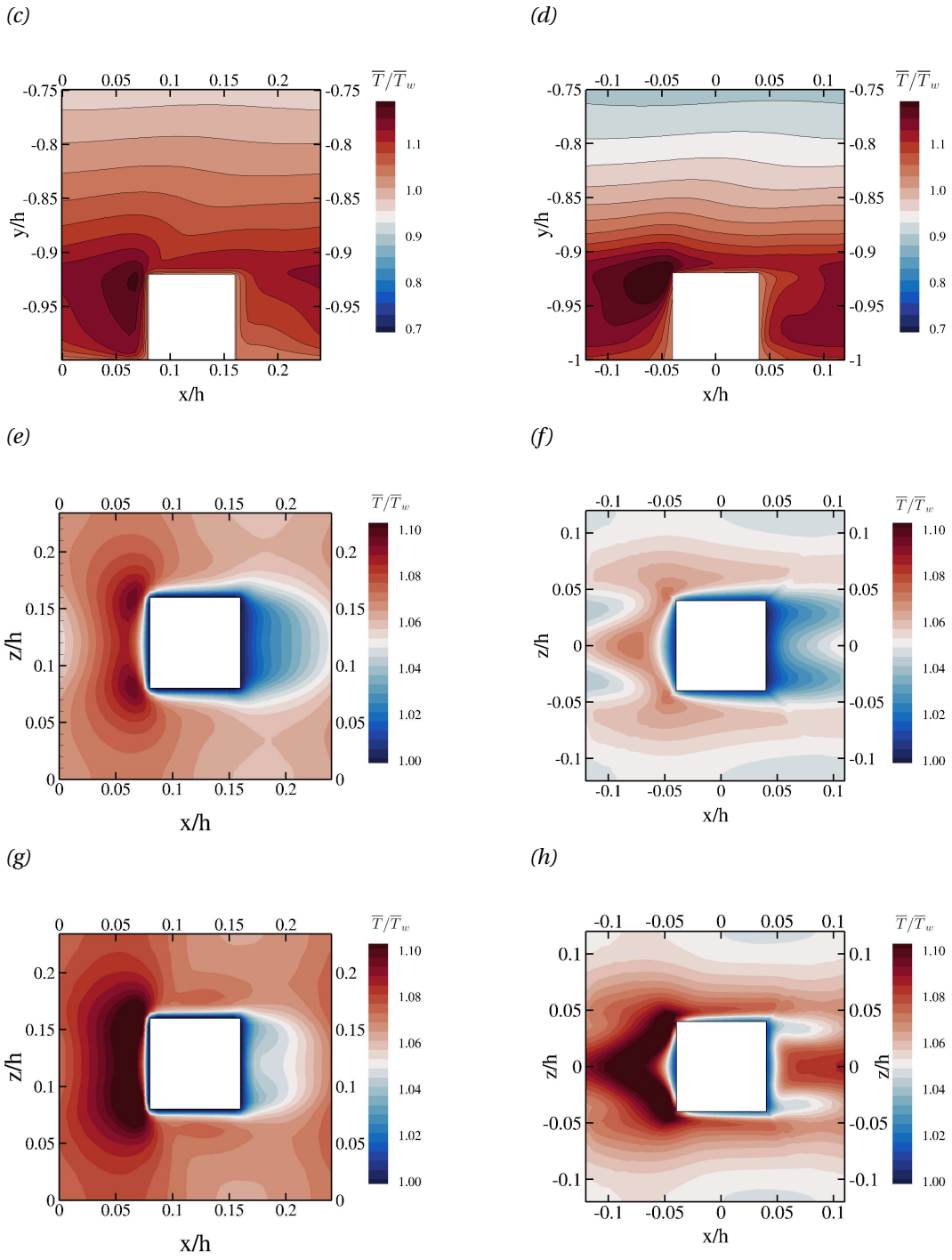

Figure 4.35: Mean flow fields of $\overline{T}_w/\overline{T}_w$ of $3D$ cube roughness element at (a-d) $x-y$ plane extracted along the spanwise direction through the center of the channel and (e-h) $x-z$ plane extracted at a wall normal height of $y^+ \approx 20$. Left column of images are results from DNS and right column of images are results from RANS. (a,b,e,f) $Re_\tau \approx 500$ and (c,d,g,h) $Re_\tau \approx 1000$ at $M_b = 2$.

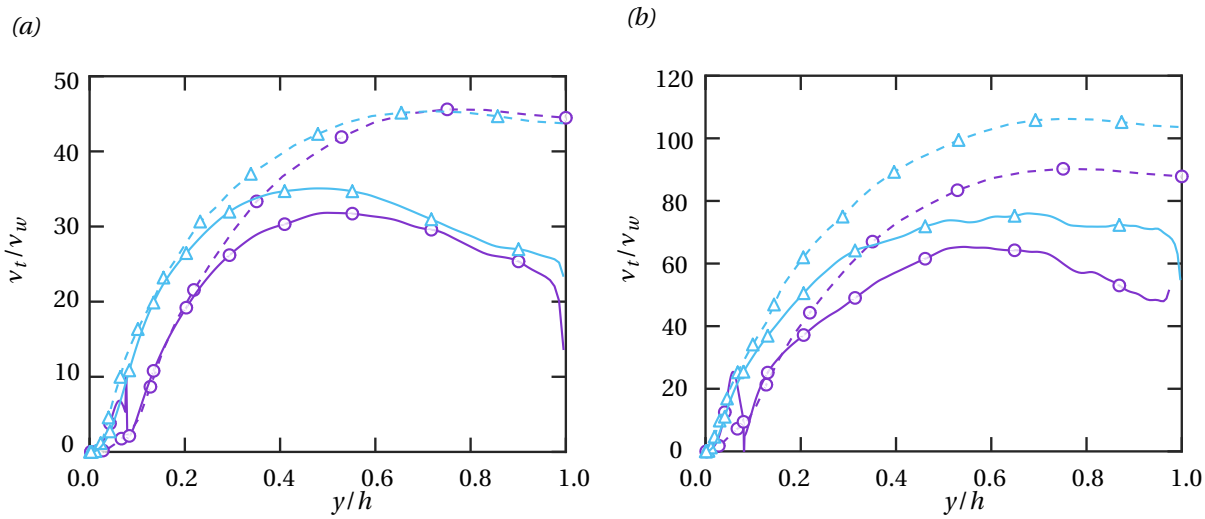

Figure 4.36: Profile of eddy viscosity scaled by viscosity at the wall at (a) $Re_\tau \approx 500$ and (b) $Re_\tau \approx 1000$ and $M_b = 2$ of smooth wall (triangles) and rough wall (circles) computed using DNS (solid lines) and RANS SA model (dashed lines).

roughness crest.

5

Conclusions and recommendations for future work

Supersonic flow over rough walls find application in ablative TPS that are used to protect the surface from excessive thermal loads. The surface is rough due to the presence of TPS in the form of tiles even before they start ablating. This pattern of roughness elements on these surfaces cause an increase in the net drag and heat transfer when compared to a smooth wall. As opposed to incompressible flow over roughness, there is no consensus on certain topics involving supersonic roughness such as outer layer similarity, delineation of the roughness regimes, validity of equivalent roughness height in characterising roughness effects and accuracy of compressibility transformations. This is mainly because of the limited number of experimental studies on supersonic roughness performed over the years. Except for a single study, there are no computational studies reported in literature either. The usage of DNS as a computational tool to study supersonic roughness is computationally expensive since resolving the roughness geometry requires even finer grid sizes than canonical DNS.

Usage of smaller domains known as minimal-span channels have shown success in studying incompressible roughness (MacDonald et al., 2017). However, this has not been tested for compressible flows. Another approach is to model the effect of roughness that has displayed promising capabilities in emulating certain important features of rough walls in incompressible flows at a fraction of the cost of studying fully resolved roughness (Busse and Sandham, 2012). While this has shown to work for incompressible flows, its extension to compressible flows has not been done yet. Lastly, a popular, cost-effective choice would be to use RANS where all the turbulent scales of motion are modeled giving an averaged flow field. The goal was to perform a fully resolved RANS simulation of supersonic roughness to see if the prediction of ΔU^+ and subsequently k_s^+ is accurate. This would allow implementation of wall models in RANS for roughness that require k_s^+ as input to impose the log-law with the velocity shift.

The goal of the current thesis was to explore the following lower cost alternatives to fully resolved DNS while studying supersonic flow over roughness

1. Minimal-span channel by MacDonald et al. (2017)
2. Parametric forcing approach by Busse and Sandham (2012)
3. RANS of resolved roughness

This was first done by analysing an already existing database of fully resolved $3D$ cube roughness geometry at roughness Reynolds numbers $k^+ \approx 40, 80$ for Mach 2 and Mach 4. This addressed the knowledge gaps in supersonic roughness. It was then followed by using the computational techniques in 1), 2) and 3) to answer the following research questions

- Can approaches 1), 2) and 3) be used to accurately predict the drag variation over supersonic roughness, namely predict ΔU^+ and k_s^+?
- Can approaches 1), 2) and 3) be used to accurately predict the heat transport over supersonic roughness, namely predict the Stanton number?

5.1. Conclusions

The analysis of DNS data of fully resolved cube roughness reveals many similarities with incompressible roughness when it comes to drag increase. However, the increase in heat transfer is far more complicated. The effect of roughness extends into the outer region of the temperature field. The minimal-span channel is capable of accurately predicting the drag in the compressible case. This is due to the presence of outer layer similarity. The accuracy in heat transfer predictions cannot be determined due to the lack of outer layer similarity in the thermodynamic statistics. This makes it difficult to judge the capability of using minimal-span channel for making heat transfer predictions. The cost savings achieved through the usage of minimal-span channel when compared to full channel DNS is a factor of $O(10^2)$ as shown in Table 5.1.

Approach	Reference	M_b	k^+	ΔU^+ error (%)	Heat transfer increase error (%)	Order of cost reduction factor
Modeled	3D Cube roughness	2	39.85	3.60	27.77	10^2
	3D Cube roughness	2	82.62	0.23	15.63	10^2
	3D Cube roughness	4	41.48	9.10	29.3	10^2
	3D Cube roughness	4	85.76	4.98	26.67	10^2
Minimal-span channel	-	2	37.26	-	-	10^2
	-	2	88.86	-	-	10^2
RANS	3D Cube roughness	2	39.44	74.87*	63.78	10^5
	3D Cube roughness	2	83.04	43.21*	47.87	10^5

Table 5.1: Comparison of drag and heat transfer increase between the three approaches (modeled roughness, minimal-span channel and RANS) and full channel DNS. M_b is the bulk Mach number, k^+ is the roughness Reynolds number, ΔU^+ is the mean velocity shift computed using Volpiani (Volpiani et al., 2020) transformation. * mean velocity shift computed using untransformed profile.

The modeled roughness shows good outer layer similarity with the smooth wall results at $M_b = 2$ and $M_b = 4$ when the roughness height parameter H is increased. This is observed for the density-scaled turbulent stresses and mean velocity defect profiles. The presence of outer layer similarity reveals the good accuracy with which drag predictions can be made using the modeled roughness approach. Although the effect of roughness is simulated, the exact recovery of roughness effects observed in the case of fully resolved DNS is not possible. In case of heat transfer, the general trends are captured when compared to fully resolved DNS data. However, the accurate prediction of heat transfer is still far more complicated when compared to accurate prediction of drag. Additionally, the modeled roughness approach cannot recover the equivalent roughness height k_s from the model parameters *a priori*. This issue is similar to the lack of a direct relation between k_s and k and represents an inherent limitation of the model. However, the model can be used in conjunction with fully resolved DNS. The estimation of k_s using ΔU^+ requires DNS of at least two roughness Reynolds numbers. It is possible to reduce the cost of performing fully resolved DNS of supersonic flow over rough walls by less than half. This can be done by matching the mean velocity profile computed using modeled roughness with the DNS data of fully resolved roughness for a given geometry, at a given k^+. The exponential relation between H^+/H^+_{norm} and k^+_s allows the estimation of k^+_s without performing the fully resolved DNS at a second k^+. This is one of the strengths of the model. Before performing this exercise, it is important to tune the model correctly for different geometries, friction Reynolds numbers and Mach numbers.

The results from fully resolved RANS using SA model at $M_b = 2$ and $k^+ \approx 40$ indicate that for a cube roughness element, there are large discrepancies in the untransformed mean velocity profile of the rough wall when compared to the results from DNS. These discrepancies reduce when k^+ is increased (and enters the fully rough regime) as shown in Table 5.1. However, these discrepancies are still too large to accurately employ RANS SA model for roughness prediction in supersonic flow over cube roughness element. The mean temperature and density profiles of rough wall using RANS SA model show deviations from the DNS results. There are also discrepancies observed between the RANS SA model and DNS results in the flow structures when the mean flow field of streamwise velocity in the $x-y$ plane is examined. The streamsie velocity flow field in the $x-z$ plane also presents similar discrepancies. The mean temperature contours are markedly different in both $x-y$ and $x-z$ planes of RANS SA model when compared to DNS. These point towards the weakness of RANS SA model to make realistically accurate roughness drag and heat transfer predictions at Mach 2 for cube roughness geometry in supersonic flows. The goal was to check if RANS of fully resolved

roughness using SA model is able to accurately predict ΔU^+ which is required as input for wall models.

5.2. Recommendations for future work

1. In addition to the compressibility transformations used in this thesis, a very recent one by Griffin et al. (2021) has shown great accuracy and is applicable to all canonical wall flows such as channel, pipe and boundary layers and all wall conditions i.e. with or without heat transfer. It is also applicable for the entire inner layer (viscous sub-layer, buffer and logarithmic layers). It would be interesting to consider this particular transformation.

2. The roughness geometries investigated were cube and bar roughness in this thesis. An interesting extension would be to perform a minimal-span channel DNS for diamond roughness element at $k^+ \approx 40$ and make a comparison with the modeled roughness profiles. This will allow the estimation of k_s without having to perform the minimal-span channel simulation at $k^+ \approx 80$. This enables the verification of the minimal-span channel concept for another $3D$ roughness geometry, the diamond roughness element. The minimal-span channel DNS has been performed at $M_b = 2$. By increasing the Mach number to $M_b = 4$ or higher, effects of variable Mach number in a minimal-span channel configuration can also be studied. Finally, a full-span channel DNS of bar roughness can also be performed to compare the results with the minimal-span channel.

3. The heat transfer effects could not be fully replicated by the modeled roughness approach. One way to overcome this is to use a different modelling approach for heat transfer term that is added to the energy equation. The term uses local quantities such as local temperature and local Mach number. It would be interesting to consider the temperature and Mach number at the hypothetical roughness crest ($y \approx 2H$) to see if it improves heat transfer predictions.

4. The accuracy of mean velocity shift for cube roughness improved with the increase in roughness Reynolds number. It would be interesting to check whether a further increase in roughness Reynolds number would improve the accuracy. The analysis has been conducted for a single roughness geometry (cube roughness) using RANS. It would be interesting to see the accuracy of RANS in capturing the roughness effects in supersonic flow when different geometries are considered. Additionally, another potential area of future work could be the testing of different RANS models, in particular, Reynolds stress models and non-linear eddy-viscosity models.

Bibliography

Abderrahaman-Elena, N., Fairhall, C. T., and García-Mayoral, R. Modulation of near-wall turbulence in the transitionally rough regime. *J.Fluid.Mech*, 865:1042–1071, 2019.

Berg, D. Surface roughness effects on a mach 6 turbulent boundary layer. *AIAA. J*, 17(9):929–930, 1979.

Bernardini, M., Modesti, D., Salvadore, F., and Pirozzoli, S. Streams: A high-fidelity accelerated solver for direct numerical simulation of compressible turbulent flows. *Comput. Phys. Commun.*, 263:107906, 2021.

Bowersox, R. Survey of high-speed rough wall boundary layers: Invited presentation. In *37th AIAA Fluid Dynamics Conference and Exhibit*, page 3998, 2007.

Bradshaw, P. Compressible turbulent shear layers. *Annu. Rev. Fluid Mech.*, 9(1):33–52, 1977.

Busse, A. and Sandham, N. D. Parametric forcing approach to rough-wall turbulent channel flow. *J.Fluid.Mech*, 712:169–202, 2012.

Canning, T. N., Chapman, G., Tauber, M., and Wilkins, M. Orderly three-dimensional processes in turbulent boundary layers on ablating bodies. *AGARD Proceedings No. 30, Paper No. 6*, 1968.

Cebeci, T. and Smith, A. Analyses of turbulent boundary layers, acad. *Press, New York*, 1974.

Chin, C., Ooi, A., Marusic, I., and Blackburn, H. The influence of pipe length on turbulence statistics computed from direct numerical simulation data. *Phys.Fluids*, 22(11):115107, 2010.

Chung, D., Monty, J., and Ooi, A. An idealised assessment of townsend's outer-layer similarity hypothesis for wall turbulence. *J.Fluid.Mech*, 742, 2014.

Chung, D., Chan, L., MacDonald, M., Hutchins, N., and Ooi, A. A fast direct numerical simulation method for characterising hydraulic roughness. *J.Fluid.Mech*, 773:418–431, 2015.

Chung, D., Hutchins, N., Schultz, M. P., and Flack, K. A. Predicting the drag of rough surfaces. *Annu. Rev. Fluid. Mech*, 53:439–471, 2021.

Clauser, F. H. Turbulent boundary layers in adverse pressure gradients. *J. Aeronaut. Sci.*, 21(2):91–108, 1954.

Clauser, F. H. The turbulent boundary layer. In *Adv. Appl. Mech.* 1956.

Coleman, G. N., Kim, J., and Moser, R. A numerical study of turbulent supersonic isothermal-wall channel flow. *J.Fluid.Mech*, 305:159–184, 1995.

Czarnecki, K. *The problem of roughness drag at supersonic speeds*, volume 3589. National Aeronautics and Space Administration, 1966.

Danberg, J. E. Characteristics of the turbulent boundary layer with heat and mass transfer: data tabulation. Technical report, NAVAL ORDNANCE LAB WHITE OAK MD, 1967.

De Vanna, F., Picano, F., and Benini, E. A sharp-interface immersed boundary method for moving objects in compressible viscous flows. *Computers & Fluids*, 201:104415, 2020.

Duan, L. and Martin, M. Direct numerical simulation of hypersonic turbulent boundary layers. part 4. effect of high enthalpy. *J.FLuid.Mech*, 684:25, 2011.

Ducros, F., Ferrand, V., Nicoud, F., Weber, C., Darracq, D., Gacherieu, C., and Poinsot, T. Large-eddy simulation of the shock/turbulence interaction. *J.Comput. Phys*, 152(2):517–549, 1999.

Ekoto, I. W., Bowersox, R. D., Beutner, T., and Goss, L. Supersonic boundary layers with periodic surface roughness. *AIAA J.*, 46(2):486–497, 2008.

Flack, K. A. and Schultz, M. P. Roughness effects on wall-bounded turbulent flows. *Phys. Fluids*, 26(10):101305, 2014.

Flack, K. A., Schultz, M. P., and Shapiro, T. A. Experimental support for townsend's reynolds number similarity hypothesis on rough walls. *Phys. Fluids*, 17(3):035102, 2005.

Flores, O. and Jiménez, J. Hierarchy of minimal flow units in the logarithmic layer. *Phys. Fluids*, 22(7):071704, 2010.

Foysi, H., Sarkar, S., and Friedrich, R. Compressibility effects and turbulence scalings in supersonic channel flow. *J.Fluid.Mech*, 509:207–216, 2004.

Furuya, Y., Miyata, M., and Fujita, H. Turbulent boundary layer and flow resistance on plates roughened by wires. *J. Fluids Eng.*, 98(4):643–643, 1976.

Gaudet, L. and Winter, K. Measurements of the drag of some characteristic aircraft excrescences immersed in turbulent boundary layers. Technical report, R.A.E Farnborough (U.K.), 1973.

Gaviglio, J. Reynolds analogies and experimental study of heat transfer in the supersonic boundary layer. *Int. J. Heat Mass Transf.*, 30(5):911–926, 1987.

Goddard Jr, F. E. Effect of uniformly distributed roughness on trubulent skin-friction drag at supersonic speeds. *J. Aerosp. Sci.*, 26(1):1–15, 1959.

Griffin, K. P., Fu, L., and Moin, P. Velocity transformation for compressible wall-bounded turbulent flows with and without heat transfer. *Proc. Natl. Acad. Sci.*, 118(34), 2021.

Guarini, S. E., Moser, R. D., Shariff, K., and Wray, A. Direct numerical simulation of a supersonic turbulent boundary layer at Mach 2.5. *J. Fluid Mech.*, 414(1):1–33, 2000.

Hama, F. R. Boundary layer characteristics for smooth and rough surfaces. *Trans. Soc. Nav. Arch. Marine Engrs.*, 62:333–358, 1954.

Hill, J., Voisinet, R., and Wagner, D. Measurements of surface roughness effects on the heat transfer to slender cones at mach 10. In *18th Aerospace Sciences Meeting*, page 345, 1980.

Huang, P., Coleman, G., and Bradshaw, P. Compressible turbulent channel flows: Dns results and modelling. *J.Fluid.Mech*, 305:185–218, 1995.

Hwang, Y. Near-wall turbulent fluctuations in the absence of wide outer motions. *J.Fluid.Mech*, 723:264–288, 2013.

Jiménez, J. Turbulent flows over rough walls. *Annu. Rev. Fluid Mech.*, 36:173–196, 2004.

Jiménez, J. and Moin, P. The minimal flow unit in near-wall turbulence. *J.Fluid.Mech*, 225:213–240, 1991.

Jiménez, J. and Pinelli, A. The autonomous cycle of near-wall turbulence. *J.Fluid.Mech*, 389:335–359, 1999.

Kim, J., Moin, P., and Moser, R. Turbulence statistics in fully developed channel flow at low Reynolds number. *J. Fluid Mech.*, 177:133–166, 1987.

Kistler, A. L. Fluctuation measurements in a supersonic turbulent boundary layer. *Phys.Fluids*, 2(3):290–296, 1959.

Klebanoff, P. Characteristics of turbulence in a boundary layer with zero pressure gradient. Technical report, NATIONAL BUREAU OF STANDARDS GAITHERSBURG MD, 1955.

Kocher, B. D., Combs, C. S., Kreth, P. A., and Schmisseur, J. D. Characterizing the streamwise development of surface roughness effects on a supersonic boundary layer. AIAA Paper 4047, 2018.

Krogstad, P.-Å., Antonia, R., and Browne, L. Comparison between rough-and smooth-wall turbulent boundary layers. *J. Fluid. Mech*, 245:599–617, 1992.

Krogstad, P.-Å., Andersson, H., Bakken, O., and Ashrafian, A. An experimental and numerical study of channel flow with rough walls. *J.Fluid.Mech*, 530:327–352, 2005.

Krogstadt, P.-Å. and Antonia, R. Surface roughness effects in turbulent boundary layers. *Experiments in fluids*, 27(5):450–460, 1999.

Kunkel, G. J., Allen, J. J., and Smits, A. J. Further support for townsend's reynolds number similarity hypothesis in high reynolds number rough-wall pipe flow. *Phys. Fluids*, 19(5):055109, 2007.

Laganelli, A. and Nestler, D. Surface ablation patterns-a phenomenology study. *AIAA J.*, 7(7):1319–1325, 1969.

Larson, H. and Mateer, G. Cross-hatching-a coupling of gas dynamics with the ablation process. AIAA Paper 68-670, 1968.

Latin, R. M. and Bowersox, R. D. Flow properties of a supersonic turbulent boundary layer with wall roughness. *AIAA J.*, 38(10):1804–1821, 2000.

Lee, J. H., Sung, H. J., and Krogstad, P.-Å. Direct numerical simulation of the turbulent boundary layer over a cube-roughened wall. *J.Fluid.Mech*, 669:397–431, 2011.

Leonardi, S., Orlandi, P., and Antonia, R. A. Properties of d-and k-type roughness in a turbulent channel flow. *Phys. Fluids*, 19(12):125101, 2007.

Lozano-Durán, A. and Jiménez, J. Effect of the computational domain on direct simulations of turbulent channels up to re τ= 4200. *Phys. Fluids*, 26(1):011702, 2014.

Luker, J. J., Bowersox, R. D., and Buter, T. A. Influence of curvature-driven favorable pressure gradient on supersonic turbulent boundary layer. *AIAA J.*, 38(8):1351–1359, 2000.

MacDonald, M., Chung, D., Hutchins, N., Chan, L., Ooi, A., and García-Mayoral, R. The minimal-span channel for rough-wall turbulent flows. *J.Fluid.Mech*, 815:5–42, 2017.

Maeder, T. *Numerical investigation of supersonic turbulent boundary layers*, volume 394. ETH Zurich, 2000.

Maise, G. and McDonald, H. Mixing length and kinematic eddy viscosity in a compressible boundary layer. *AIAA J.*, 6(1):73–80, 1968.

Mochizuki, M. Hot-wire investigations of smoke patterns caused by a spherical roughness element. *Natural Sci. Report, Ochanomizu University*, 12(2):87–101, 1961.

Modesti, D. and Pirozzoli, S. Reynolds and mach number effects in compressible turbulent channel flow. *Int.J.Heat.Fluid.Flow*, 59:33–49, 2016.

Modesti, D. and Pirozzoli, S. A low-dissipative solver for turbulent compressible flows on unstructured meshes, with openfoam implementation. *Comput. Phys*, 152:14–23, 2017.

Morkovin, M. V. Effects of compressibility on turbulent flows. *Mécanique de la Turbulence*, 367:380, 1962.

Moser, R. D., Kim, J., and Mansour, N. N. Direct numerical simulation of turbulent channel flow up to re τ= 590. *Phys.Fluids*, 11(4):943–945, 1999.

Natali, M., Kenny, J., and Torre, L. Thermoset nanocomposites as ablative materials for rocket and military applications. In *Thermosets*, pages 477–509. Elsevier, 2018.

Nikuradse, J. et al. *Laws of flow in rough pipes (Vol. 2)*. National Advisory Committee for Aeronautics Washington, 1950.

Orszag, S. A. and Patterson Jr, G. Numerical simulation of three-dimensional homogeneous isotropic turbulence. *Physical Review Letters*, 28(2):76, 1972.

Patel, A., Peeters, J. W., Boersma, B. J., and Pecnik, R. Semi-local scaling and turbulence modulation in variable property turbulent channel flows. *Phys.Fluids*, 27(9):095101, 2015.

Peltier, S., Humble, R., and Bowersox, R. Crosshatch roughness distortions on a hypersonic turbulent boundary layer. *Phys.Fluids*, 28(4):045105, 2016.

Perry, A. E., Schofield, W. H., and Joubert, P. N. Rough wall turbulent boundary layers. *J. Fluid Mech.*, 37(2): 383–413, 1969.

Pirozzoli, S. Generalized conservative approximations of split convective derivative operators. *J.Comput. Phys*, 229(19):7180–7190, 2010.

Pope, S. B. Turbulent flows, 2001.

Prandtl, L. 7. bericht über untersuchungen zur ausgebildeten turbulenz. *J. Appl. Math. Mech*, 5(2):136–139, 1925.

Raupach, M., Antonia, R., and Rajagopalan, S. Rough-wall turbulent boundary layers. *Appl. Mech. Rev.*, 44(1): 1–25, 1991.

Reda, D., KETTER, F., JR, and Fan, C. Compressible turbulent skin friction on rough and rough/wavy walls in adiabatic flow. In *7th Fluid and PlasmaDynamics Conference*, page 574, 1974.

Richardson, L. Weather prediction by numerical processes, cambridge univ. *P., London*, 1922.

Schlichting, H. and Gersten, K. *Boundary-layer theory*. Springer, 2016.

Sharif, M. and Guo, G. Computational analysis of supersonic turbulent boundary layers over rough surfaces using the k–ω and the stress–ω models. *Appl.Math.Model*, 31(12):2655–2667, 2007.

Smits, A. J. and Dussauge, J.-P. *Turbulent shear layers in supersonic flow*. Springer Science & Business Media, 2006.

Spalart, P. and Allmaras, S. A one-equation turbulence model for aerodynamic flows. In *30th aerospace sciences meeting and exhibit*, page 439, 1992.

Spina, E. F., Smits, A. J., and Robinson, S. K. The physics of supersonic turbulent boundary layers. *Annu. Rev. Fluid Mech.*, 26(1):287–319, 1994.

Stock, H. W. Surface patterns on subliming and liquefying ablation materials. *AIAA J.*, 13(9):1217–1223, 1975.

Sutton, G. W. Ablation of reinforced plastics in supersonic flow. *J. Aerosp. Sci.*, 27(5):377–385, 1960.

Toh, S. and Itano, T. Interaction between a large-scale structure and near-wall structures in channel flow. *J.Fluid.Mech*, 524:249–262, 2005.

Townsend, A. *The structure of turbulent shear flow*. Cambridge university press, 1980.

Trettel, A. and Larsson, J. Mean velocity scaling for compressible wall turbulence with heat transfer. *Phys.Fluids*, 28(2):026102, 2016.

Trevino, L. and Candler, G. V. Numerical simulation of regular surface patterns on sublimating ablative materials. In *53rd AIAA Aerospace Sciences Meeting*, page 1452, 2015.

Tyson, C. and Sandham, N. Numerical simulation of fully-developed compressible flows over wavy surfaces. *Int.J.Heat.Fl.Flow*, 41:2–15, 2013.

Uyanna, O. and Najafi, H. Thermal protection systems for space vehicles: A review on technology development, current challenges and future prospects. *Acta Astronaut.*, 2020.

Van Driest, E. R. Turbulent boundary layer in compressible fluids. *J.Aero.Sci.*, 18(3):145–160, 1951.

Venkatapathy, E., Szalai, C. E., Laub, B., Hwang, H. H., Conley, J. L., Arnold, J., and ARC, N. Thermal protection system technologies for enabling future sample return missions. *White paper submitted to the Planetary Science Decadal Survey, National Research Council, Washington, DC*, 2009.

Volpiani, P. S., Iyer, P. S., Pirozzoli, S., and Larsson, J. Data-driven compressibility transformation for turbulent wall layers. *Phys.Rev.Fluids*, 5(5):052602, 2020.

Walz, A. Compressible turbulent boundary layers with heat transfer and pressure gradient in flow direction. *J. Research Natl. Bur. Standards*, 63, 1959.

Weller, H. G., Tabor, G., Jasak, H., and Fureby, C. A tensorial approach to computational continuum mechanics using object-oriented techniques. *Comput. Phys*, 12(6):620–631, 1998.

Wenzel, C., Selent, B., Kloker, M., and Rist, U. Dns of compressible turbulent boundary layers and assessment of data/scaling-law quality. *J.Fluid.Mech*, 842:428, 2018.

Wu, Y. and Christensen, K. T. Spatial structure of a turbulent boundary layer with irregular surface roughness. *J.Fluid.Mech*, 655:380, 2010.

Wu, Y. and Christensen, K. Outer-layer similarity in the presence of a practical rough-wall topography. *Phys.Fluids*, 19(8):085108, 2007.

Zhang, Y.-S., Bi, W.-T., Hussain, F., Li, X.-L., and She, Z.-S. Mach-number-invariant mean-velocity profile of compressible turbulent boundary layers. *Physical review letters*, 109(5):054502, 2012.

Zhang, Y.-S., Bi, W.-T., Hussain, F., and She, Z.-S. A generalized reynolds analogy for compressible wall-bounded turbulent flows. *J.Fluid.Mech*, 739:392–420, 2014.